

# **A facile approach to bimetallic supported catalysts using preorganized molecular single-source precursors**

vorgelegt von

M.Sc.

Stephanie Sybille Linke

von der Fakultät II – Mathematik und Naturwissenschaften

der Technischen Universität Berlin

zur Erlangung des akademischen Grades

Doktor der Naturwissenschaften

- Dr. rer. nat. -

genehmigte Dissertation

Promotionsausschuss:

Vorsitzender: Prof. Dr. Roel van de Krol (TU Berlin)

Gutachter: Prof. Dr. Matthias Drieß (TU Berlin)

Gutachter: Prof. Dr. Christian Müller (FU Berlin)

Tag der wissenschaftlichen Aussprache: 30. April 2019

Berlin 2019



## Danksagung

Mein tiefer Dank gilt meinen beiden Betreuern, Herrn Prof. Dr. Matthias Drieß und Herrn Dr. Frank Rosowski, die mir während des gesamten Zeitraums stets mit Rat und Tat zur Seite standen, mir durch zahlreiche Diskussionen immer neue Wege aufzeigten, und mir so ermöglichten, mich fachlich und persönlich weiterzuentwickeln.

Weiter möchte ich mich bei BasCat – UniCat BASF JointLab für die interessante Aufgabenstellung und die Möglichkeit zur Durchführung dieser Doktorarbeit bedanken. Vielen Dank auch an das StE Team von BASF SE, hte, und FHI, bestehend aus Ekkehard Schwab, Christiane Kuretschka, Stephan Schunk, Sven Titlbach, Harry Kaiser, Robert Schlögl, und Annette Trunschke, für die erfolgreiche Zusammenarbeit und den wissenschaftlichen Input.

Mein großer Dank gilt unserem Synthese-Gruppenleiter Raoul Naumann d'Alnoncourt. Danke für deine mitreissende Begeisterung für die heterogene Katalyse und deinen unermüdlichen Willen, dein Wissen weiterzugeben.

Zudem gilt mein Dank dem allerersten BasCat Team, bestehend aus Christian Schulz, Verena Stempel, Michael Geske, und Raoul Naumann d'Alnoncourt, für die gegenseitige Unterstützung, den Humor und den unermüdlichen Elan während der Aufbauphase.

Vielen Dank außerdem dem gesamten BasCat Team für die gute Zusammenarbeit. Mein besonderer Dank gilt dabei meinen ehemaligen Bürokollegen Kristian Knemeyer und Piyush Ingale, sowie dem Syntheselabor, Anton Sagaltchik und Stephen Lohr. Danke für die tolle Arbeitsatmosphäre!

Danke außerdem an Lara Schäfer, Andrea Rahmel und Emanuela Toussaint für die Hilfe bei allen bürokratischen und organisatorischen Hürden.

Desweiteren möchte ich mich für die Durchführung zahlreicher Messungen bedanken: Bei Annette Trunschke, Maria Dimitrakopoulou, und Maike Hashagen für die Durchführung der DRIFTS Messungen, Dank an Marc Willinger und Xing Huang für die

TEM Messungen, Paula Nixdorf für die Einkristallmessungen, Dank an Maria Unterweger für die XRD Messungen, Christina Eichenauer für die BET Messungen, Olaf Timpe für die XRF Messungen, Harald Link, Cornelia Weh und Benjamin Paul für die ICP Messungen, Julia Bauer für die katalytische Testung und die Sorptionsmessungen, Jan-Dirk Epping und Samantha Voges für die NMR Messungen, Juana Krone und Sigrid Imme für die Elementaranalysen, und Stefan Schutte für die praktische Hilfe bei allem was rund um das Labor anfällt.

Ferner möchte ich mich bei meinem Praktikanten bzw. Masteranden Alessandro Nagel für die hervorragende Laborarbeit und die gute Zusammenarbeit bedanken.

Mein weiterer Dank gilt Sophia, Stefan, Lukas, Linda, Ina, Lisa, Roxana, Marina, Daniel, Nathalie und Kerstin für die jahrelange Freundschaft, unabhängig von Tageszeit und Aufenthaltsort.

Danke dir, Alex, für die wertvolle Unterstützung auf den letzten Metern!

Mein großer Dank gilt meinen Eltern und meiner Schwester: Danke euch für die Unterstützung während des Studiums, das stete Vermitteln von Optimismus und Kämpfergeist, und euren unerschütterlichen Glauben an mich.

*Four to six weeks in the lab can save you an hour in the library.*

G. C. Quarderer, Dow Chemical Co.

## Contents

1	Introduction .....	1
1.1	Importance of nanoalloys and bimetallic catalysts .....	1
1.2	Synthesis methods towards supported catalysts.....	3
1.3	Co-Cu, Co-Pt, and Cu-Fe alloys: State of the art .....	7
1.4	SSP approach towards supported alloy catalysts .....	9
1.5	Synthesis gas conversion to ethanol: State of the art .....	12
2	Motivation and objectives .....	15
3	Results and discussion .....	17
3.1	The Co-Pt system .....	17
3.1.1	Synthesis of the SSP .....	17
3.1.2	Decomposition and characterization of the unsupported SSP .....	19
3.1.3	Supporting of the SSPs .....	21
3.1.4	Decomposition of supported SSPs .....	22
3.1.5	Synthesis of the reference catalysts .....	23
3.1.6	Characterization of catalysts: SSP vs. Col .....	23
3.1.7	Application in syngas conversion.....	37
3.1.8	Investigation of spent catalysts .....	39
3.1.9	Discussion: Co-Pt catalysts .....	43
3.2	The Co-Cu system .....	47
3.2.1	Synthesis of the SSP .....	47
3.2.2	Decomposition and characterization of the unsupported SSP .....	49
3.2.3	Supporting of the SSPs .....	51
3.2.4	Decomposition of supported SSPs .....	52
3.2.5	Synthesis of the reference catalyst .....	53
3.2.6	Characterization of catalysts.....	53

3.2.7	Application in syngas conversion.....	64
3.2.8	Investigation of spent catalysts.....	67
3.2.9	Discussion: Co-Cu catalysts.....	71
3.3	The Cu-Fe system.....	73
3.3.1	Synthesis of the SSPs.....	73
3.3.2	Decomposition and characterization of the unsupported SSPs.....	75
3.3.3	Supporting of the SSPs.....	79
3.3.4	Decomposition of supported SSPs.....	79
3.3.5	Synthesis of reference catalysts.....	81
3.3.6	Characterization of catalysts.....	82
3.3.7	Application in syngas conversion.....	96
3.3.8	Investigation of spent catalysts.....	100
3.3.9	Discussion: Cu-Fe catalysts.....	103
4	Summary and outlook.....	107
5	Experimental.....	116
5.1	General remarks.....	116
5.2	Analytical methods.....	116
5.3	Purchased starting materials.....	119
5.4	Preparation and characterization of starting materials.....	121
5.5	Preparation and characterization of SSPs.....	125
5.6	Supporting of the SSPs.....	128
5.7	Thermolysis of the SSPs.....	128
5.8	Synthesis of reference catalysts.....	129
5.9	Catalytic testing.....	130
6	Appendix.....	131
6.1	STEM analysis.....	131

6.2	Physisorption isotherms .....	132
6.2.1	Co-Pt .....	132
6.2.2	Co-Cu .....	133
6.2.3	Cu-Fe.....	134
6.3	XRD analysis.....	138
6.3.1	Values used for calculation of particle sizes .....	138
6.3.2	Co-Pt .....	139
6.3.3	Cu-Fe.....	140
6.4	DRIFTS .....	141
6.5	Catalytic data .....	142
6.5.1	Co-Pt .....	142
6.5.2	Co-Cu .....	142
6.5.3	Cu-Fe.....	143
6.6	Citations .....	144
6.7	Abbreviations .....	162

## Abstract

Aim of this work was the development of a purposeful bottom-up synthesis route towards supported polymetallic alloy catalysts, allowing precise control over stoichiometry and mixing pattern of the respective metals on the support, and being applicable even towards metals with thermodynamically unfavorable mixing behavior. Thus, the single-source precursor (SSP) approach was developed, making use of the intrinsic mixing pattern and the pre-defined metal-to-metal ratio being present in heterobimetallic complexes, the SSPs. Further characterizations of an ideal SSP are containment of small, volatile ligands, that do not comprise any “poisoning” elements and allow mild decomposition of the SSPs for formation of the final catalyst without sintering. The SSP method was established by using three systems comprising Co-Pt, Co-Cu, and Cu-Fe:

- a) *trans*-PtPy<sub>2</sub>[Co(CO)<sub>4</sub>]<sub>2</sub> for the Co-Pt system,
- b) Et<sub>4</sub>N{Cu[Co(CO)<sub>4</sub>]<sub>2</sub>} representing the Co-Cu system, and
- c) [Et<sub>4</sub>N]<sub>3</sub>Cu<sub>5</sub>Fe<sub>4</sub>(CO)<sub>16</sub> and Na<sub>2</sub>Cu<sub>6</sub>Fe<sub>4</sub>(CO)<sub>16</sub> • 3 THF for the Cu-Fe system.

The precursors were synthesized, immobilized, activated, and characterized using X-ray diffraction (XRD), inductively coupled plasma optical emission spectroscopy (ICP-OES), X-ray fluorescence (XRF), Brunauer-Emmet-Teller (BET) isotherm, transmission electron microscopy (TEM), and diffuse reflectance infrared fourier transform spectroscopy (DRIFTS) measurement, respectively. In parallel, corresponding reference catalysts were prepared *via* conventional methods, that is co-impregnation (CoI) of metal salts, and investigated in the same manner. Finally, the catalysts were applied towards the conversion of synthesis gas (syngas) to ethanol (StE). The results of analytic investigations and the catalytic testing were used to compare the different synthesis routes.

In the first part, the Co-Pt system is discussed. Since Co-Pt alloys are known to be thermodynamically stable even as unsupported solid over a wide temperature and stoichiometry range, the Co-Pt system is used as a model case. Like this, it was proven that the SSP approach leads to homogeneously dispersed, small alloy nanoparticles.

STEM and especially DRIFTS analysis stated immense differences between the activated SSP and Col catalysts. Thus, the SSP catalyst consisted of smaller nanoparticles with an increased Co-content on the particles surface, whereas the alloy nanoparticles of the Col catalyst are bigger with a pronounced Pt-surface functionality.

The second system, that is Co-Cu, is more demanding, since single-phase Co-Cu alloys are thermodynamically not stable in the bulk in the desired temperature and stoichiometry range but are reported to exist in form of supported nanoparticles. In this case, the compounds achieved *via* the SSP approach show distinct morphological superiority, that is smaller and better dispersed particles, compared to the reference catalyst. In both cases, single-phase alloys were formed.

The third system investigated is the most complex one for several reasons: First, the phase diagram of Cu-Fe resembles the one of Co-Cu, which means that for the desired ratio, formation of thermodynamically stable alloys is not possible. Furthermore, only few documentations of metastable single-phase Cu-Fe alloys exist, mainly under extreme conditions. On the other hand, the investigated SSPs consist of 9-10 atoms in the complex core, thus probability of particle migration is theoretically decreased due to the higher mass compared to the smaller Co-Pt and Co-Cu systems. In this case, again major differences between fresh SSP and Col catalysts were detected, like better dispersion on the support, reduced particle size, and increased intimacy of the metals in case of the SSP catalysts. Nevertheless, formation of single-phase alloy particles could not be demonstrated in both cases.

Subsequently, all materials were applied in the StE reaction. In all cases, the synergistic effect led to formation of higher alcohols, which could not be achieved by the corresponding monometallic reference catalysts. Nevertheless, the morphological superiority of the SSP catalysts was not represented in the catalytic results. It is assumed that under reaction conditions, approximation of SSP and Col catalysts take place, caused by particle migration due to increased temperature, pressure, and adsorption-desorption processes. This is in accordance to existing literature. Thus, even if the cooperative effect of the integrated metals leads to the formation of the desired product, just as predicted by several calculations and modellings, it is currently not possible to make use of their full synergistic potential. Follow-up work should focus on stabilizing monophasic nanoparticles, e.g. by variation of the supporting material.

## Deutsche Kurzfassung

Ziel dieser Arbeit war die Entwicklung einer neuen Methode zur zielgerichteten Synthese geträgerter polymetallischer Legierungskatalysatoren, welche eine präzise Kontrolle über Stöchiometrie und Durchmischungsverhalten der jeweiligen Metalle auf dem Träger ermöglicht, und so sogar auf Metallsysteme mit thermodynamisch benachteiligtem Durchmischungsverhalten anwendbar ist. Die demnach entwickelte Methode basiert auf organometallischen Komplexen, den Single-Source-Präkursoren (SSPs), und profitiert von deren vordefinierten Metall-Metall-Stöchiometrien, sowie direkten Metallbindungen, was eine atomare Durchmischung der Komponenten in der molekularen Vorstufe garantiert. Darüber hinaus besitzen geeignete Komplexe leichtflüchtige Liganden, welche bei niedrigen Temperaturen desorbieren, und somit eine milde Aktivierung der Katalysatoren ermöglichen. Dies verspricht im Gegensatz zu etablierten Metallsalzpräkursoren einen weiteren intrinsischen Vorteil, da hohe Kalzinierungstemperaturen und somit Sintern der Nanopartikel schon vor der katalytischen Testung vermieden werden kann. Die SSP-Methode wurde anhand von drei Katalysatorsystemen, bestehend aus Co-Pt, Co-Cu und Cu-Fe, etabliert:

- a) das Co-Pt-System mit dem Komplex *trans*-PtPy<sub>2</sub>[Co(CO)<sub>4</sub>]<sub>2</sub>,
- b) das Co-Cu-System mit dem Komplex Et<sub>4</sub>N{Cu[Co(CO)<sub>4</sub>]<sub>2</sub>}, und
- c) das (Na-)Cu-Fe-System mit den Komplexen [Et<sub>4</sub>N]<sub>3</sub>Cu<sub>5</sub>Fe<sub>4</sub>(CO)<sub>16</sub>, und Na<sub>2</sub>Cu<sub>6</sub>Fe<sub>4</sub>(CO)<sub>16</sub> • 3 THF.

Die SSPs wurden synthetisiert, geträgert, aktiviert, und mithilfe von Röntgenbeugung (XRD), optischer Emissionsspektrometrie mit induktiv gekoppeltem Plasma (ICP-OES), Röntgenfluoreszenz (XRF), Brunauer-Emmet-Teller (BET) Messung, Transmissionselektronenmikroskopie (TEM), und diffuser Reflexions-Fouriertransformationsinfrarotspektroskopie (DRIFTS) charakterisiert. Parallel dazu wurden die entsprechenden Referenzkatalysatoren über etablierte Synthesemethoden, d.h. Co-Imprägnierung (CoI) von Metallsalzen, hergestellt, und analog zu den entsprechenden SSP-Katalysatoren charakterisiert. Schlussendlich

wurden die so hergestellten Materialien als Katalysatoren für die Umsetzung von Synthesegas (Syngas) zu höheren Alkoholen getestet.

Im ersten Teil der Doktorarbeit wurde das Co-Pt-System als Fallstudie für die Etablierung der SSP-Route herangezogen. Grundlage ist, dass Co-Pt-Legierungen laut Phasendiagramm im gewünschten Temperatur- und Stöchiometriebereich sogar ungeträgert stabil sind. Letztendlich konnten so homogen dispergierte, legierte Nanopartikel hergestellt werden, wobei die SSP-Katalysatoren durchschnittlich aus kleineren Nanopartikeln mit erhöhtem Co-Oberflächenanteil bestanden, die entsprechenden Referenzkatalysatoren aber größere Nanopartikel mit einer deutlichen Pt-Oberflächenfunktionalisierung enthalten.

Im zweiten Teil der vorliegenden Doktorarbeit wurde das Co-Cu-System untersucht. Hier stellt die Durchmischung der Metalle eine größere Herausforderung dar, da laut Phasendiagramm keine thermodynamisch stabilen Legierungen im relevanten Temperatur- und Stöchiometriebereich existieren. Vorhergehende Studien zeigten aber, dass derartige Legierungen als geträgerte Nanopartikel hergestellt werden können. Dies gelang auch mithilfe der hier verwendeten Ansätze. Dabei zeigte sich ein deutlicher Vorteil der SSP-Methode, da sich die derart hergestellten Materialien durch kleinere, besser dispergierte Nanopartikel gegenüber den Referenzkatalysatoren auszeichneten.

Im dritten und komplexesten Fall, dem Cu-Fe-System, ist laut Phasendiagramm ebenfalls die Existenz einer thermodynamisch stabilen Legierung im betrachteten Temperatur- und Stöchiometriebereich nicht möglich. Auch vorhandene Studien bezüglich geträgerter Materialien bestätigen die Existenz einphasiger metastabiler Legierungen nur in Ausnahmefällen, d.h. unter extremen Bedingungen, welche für katalytische Materialien nicht relevant sind. Zusätzlich zeichnet dieses System sich dadurch aus, aus 9-10 Metallatomen anstatt aus drei Metallzentren, wie im Falle der Co-Pt- und Co-Cu-Komplexe, aufgebaut zu sein, was aufgrund der höheren Masse Partikelmigration theoretisch erschweren sollte. Somit manifestierte sich trotz der erschwerten Bedingungen auch in diesem Fall die Überlegenheit des SSP-Ansatzes in Form von besser dispergierten, kleineren Nanopartikeln mit einer erhöhten Durchmischung der Metalle verglichen zu den co-imprägnierten

Referenzkatalysatoren. Allerdings konnte in beiden Fällen keine einphasige Legierung nachgewiesen werden.

Alle Katalysatoren wurden letztendlich auf ihre Funktion bezüglich der Umsetzung von Syngas zu Ethanol getestet. In allen Fällen führte der synergistische Effekt zur Bildung höherer Alkohole, was durch die entsprechenden monometallischen Systeme nicht erreicht werden konnte. Die morphologische Überlegenheit der SSP-Katalysatoren hat sich dagegen nicht in den katalytischen Ergebnissen abgebildet. Dies wird auf eine Angleichung der Systeme während der katalytischen Testung durch Oberflächenrestrukturierung als Folge von erhöhter Temperatur, Druck, und Adsorptions-Desorptionsprozessen zurückgeführt, was im Einklang mit bestehenden Literaturstudien ist. Obwohl der kooperative Effekt der eingesetzten Metalle demnach zur Bildung des gewünschten Produktes führt, wie es von mehreren Modellen und Kalkulationen vorhergesagt wurde, ist es folglich derzeit nicht möglich, auf das volle synergistische Potential zuzugreifen. Folgearbeiten sollten sich dementsprechend auf die Stabilisierung von geträgerten bimetallic Nanopartikeln unter Reaktionsbedingungen konzentrieren, was vor allem durch Veränderung des Trägermaterials erreicht werden könnte.



# 1 Introduction

## 1.1 Importance of nanoalloys and bimetallic catalysts

The term “alloy” is generally used for compounds in which two or more metals are mixed on an atomic level. Within the class of alloys, distinction is made between solid-solution alloys and intermetallic compounds. In bimetallic solid-solution alloys, the guest metal is randomly distributed in the crystal lattice structure of the host metal either in a substitutional or in an interstitial way, whereas in intermetallics, the two metals build up distinct crystal structures in a highly ordered manner.[1] All three cases have in common that the chemical components are present in a single homogeneous phase.

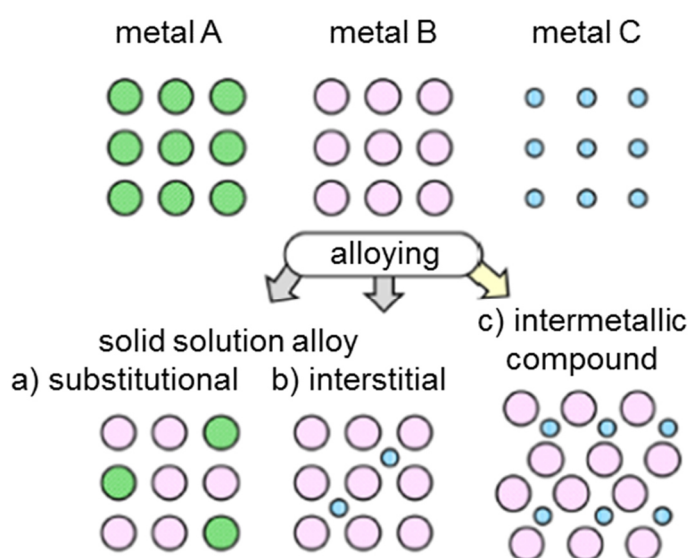


**Figure 1:** Different alloy mixing patterns described by Furukawa et al.: a) Substitutional solid solution alloy, b) interstitial solid solution alloy, c) intermetallic compound.[1]

The mixing pattern of alloys depends on several factors like the relative size of the atoms, the crystal structures of the constituents, and their electronic behavior. Thus, metals with highly similar characteristics tend to form solid solutions, whereas metals with strongly differing properties rather form intermetallics.

Different than bulk alloys, nanoalloys are size-limited aggregates that consist of a few up to millions of atoms. Due to their unique structural and electronic properties, they have aroused interest in electronics, engineering and catalysis. For example, Pt-Ru nanoalloys have been used in electrocatalysis as low temperature fuel cell catalysts,[2] and Ag-Au core-shell nanoalloys have been used as biodiagnostic agents for DNA detection.[3] As in the case of bulk alloys, the mixing and ordering of nanoalloys is dependent on factors like relative atomic sizes and electronic structure of the constituents.[4] Nevertheless, in case of size-limited alloys like nano- or surface alloys, further effects have to be considered. These finite size effects result from a complex interaction of thermodynamic factors, such as the relative surface energies, and kinetic parameters like diffusion barriers, and allow formation of different structures compared to their bulk analogues.[4,5] Like this, even mixing of elements that are immiscible in the bulk is possible, for example iron and silver, or gold and nickel.[6,7]

Since their chemical and physical properties may be adjusted by changing composition, atomic ordering, or particle size, nano- and surface alloys are promising candidates for tailoring properties of heterogeneous catalysts.[4] Already in the late 1970ies, Sinfelt discussed the possibilities of reactivity tuning that emerge from synergistic effects by alloying two metals on a substrate surface.[8] In addition to so far discussed electronic “ligand” effects, he also took into account geometric effects of surface alloys playing a crucial role in selectivity tuning, e.g. by formation of “ensembles”. [8] The concept of “ensemble” effects, that means the necessity of a critical amount of surface atoms in order to enable catalytic reactions, is further pointed out by Ponc: Regarding the example of hydrocarbon reactions over Pt-Re, Pt-Ir, or Ir-Os, it was thus shown that alloys of two transition metals being both active in the respective reaction show a maximum on the activity-alloy curve.[9] Since the exact mechanism of catalyst improvement by alloying is often unknown, the phenomenon is mainly summarized by the term “synergism” and has been proven in many examples. Like that, the lifetime of a platinum catalyst employed in naphtha reforming could be increased by more than eight times by alloying with Re, whereas its activity increased for approximately three times upon alloying with Ir.[9]

With regard to the importance of supported systems that are leaving catalysts in the desired high-surface area form, further factors like support effects have to be considered.[5] Thus, the choice of the carrier material is of utmost importance, since

additional metal-support interactions might occur and ideally can help to prevent dealloying and surface segregation. On the other hand, catalysis is a non-equilibrium process with numerous species interacting with the solid catalyst over the length of a catalytic reactor. Those adsorbates can lead to a large amount of different surface configurations being present *in situ* along the catalyst bed.[5] Moreover, most heterogeneous catalysts operate under demanding conditions, that is elevated temperature and pressure. This energy input might also lead to a change of the alloy surface composition, since diffusion barriers are more easily overcome. Hence, the aforementioned AuNi surface alloy, which is not thermodynamically stable in the bulk but existent under ultra-high vacuum conditions, undergoes dealloying when exposed to increased CO pressure, caused by formation of volatile Ni-carbonyl species.[10] Consequently, AuNi alloy catalysts are not suitable for reactions containing CO, but might find application in reactions with different adsorbants involved.

## **1.2 Synthesis methods towards supported catalysts**

Heterogeneous catalysts are ideally constituted from small particles, since this means an extension of accessible surface area compared to bulk materials, thus an immense increase in activity. Unfortunately, the treatments yielding the final catalyst, as well as the conditions of catalytic reactions themselves often lead to sintering of small particles. In order to prevent sintering and to stabilize the active surface area, the active component is preferably immobilized on an appropriate support (**Figure 2**).[11] In general, porous materials are used as supports, e.g. silica, alumina, or carbon species.

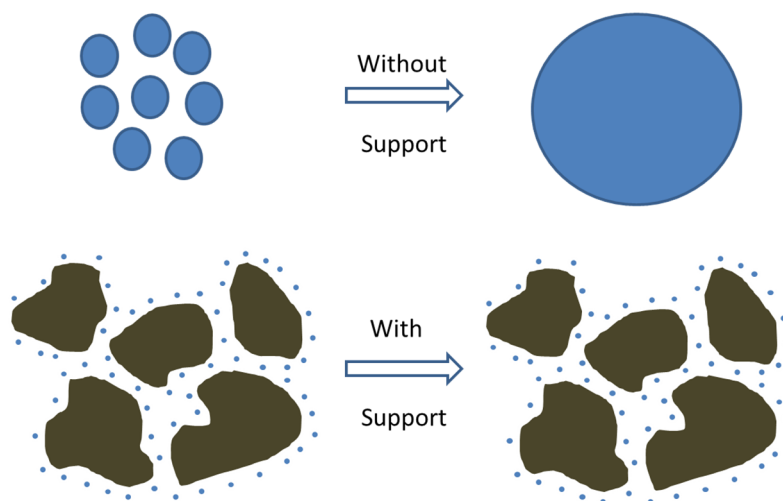


**Figure 2:** Top: Sintering of unsupported active species. Bottom: Supported thermostable active particles.[11]

To date, the two most common methods for the synthesis of supported catalysts are the precipitation method and the impregnation method.

Precipitation is a technique used to produce supported catalysts from supersaturated precursor solutions. A change of reaction conditions such as temperature, pH value, or evaporation is the driving force of a controlled precipitation. In co-precipitation, a special form of precipitation, the support and the active metal salts are dissolved and subsequently mixed, which leads to a nucleation and growth of a solid precursor. After nucleation and aging, washing steps are performed to remove undesired residuals, e.g. nitrates, sodium, and potassium (**Figure 3**). These residuals can lead to agglomeration and particle sintering in the following thermal treatment.



**Figure 3:** Mechanism of co-precipitation: The precipitated pre-catalyst ages and further calcination forms the final catalyst.[12]

In the next step, the crystalline material is calcined, thus becoming the final catalyst.

Impregnation is among the simplest and least expensive preparation methods to immobilize precursors onto suitable supports.[13] The goal is to create a high metal surface area which can be achieved by a high dispersion of precursor and mild thermal treatment. Precursors such as inorganic metal salts are commonly solved in water due to their high solubility. Among these inorganic salts are metal nitrates, oxalates, carbonates, sulfates, or chlorides. Organometallic precursors on the other hand are often moisture- and air-sensitive and therefore organic solvents are used instead. Impregnation can be divided in mainly three different steps (**Figure 4**): 1) Contact of the precursor solution with the support, 2) drying of the pre-catalyst, and 3) thermal treatment of the pre-catalyst to form the final, active catalyst.

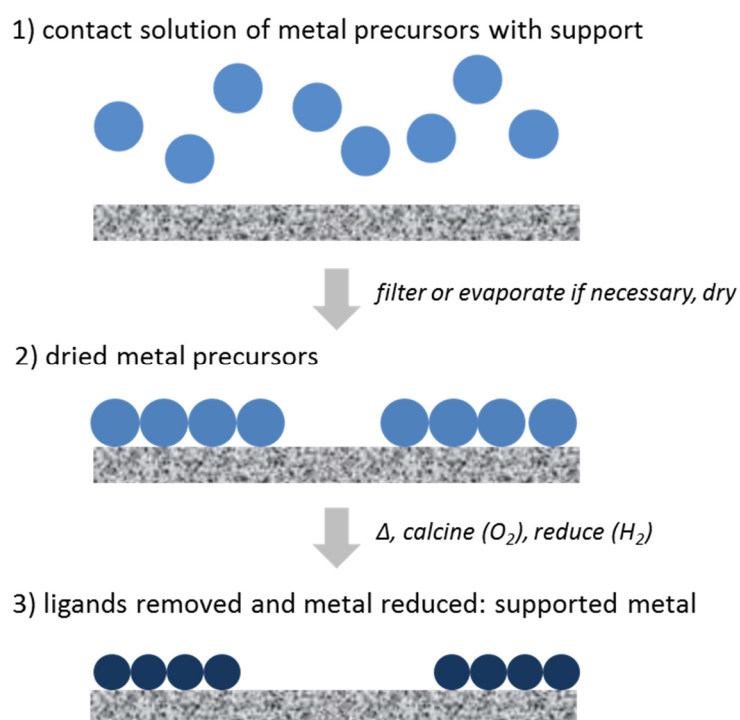


**Figure 4:** Stages of catalyst preparation by impregnation. 1) Contact of precursor solution with support; 2) filtration or evaporation and additional drying of deposited precursors; 3) removal of ligands through calcination/reduction.[13]

There are two main methods for contacting the precursor solution with the support: a) wet impregnation, and b) dry impregnation. Wet impregnation (WI) uses an excess of

solution to solve the precursors, and is also known as diffusional impregnation, since the driving force of this process is diffusion due to a concentration gradient between the precursor solution and the pores.[14] WI includes additional filtration or evaporation of abundant solvent. The driving force of the dry impregnation on the other hand is capillary force.[12] The transfer of the precursor solution into the pores takes place due to the capillary pressure difference  $\Delta p$  across the hemispherical meniscus in the pore. This process is described in accordance to the Young-Laplace equation (eq.):[12]

$$\Delta p = \left( \frac{2\gamma_{lv}}{r_p} \right) * \cos\theta \quad (\text{Eq. 1})$$

where  $r_p$  is the pore radius,  $\gamma_{lv}$  is the liquid-vapor interfacial tension and  $\theta$  the solid-liquid wetting angle. Dry impregnation is also known as capillary impregnation because of its driving force, and furthermore as incipient wetness impregnation (IWI) because the impregnated pre-catalyst appears to be dry at a macroscopic level.

The drying step, which follows the impregnation, usually is a three-stage process and comprises a phase of temperature increase, a stage where the temperature is kept constant, and a phase of decreasing temperature. Drying has a strong influence on the final catalyst as numerous physical effects occur, e.g. adsorption of the active metal onto the support, transport of the solvent, or mass and heat transfer.[13] All those physical effects can lead to redistribution of the metal profile.

The last step is activation, where the deposited metal precursor is converted into the active component.[12] Activation is in general performed by a calcination step in stagnant or flowing air to form a metal oxide, followed by a reduction step in case metallic particles are desired. The thermal treatment is of high importance, as activation conditions such as gas flow, temperature, and heating rate determine the size and composition of the nanoparticles and consequently the catalytic activity.

### 1.3 Co-Cu, Co-Pt, and Cu-Fe alloys: State of the art

According to the conferring phase diagram, Co-Pt alloys are thermodynamically stable over a wide temperature and stoichiometry range (Figure 5).[15,16]

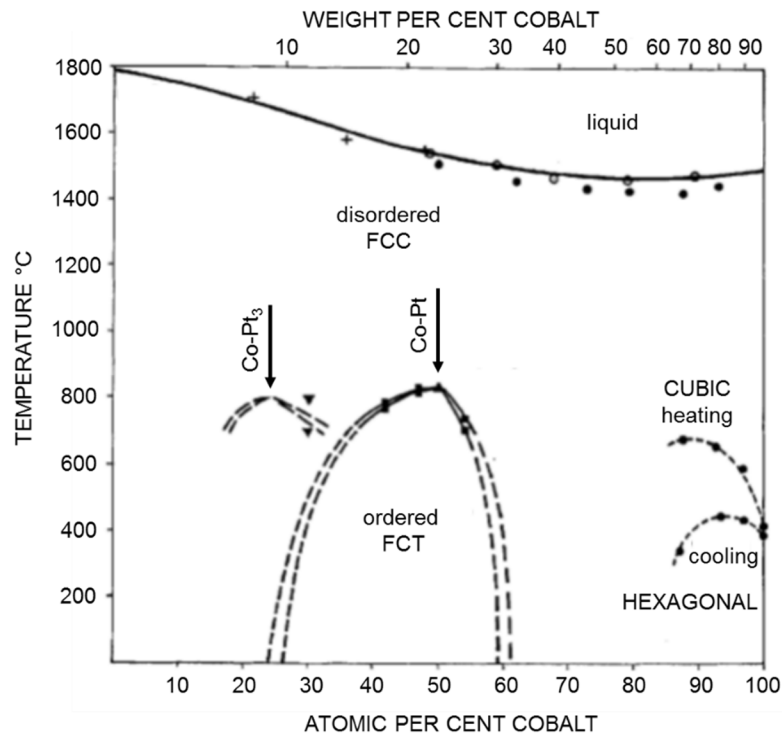


**Figure 5:** Binary phase diagram of Co and Pt (FCC: face-centered cubic, FCT: face-centered tetragonal).[15]

Hence, numerous Co-Pt alloys have been reported in the last years. They often find use as ultrahigh-density magnetic recording media because of their high magnetic anisotropy with associated high magnetic susceptibility and coercivity.[4] The group of Park and Cheon synthesized core-shell particles and intermixed  $\text{Co}_1\text{Pt}_3$  and  $\text{Co}_1\text{Pt}_1$  nanoalloys with diameters of 10 nm.[17] The intermixed Co-Pt alloys were formed *via* redox transmetalation reaction from  $\text{Co}_2(\text{CO})_8$  and  $\text{Pt}(\text{hfac})_2$  as precursors without any additional reductants. Reaction of preformed Co particles with  $\text{Pt}(\text{hfac})_2$  on the other hand leads to core-shell particles. Both reactions led to highly dispersed particles, and the compositions could be easily changed by altering the ratio of reactants. *Petridis et*

*al.* reported a synthesis for Co-Pt nanopolypods by thermolytic reduction of  $\text{Co}(\text{OAc})_2$  and  $\text{Pt}(\text{acac})_2$ . [18]

Co-Cu alloys have attracted interest because these particles show giant magneto resistance behavior which suits for electronic devices. Due to the low solubility of one metal into the other, bulk Co-Cu alloys do not exist in the temperature area relevant for most catalytic reactions (**Figure 6**). [19,20]

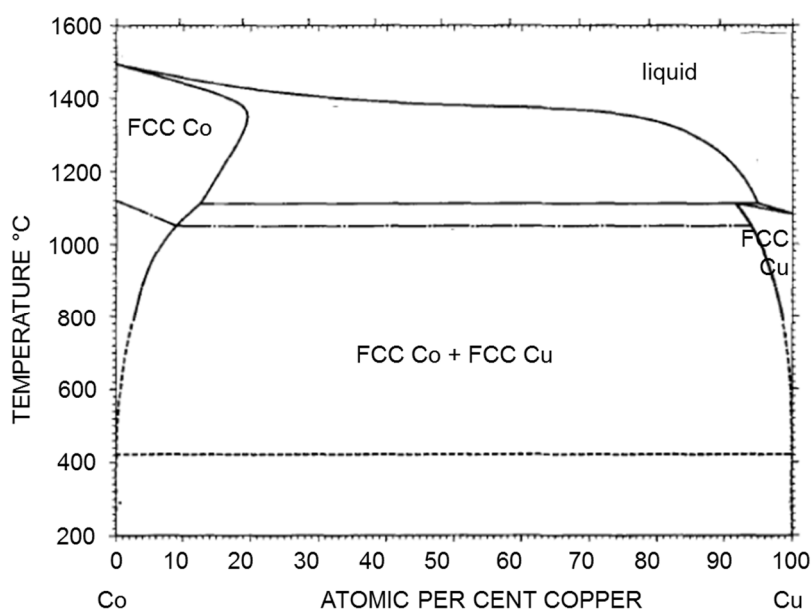


**Figure 6:** Binary phase diagram of Co and Cu. [19,20]

On a nanoscale, the electronic properties of the metals change, resulting in a higher miscibility of the metals and allowing alloy formation. Various physical and chemical procedures have been used to produce metastable alloys of Co-Cu, among them electrochemical deposition, [21] micro emulsion technique, [22] melt-spinning method, [23] and arc-melting. [24] Like this, *Wang et al.* synthesized  $\text{Cu}_{88}\text{Co}_{12}$  nanograins with a diameter of 15 nm by arc-melting of high purity Cu and Co. [24]

Regarding the Cu-Fe system, only very few reports of formation of bulk alloys exist, mainly in extreme conditions. For example, in 1996, *Drbohlav et al.* reported formation of a  $\text{Cu}_{80}\text{Fe}_{20}$  alloy using melt-spun technique. [25] They melted metallic Fe and metallic Cu in a quartz reactor under argon atmosphere and examined the composition

under annealing temperatures *via* TEM and SEM. However, at room temperature (r.t.) phase segregation of Cu and Fe took place. This fits to the corresponding binary phase diagram, according to which bulk single-phase alloys are only thermodynamically stable at very low concentrations of one metal diluted in the other one, and at extremely elevated temperatures (**Figure 7**).[26–28] Nevertheless, since the situation changes on a nanoscale, formation of supported alloy nanoparticles might be possible as seen for Co-Cu alloys.

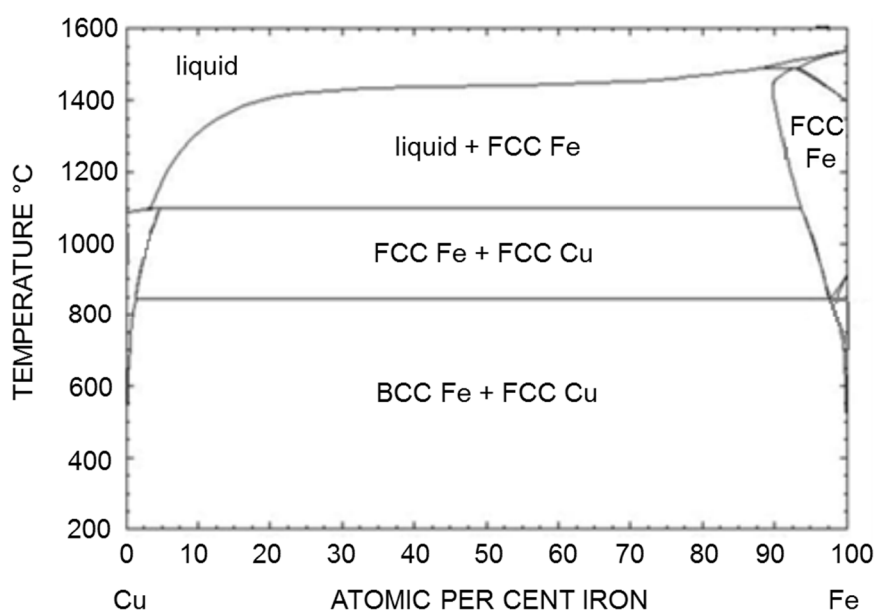


**Figure 7:** Binary phase diagram of Cu and Fe (BCC: body-centered cubic).[26–28]

#### 1.4 SSP approach towards supported alloy catalysts

To date, mainly as-described dual-source synthesis routes are usually implied to attain bi- or polymetallic catalysts. Those preparation techniques, e.g. impregnation of the support with solutions of different metal salts, are economically favored, but still bear several disadvantages. Thus, using multiple sources as starting materials often yield irregular materials.[29] Such non-uniform surfaces might cause a decrease of the catalytic performance due to the heterogeneity of active sites.[30] Furthermore, the activity of a catalytic particle is dependent on the specific surface area, thus directly proportional to the dispersion of the particles on the support. Generally, the efficiency of a catalytic particle can be enhanced by diminishing its dimensions. It was shown

that the utilization efficiency of a cubic Pt particle could be increased from 9.5 % to 26 % by reducing its length from 11.1 to 3.9 nm.[31] Hence, development of methods allowing a precise control of the distribution and composition over the supported nanoparticles are crucial for improvement of the catalytic performance.

A promising alternative to traditional methods for the synthesis of supported bimetallic catalysts is the employment of organometallic complexes as precursors, the single-source precursors (SSPs). To date, several workgroups used the SSP approach to successfully prepare heterogeneous catalysts (**Table 1**).[32–37]

**Table 1:** Examples of heterogeneous catalysts synthesized via (I)WI of SSPs.

Precursor	Catalyst	Application	Reference
[Et <sub>4</sub> N] <sub>2</sub> [Pd <sub>6</sub> Ru <sub>6</sub> (CO) <sub>24</sub> ]	Pd <sub>6</sub> Ru <sub>6</sub> / SiO <sub>2</sub>	Hydrogenation of cyclic polyenes and aromatics	[32]
Pt <sub>2</sub> Ru <sub>4</sub> (CO) <sub>18</sub>	Pt <sub>2</sub> Ru <sub>4</sub> / Al <sub>2</sub> O <sub>3</sub>	No application	[33]
[Et <sub>4</sub> N] <sub>4</sub> [Au <sub>4</sub> Fe <sub>4</sub> (CO) <sub>16</sub> ]	Au <sub>4</sub> Fe <sub>4</sub> / TiO <sub>2</sub>	Toluene oxidation	[34]
[Re <sub>2</sub> Pt(CO) <sub>12</sub> ]	Re <sub>2</sub> Pt <sub>1</sub> / Al <sub>2</sub> O <sub>3</sub>	Dehydrogenation of methylcyclohexane	[35]
PtRu <sub>5</sub> C(CO) <sub>16</sub>	Pt <sub>1</sub> Ru <sub>5</sub> / C	No application	[36]
[PPN] <sub>2</sub> [Ru <sub>10</sub> Pt <sub>2</sub> C <sub>2</sub> (CO) <sub>28</sub> ]	Ru <sub>10</sub> Pt <sub>2</sub> / SiO <sub>2</sub>	Hydrogenation of benzoic acid, dimethyl terephthalate, and naphthalene	[37]
[Ph <sub>4</sub> N] <sub>2</sub> [Ru <sub>5</sub> PtC(CO) <sub>15</sub> ]	Ru <sub>5</sub> Pt <sub>1</sub> / SiO <sub>2</sub>	Hydrogenation of benzoic acid, dimethyl terephthalate, and naphthalene	[37]

Other than the already described poly-source methods, the SSP method allows to establish a predefined metal-to-metal ratio, that is well represented on the support after the deposition process.[38] Furthermore, employment of SSPs bearing small and volatile ligands give the possibility of catalyst activation under mildest conditions, whereas calcination steps of metal salts often require high temperatures, thus fostering undesired sintering processes.

After the SSP is grafted, e.g. by reaction of functional surface groups with the complex, it is converted to the actual catalyst. In this step, the ligands are released, which might be achieved by exposure to elevated temperatures or *in vacuo*. Meanwhile, the metal centers stay on the support in direct proximity. As a result, different nanostructured

morphologies are possible, depending on a variety of factors like the relative bond strength between the two components M1 and M2, surface energies of the bulk elements M1 and M2, their relative atomic sizes, or electronic and magnetic effects:[4]

a) Single-phase alloy particles, b) separated particles, or c) core-shell particles (Figure 8).



**Figure 8:** SSP route towards supported bimetallic catalysts. Starting from the SSP, the complex is first deposited on the support and final decomposition generates the final catalyst.

Like this, the SSP route takes advantage of the well-defined atomic ratios and the proximity of the metals within the metalorganic complex. Using SSPs bearing direct metal-to-metal bonds should further facilitate formation of single-phase alloys due to the inherent mixing of the metals within the complex. The mild decomposition conditions could possibly impede phase segregation that would otherwise take place during calcination steps of metal salts at elevated temperatures. Thus, the SSP approach might give access to nanoalloys even in cases where the bulk alloys are thermodynamically not stable, and where conventional pathways towards supported alloy catalysts fail. The importance of thoroughly mixing of the different components in bimetallic catalysts is well-proven. In the most extreme case of mixing, that is alloying of two metals, a notable increase of selectivity can appear.[9] It was even shown that alloys of two transition metals, which are both active in a certain reaction, have a maximum on the activity-alloy composition curve, e.g. with regards to hydrocarbon reactions.[9] Several explanations may account for that: Either the necessity of certain ensemble sizes on the catalyst surface,[39] change of the metals d-character,[40] creation or elimination of special defect sites,[9] the effect of strain,[41,42] or suppression of self-poisoning.[9] Regardless of the countless numbers of possible explanations, the beneficial effects of alloying have already been proven for several bimetallic catalysts, e.g. for the catalytic synthesis of higher alcohols (HAS).[43] In this case, the importance lies in the availability of two different types of active sites with

one dissociating CO and forming surface alkyl species (usually the Fischer-Tropsch (FT) element, that is Fe, Co, etc.), and the other one catalyzing non-dissociative CO adsorption, thus enabling CO insertion and alcohol formation (e.g. on Cu).[43,44] Subramanian et al. prepared a series of unsupported CuCo alloy nanoparticles and compared their catalytic behaviour to Cu@Co core-shell nanoparticles, showing an improved selectivity towards higher alcohols on the alloyed nanoparticles.[45] Xiao et al. prepared a series of unsupported CuFe model catalysts and tested them for HAS, thus proving the importance of interaction of the two components *via* an atomic distance.[43] Still, due to the complexity of the HAS system, usually unsupported catalysts are employed as model catalysts in order to avoid enhanced complexity, e.g. by metal-support interactions. Xiao et al. emphasize the importance of development of controlled synthesis methods to obtain supported dual catalysts bearing a specific site structure.[43]

### **1.5 Synthesis gas conversion to ethanol: State of the art**

As the concerns of climate change, the rising of the crude oil price, and the depletion of fossil fuel resources increase, the interest in alternatives for petroleum-derived compounds grows.[46] One possible alternative is ethanol produced by the conversion of synthesis gas (syngas, CO + H<sub>2</sub>). Ethanol is an important higher alcohol, since it is known to be used for the synthesis of a variety of bulk chemicals, and furthermore used as a potential source for hydrogen fuel cells.[47–50] A common way to gain ethanol in form of bioethanol is the fermentation of biomass such as starch, cellulose, hemicellulose, and lignin. Bioethanol has been used as a fuel additive due to its combustion efficiency in automobiles and its ability to raise the octane number of gasoline.[51] However, there are disadvantages for this pathway, like high costs due to energy-intensive distillation steps, and low selectivity.[52–54]

A wide range of heterogeneous catalysts have been investigated for the conversion of syngas to ethanol (StE). These catalysts are generally categorized in four different families: (a) Rh-based catalysts, (b) Mo-based catalysts, (c) modified methanol synthesis (MS) catalysts, and (d) modified FT synthesis catalysts.

Rh-based catalysts with different promoters have been reported to attain the highest selectivity ( $S_{\text{EtOH}}$ : 54 %) and high CO conversions ( $X_{\text{CO}}$ : 39%) towards C<sub>2+</sub>

oxygenates.[55–57] The second catalyst family for StE comprises Mo-based catalysts, among them  $\text{Mo}_2\text{C}$ ,  $\text{MoS}_2$ ,  $\text{MoP}$  and  $\text{MoO}_x$ . Mo-based catalysts reached CO conversions up to 18 % and selectivity towards ethanol up to 36 %.[58–60] The third catalyst family for StE are modified MS catalysts. MS catalysts reached CO conversions up to 54 % and selectivity towards ethanol up to 9 %.[61,62] The last group of catalysts for StE are the modified FT synthesis catalysts, containing Co-Cu and Cu-Fe as the main components. FT-type catalysts reached CO conversions up to 57 %, and selectivity towards ethanol up to 28 %.[63–65] The group of Ramirez suggested a simplified surface reaction mechanism towards higher-alcohols, based on a combination of FT synthesis and MS reaction mechanisms (**Figure 9**).[66]

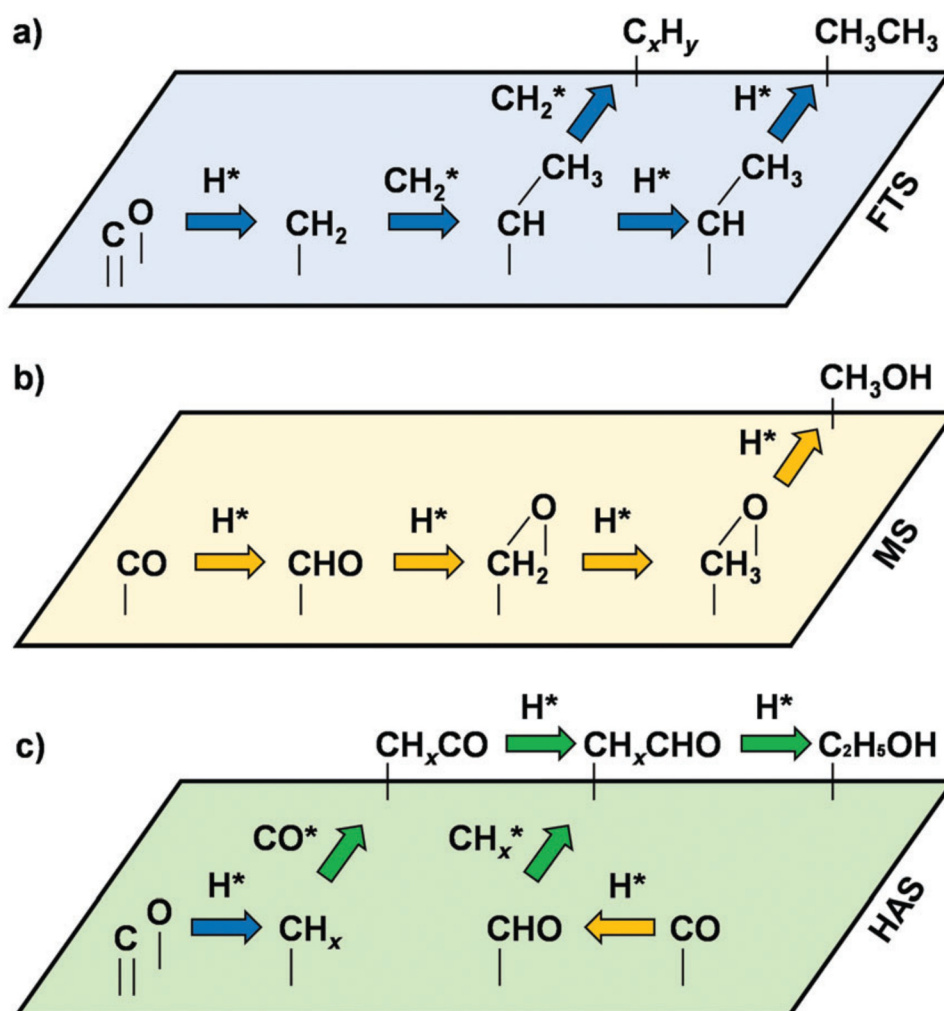


**Figure 9:** Simplified suggested pathway towards c) HAS, based on the reaction mechanisms for a) FT synthesis, and b) MS.[66]

Even though research on the StE conversion reaction has enabled distinct improvement in the last decades, still numerous challenges remain: (i) the selectivity to ethanol is still comparably low, (ii) catalyst activities are still low as  $X_{CO}$  barely reaches 50 %, and (iii) to many other main products such as hydrocarbons,  $C_{3+}$  oxygenates and  $CO_2$ , are produced. In 2014 the group of Nørskov published a study for the conversion of StE directing those issues.[67] The group investigated HA formation *via* density functional theory (DFT) calculations and put special focus on the insertion of adsorbed CO into  $CH_x$  ( $x = 0-3$ ). In order to simplify the reaction path, special attention was put on the formation of ethanol as the simplest higher alcohol, and furthermore only transition metals with (211) facets were taken into consideration. Moreover, methane and methanol were considered as side products for consideration of the product selectivity.

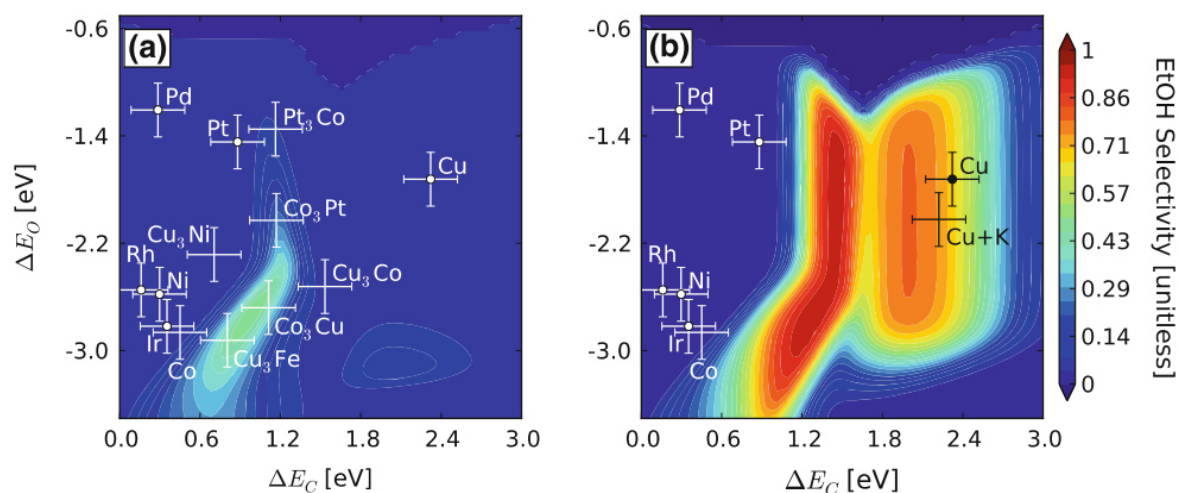


**Figure 10:** Ethanol selectivity for several alloys and single metals combined with relations of carbon ( $\Delta E_C$ ) and oxygen ( $\Delta E_O$ ) binding energies with methanol pressure of a) 0 bar and b) 15 bar. Reaction conditions are: Temperature: 593 K; 30 bar  $CO$ ; 60 bar  $H_2$ ; 0.01 bar  $H_2O$ .[67]

**Figure 10** shows diagrams correlating ethanol selectivity for different mono- and bimetallic catalysts with carbon ( $\Delta E_C$ ) and oxygen ( $\Delta E_O$ ) binding energies for methanol pressure of a) 0 bar, and b) 15 bar. Hence, ethanol selectivity in the range of 40-50 % might be achieved by utilization of alloys of  $Co_3Cu$ ,  $Co_3Pt$  and  $Cu_3Fe$  as catalysts in syngas conversion.

## 2 Motivation and objectives

To date, mainly dual-source synthesis routes are utilized to attain bi- or polymetallic catalysts. Those preparation techniques bear several disadvantages, e.g. producing non-uniform surfaces with poorly mixed metals, eventually leading to a decline of the catalytic performance due to the heterogeneity of active sites. Hence, development of a method that allows precise control of the bi- or even polymetallic particles is severely needed in order to make most use of synergism.

Thus, this work describes the development of a bottom-up synthesis route towards supported Co-Pt, Co-Cu, and Cu-Fe nanoparticles *via* the SSP route. The three bimetallic systems were chosen due to their importance in catalytic reactions, as well as their strongly differing mixing behaviors. According to the respective phase diagrams, only the Co-Pt system forms thermodynamically stable alloys in the temperature range relevant for catalytic applications, as well as for the respective metal-to-metal ratios. Whereas Co-Cu as well as Cu-Fe alloys are not thermodynamically stable in the bulk according to their phase diagrams, Co-Cu alloys nevertheless were already found to be stable as supported nanoparticles. In contrast, supported Cu-Fe alloy nanoparticles were only found to be existing under extreme conditions not relevant for catalytic applications.

The SSPs employed as starting materials ought to fulfil several criteria: 1.) The complex should bear only small, lightweight molecules which are consequently quite volatile already at low temperatures. 2.) Furthermore, those ligands ought to consist only of elements that are not known as catalyst poison for the SSPs components, e.g. chlorine or sulfur.[68–72] 3.) Regarding the complex' structure, the metals should be connected *via* direct metal-to-metal bonds. As already mentioned before, this circumstance possibly helps to facilitate alloy formation, since mixing of the metals is inherent in the complex. 4.) The SSP should be literature known, and accessible within few synthesis steps.

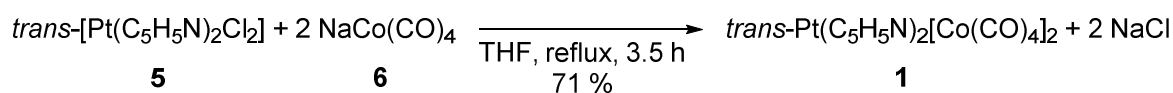
Hence, four catalyst systems were identified to fit these criteria:

- a) *trans*-PtPy<sub>2</sub>[Co(CO)<sub>4</sub>]<sub>2</sub> (**1**) as Co-Pt SSP,
- b) Et<sub>4</sub>N{Cu[Co(CO)<sub>4</sub>]<sub>2</sub>} (**2**) as Co-Cu SSP,
- c) [Et<sub>4</sub>N]<sub>3</sub>Cu<sub>5</sub>Fe<sub>4</sub>(CO)<sub>16</sub> (**3**) as Cu-Fe SSP, and
- d) Na<sub>2</sub>Cu<sub>6</sub>Fe<sub>4</sub>(CO)<sub>16</sub> • 3 THF (**4**) as alkali-doped Cu-Fe SSP, further denoted as Na-Cu-Fe SSP.

The following chapters describe the synthesis, supporting, activation, and characterization of those SSP complexes. Furthermore, the morphology of the SSP catalysts is compared to corresponding reference catalysts synthesized *via* conventional methods, that is co-impregnation (CoI) of metal salts. Finally, all catalysts were applied in a catalytic test reaction for further comparison. Since ethanol formation from syngas on bifunctional catalysts was identified to be highly dependent on the manner of mixing of the components on an atomic level,[43] and since Cu-Fe-, Co-Pt-, and Co-Cu catalysts are predicted to be active and selective for StE conversion,[67] this reaction was chosen in order to compare the catalytic behavior of SSP and CoI catalysts.







**Scheme 3:** Synthesis of *trans*-Pt(C<sub>5</sub>H<sub>5</sub>N)<sub>2</sub>[Co(CO)<sub>4</sub>]<sub>2</sub> (**1**) according to Pearson and Dehand.[74]

The Co-Pt SSP (**1**) was identified by using fourier transform infrared (FT-IR) spectroscopy, elemental analysis, and single-crystal X-ray diffraction (XRD) measurement (see chapter 5.5 Preparation and characterization of SSPs).

### 3.1.2 Decomposition and characterization of the unsupported SSP

In the next step, the unsupported complex Co-Pt SSP (**1**) was decomposed to identify the ideal activation conditions for the final catalyst. Thus, thermolysis in hydrogen atmosphere was performed and monitored *via* mass spectroscopy (MS) (**Figure 12**).

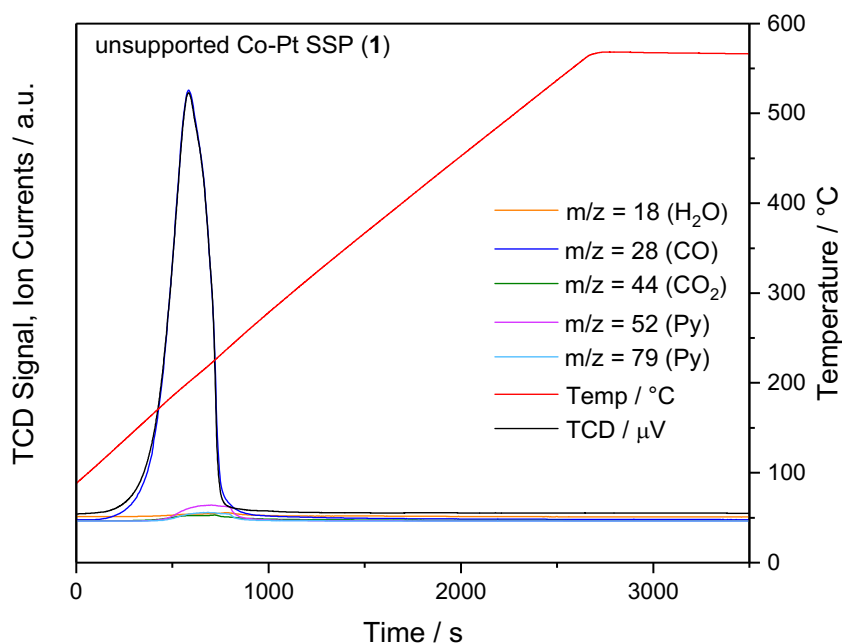


**Figure 12:** Thermolysis profile of the Co-Pt SSP (**1**) in H<sub>2</sub> atmosphere, monitored via MS.

Monitoring *via* MS shows release of the carbonyl ligands in one single step, while the pyridine ligand is decomposed in fragments. The release of CO ligands occurs at  $\sim 130$ - $240$  °C. The signal of the thermal conductivity detector (TCD) shows no H<sub>2</sub> consumption. Additionally, there is no release of H<sub>2</sub>O or CO<sub>2</sub>, consequently there is no redox reaction of the SSP taking place.

Investigation of the bulk material *via* XRD measurement proves formation of a microcrystalline material, with sharp reflexes occurring in between those of database-known CoPt- and Co<sub>3</sub>Pt-alloys. Additionally, the reflexes are not in accordance with the ones of the single metals, strongly indicating successful formation of the Co<sub>2</sub>Pt alloy (**Figure 13**). Those results are in accordance with the phase diagram, predicting that a mixture of Co and Pt in the ratio of 2:1 is alloying in the disordered face-centered cubic lattice structure in the respective temperature range.[15]

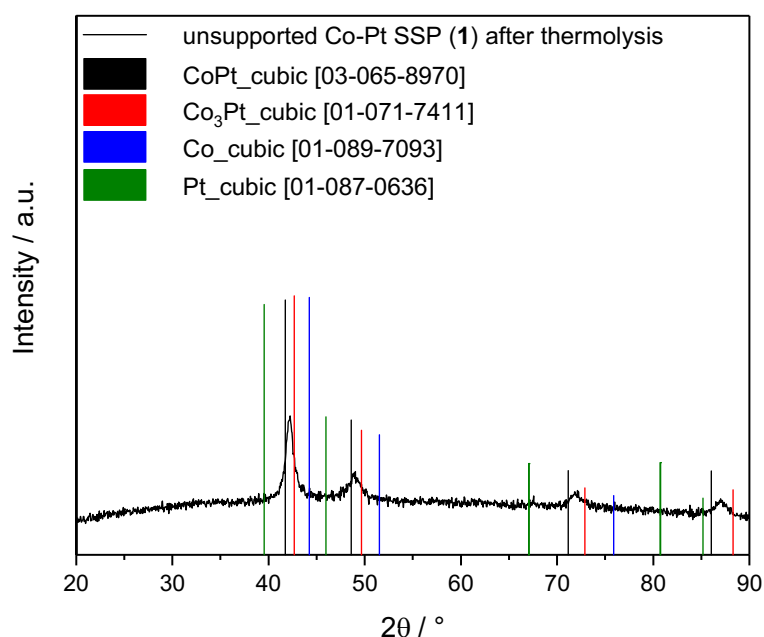


**Figure 13:** XRD analysis of the Co-Pt SSP (1) after decomposition in H<sub>2</sub> atmosphere and comparison to database entries for metallic Co and Pt as well as for known Co-Pt alloys.

Average particle sizes can be estimated from the XRD by applying Scherrer equation [78]:

$$D = \frac{K * \lambda}{\beta * \cos \theta} \quad (\text{Eq. 2})$$

with D being the average crystallite size, K being a dimensionless factor which depends on the shape and size of the particle and is usually between 0.9 – 1.2 (in these measurements, a factor of 0.9 was used which is typical for spherical particles),  $\beta$  being the line broadening at half the maximum intensity (full width at half maximum, FWHM), after subtracting the instrumental line broadening, in radians,  $\lambda$  being the X-ray wavelength (here  $K_{\alpha} = 1.541874 \text{ \AA}$ ), and  $\theta$  being the Bragg angle in degrees. This yields an approximate particle size of 8.66 nm for the Co<sub>2</sub>Pt particles detected for the unsupported decomposed Co-Pt SSP (1). Values of  $\beta$  and  $\theta$  inserted into Scherrer equation are listed in **Table A1**.

### 3.1.3 Supporting of the SSPs

Four Co-Pt SSP catalysts were prepared by immobilizing *trans*-PtPy<sub>2</sub>[Co(CO)<sub>4</sub>]<sub>2</sub> (1) on commercially available SiO<sub>2</sub> via WI or by (sequential) IWI (SIWI), from anhydrous, degassed organic solvents with a theoretical loading of 0.5, 1.0, 3.0, and 5.0 wt.% regarding Pt (**Table 2**). The supporting material was dried at 100 °C *in vacuo* prior to use in order to remove residual H<sub>2</sub>O.

**Table 2:** Overview of SSP catalysts prepared by impregnation of *trans*-PtPy<sub>2</sub>[Co(CO)<sub>4</sub>]<sub>2</sub> (1) on SiO<sub>2</sub>.

Catalyst	Impregnation method	Theoretical loading [wt.%]	
		Pt	Co
8	WI	5.00	3.02
9	SIWI	5.00	3.02
10	IWI	1.00	0.60

### 3.1.4 Decomposition of supported SSPs

The supported Co-Pt SSP (**8**) was decomposed by applying two heating steps (130 °C for 6 h, and 165 °C for 5 h, **Figure 14**) in H<sub>2</sub> atmosphere. This temperature program was chosen according to the onset of ligand release as monitored for the unsupported SSP (**1**). The lower end temperature is supposed to avoid sintering of the supported metal particles.

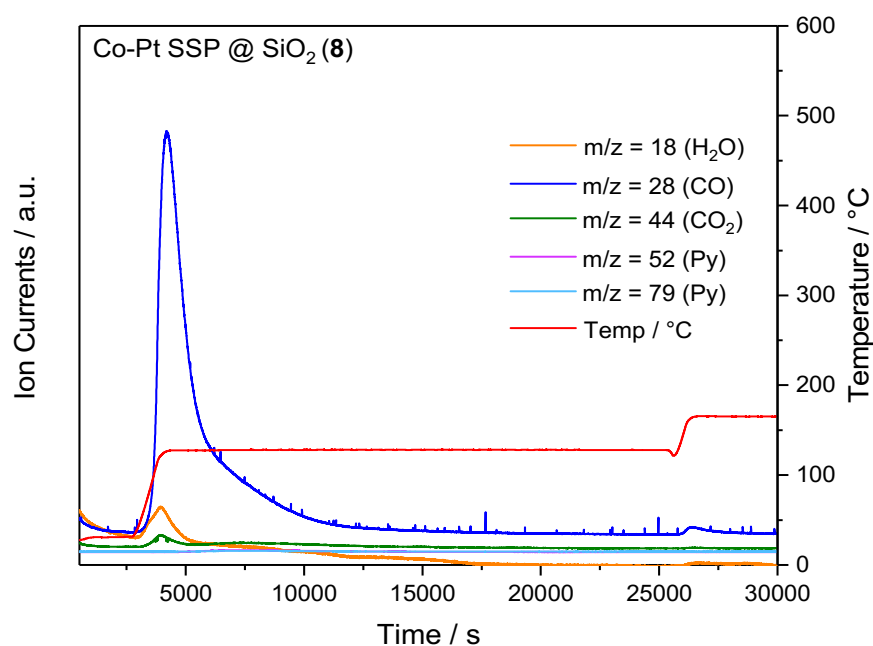


**Figure 14:** Thermolysis profile of the Co-Pt SSP supported on SiO<sub>2</sub> (**8**) in H<sub>2</sub> atmosphere, monitored via MS.

The thermolysis profile of catalyst **8** shows that almost all ligands are released during the first heating plateau, indicating that very mild conditions are sufficient for formation of the final catalyst. As in the case of the unsupported catalyst, CO as well as pyridine ligands are released in parallel. Release of a fragment with  $m/z = 18$  can be attributed to H<sub>2</sub>O left on silica after thermal treatment. Compared to the thermolysis profile of the unsupported SSP **1**, the ligands generally desorb at lower temperatures in a region of 75-130 °C. This can be explained by transfer of electron density from the hydroxyl

groups of the support to the metal centers during physisorption, resulting in weakened metal-carbonyl as well as metal-pyridine bonds, and thus ligand detachment at lower temperatures.

### 3.1.5 Synthesis of the reference catalysts

Regarding the Co-Pt-system, four CoI reference catalysts were synthesized via IWI on silica and subsequent calcination according to the literature (**Table 3**).[73,79]

**Table 3:** Overview of Co-Pt reference catalysts synthesized via IWI of dual-source precursors

Catalyst	Dual-source precursors	Theoretical loading [wt.%]	
		Pt	Co
11	Co(NO <sub>3</sub> ) <sub>2</sub> • 6 H <sub>2</sub> O, Pt(NH <sub>3</sub> ) <sub>4</sub> (NO <sub>3</sub> ) <sub>2</sub>	5.00	3.00
12	Co(NO <sub>3</sub> ) <sub>2</sub> • 6 H <sub>2</sub> O, Pt(NH <sub>3</sub> ) <sub>4</sub> (NO <sub>3</sub> ) <sub>2</sub>	1.00	0.60
13	Pt(NH <sub>3</sub> ) <sub>4</sub> (NO <sub>3</sub> ) <sub>2</sub>	5.00	/
14	Co(NO <sub>3</sub> ) <sub>2</sub> • 6 H <sub>2</sub> O	/	3.00

Since calcination of impregnated metal salts is performed in order to get rid of the inorganic counter ions and to oxidize the metal, at least the thermal decomposition temperature of the metal salts has to be applied. In this case, the reference catalysts are calcined up to 550 °C to remove the crystal water and ammonia ligands, and especially to transform the nitrates into volatile nitrous gases. This temperature lies ~400 °C above the one needed for SSP decomposition, thus having a highly increased energy input which fosters the danger of particle migration and dealloying.

### 3.1.6 Characterization of catalysts: SSP vs. CoI

#### 3.1.6.1 Elemental analysis for determination of metal loading on the support

After catalyst activation, the loading of the metals on the support was investigated by means of X-ray fluorescence (XRF), or inductively coupled plasma atomic emission spectroscopy (ICP-OES). The results for are summarized in **Table 4**.

**Table 4:** Results of XRF/ICP-OES analysis of Co-Pt SSP catalysts **8-10** and Co-Pt Col catalysts **11-14**.

Catalyst	Method	Pt loading [wt.%]		Co loading [wt.%]		Co : Pt	
		Theoretical	Analysis	Theoretical	Analysis	Theoretical	Analysis
<b>8</b>	ICP-OES	5.00	4.2	3.02	2.5	1 : 1.66	1 : 1.68
<b>9</b>	XRF	5.00	5.57	3.02	3.02	1 : 1.66	1 : 1.84
<b>10</b>	ICP-OES	1.00	1.02	0.60	0.64	1 : 1.66	1 : 1.67
<b>11</b>	XRF	5.00	4.84	3.00	2.96	1 : 1.66	1 : 1.63
<b>12</b>	XRF	1.00	1.01	0.60	0.58	1 : 1.66	1 : 1.74
<b>13</b>	XRF	5.00	4.84	/	/	/	/
<b>14</b>	XRF	/	/	3.00	2.82	/	/

ICP-OES analysis shows a highly diminished metal loading in case of the sample prepared *via* WI (**8**, ~20%). One possible explanation is the low solubility of the complex which may facilitate co-crystallization of the SSP next to the support during impregnation, and consequently result in a highly irregular SSP distribution. This is validated by analysis *via* Scanning Transmission Electron Microscopy (STEM), showing domains of unsupported Co-Pt particles (**Figure A1**). In contrast, analysis of catalysts **9** and **10** prepared *via* (S)IWI shows high agreement of theoretical to measured metal loadings, which reaffirms that impregnation driven by capillary forces eliminates co-crystallization. In case of higher metal loadings, issues caused by low solubility can be circumvented by stepwise impregnation. Catalyst **9** prepared *via* IWI shows Pt-enrichment (deviation ~11 %). For the other two SSP catalysts (**8** and **10**), the metal-to-metal ratio is preserved very well. Regarding the Col catalysts, the metal loadings are generally slightly decreased compared to the theoretical values (deviation 1-3%). A slight Pt-enrichment is observed for catalyst **12** (deviation ~5%). The relative standard deviation (RSD) for ICP-OES and XRD measurements is less than 1% in all cases described, and thus does not strikingly contribute to the aberrations.

### 3.1.6.2 Physisorption experiments for characterization of specific surface area, pore volume, and pore radii

Physisorption isotherms of the catalysts were measured by N<sub>2</sub> adsorption-desorption experiments. The isotherms were consequently used for calculation of the specific surface area *via* multipoint Brunauer-Emmett-Teller (BET) method, as well as

respective pore volume and radii using the model of Barrett, Joyner, and Halenda (BJH).[80,81] The results are summarized in **Table 5**, and compared to unloaded SiO<sub>2</sub> (entry **15**).

**Table 5:** Pore volume, pore radius, and surface area of SiO<sub>2</sub> (**15**), and Co-Pt SSP catalysts **9** and **10**, Co-Pt Col catalysts **11** and **12**, and reference catalysts **13** and **14**.

Catalyst	Loading [wt.%]		Pore volume [mL/g]	Pore radius [Å]	Surface area [m <sup>2</sup> /g]
	Co	Pt			
<b>15</b>	/	/	0.75	30.0	480
<b>9</b>	3.02	5.57	0.73	34.1	426
<b>10</b>	0.64	1.02	0.77	32.0	481
<b>11</b>	2.96	4.84	0.70	31.9	435
<b>12</b>	0.58	1.01	0.77	33.2	465
<b>13</b>	/	4.84	0.76	33.7	451
<b>14</b>	2.82	/	0.76	34.0	444

As expected, the specific surface area of unloaded SiO<sub>2</sub> (**15**) is higher than that of loaded SiO<sub>2</sub> in all cases except of catalyst **10**. In this case, the metals loading is quite low, which explains the almost unaltered surface area compared to unloaded SiO<sub>2</sub>. Furthermore, there is a trend for the specific surface area to be approximately inversely proportional to the metal loading (catalyst **9** > **11** > **13** > **14** > **10** > **12** > **15**). This is anticipated since the surface area naturally reduces with higher coverage. For all catalysts, pore volume and pore radius stay in the same range as for unloaded SiO<sub>2</sub>, suggesting successful precursor deposition without major change of the morphology of the supporting material, e.g. due to clogging.

The shape of the isotherms corresponds to a Type IV adsorption isotherm according to the International Union of Pure and Applied Chemistry (IUPAC) in all cases (isotherms depicted in **Figures A2-A4**).[82] This indicates relatively weak adsorbent-adsorbate interactions in the low  $p/p^0$  range, and molecular clustering followed by nanopore filling at higher  $p/p^0$ . [83] The typical hysteresis originates from capillary condensation in the mesopores of the material. Desorption of the adsorbate results from formation of liquid at relatively low pressure compared to the adsorption.

### 3.1.6.3 Investigation of the catalysts' bulk structure by means of powder XRD

For investigation of the bulk structure of the catalysts, XRD measurements were performed. Thus, the Col catalysts were calcined, whereas the SSP catalysts were activated under reducing atmosphere as described before. XRD measurements were then performed in air. In case of all SSP catalysts **8-10**, only the broad reflex at  $20^\circ$  belonging to the amorphous silica support can be detected, confirming integral homogeneity (**Figure A13**). The same result is achieved for the bimetallic Col catalyst **12** (**Figure A13**). In case of the higher loaded bimetallic Col catalyst **11**, reflexes belonging to metallic Pt (Fm3m) as well as cubic  $\text{Co}_3\text{O}_4$  (Fd3m) are detected *via* XRD (**Figure 15**).

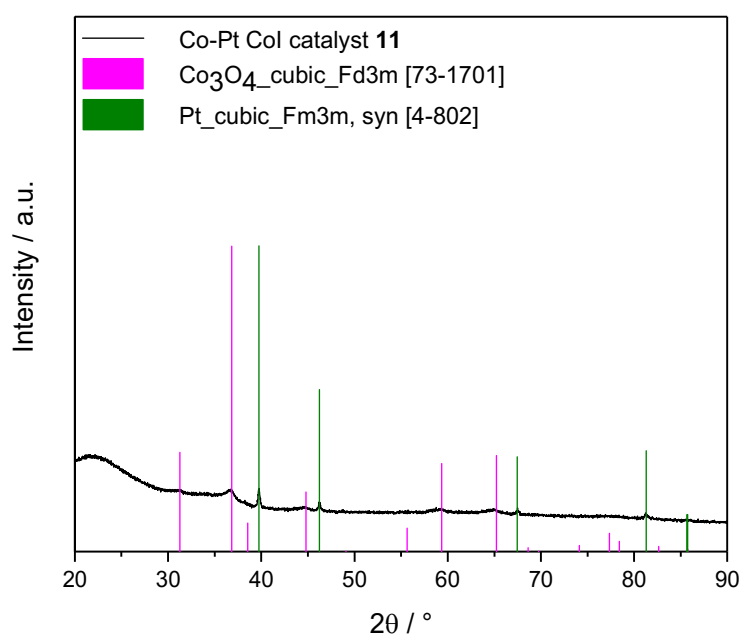


**Figure 15:** Powder XRD of Co-Pt Col catalyst **11**, stacked with database XRD patterns of cubic, metallic Pt (Fm3m), and cubic  $\text{Co}_3\text{O}_4$  (Fd3m).

Application of the Scherrer equation to the reflexes detected for catalyst **11** shows that the metallic Pt particles have an average size of approximately 38.4 nm, whereas the  $\text{Co}_3\text{O}_4$  particles have an average size of about 7.6 nm. It could be seen from the

unsupported, decomposed Co-Pt SSP (**1**) that Co<sub>2</sub>Pt alloy particles are stable at a size of ~9nm. Thus, segregation and sintering seem to be caused by the harsh calcination conditions in case of catalyst **11**. For the corresponding SSP catalyst **9**, no distinct crystallites are detected *via* XRD, thus proving that achieving integral homogeneity generally is possible even at increased metals loading by applying the milder SSP method instead of the nitrate route. Further investigation of catalyst **9**, e.g. *via* STEM would be necessary to prove existence of the Co<sub>2</sub>Pt alloy.

Powder XRD of the monometallic Pt reference catalyst **13** shows characteristic reflexes for metallic, cubic Pt, with an average crystallite size of 8.1 nm (**Figure 16**).

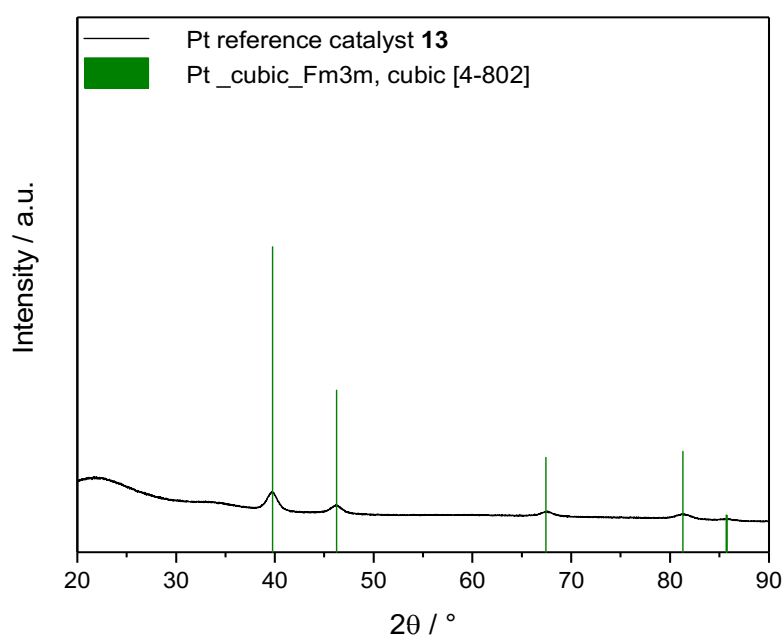


**Figure 16:** Powder XRD of CoI catalyst **13**, stacked with database XRD patterns of cubic, metallic Pt.

Regarding the XRD analysis of the monometallic Co reference catalyst **14**, cubic Co<sub>3</sub>O<sub>4</sub> particles with an approximate size of 6.8 nm are detected (**Figure 17**).

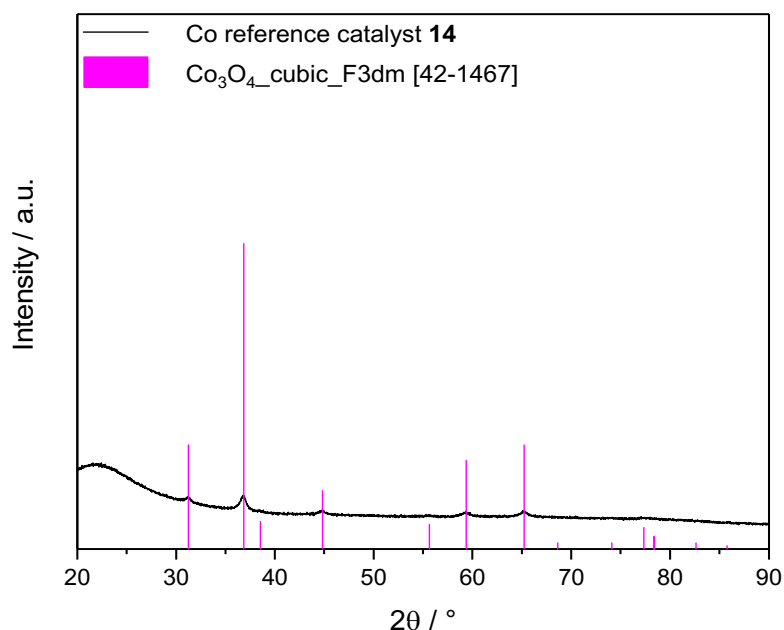


**Figure 17:** Powder XRD of CoI catalyst **14**, stacked with database XRD pattern of cubic Co<sub>3</sub>O<sub>4</sub>.

Thus, the size of the Co<sub>3</sub>O<sub>4</sub> particles in CoI catalyst **14** are in the same range as in case of the bimetallic CoI catalyst **11**, whereas the Pt particles from the monometallic reference catalyst **13** are much smaller. Since the calcination temperature as well as the metals loading is the same in all cases, the presence of Co fosters growth of larger Pt particles in the bimetallic CoI catalyst **11**.

#### 3.1.6.4 Investigation of surface morphology and composition of the activated catalysts using STEM and EDX measurements

In order to get more information about the morphology of the catalysts in the working state, SSP catalyst **10** and the corresponding calcined CoI catalyst **12** were reductively activated and characterized *via* electron microscopy. Thus, SSP catalyst **10** was activated in a procedure based on the results of the thermolysis in H<sub>2</sub> (**Figure 14**), that is first heating to 128°C for 6 h, then to 165°C for 5 h, and finally to 260 °C for 1 h in an atmosphere of flowing 10% H<sub>2</sub>/N<sub>2</sub>. In order to compare both catalysts in their active state during syngas conversion, calcined CoI catalyst **12** was reduced, too, by first

heating to 210 °C for 5 h, and then to 280 °C for 5 h to ensure complete reduction. Then, both catalysts **10** and **12** were installed in the microscope and analyzed under inert atmosphere without any air contact.

**Figure 18** shows the results of STEM of the reduced SSP catalyst **10** (left) in comparison to the activated Col catalyst **12** (right):

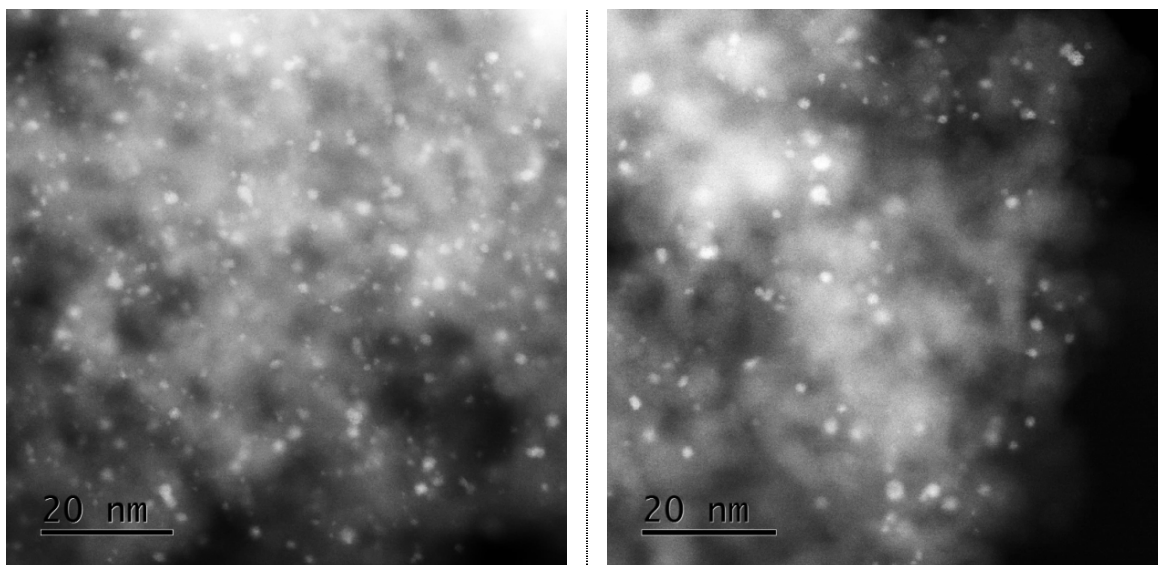


**Figure 18:** STEM analysis of Co-Pt SSP catalyst **10** (left) and Co-Pt Col catalyst **12** (right).

The images show that in both cases, small nanoparticles are homogeneously dispersed on the silica support. Comparison of the particle size distribution shows that the SSP catalyst bears slightly smaller particles than the corresponding Col catalyst, with a distribution maximum at below 1 nm (**Figure 19**). The maximum of the Col particles is found at a particle diameter size slightly above 1 nm.

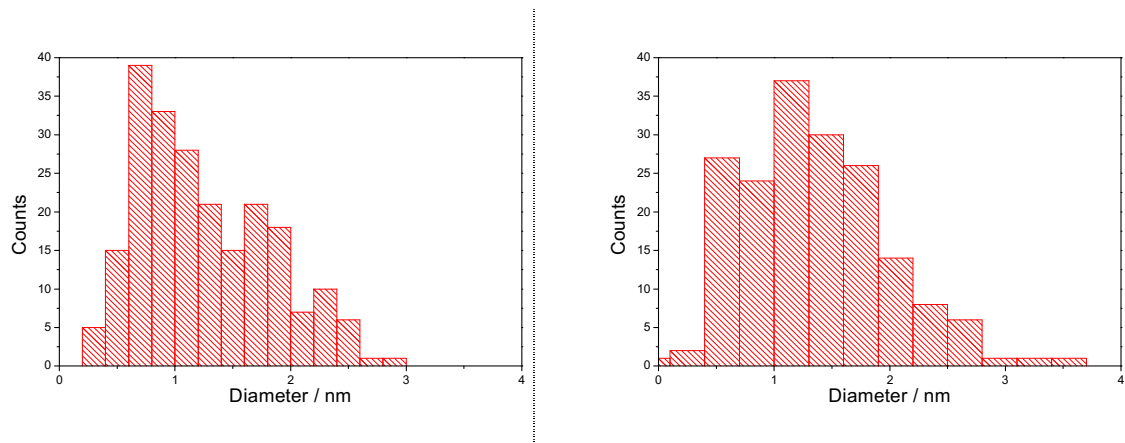


**Figure 19:** Particle size distribution of Co-Pt SSP catalyst **10** (left), and Col catalyst **12** (right).

Further comparison of the lattice fringes shows that in both cases (SSP and Col), the d-spacing of the (111) plane of the crystalline particles lies between those of Pt (111) and Co (111) (2.24 Å respectively 2.05 Å), strongly indicating Co-Pt alloy formation (**Figure 20**).

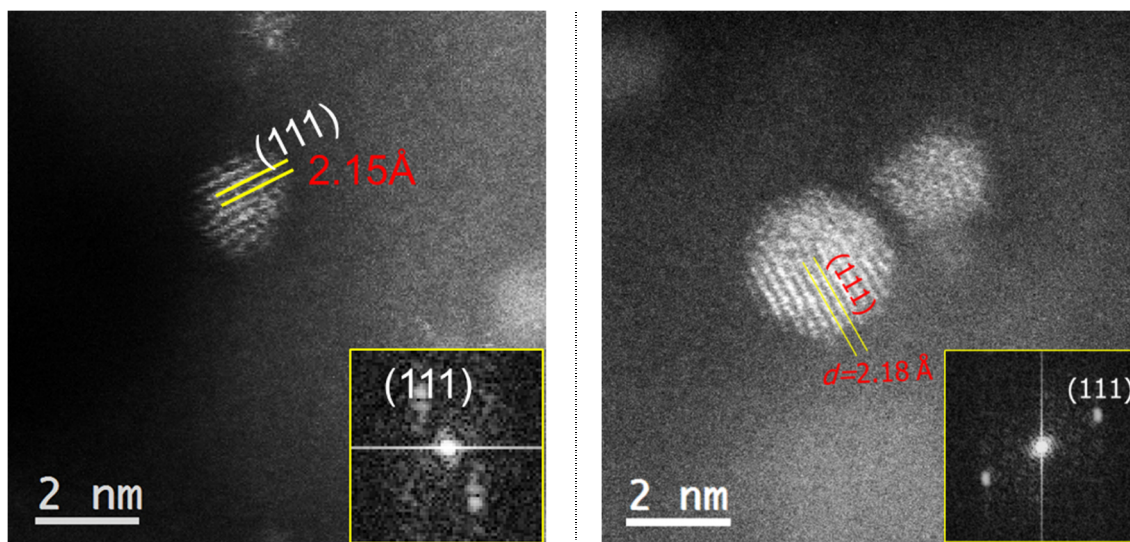


**Figure 20:** Analysis of d-spacing of SSP catalyst **10** (left) and Col catalyst **12** (right) via STEM, showing an (111) d-spacing of 2.15 Å for the SSP catalyst, and a (111) d-spacing of 2.18 Å regarding the Col catalyst.

Further analysis of the supported crystallites *via* energy-dispersive X-ray spectroscopy (EDX) line scans shows overlap of both metals over the entire investigated area, again strongly indicating Co-Pt alloy formation (**Figure 21**).

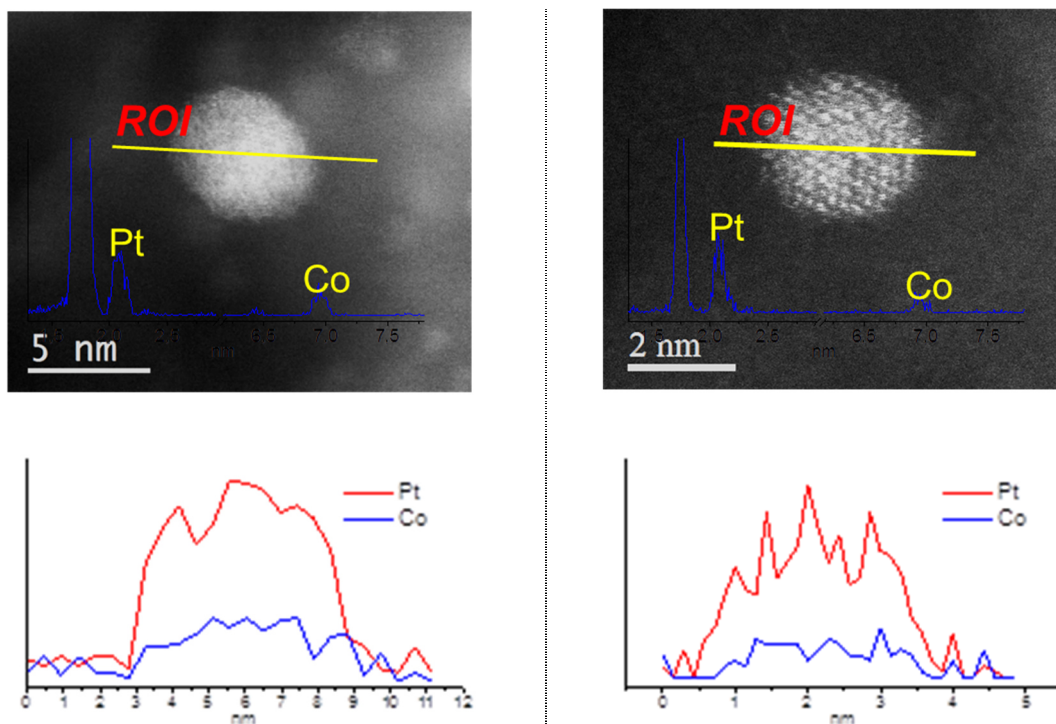


**Figure 21:** EDX line scans on particles of SSP catalyst **10** (left) and Col catalyst **12** (right).

The 5 nm sized SSP catalyst particle investigated *via* EDX line scan does not appear in the particle size distribution, since it was an exception and thus statistically not relevant. Nevertheless, it was chosen for EDX line scan in order to enable this analytical method which is hardly feasible using smaller particles.

However, exact quantification of the atomic composition of the particles cannot be done due to their small size. To determine the exact atomic composition, additional analytics such as X-ray photoelectron spectroscopy (XPS) are needed. Nevertheless, the results obtained *via* STEM and EDX measurement crucially point towards successful Co<sub>2</sub>Pt-alloy formation in both cases within the methodical possibilities. As already indicated by the results obtained from XRD measurements, the SSP approach results in smaller supported particles.

### 3.1.6.5 CO pulse chemisorption for characterization of the metal dispersion

Subsequently, CO pulse chemisorption was performed for determination of the metal dispersion, as well as the average particle size (assuming 1:1 adsorption on metal surface and full coverage). The thus achieved average particle sizes of 1.7 nm for the SSP catalyst (**10**), and 2.6 nm for the Col catalyst (**12**), are in very good agreement with the results obtained from TEM measurements. Additionally, the SSP catalyst bears a 21 % higher dispersion than the Col derived catalyst (**Table 6**).

**Table 6:** Comparison of CO adsorption, calculated dispersion, and theoretical particle size of SSP (**10**) and Col (**12**) catalyst.

Catalyst	CO Adsorption [ $\mu\text{mol/g}$ ]	Theoretical particle size [nm]	Dispersion [%]
<b>10</b>	428	1.7	61
<b>12</b>	339	2.6	40

### 3.1.6.6 Investigation of the surface functionality of activated catalysts via DRIFTS Analysis

In characterization of supported catalysts, vibrational spectroscopies are a valuable tool, since they can be used for studying the nature of surface functional groups, where XRD techniques are not suitable. This applies here, since XRD is a bulk method and ideally only proving integral homogeneity. In case of supported catalysts, common transmission techniques also fail, since the materials studied are strongly scattering with a particle size much larger than the wavelength of the IR radiation in the region of interest ( $\lambda \geq d$ ). Furthermore, the importance of vibrational spectroscopy arises from the possibility of application under *in situ* conditions. Thus, the as-prepared catalysts were further investigated *via* diffuse reflectance infrared transform spectroscopy (DRIFTS), which allows characterization of strongly scattering powder samples without preceding sample preparation, e.g. pelleting. Just as in case of the TEM measurements, all catalysts were activated in H<sub>2</sub> atmosphere at increased temperature and analyzed *via* DRIFTS without prior air contact. Like this, the conditions prevailing during catalytically driven reduction reactions should be approximated. In DRIFTS analysis, comparison of the absolute absorbance of bands

is not reasonable, since the IR pathway is influenced by the sample absorptivity, which depends on factors like metal content, level of reduction, and particle sizes, and therefore differs for each sample. Thus, only the band position and relative intensity are discussed in the following. For analysis, the data was processed *via* Schuster-Kubelka-Munk function.[84]

Thus, the CO adsorption on monometallic reference as well as bimetallic catalysts was investigated. The results are shown in **Figure 22** and **Figure 23**. CO adsorption on the monometallic reference catalysts was performed first. The catalysts were activated by heating in a feed of 13 % H<sub>2</sub> in Ar and with a ramp of 10 K/min to a temperature plateau of 360 °C for 1 h, and eventually cooling to r.t. As expected, the DRIFTS spectrum of Pt reference catalyst (**13**) shows a peak at 2048 cm<sup>-1</sup> with tailing towards lower wavenumbers with increasing amount of CO, ending at 2074 cm<sup>-1</sup> for 73.2 mbar. This is in accordance to the literature, where a band at 2080 cm<sup>-1</sup> was identified as the  $\nu^{12}\text{CO}$  frequency of linearly bound CO on Pt at full coverage, and a band at 2052 cm<sup>-1</sup> corresponding to single CO.[85] This behavior is interpreted as the sum of two effects: competition of back-donation of metal *d* electrons, as well as variations in coupling of the <sup>12</sup>CO dipoles.[85]

In accordance to existing literature, CO exposure at r.t. on the Co reference catalyst (**14**) did not show pronounced adsorption of CO on cobalt sites, but mainly bands belonging to the rotational bands of free CO.[86] By zooming in, three minor bands can be detected and assigned to terminal CO on Co<sup>0</sup> (2030 cm<sup>-1</sup>).[86] Since the two bands at 1893 and 1809 cm<sup>-1</sup> repeatedly appears in all IR spectra, also those ones concerning the Co-Cu and Cu-Fe systems, they are interpreted as artefacts caused by the measurement.

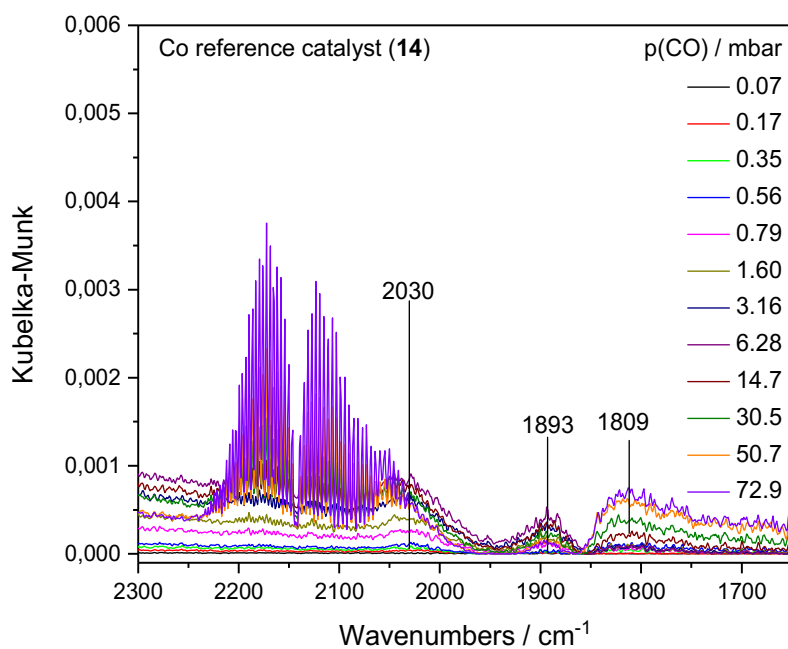
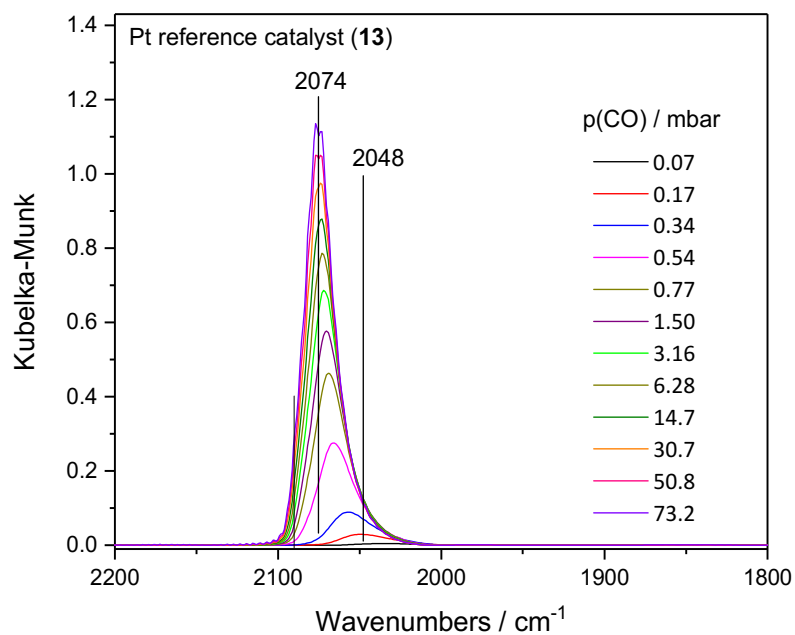


**Figure 22:** DRIFTS monitoring of CO adsorption on supported, activated Pt reference catalysts (13, top), and Co reference catalysts (14, bottom).

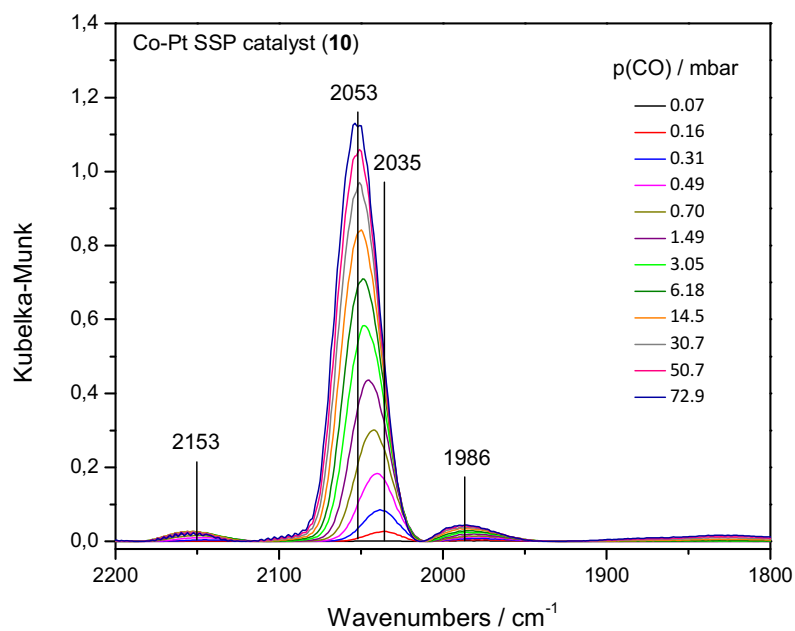
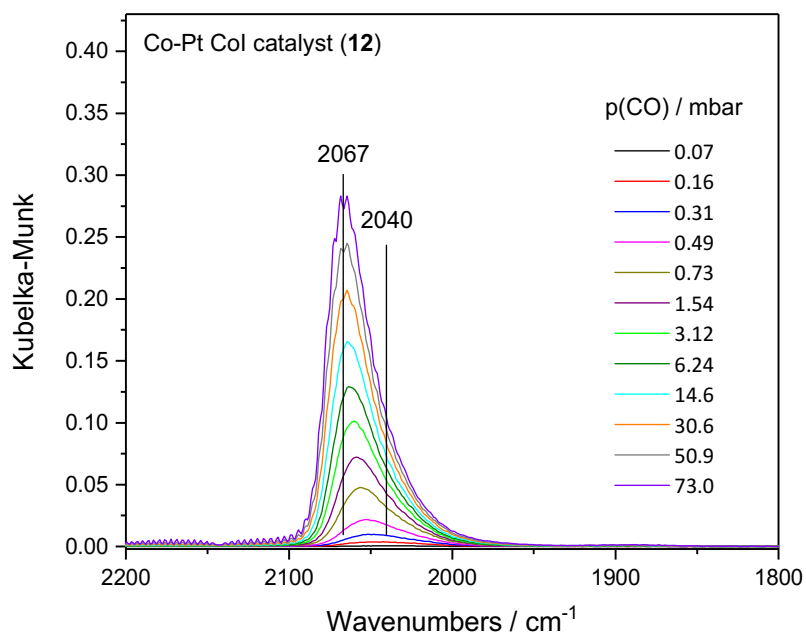


**Figure 23:** DRIFTS monitoring of CO adsorption on supported, activated Co-Pt Col catalyst (12, top), and Co-Pt SSP catalyst (10, bottom).

The measurement was repeated using the Co-Pt Col catalyst (**12**). The catalyst was activated by heating in a feed of 13 % H<sub>2</sub> in Ar and with a ramp of 10 K/min to a temperature plateau of 120 °C for 1 h, and eventually cooled to r.t. prior to measurement. Here, the catalyst shows a first band at 2040 cm<sup>-1</sup> for 0.17 mbar CO, ending at 2067 cm<sup>-1</sup> for 73.0 mbar. The red shift can be explained by the influence of Co, since Co-(νCO) vibrations are typically located at lower wavenumbers compared to the corresponding Pt-(νCO) vibrations (2034-2025 cm<sup>-1</sup> vs. 2065-2058 cm<sup>-1</sup>).[79] The bands are not symmetrically shaped, but show tailing towards lower wavenumbers, just like the Pt-sample (**13**), indicating a heterogeneous distribution of carbonyls on the crystallites, e.g. by clustering or formation of islands.[85]

In case of the Co-Pt SSP sample (**10**), the catalyst was activated as elaborated *via* thermolysis in H<sub>2</sub> atmosphere, monitored by MS, by heating in a feed of 13 % H<sub>2</sub> in Ar and with a ramp of 10 K/min to a first temperature plateau of 115 °C for 1 h, then cooled to r.t., heated to a second plateau of 150 °C for 1 h, and eventually cooled to r.t. prior to measurement. The bands at the beginning of CO adsorption (2035 cm<sup>-1</sup>) and at the end of CO dosing (2053 cm<sup>-1</sup>) are red shifted towards lower wavenumbers compared to the Pt as well as the Co-Pt Col catalyst (**13** and **12**), indicating suppression of Pt surface functionality, e.g. by increasing influence of Co due to an increased mixture of the two metals on the surface caused by alloying. Additionally, the bands are symmetrically shaped and do not show tailing towards lower wavenumbers as observed for mere Pt (**13**) or for the Co-Pt Col catalyst (**12**), indicating a homogeneous manner of carbonyl distribution on the crystallites.[85] Furthermore, additional bands at 2202, 2153, and 1986 cm<sup>-1</sup> can be observed, with the latter one indicating bridged and multi-bonded CO on cobalt.[79] The band at 2153 cm<sup>-1</sup> is designated to Co<sup>n+</sup>-carbonyls.[87] Since the SSP catalyst (**10**) shows approximately four times higher adsorption than the respective Col catalyst (**12**) at full adsorption, the latter one consists of considerably bigger particles.[88] This finding is in agreement with the results from CO chemisorption as well as STEM measurement.

Thus, the freshly prepared Col catalyst (**12**) consists of considerably bigger particles, that have a pronounced Pt-surface functionality, whereas the SSP catalyst (**10**) is constituted of smaller particles with a Co-surface functionality.

### 3.1.7 Application in syngas conversion

After supporting, decomposition, and characterization, the SSP catalyst **10**, the monometallic reference catalysts **13** and **14**, and the bimetallic CoI reference catalyst (**12**) were tested for the conversion of synthesis gas to ethanol in a fixed bed reactor. The samples were pre-treated at 54 bar and 265 °C for 1 h in a flow of 58.3 ml/min of 5 %H<sub>2</sub>/N<sub>2</sub>. The reactors were then cooled to the reaction temperature, that is 260 °C. The measurement was performed with a pressure of 54 bar, a CO:H<sub>2</sub> ratio of 2:1, temperature steps of 260, 280, 300, 320, 300, 280, and 260 °C, and a gas hourly space velocity (GHSV) of 3500 h<sup>-1</sup>. The total flow rate used was 58.3 mL/min. For the following discussion, activities are determined on basis of the highest CO conversions at 320 °C. Product selectivity is discussed at 320 °C except for the Co reference catalyst (**14**). In this case, the CO conversion at 260 °C was chosen to compare results at similar CO conversions. Furthermore, C<sub>2+</sub> alkanes are defined as *n*-alkanes with a carbon number of at least two, and olefins contain ethylene, propene, and 1-butene. All higher hydrocarbons (branched) are summarized as C<sub>4+</sub> hydrocarbons.

During catalytic testing of the Co-Pt SSP catalysts with a theoretical Pt-loading of 5.00 wt.% (**8**, **9**, and **11**), hot spots occurred. Hence, the measurements were repeated using catalysts with a lower loading of 1.00 wt.% regarding Pt. The results regarding CO conversion are summarized in **Table 7**. The monometallic Co catalysts **14** shows by far the highest activity ( $X_{\text{CO}} = 24\%$ ). The activity of the remaining three catalysts is in the same range and comparatively low between 2.7 and 3.1 % CO conversion.

**Table 7:** Overview of CO conversion of Co-Pt SSP, CoI, and monometallic reference catalysts, obtained at 320 °C.

Entry	Type of catalyst	Measured Co loading [wt.%]	Measured Pt loading [wt.%]	X <sub>co</sub> [%]
<b>13</b>	Pt reference	/	4.84	2.7
<b>14</b>	Co reference	2.82	/	24
<b>10</b>	Co-Pt SSP	0.64	1.02	3.1
<b>12</b>	Co-Pt CoI	0.58	1.01	2.9

The product spectra of the four catalysts were determined *via* gas chromatography (GC) and summarized in **Table 8**. For better comparability of the different catalysts, results measured at similar conversions and therefore at different temperatures are used.

**Table 8:** Catalytic performance of Co-Pt SSP catalyst (**10**), Co-Pt Col catalyst (**12**), Pt reference catalyst (**13**) measured at 320 °C, and Co reference catalyst (**14**), measured at 260 C. Conversion and selectivities are given in %.

Cat.	X(CO)	S(CH <sub>4</sub> )	S(C <sub>2+</sub> Alkanes)	S(Olefins)	S(MeOH)	S(EtOH)	S(PrOH)	S(CO <sub>2</sub> )	S(C <sub>2+</sub> Oxy)	S(C <sub>4+</sub> CHs)
<b>13</b>	2.7	13	36	0.1	0	0.2	0.4	0	3.4	48
<b>14</b>	5.5	29	20	9.4	8.1	0	0.2	0	1.5	32
<b>10</b>	3.1	16	9.6	0.7	52	1.7	4.2	12	0.9	3.4
<b>12</b>	2.9	18	7.6	0.5	54	2.1	3.9	9.1	1.0	3.2

As expected, Pt works as hydrogenation catalyst and does not dissociate CO, thus is mainly forming higher alkanes and no alcohols. Therefore, 13 % methane, 36 % C<sub>2+</sub> alkanes, and 48 % C<sub>4+</sub> hydrocarbons are obtained over the Pt reference catalyst (**13**).

Co is a known FT catalyst, which is reflected in the results obtained over the Co reference catalyst (**14**), forming mainly alkanes (29 % methane, 20 % C<sub>2+</sub> alkanes), olefines (9.4 %), C<sub>4+</sub> hydrocarbons (32 %), and MeOH (8.1 %).

A synergistic effect is observed on both bimetallic catalysts (**10**) and (**12**), where the product spectrum is dominated by the formation of alcohols. Thus, methanol, ethanol, and propanol are formed in almost equal amounts with methanol being the main product (54 % and 52 %). Since barely no higher alcohols are formed over the monometallic reference catalysts, the synergistic effect of both metals is needed for ethanol formation, as predicted in the literature.[67,73] Additionally, methane is formed as the second main product due to FT functionality, followed by CO<sub>2</sub> being a product from water gas shift reaction. Since the results obtained over both bimetallic catalyst systems are almost equal, the morphological differences of the fresh catalysts obtained *via* the differing synthesis routes are not stable under testing conditions, where both catalysts seem to form highly similar active surface sites. The results are summarized in **Figure 24**.

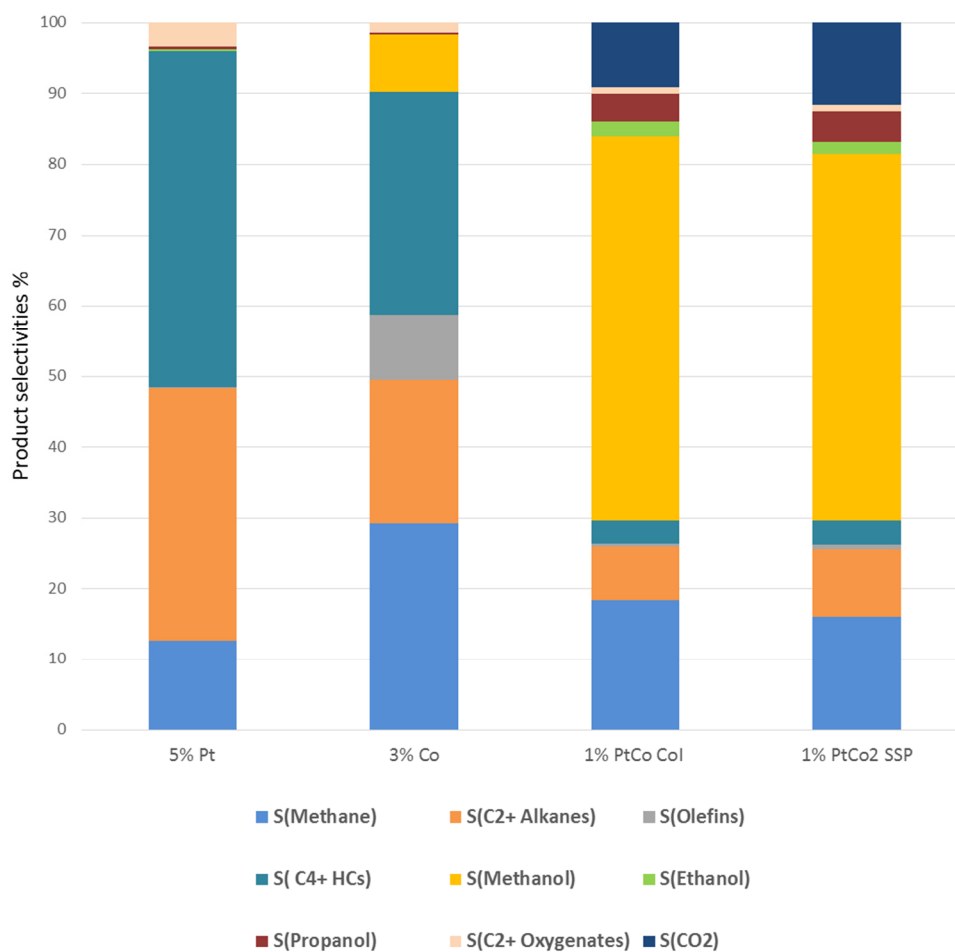


**Figure 24:** Product spectrum determined at 320 °C, except for the Co reference catalyst (260 °C). From left to right: Monometallic Pt-catalyst (**13**); monometallic Co-catalyst (**14**), Co-Pt SSP catalyst (**10**), and Co-Pt Col catalyst (**12**).

### 3.1.8 Investigation of spent catalysts

#### 3.1.8.1 Investigation of the bulk structure *via* XRD analysis

Investigation of the spent catalysts *via* XRD did not show pronounced peaks but gave hint towards the existence of cubic CoO particles in both cases (**Figure 25**). Application of Scherrer equation (**Eq. 2**) yielded CoO particle sizes of 35.9 nm regarding the Co-Pt SSP catalyst (**16**), and 30.2 nm in case of the Col catalyst (**17**). Before catalytic measurement, both catalysts showed only the broad reflex at 20 ° belonging to the amorphous silica support, confirming integral homogeneity (**Figure A13**). Thus, XRD spectra of the spent catalysts give hint towards sintering of Co particles during syngas reaction.

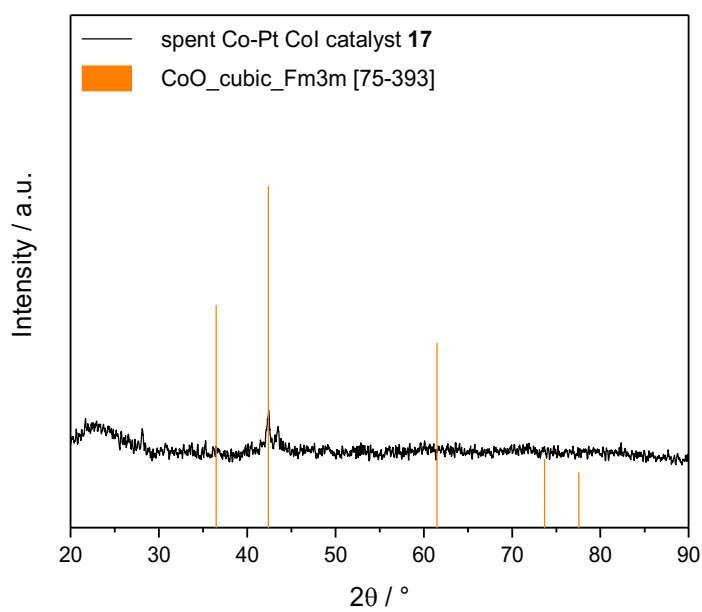
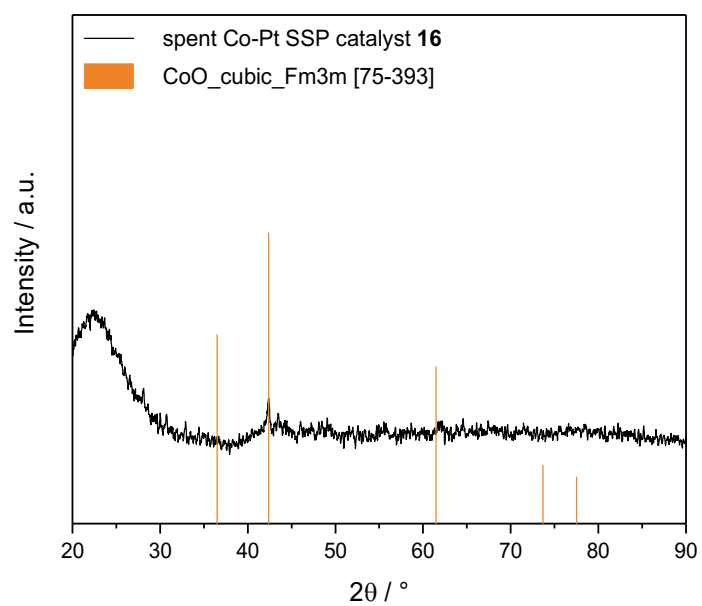


**Figure 25:** Powder XRD of spent Co-Pt SSP catalyst **16** (top), and spent Col catalyst **17** (bottom), stacked with database XRD pattern of cubic CoO.

### 3.1.8.2 Investigation of the surface functionality *via* DRIFTS analysis

After catalytic testing, the spent Pt-Co SSP catalyst (**16**) and the corresponding Col catalyst (**17**) were furthermore investigated *via* DRIFTS in order to determine the surface morphology during the catalytic testing. Thus, the spent catalysts were heated up to 250 °C with a ramp of 10 K/min in a reducing atmosphere of 13 %H<sub>2</sub>/Ar. After 1 h holding time, the catalysts were cooled down to r.t. The gaseous atmosphere was removed *in vacuo*, and CO adsorption experiments were performed (**Figure 26**).

Whereas both catalysts have a peak at 2063 cm<sup>-1</sup> at the end of measurement (~73 mbar CO), a minor difference of 5 cm<sup>-1</sup> between SSP (**16**) and Col (**17**) sample appears in the beginning of CO adsorption experiments (0.16 mbar CO). Bands in this area usually indicate terminally bound CO on Pt at differing coverage.[85] In both cases, the bands are not symmetrically shaped, but exhibit tailing towards lower wavenumbers, just like the Co-Pt Col catalyst before testing (**12**), and unlike the corresponding Co-Pt SSP catalyst (**10**). This can be explained by formation of a heterogeneous layer of carbonyls on the crystallites, e.g. by clustering or formation of islands.[85] The spent Col catalyst (**17**) shows slightly less adsorption than the spent SSP catalyst (**16**), thus indicating bigger particles.[88]

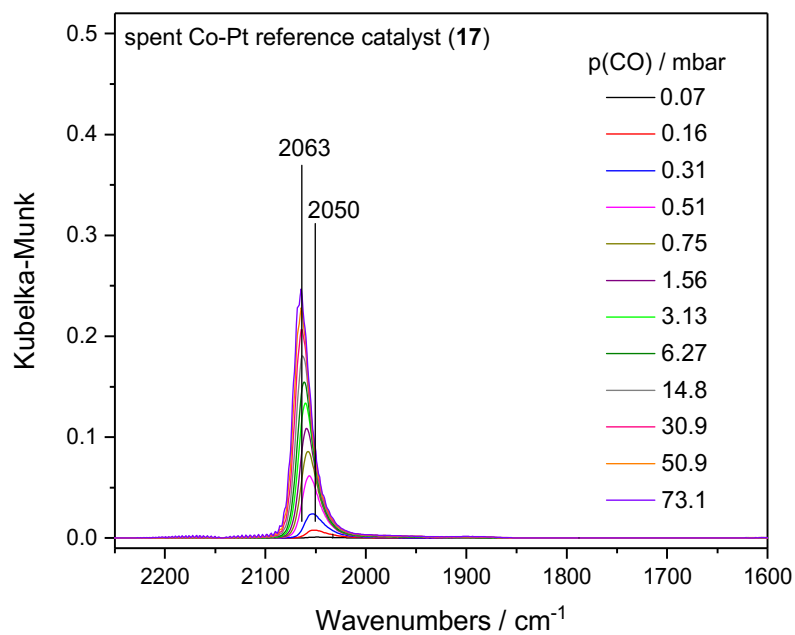
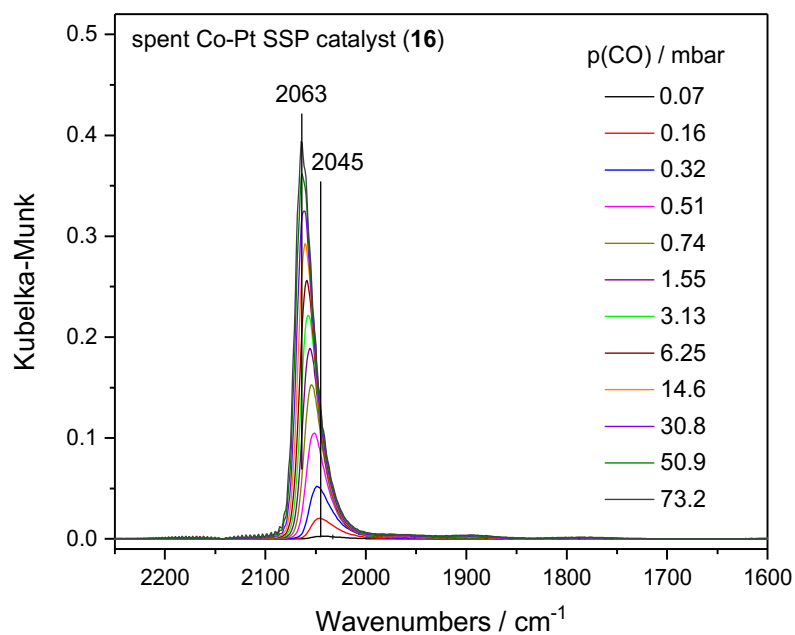


**Figure 26:** Comparison of DRIFTS spectra measured during CO chemisorption on spent Co-Pt SSP catalyst (16, top), and Col catalyst (17, bottom).

### 3.1.9 Discussion: Co-Pt catalysts

Regarding the analytics of the Co-Pt system, several conclusions can be drawn. First, it can be stated that the success of the SSP approach is highly dependent from the preparation route, showing a crucial improvement when employing (S)IWI instead of WI, and best results for the catalyst prepared *via* IWI and a low loading (**10**). In this case, the metal-to-metal ratio is preserved very well, differing from the respective reference catalyst prepared *via* conventional methods (**12**). Whereas BET analysis gives good results for all catalyst systems, XRD analysis shows further superiority of the SSP catalysts: No reflexes can be detected for all the SSP catalysts (**8-10**) as well as the low-loaded Col catalyst (**12**), indicating integral homogeneity of the catalysts. Other than that, the higher loaded Col catalyst (**11**) and the two single-metal reference catalysts (**13** and **14**) show reflexes that indicate the formation of particles with sizes up to 38.4 nm according to Scherrer equation. In case of the Col catalyst **11**, those reflexes can be denoted to metallic Pt and  $\text{Co}_3\text{O}_4$ , showing that the Col impregnation method does not lead to the desired alloy. Further analysis *via* TEM of the two most promising systems, that is SSP catalyst **10** prepared *via* IWI, and Col catalyst **12**, was outlined after activation of both catalysts in  $\text{H}_2$  atmosphere. The TEM measurement was then performed under inert gas without previous air contact of the catalysts. Like this, better insights to the catalysts under working conditions ought to be attained. STEM and EDX analysis show well dispersed alloy nanoparticles in both cases. Comparison of particle sizes shows slightly smaller particles on the SSP catalyst with a distribution maximum at below 1 nm. Calculations based on CO pulse chemisorption experiments fortify the results obtained from STEM analysis, that is a very low theoretical particle size for the SSP catalysts (**10**), and only marginally bigger particles on the respective Col catalyst (**12**). Further calculations showed a 21 % better dispersion on the SSP catalyst (**10**) compared to the Col catalyst (**12**). DRIFTS analysis of the catalysts surface shows pronounced differences of the morphologies of the catalysts before testing, that are not sustained during the testing. Thus, the freshly prepared Col catalyst (**12**) consists of considerably bigger particles, that have a pronounced Pt-surface functionality. The unsymmetrical band shape further confirms the theory of a pronounced Pt-surface functionality, since formation of CO islands due to clustering of CO molecules is a literature-reported phenomenon for adsorption of carbon monoxide at low coverages on alumina-supported

platinum.[85,89] This behavior leads to a heterogeneous distribution of the CO molecules over the metal particles.[85,89]

The as-prepared SSP catalyst (**10**) on the other hand is constituted of smaller particles with an increased Co-content on the particles surface. The symmetric band shape indicates homogeneous carbonyl distribution over the particles, hence no Pt-surface functionality. Regarding the SSP catalyst (**10**), several further bands appear during CO pulsing, and can be assigned to Co-species, thus fostering the theory of an increased Co-surface functionality. The latter result is in accordance with a study of Dees and Ponec, reporting that bulk Pt-Co alloyed phases were observed for different Pt/Co ratios on silica-supported materials, but also suggested that the metal surface of bimetallic Pt/Co particles was enriched by cobalt.[90] Regarding bimetallics, the phenomenon of surface segregation in the presence of adsorbates like O<sub>2</sub>, H<sub>2</sub>, or CO has indeed often been described.[5] In 2010, Menning and Chen investigated extended metallic Pt-Co surfaces and suggested that the surface was constituted of a Pt layer in vacuum or the presence of H<sub>2</sub>, while a Co layer was present at the surface under O<sub>2</sub>.<sup>[91]</sup> This might explain the different morphologies of the SSP catalyst and the Col catalyst, since the first one is calcined in H<sub>2</sub>/Ar atmosphere, whereas the second one has to be calcined in air. The Col catalyst (**12**) is activated under reducing conditions before DRIFTS measurement, but still shows pronounced Pt-surface functionality afterwards.

Investigation of the spent catalysts *via* XRD indicates existence of big cubic CoO particles in both cases (35.9 nm regarding the Co-Pt SSP catalyst **16**, and 30.2 nm in case of the Col catalyst **17**). Since Co does not adsorb CO at r.t., those particles are detected *via* DRIFTS measurement. [86]

According to DRIFTS analysis of the reduced spent catalysts (**16** and **17**) there is strong resemblance to the Col catalyst before catalytic testing (**12**), showing again pronounced Pt-surface functionality. This is in accordance with the literature, since Mayrhofer and co-workers proposed that segregation can occur in the presence of CO, leading to preferential migration of Pt to the surface due to the formation of the stronger Pt-CO as compared to Co-CO.<sup>[92]</sup> This strongly indicates that the morphological differences between the fresh samples are not stable to the conditions of catalytic testing.

The theory of morphological approximation during implementation of the catalysts in the reactor, respectively during catalytic testing, is strongly supported from the results of catalytic testing, showing a highly similar activity and product spectrum on both catalysts. In 2016, Lorito et al. studied the reconstruction of ceria-supported Pt-Co particles under conditions usually used for FT reaction.[79] After reduction at 450 °C, they identified surface alloyed phases, which then gradually formed Co-rich domains under a CO/H<sub>2</sub> feed at 220 °C and atmospheric pressure. This strongly favors the theory of surface reconstruction of our samples under reaction conditions. Lorito et al. furthermore identified formation of Pt-rich and Co-rich domains under the as-described conditions.[79] Based on their findings, they suggested that Pt is catalytically inactive for CO hydrogenation, being poisoned by CO.[79] The role of Pt in Co-Pt FT catalysts has been subject of many studies, suggesting either facilitation of the reduction of cobalt oxide precursors into the active phase, that is metallic cobalt,[93,94] or alternatively to improve cobalt dispersion.[95]

These data suggest that after exposure to the conditions used for syngas conversion, Pt surface functionality is established for both bimetallic catalysts, leading to poisoning of the catalyst, since Pt itself does not play a pronounced catalytic role for syngas conversion, as shown on the monometallic reference catalyst (**13**). Comparison of activities support this assumption, since both bimetallic catalysts show similar low conversion like the monometallic Pt catalyst (**13**), being markedly decreased compared to the monometallic Co catalyst (**14**).

As expected, almost no alcohol formation takes place on the monometallic Pt catalyst (**13**). In contrast, the monometallic Co catalyst (**14**) shows noteworthy selectivity towards methanol of 8.14 %. The furthermore largely increased methanol formation on both bimetallic catalysts of 51.9 and 54.3 %, respectively, is supposed to be due to an improved dispersion of cobalt, as it was shown on alumina-supported cobalt catalysts that methanol was formed *via* hydrogenation of formates located at the support-cobalt interface.[96]

Surface reconstruction mechanisms are widely discussed in the literature, since catalyst sintering is a serious limitation factor regarding catalytic performance. Thus, several models for material transport processes are reported, e.g. *via* transport of

monomers (Wynblatt-Gjostein model),[97] which has been found to apply for Al<sub>2</sub>O<sub>3</sub> supported Platinum.

Another important factor influencing sintering behavior of nanoparticles is the temperature. Bian et al. investigated the sintering behavior of calcined SiO<sub>2</sub> supported Co catalysts and showed that an increase of the temperature to 240 °C accelerated the growth of Co crystallites with an especially pronounced effect of small cobalt crystallites with a size of 6-10 nm.[98] This might explain the similarity of catalytic results obtained on the bimetallic Co-Pt catalysts (**10** and **12**), which is in contrast to the morphological differences observed *via* preceding analysis. Additionally, the Hüttig temperature for both metals is higher or only slightly lower to the highest temperature applied during catalytic testing for StE conversion (Co: ~253 °C, Pt: 335 °C),[99] which gives a further explanation for sintering of the small supported Co-Pt particles. Thus, adjustment of the testing conditions would be reasonable.

Since the conditions applied during FT reaction are quite similar to those used for StE conversion, it is probable that similar mechanisms caused the morphology changes observed in our studies. Thus, further analytics of the spent catalysts, e.g. *via* TEM would be required.

In general, the predications made by Medford et al. are correct as far as synergism between Co and Pt is necessary to form ethanol,[67] but in contrast, the desired catalyst system seems to be unstable under reaction conditions and therefore not applicable for the StE reaction without further modifications. Thus, the ethanol selectivity on a Co<sub>2</sub>Pt alloy does not fit the calculations obtained *via* DFT; predicting a selectivity of 15-30 %. Another reason for the remarkably increased selectivity is the inclusion of further side products, that were not considered in the DFT calculations.

## 3.2 The Co-Cu system

### 3.2.1 Synthesis of the SSP

The literature-known complex  $\text{Et}_4\text{N}\{\text{Cu}[\text{Co}(\text{CO})_4]_2\}$  (**2**) was chosen as Co-Cu SSP following the same argumentation as in the case of the Co-Pt SSP. **Figure 27** shows ORTEP diagrams of the  $\{\text{Cu}[\text{Co}(\text{CO})_4]_2\}$ -anion in the eclipsed as well as in the staggered form according to Darensbourg and co-workers.[100]

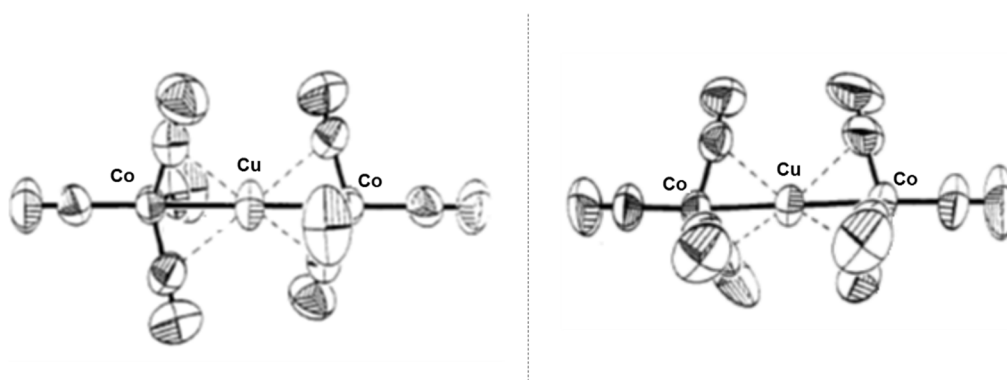
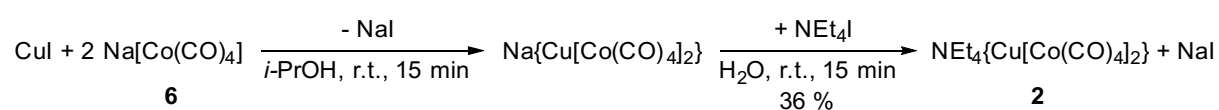


**Figure 27:** ORTEP diagram of the  $\{\text{Cu}[\text{Co}(\text{CO})_4]_2\}$ -anion in the staggered (left) and in the eclipsed form (right) according to Darensbourg and co-workers.[100]

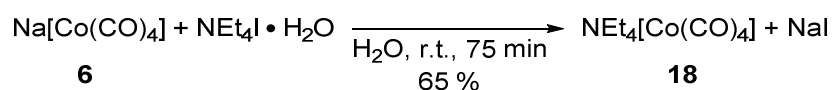
In the first step, sodium tetracarbonylcobaltat(I) (**6**) was synthesized as described for the Co-Pt SSP (**1**) according to Banerjee and co-workers.[77] For synthesis of the desired Co-Cu SSP complex (**2**), two different routes were followed. The first one comprises reacting two equivalents (equiv.) of the as-prepared sodium metallate (**6**) with copper iodide to yield  $\text{Na}\{\text{Cu}[\text{Co}(\text{CO})_4]_2\}$ , which is directly converted without isolation in a salt-metathesis reaction with tetraethyl ammonium iodide to the final complex,  $\text{NEt}_4\{\text{Cu}[\text{Co}(\text{CO})_4]_2\}$  (**2**, **Scheme 4**).[101]



**Scheme 4:** Synthesis of  $\text{NEt}_4\{\text{Cu}[\text{Co}(\text{CO})_4]_2\}$  (**2**) according to Chini and co-workers.[101]

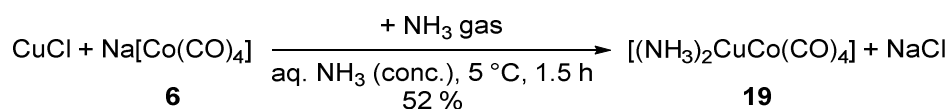
The Co-Cu SSP (**2**) was characterized by FT-IR spectroscopy and elemental analysis (see chapter 5.5).

Since isolation of the desired complex synthesized *via* the first route needed several approaches, an alternative route towards the desired complex (**2**) was followed in parallel. Therefore, two further starting materials had to be synthesized. The first compound, tetraethylammonium tetracarbonyl cobaltat(I) (**18**), was yielded *via* salt metathesis reaction of sodium tetracarbonylcobaltat(I) (**6**) with tetraethylammonium iodide monohydrate (**Scheme 5**):



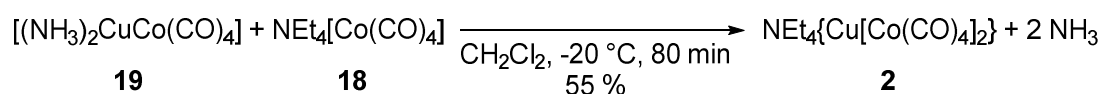
**Scheme 5:** Synthesis of  $\text{NEt}_4[\text{Co(CO)}_4]$  (**18**) according to Fuchs and Klüfers.[102]

The second compound,  $[(\text{NH}_3)_2\text{CuCo(CO)}_4]$  (**19**), was synthesized by reacting sodium tetracarbonylcobaltat(I) (**6**) with an equimolar amount of  $\text{CuCl}$ , and subsequent saturation with gaseous ammonia (**Scheme 6**):



**Scheme 6:** Synthesis of  $[(\text{NH}_3)_2\text{CuCo(CO)}_4]$  (**19**) according to Achternbosch and co-workers.[103]

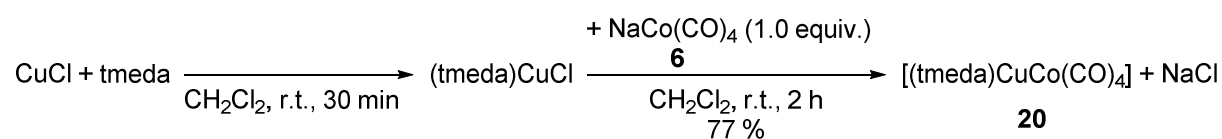
The two starting compounds (**18** and **19**) were finally converted to the desired complex (**2**) following a procedure described by Fuchs and Klüfers (**Scheme 7**):[102]



**Scheme 7:** Synthesis of  $\text{NEt}_4\{\text{Cu[Co(CO)}_4\text{]}_2\}$  (**2**) according to Fuchs and Klüfers.[102]

Again, the desired complex was identified by FT-IR spectroscopy as well as elemental analysis (see chapter 5.5).

Additionally, replacement of  $[(\text{NH}_3)\text{CuCo}(\text{CO})_4]$  (**19**) with  $[(\text{tmeda})\text{CuCo}(\text{CO})_4]$  (**20**), regarding the just-mentioned conversion with  $\text{NEt}_4[\text{Co}(\text{CO})_4]$  (**18**) towards  $\text{NEt}_4\{\text{Cu}[\text{Co}(\text{CO})_4]_2\}$  (**2**), was tried. Thus,  $[(\text{tmeda})\text{CuCo}(\text{CO})_4]$  (**20**) was synthesized according to Doyle and co-workers by conversion of  $\text{CuCl}$  with  $\text{tmeda}$  towards  $(\text{tmeda})\text{CuCl}$ , and subsequent conversion of this intermediate without preceding isolation with  $\text{NaCo}(\text{CO})_4$  (**6**, **Scheme 8**):[104]



**Scheme 8:** Synthesis of  $[(\text{tmeda})\text{CuCo}(\text{CO})_4]$  (**20**) according to Doyle and co-workers.[104]

The subsequent conversion of  $[(\text{tmeda})\text{CuCo}(\text{CO})_4]$  (**20**) with  $\text{NEt}_4[\text{Co}(\text{CO})_4]$  (**18**) using the same conditions as in the appropriate procedure using  $[(\text{NH}_3)\text{CuCo}(\text{CO})_4]$  (**19**) did not yield the desired complex  $\text{NEt}_4\{\text{Cu}[\text{Co}(\text{CO})_4]_2\}$  (**2**), but ended in crystallization of the starting materials. Thus, a possible reason is stronger binding by the bidentate  $\text{tmeda}$  ligand towards the copper atom in  $[(\text{tmeda})\text{CuCo}(\text{CO})_4]$  (**20**) compared to monodentate  $\text{NH}_3$  in  $[(\text{NH}_3)\text{CuCo}(\text{CO})_4]$  (**19**).

### 3.2.2 Decomposition and characterization of the unsupported SSP

Thermolysis of  $\text{Et}_4\text{N}\{\text{Cu}[\text{Co}(\text{CO})_4]_2\}$  (**2**) up to  $550\text{ }^\circ\text{C}$  in  $\text{H}_2$  atmosphere showed release of  $\text{CO}$  in two defined steps, starting at  $\sim 120\text{ }^\circ\text{C}$  and at  $\sim 220\text{ }^\circ\text{C}$ , respectively (**Figure 28**). The  $\text{Et}_4\text{N}^+$  cation is released in parallel to the second  $\text{CO}$  removal step. It undergoes thermal degradation and is therefore mainly desorbed in form of fragments of triethylamine, which is in accordance to the literature.[105] Thus, release of  $\text{CO}_2$  cannot be explicitly detected in this case, since the respective mass-to-charge ratio of  $m/z = 44$  also fits to a fragmentation product of triethylamine. Furthermore, release of

a little amount of H<sub>2</sub>O can be detected ( $m/z = 18$ ), which is attributed to Hoffmann elimination reaction taking place on the Et<sub>4</sub>N<sup>+</sup> cation.

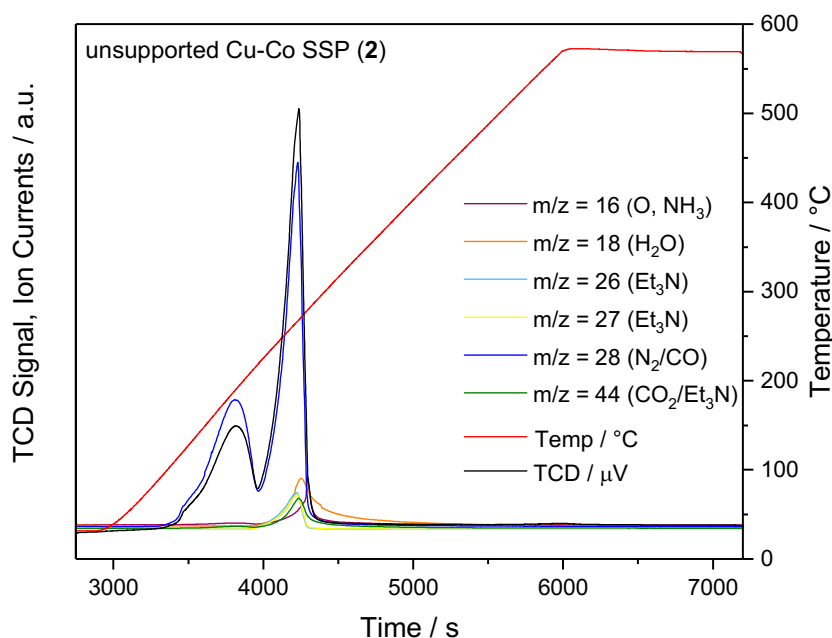


**Figure 28:** Thermolysis profile of the Co-Cu SSP (2) in H<sub>2</sub> atmosphere, monitored via MS.

Analysis *via* XRD measurement in air shows small reflexes at 43, 50, 74, and 89° caused by metallic Cu, as well as reflexes at 44, 51, 75, and 92°, that are in accordance to database entries for metallic Co, both being present in cubic lattice structure (**Figure 29**). This result is in accordance to calculated solution data, suggesting that Co and Cu in a ratio of 2:1 are existent in two separate phases in the decisive temperature range.[19] Due to the partial overlap of the biggest reflexes at 43 respectively 44°, and the low ratio of signal-to-noise of all signals, calculation of crystallite sizes using Scherrer equation is not reasonable.

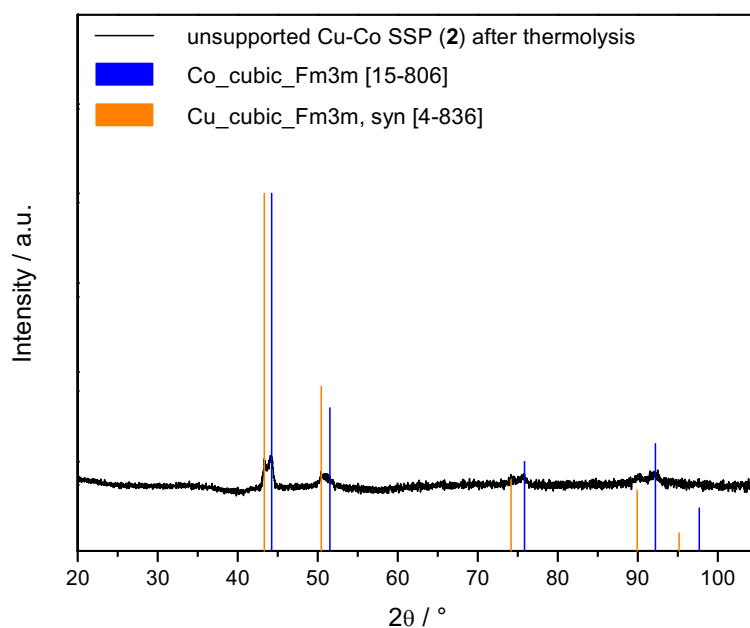


**Figure 29:** XRD analysis of the unsupported Co-Cu SSP (2) after decomposition in  $H_2$  atmosphere and comparison to database entries for metallic Co and Cu.

### 3.2.3 Supporting of the SSPs

Two Cu-Co SSP catalysts were prepared by immobilization of  $Et_4N\{Cu[Co(CO)_4]_2\}$  (2) on commercially available  $SiO_2$  via SIWI from anhydrous, degassed dimethylformamide (DMF) with a theoretical loading of 3.0 wt% and 5.0 wt% regarding Co (Table 9).

**Table 9:** Overview of SSP catalysts prepared by impregnation of  $Et_4N\{Cu[Co(CO)_4]_2\}$  (2) on  $SiO_2$ .

Entry	Impregnation Method	Theoretical Loading [wt.%]	
		Co	Cu
21	SIWI	3.00	1.62
22	SIWI	5.00	2.70

### 3.2.4 Decomposition of supported SSPs

The supported Co-Cu SSP (**21**) was decomposed by applying two heating steps (190 °C for 4 h, and 260 °C for 4 h, **Figure 30**). Again, the temperature program was chosen according to the onset of ligand release monitored for the unsupported SSP (**2**). The diminished end temperature is supposed to avoid sintering of the supported metal particles.

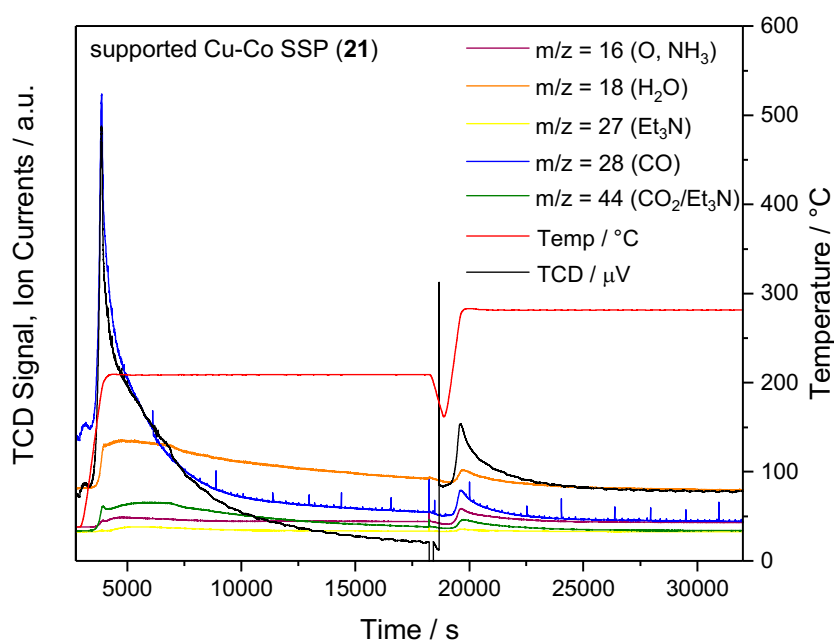


**Figure 30:** Thermolysis profile of the Co-Cu SSP supported on SiO<sub>2</sub> (**21**) in H<sub>2</sub> atmosphere, monitored via MS.

The thermolysis profile shows that most of the ligands and cations are released during the first heating plateau. The release takes place in parallel, and just as in the case of the unsupported SSP (**2**), the Et<sub>4</sub>N<sup>+</sup> cation undergoes thermal degradation and is therefore mainly desorbed in form of fragments of triethylamine, which is in accordance to the literature.[105] Thus, release of CO<sub>2</sub> cannot be explicitly detected, since the respective mass-to-charge ratio of m/z = 44 also fits to a fragmentation intermediate of triethylamine. Furthermore, release of a little amount of H<sub>2</sub>O can be detected (m/z = 18), which is attributed to Hoffmann elimination reaction taking place on the Et<sub>4</sub>N<sup>+</sup> cation, as well as to H<sub>2</sub>O left on the silica support.

### 3.2.5 Synthesis of the reference catalyst

The reference catalyst for the Co-Cu-system, catalyst **23**, was synthesized *via* IWI of the corresponding nitrates with a loading of 5.00 wt.% regarding Co, and 2.70 wt.% regarding Cu, and subsequently calcined at 300 °C for 3 h, on the basis of literature procedures (see chapter **5.8**).[106,107]

### 3.2.6 Characterization of catalysts

#### 3.2.6.1 Elemental analysis for determination of metal loading on the support

ICP-OES measurements were proceeded to determine the metal loading of the catalysts. The results are listed in **Table 10**.

**Table 10:** Analysis via ICP-OES of SSP catalysts (**21** and **22**) and of the Col catalyst (**23**).

Catalyst	Cu loading [wt.%]		Co loading [wt.%]		Cu : Co	
	Theoretical	Analysis	Theoretical	Analysis	Theoretical	Analysis
<b>21</b>	2.70	2.25	5.00	4.50	1 : 1.9	1 : 2.0
<b>22</b>	1.62	1.35	3.00	2.65	1 : 1.9	1 : 2.0
<b>23</b>	2.70	2.49	5.00	4.32	1 : 1.9	1 : 1.7

ICP-OES analysis of the SSP catalysts (**21** and **22**) shows a slightly diminished measured loading compared to the theoretical value, which is probably caused by use of a syringe filter during addition of the SSP solution to the support. Still, the metal-to-metal ratio is very well preserved (deviation of 5 % in both cases). In case of the reference catalyst (**23**), the metals loading is also slightly reduced. The metal-to-metal ratio is not as well preserved as in case of the SSP catalyst with a deviation of 11 %. Again, the RSD for as-performed ICP-OES measurements is less than 1% in all cases described, and thus does not strikingly contribute to the aberrations.

### 3.2.6.2 Physisorption experiments for characterization of specific surface area, pore volume, and pore radii

The specific pore volume and radius as well as the respective surface area of the Co-Cu catalysts were calculated using BET and BJH theory after physisorption experiments using N<sub>2</sub>.<sup>[80,81]</sup> The results for the Co-Cu catalysts are summarized in **Table 11**, and compared to unloaded SiO<sub>2</sub> (**15**).

**Table 11:** Pore volume, pore radius, and surface area of SiO<sub>2</sub> (**15**), SSP catalysts (**21** and **22**), and of the Co catalyst (**23**).

Catalyst	Loading [wt.%]		Pore volume [mL/g]	Pore radius [Å]	Surface area [m <sup>2</sup> /g]
	Cu	Co			
<b>15</b>	/	/	0.75	30.0	480
<b>21</b>	1.35	2.65	0.72	34.2	418
<b>22</b>	2.25	4.50	0.71	34.2	411
<b>23</b>	2.49	4.32	0.70	34.5	403

As expected, the specific surface area of unloaded SiO<sub>2</sub> (**15**) is higher than that of loaded SiO<sub>2</sub> in all cases. Furthermore, the surface area is inversely proportional to the loading (catalyst **23** > **22** > **21** > **15**), which is reasonable since the coverage of surface area increases with higher loading. For all catalysts, pore volume and pore radius stay in the same range as for unloaded SiO<sub>2</sub> (**15**), suggesting successful precursor deposition without major change of the morphology of the supporting material, e.g. due to clogging.

### 3.2.6.3 Investigation of the catalysts' bulk structure by means of powder XRD

For investigation of the bulk structure of the catalysts, XRD measurements were performed. **Figure 31** shows the XRDs of SSP catalysts **21** and **22**, which were activated under reducing atmosphere as described before, and subsequently measured in air.

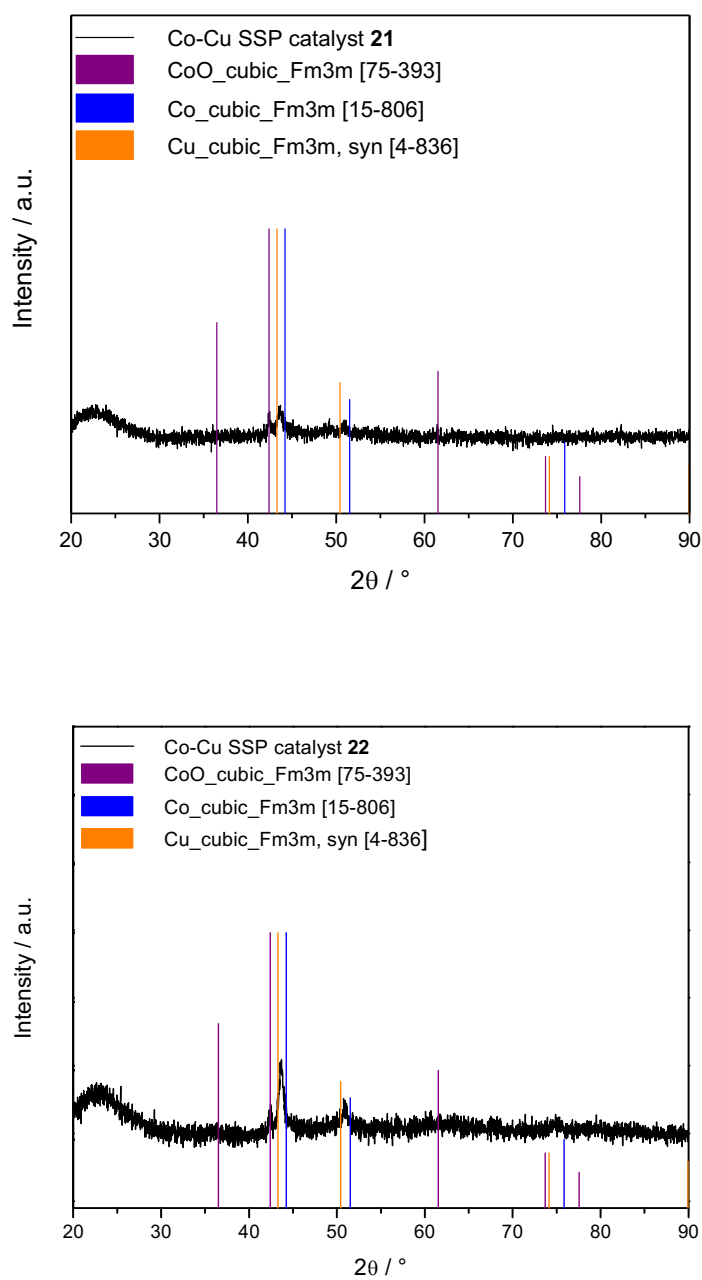


**Figure 31:** Powder XRD of SSP catalysts **21** (top) and **22** (bottom), stacked with database XRD patterns of CoO, as well as metallic Co and Cu.

In both cases, a reflex at  $42.39^\circ$  is detected, belonging to the (200) plane of cubic CoO (Fm3m), which was not present in the unsupported SSP catalyst (**2**) which was also measured under air after reductive decomposition. One possible explanation is that the supported particles in SSP catalysts **21** and **22** are smaller and therefore much

more prone towards oxidation in air than the unsupported SSP catalyst (**2**). The reflexes at  $43.69^\circ$  and  $50.99^\circ$  are attributed to the pattern of Co-Cu alloy, since they are located between those ones of metallic Co and Cu. Application of Scherrer equation (**2**) yields a theoretical particle size of 34.1 nm regarding CoO, and 19.8 nm regarding the Co-Cu alloy for catalyst **21**, and 26.6 nm, respectively 16.4 nm for catalyst **22**.

**Figure 32** shows the XRD of CoI catalyst **23**, with reflexes fitting the pattern of cubic  $\text{Cu}_{0.92}\text{Co}_{2.08}\text{O}_4$ . Calculation of the particle sizes *via* Scherrer equation (**2**) yields a value of 12.1 nm.

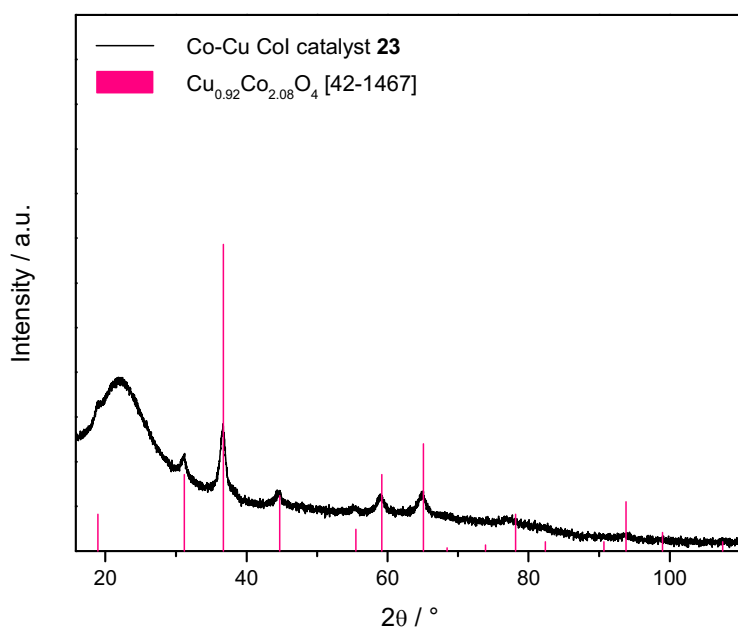


**Figure 32:** Powder XRD of Co-Cu CoI catalyst **23**, stacked with the database pattern of  $\text{Cu}_{0.92}\text{Co}_{2.08}\text{O}_4$ .

#### 3.2.6.4 Investigation of surface morphology and composition of the activated catalysts using STEM, SAED, and EDX measurements

Again, electron microscopy was used to get insight into the system under working conditions. Thus, SSP catalyst **22** was activated in an optimized procedure based on the results from thermolysis in H<sub>2</sub> monitored *via* MS, by first heating to 150 °C, then to 260 °C with a holding time of 4 h in both cases, and in an atmosphere of flowing 10 % H<sub>2</sub>/N<sub>2</sub>. To ensure comparability of both catalysts in their active state during syngas conversion, calcined CoI catalyst **23** was similarly activated in an atmosphere of flowing 10 % H<sub>2</sub>/N<sub>2</sub>, and with two heating plateaus at 210 and 280 °C which were both held for 5 h. Then, both catalysts **22** and **23** were installed in the microscope and analyzed under inert atmosphere without any air contact.

STEM images of the activated Co-Cu SSP catalyst (**22**) show a much more homogeneous dispersion of the particles on the support than for the corresponding CoI catalyst (**23**, **Figure 33**).

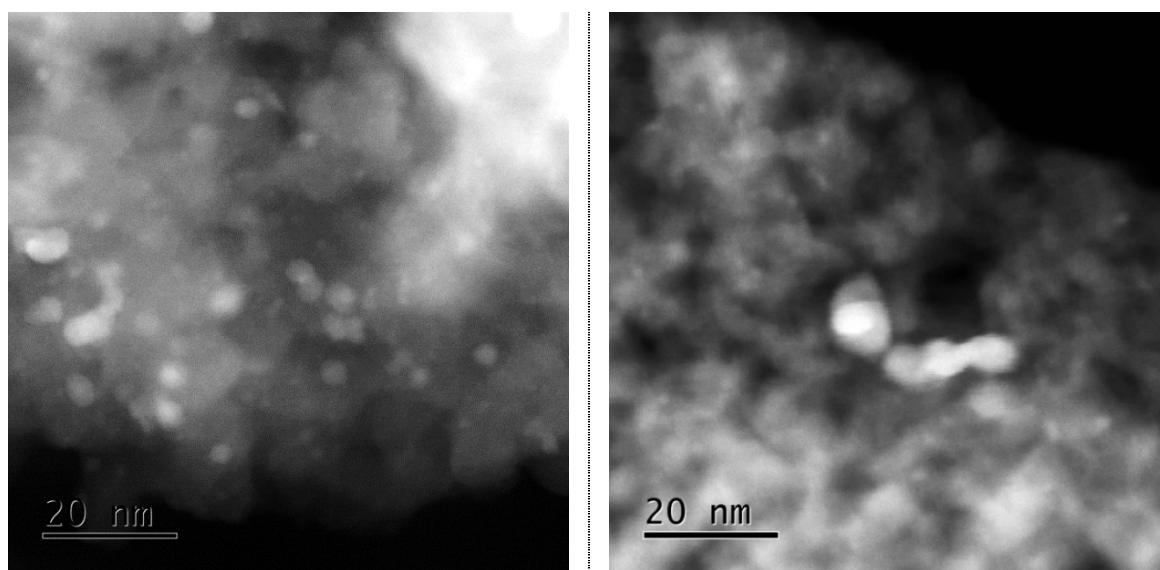


**Figure 33:** STEM analysis of SSP catalyst **22** (left), and CoI catalyst **23** (right).

In case of the CoI catalyst (**23**), heavy agglomeration of the particles on the support is detected, so that determination of the particle size distribution is not reasonable.

Regarding the Cu-Cu SSP catalyst (**22**), the particle size distribution shows a maximum at 2.8 nm (**Figure 34**).

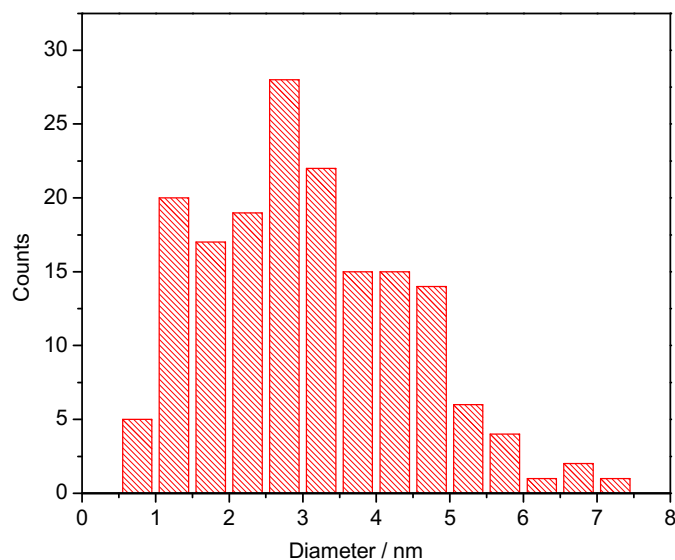


**Figure 34:** Particle size distribution of Co-Cu SSP catalyst **22**.

Investigation of the selected area electron diffraction (SAED) patterns of the two catalysts show that the investigated compounds are both crystalline with a cubic structure (**Figure 35**). Since the detected grid lines describe one crystalline structure, it can be concluded that the investigated particles are consisting of one clearly defined phase, e.g. a Co-Cu alloy, instead of two separate crystalline phases. In this case, e.g. in case of metallic Co and Cu being existent in parallel, the respective grid lines would be doubled.

Further investigation of four selected particles *via* EDX line scanning shows overlap of Co and Cu in all cases, further affirming alloy formation (**Figure 36** and **Figure 37**).

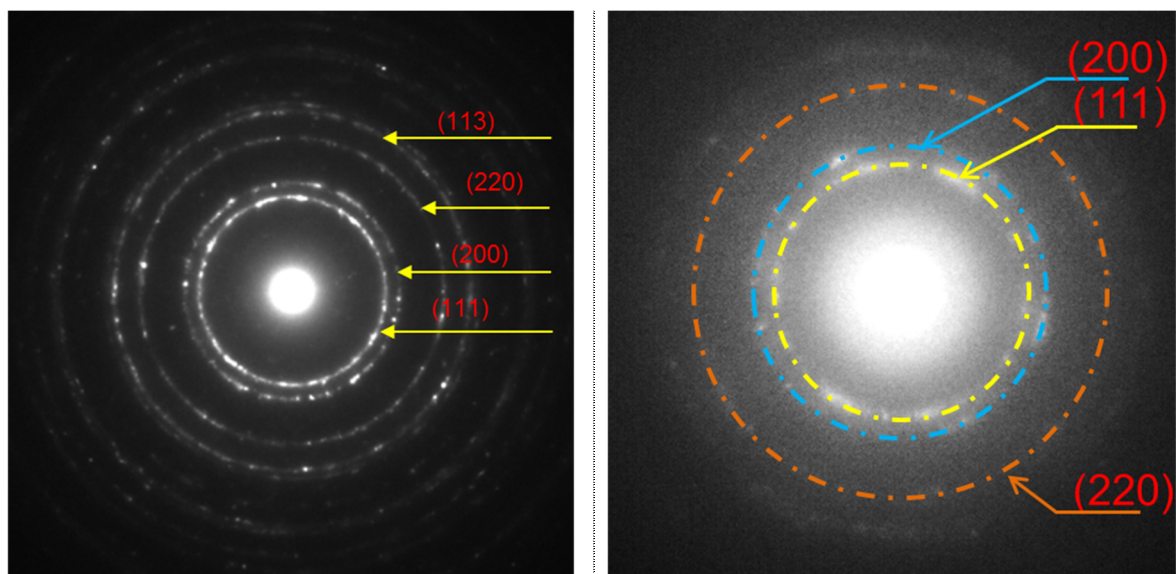


Figure 35: SAED patterns of Co-Cu SSP catalyst 22 (left), and CoI catalyst 23 (right).

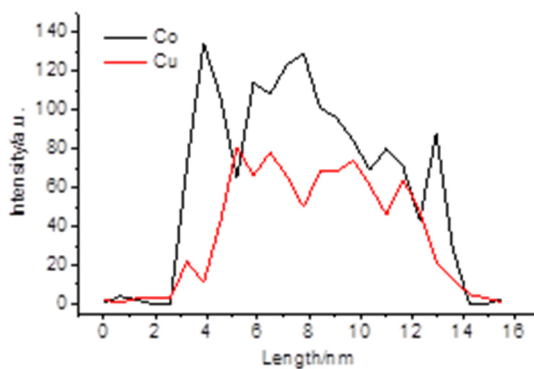
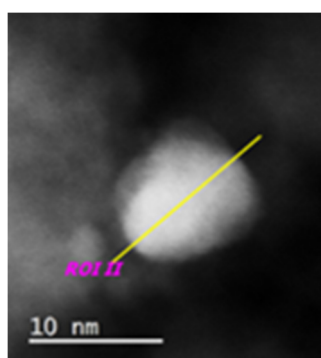
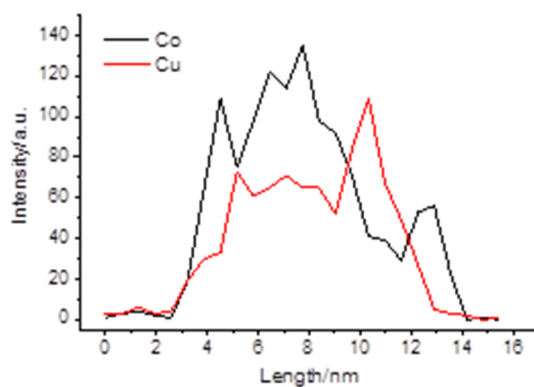
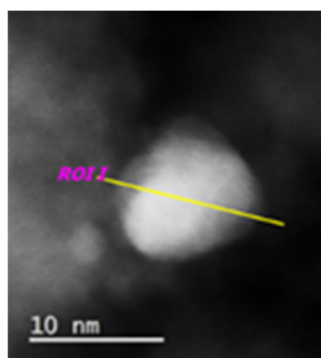
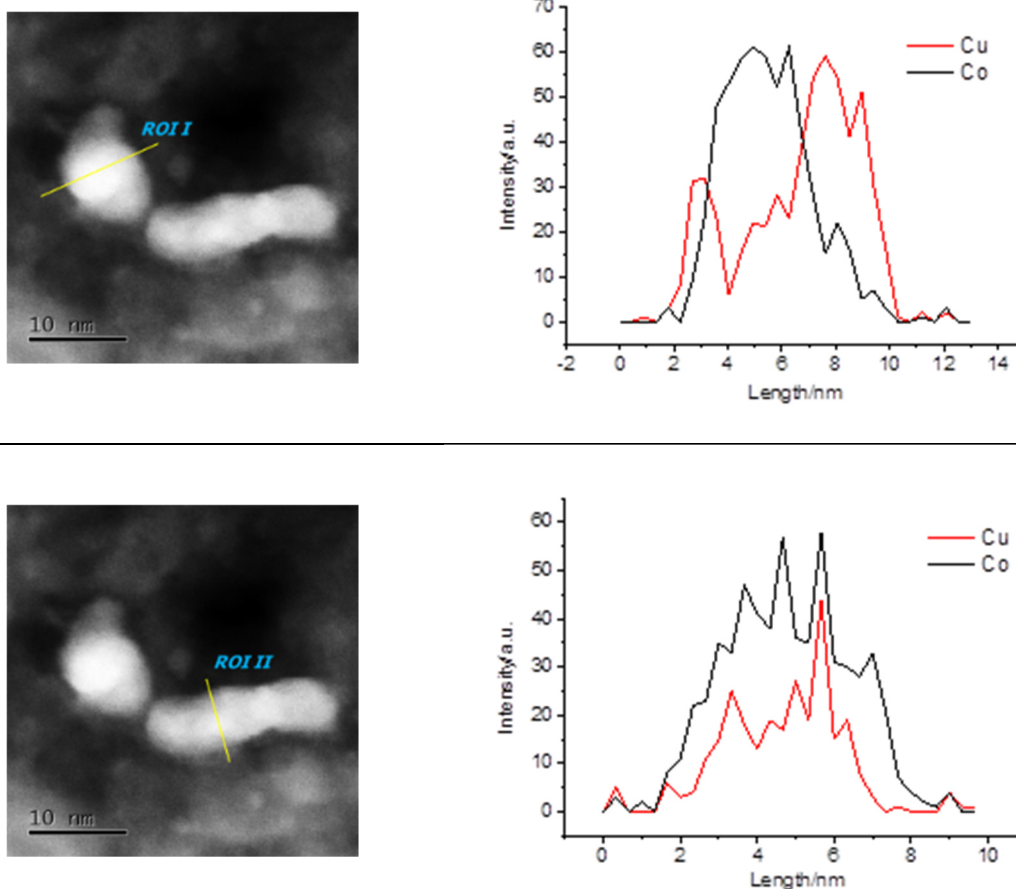


Figure 36: EDX line scans of two supported particles of the Cu-Co SSP catalyst 22.



**Figure 37:** EDX line scans of two supported particles of the CoI catalyst **23**.

### 3.2.6.5 Investigation of the surface functionality of activated catalysts via DRIFTS analysis

In order to get better understanding of the catalyst in the working state, again DRIFTS measurements were performed.

Thus, Co and Cu reference catalysts (**14** and **24**; monometallic Cu reference catalyst **24** from Cu-Fe system, see chapter 3.3.5) and Co-Cu CoI catalyst (**23**) were activated by heating with 10K/min in an atmosphere of 13 %H<sub>2</sub>/Ar to 360 °C for 1 h, and cooled to r.t. The SSP catalyst (**22**) was thermolyzed using a temperature ramp of 2 K/min, a gas flow of 13 % H<sub>2</sub>/Ar, a first heating plateau at 210 °C followed by cooling to r.t., and a second heating plateau to 280 °C with a holding time of 1 h at both plateaus. Then, CO adsorption was performed on the freshly reduced samples (**Figure 38** and **Figure 39**).

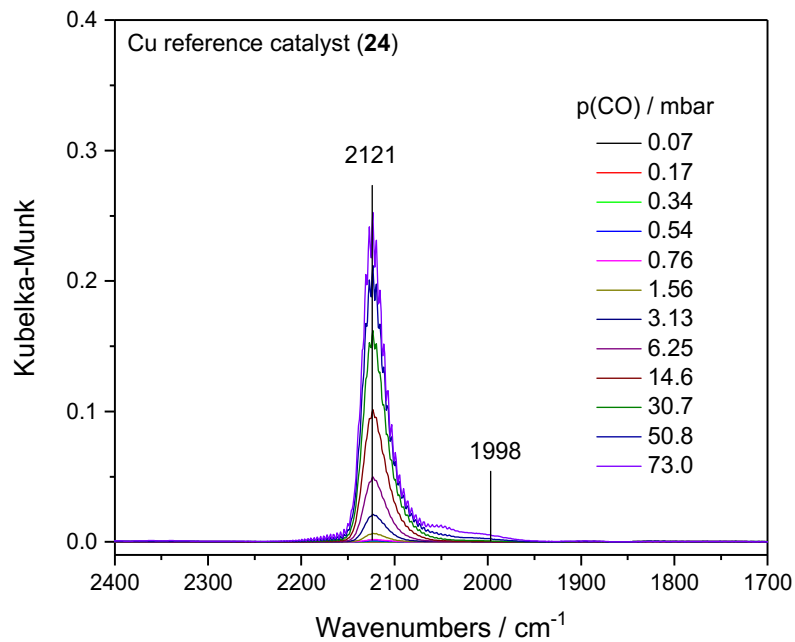
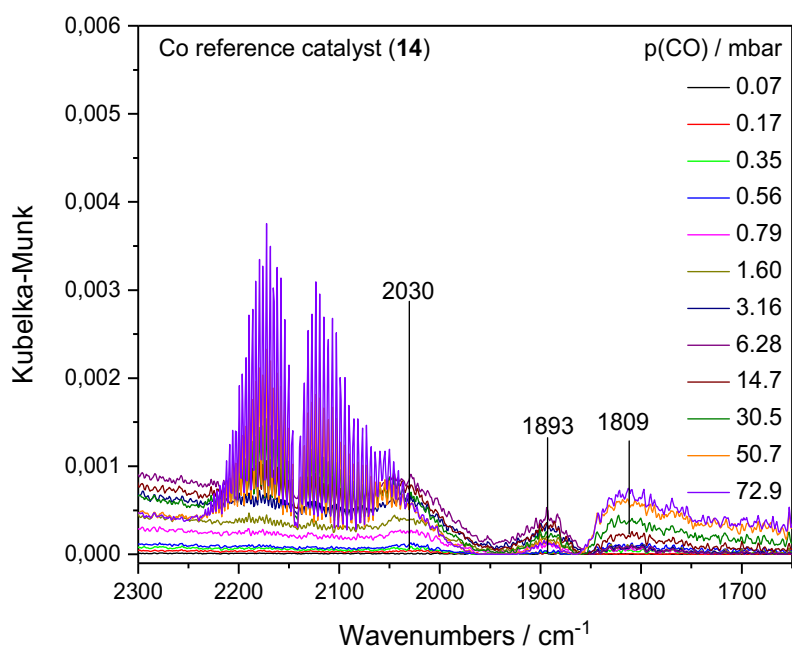


**Figure 38:** DRIFTS monitoring of CO adsorption of activated Co reference catalyst (**14**, top), and activated Cu reference catalyst (**24**, bottom).

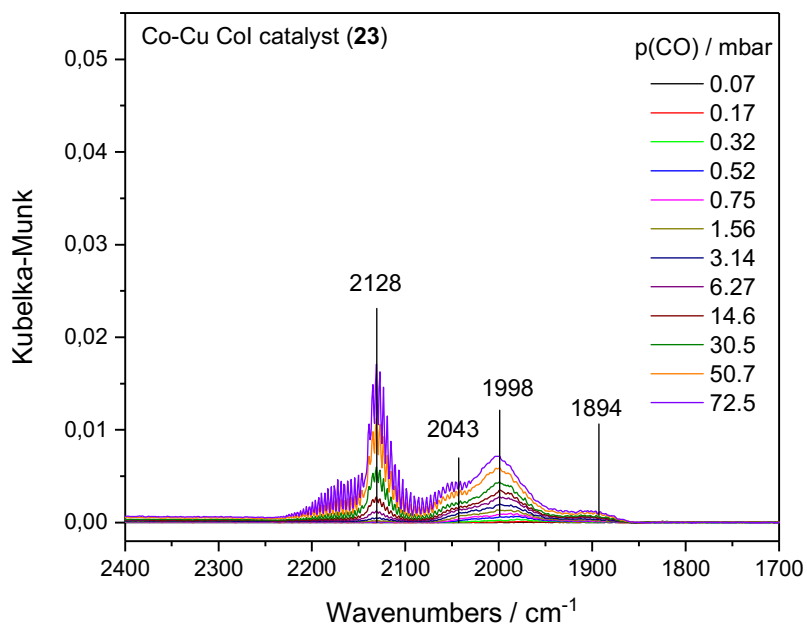
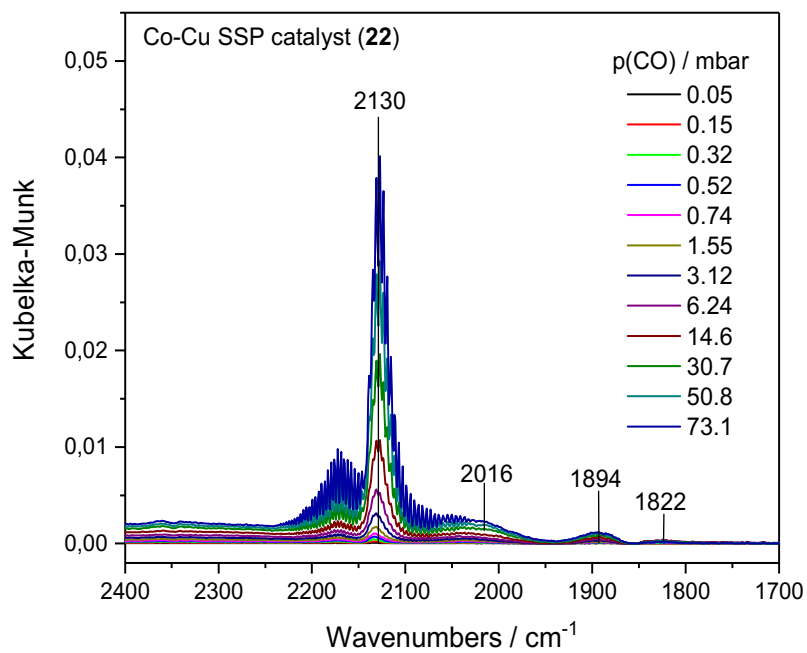


**Figure 39:** DRIFTS monitoring of CO adsorption of activated Co-Cu SSP (**22**, left), and activated Co-Cu Col (**23**, right).

In accordance to existing literature, CO exposure at r.t. on the Co reference catalyst (**14**) did not show pronounced adsorption of CO on cobalt sites, but mainly bands belonging to the rotational bands of free CO.[86] By zooming in, three minor bands can be detected and assigned to terminal CO on  $\text{Co}^0$  ( $2030\text{ cm}^{-1}$ ).[86] Since the two bands at  $1893$  and  $1809\text{ cm}^{-1}$  can also be detected on the Cu reference catalyst (**24**) as well as on the DRIFTS spectra of Co-Pt and Cu-Fe samples, they are interpreted as artefacts caused by the measurement. Compared to the Co reference catalyst, the Cu reference catalyst (**24**) shows a pronounced band at  $2121\text{ cm}^{-1}$  indicating CO linearly adsorbed on copper, as well as a smaller band at  $1998\text{ cm}^{-1}$  belonging to CO adsorbed either on  $\text{Cu}^+$  or  $\text{Cu}^0$ . [86,87] The band at  $2121\text{ cm}^{-1}$  has been discussed widely in the literature, and is mainly attributed to CO adsorbed on  $\text{Cu}^+$ . [108–112] Since the catalysts discussed here have been thoroughly reduced before their investigation *via* DRIFTS, as well as on the basis of the results observed *via* TEM, the interpretation that the band at  $2121\text{ cm}^{-1}$  belongs to  $\text{Cu}^+$  species is not reasonable. This situation was discussed in the literature before, and the respective band was instead assigned to a copper adsorption site that is electropositive due to interaction with oxygen respectively hydroxyl groups of the supporting material.[86] The main band is furthermore not symmetrically shaped but exhibits tailing towards lower wavenumbers.

In both cases, the spectra look different than those ones of the bimetallic catalysts **22** and **23**. Again, the band at  $1894\text{ cm}^{-1}$  and furthermore a small band at  $1822\text{ cm}^{-1}$  is present which repeatedly appear throughout DRIFTS spectra of all metal systems, and which are thus supposedly caused by the measurement and not significant for further discussion. Additionally, in both cases the rotational band of free CO at  $\sim 2170\text{ cm}^{-1}$  can be seen. Furthermore, in both cases bands at  $2130$  respectively  $2128\text{ cm}^{-1}$  are detected and assigned to copper that is electropositive due to interaction with the supporting material, as discussed before.[86] The group of Mavrikakis assigned the band at  $\sim 2130\text{ cm}^{-1}$  to three possible CO adsorption sites: Cu adatoms, compressed Cu surfaces, or Cu surfaces containing subsurface oxygen.[113] Regarding the SSP catalyst (**22**), an additional band at  $2016\text{ cm}^{-1}$  is observed, which can be assigned to linear CO on  $\text{Co}^0$ . [86] For the CoI catalyst (**23**), an additional band at  $2043\text{ cm}^{-1}$  indicates formation of metal- $\text{CO}_t$ , whereas a pronounced band at  $1998\text{ cm}^{-1}$  indicates linear monocarbonyls on  $\text{Co}^0$ . [86,87] Smith et al. assigned bands in the range of  $2057-$

2038  $\text{cm}^{-1}$  to CO on mixed  $\text{Co}^{\delta+}$ - $\text{Co}^0$  sites, which would give an alternate explanation for the band at 2043  $\text{cm}^{-1}$ .<sup>[86]</sup> Furthermore, in this case, the adsorption is generally quite diminished compared to the signal achieved for the monometallic Cu catalyst (**24**), which indicates a suppression of copper by a surface Co-layer. In case of the Co-Cu SSP catalyst (**22**), the same phenomenon appears, but not as pronounced as in case of the CoI catalyst (**23**). The reduced amount of adsorbed CO on the CoI catalyst (**23**) compared to the SSP catalyst (**22**) alternately indicates formation of larger particles, which is in accordance with the results from TEM analysis.<sup>[88]</sup> Interestingly, the additional band at 1998  $\text{cm}^{-1}$  detected on the Co-Cu CoI catalyst (**23**) at high CO coverage was identified in a study of Smith et al. during DRIFTS measurement under CO/H<sub>2</sub>/He atmosphere to appear on a CuCo/SiO<sub>2</sub> sample at elevated temperature (~200 °C), but in their study, the band was not stable at r.t.<sup>[86]</sup> They assigned this band to CO linearly adsorbed on a  $\text{Co}^0$  surface.

Thus, the surfaces of both catalysts are dominated by Co species, whereas the reductively activated SSP catalyst (**22**) generally consists of smaller particles.

### 3.2.7 Application in syngas conversion

In case of the Co-Cu system, four catalysts were investigated and compared regarding HAS from syngas: The Co-Cu SSP catalyst **22**, the Co-Cu CoI catalyst **23**, and two monometallic catalysts **24** (only Cu) and **23** (only Co). The metal loadings of the monometallic Co and Cu catalysts correspond those of the Co-Pt- and Cu-Fe-system, still synergistic effects on product formation can be discussed on basis of the results obtained.

The samples were pre-treated at 54 bar and 265 °C for 1 h in a flow of 58.3 ml/min of 5 %H<sub>2</sub>/N<sub>2</sub>. The reactors were then cooled to the reaction temperature at 260 °C. The measurement was performed with a pressure of 54 bar, a CO:H<sub>2</sub> ratio of 2:1, temperature steps of 260, 280, 300, 320, 300, 280, and 260 °C, and a GHSV of 3500 h<sup>-1</sup>. The total flow rate used was 58.3 ml/min. For the following discussion, activities are determined on basis of the highest CO conversions at 320 °C.

The CO conversion obtained with monometallic Cu-catalyst **24**, Co-catalyst **14**, Co-Cu SSP catalyst **22**, and Co-Cu CoI catalyst **23** are summarized in Table 12. The

bimetallic catalysts **22** and **23** show a similar high activity ( $X_{CO} = 44\%$  respectively  $42\%$ ). The Co-catalyst **14** is about half as active ( $X_{CO} = 24\%$ ). The Cu-catalyst **24** shows the lowest activity ( $X_{CO} = 5.0\%$ ).

**Table 12:** Overview of CO conversion obtained over Co-Cu SSP and CoI and monometallic reference catalysts at 320 °C.

Entry	Type of catalyst	Measured Co loading [wt.%]	Measured Cu loading [wt.%]	$X_{CO}$ [%]
<b>24</b>	Cu reference	/	4.03	5.0
<b>14</b>	Co reference	2.82	/	24
<b>22</b>	Co-Cu SSP	4.50	2.25	44
<b>23</b>	Co-Cu CoI	4.32	2.49	42

The product spectra of the four catalysts were determined *via* GC and summarized in **Table 13**. For better comparability of the different catalysts, results measured at similar conversions are used, that is at 260 °C except for the Cu reference catalyst (**24**), where results achieved at 320 °C are considered. Furthermore,  $C_{2+}$  alkanes are defined as *n*-alkanes with a carbon number of at least two, and olefins contain ethylene, propene, and 1-butene. All higher hydrocarbons (branched) are summarized as  $C_{4+}$  hydrocarbons.

**Table 13:** Catalytic performance of the Co reference catalyst (**14**), the CoCu SSP catalyst (**22**), and the CoCu CoI catalyst (**23**) determined at 260 °C, and for the Cu reference catalyst (**24**) determined at 320 °C. Conversion and selectivities are given in %.

Entry	$X(CO)$	$S(CH_4)$	$S(C_{2+}$ Alkanes)	$S(Olefins)$	$S(MeOH)$	$S(EtOH)$	$S(PrOH)$	$S(CO_2)$	$S(C_{2+}$ Oxy)	$S(C_{4+}$ CHs)
<b>24</b>	5.0	13	4.8	0.3	65	0	0	15	0.9	1.5
<b>14</b>	5.5	29	20	9.4	8.1	0	0.2	0	1.5	32
<b>22</b>	9.0	35	33	15	2.6	3.5	1.4	1.2	0.6	8.1
<b>23</b>	9.3	33	30	17	1.4	3.4	0.9	1.1	0.9	12

As expected, the main product formed on the monometallic Cu reference catalyst (**24**) is MeOH (65 %). The second main product is  $CO_2$  (15 %) which results from water-

gas shift reaction of CO with *in situ* formed H<sub>2</sub>O. No formation of higher alcohols takes place.

Co is a well-known FT catalyst, which is reflected in the results obtained over the Co reference catalyst (**14**), forming mainly alkanes (29 % methane, 20 % C<sub>2+</sub> alkanes), olefines (9.4 %), C<sub>4+</sub> hydrocarbons (32 %), and MeOH (8.1 %). Again, formation of higher alcohols is not observed.

Just as in the case of Co-Pt catalysts, both bimetallic CoI (**23**) and SSP catalyst (**22**) show a very similar product distribution which can be rationalized by similar metal loading and morphology under reducing conditions. On both catalysts, main product is methane (**22**: 35 %, **23**: 33 %), closely followed by C<sub>2+</sub> alkanes (**22**: 33 %, **23**: 30 %), olefins (**22**: 15 %, **23**: 17 %), and C<sub>4+</sub> hydrocarbons (**22**: 8.1 %, **23**: 12 %). Thus, the product spectrum strongly resembles the one of monometallic Co catalyst **14**, showing FT synthesis properties. This is in accordance with the results obtained from DRIFTS analysis, showing that the surface of both activated bimetallic catalysts is dominated by Co species. Additionally, little amount of CO<sub>2</sub> is formed as a product from water gas shift reaction.

A synergistic effect is observed on both bimetallic catalysts (**22**) and (**23**). Ethanol, methanol, and propanol are formed in almost equal amounts with ethanol being the main product (3.4 % and 3.5 %). Since no higher alcohols are formed over the monometallic reference catalysts, the synergistic effect of both metals is needed for ethanol formation, as predicted in the literature.[67,73] It can be assumed that on Co, dissociative CO adsorption and carbon chain growth takes place, whereas Cu is active for nondissociative CO adsorption and insertion. The results are summarized in **Figure 40**.

Since the product spectra obtained over both bimetallic catalyst systems are almost equal, the morphological differences of the fresh catalysts obtained *via* the differing synthesis routes and proven *via* STEM and DRIFTS measurements are not stable under testing conditions. Thus, particle size and distribution differences seem to assimilate during the catalytic reaction, yielding highly similar surface sites.

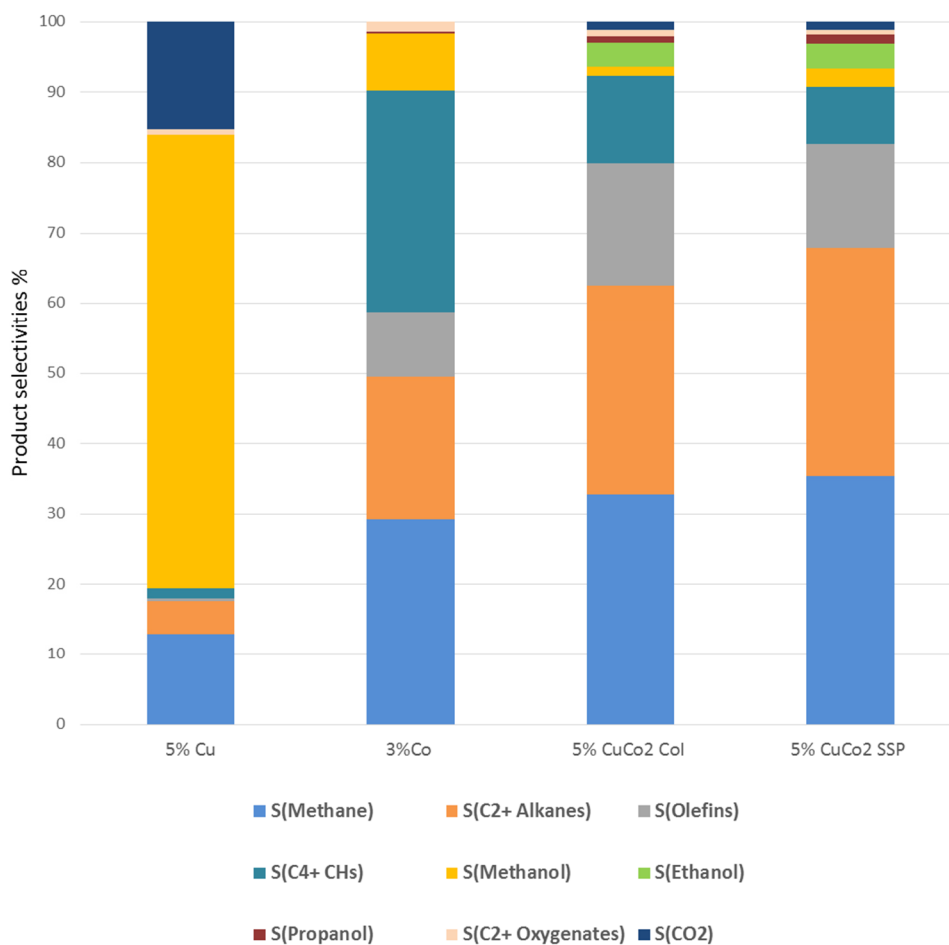


**Figure 40:** Product spectrum determined at 260 °C, except for the Cu reference catalyst (**24**, 320 °C). From left to right: Monometallic Cu-catalyst (**24**); monometallic Co-catalyst (**14**), Co-Cu SSP catalyst (**22**), and Co-Cu Col catalyst (**23**).

### 3.2.8 Investigation of spent catalysts

#### 3.2.8.1 Investigation of the bulk structure via XRD analysis

Investigation of the spent catalysts *via* XRD proves the existence of cubic Cu, Co, and CoO particles in both cases (**Figure 41**). Application of Scherrer equation (**Eq. 2**) was only possible regarding the CoO particles and yielded particle sizes of 40.5 nm in case of the SSP catalyst (**25**), and 33.2 nm in case of the Col catalyst (**26**).

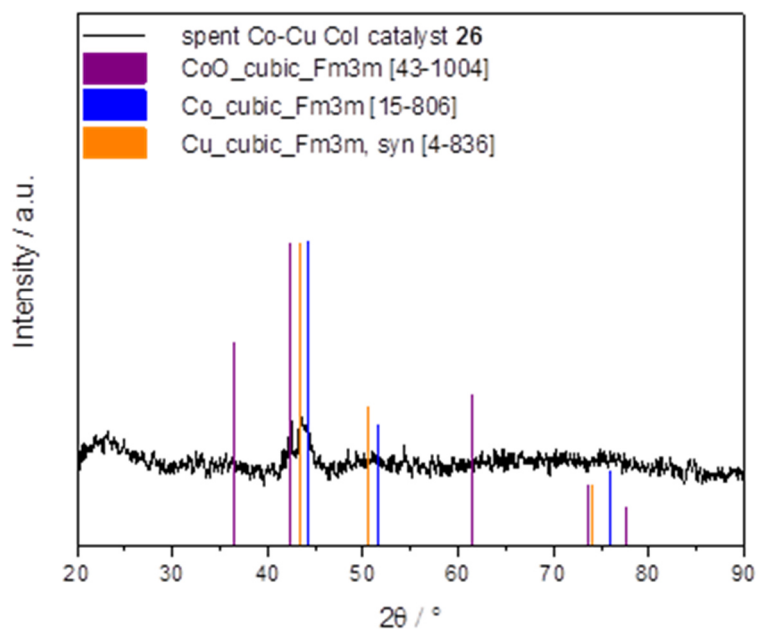
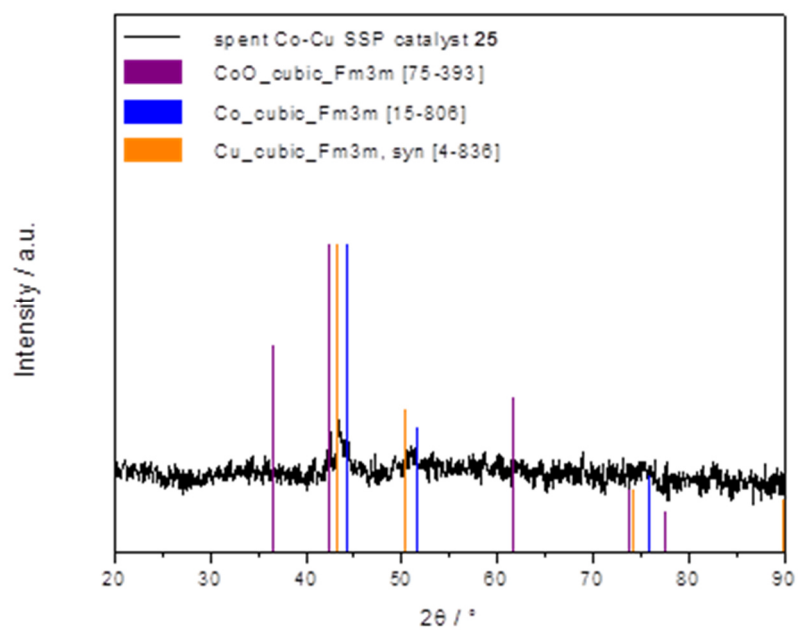


**Figure 41:** Powder XRD of spent Co-Cu SSP catalyst **25** (top) and Col catalyst **26** (bottom), stacked with database XRD patterns of cubic Cu, Co, and CoO.

Thus, the XRD spectra of both spent catalysts strongly resemble each other. Moreover, both are strongly differing from those of the corresponding fresh catalysts, where a Co-Cu alloy and CoO was detected on SSP catalyst **22**, whereas reflexes of cubic  $\text{Cu}_{0.92}\text{Co}_{2.08}\text{O}_4$  were found on Col catalyst **23**. These results foster the outcomes from catalytic testing, showing that the catalysts structures assimilate under reaction conditions.

### 3.2.8.2 Investigation of the surface functionality *via* DRIFTS analysis

After catalytic testing, the spent Co-Cu SSP catalyst (**25**) and the corresponding Col catalyst (**26**) were reduced and investigated *via* DRIFTS in order to investigate the catalysts' surfaces under *in situ* conditions. Thus, the catalysts were again activated using 13 % $\text{H}_2$ /Ar at 250 °C for 1 h, and after cooling to r.t. and removal of the gaseous atmosphere *in vacuo*, CO adsorption experiments were performed (**Figure 42**). In both cases, only very poor adsorption can be detected, indicating dominance of cobalt functionality on the surface. Furthermore, in both cases the rotational bands of free CO at  $\sim 2170$  and  $2121\text{ cm}^{-1}$ , as well as the measurement artefacts at  $1894$  and  $1825\text{ cm}^{-1}$  are found and not further considered. The slight pronunciation of the rotational band of free CO at  $\sim 2123\text{ cm}^{-1}$  on the spent Col catalyst (**26**) gives hint towards metallic Cu.[86] The Co-Cu SSP catalyst (**25**) has an additional CO adsorption band at  $1946\text{ cm}^{-1}$  that belongs to bridged and multi-bonded CO on cobalt.[79] Other than that, the Co-Cu Col catalyst (**26**) has additional bands at  $2054\text{ cm}^{-1}$  and  $1997\text{ cm}^{-1}$ . The band at  $2054\text{ cm}^{-1}$  lies in a range that has been widely discussed in the literature, and was interpreted to denote e.g. CO adsorbed on defect sites,[114] CO linearly adsorbed on  $\text{Co}^{\delta+}$  sites,[115–119] cobalt polycarbonyls,[120] especially when they appear together with lower-frequency bands as in the case of the spent Col catalyst (**26**),[121] or some combination of the above.[122–124] The band at  $1997\text{ cm}^{-1}$  is assigned to linear monocarbonyl on  $\text{Co}^0$ . [87]

Comparison with the DRIFTS results from fresh catalysts **22** and **23** (**Figure 39**) shows that in both cases the intensity of CO adsorption decreased by a factor of  $\sim 10$ , which might be caused by bigger particle sizes.

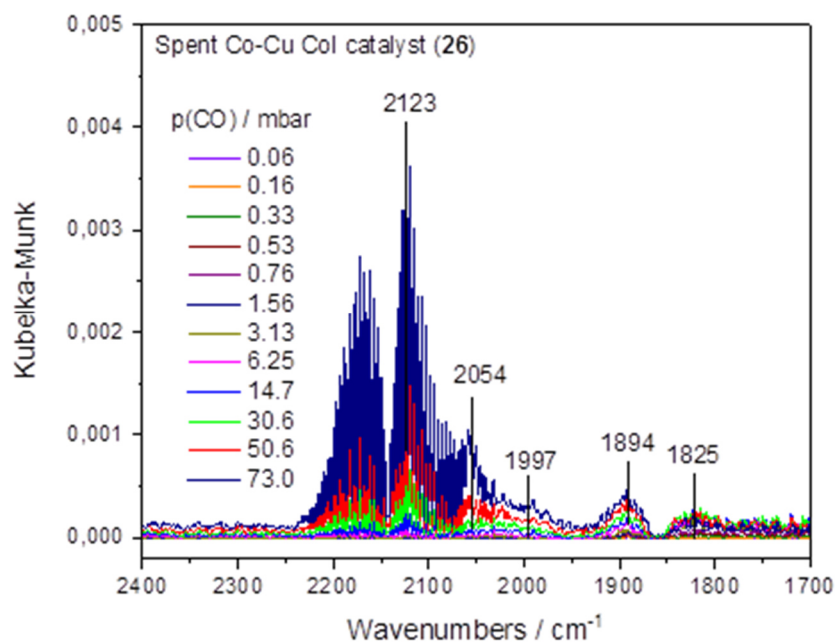
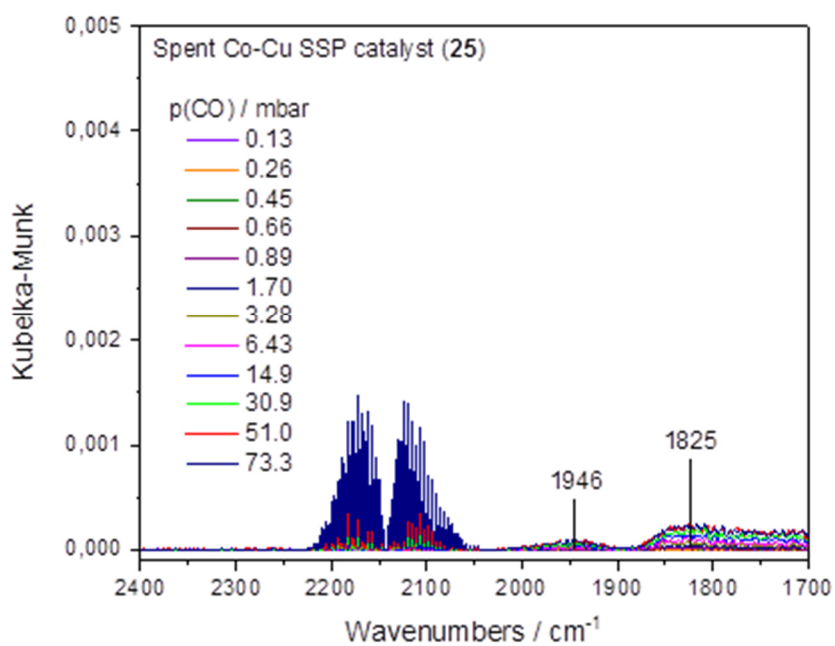


**Figure 42:** Comparison of DRIFTS spectra measured during CO chemisorption on spent Co-Cu SSP catalyst (25, top), and Col catalyst (26, bottom).

Furthermore, an increased Co surface coverage might account for the strong decline in intensity, since Co suppresses CO adsorption compared to Cu as can be seen on the DRIFTS spectra of the monometallic reference catalysts (**Figure 38**). The theory of a dominating Co-surface coverage is fostered by the fact that all detected bands can be assigned to Co-species.

### 3.2.9 Discussion: Co-Cu catalysts

In case of the Co-Cu catalysts, again superiority regarding the maintenance of the metal-to-metal ratio of the SSP catalysts (**21** and **22**) compared to the Col catalyst (**23**) could be proven. For all catalysts, no anomalies regarding pore volume, pore radius, or surface area are detected *via* BET analysis. XRD analysis reveals that for both SSP catalysts (**21** and **22**), 16.4-34.1 nm sized particles of Co-Cu alloy and CoO are present in parallel, whereas the corresponding Col catalyst (**23**) exists of ~12.1 nm big particles of cubic  $\text{Cu}_{0.92}\text{Co}_{2.08}\text{O}_4$ . This is a first evidence that also in the case of the Co-Cu system, the SSP approach leads to different compounds than the Col method. STEM, SAED, and EDX analysis of two catalysts that were reductively activated and measured without air contact show severe differences between the samples, that is likely alloy formation in both cases, but well dispersed, small particles in case of the SSP catalyst (**22**), and agglomerated particles on the Col catalyst (**23**). Thus, putting together the results from XRD and TEM, it can be concluded that the final Col catalyst mainly consists of  $\text{Cu}_{0.92}\text{Co}_{2.08}\text{O}_4$ , and is reduced to Cu-Co alloy particles upon reductive activation. Contrary, small alloy nanoparticles are formed on the SSP catalyst (**22**) upon reductive activation. Investigation of the freshly prepared catalysts without further air contact *via* DRIFTS confirms the existence of smaller particles on the reductively activated SSP catalyst, which is due to the lower activation temperature needed for the SSP catalyst (260 °C) compared to the calcination temperature of the Col catalyst (300 °C).

In contrast to the results of characterization of the fresh catalysts, again, extremely similar results are obtained upon catalytic testing for StE conversion on both bimetallic systems. Both catalysts show very comparable CO conversion rates ( $X_{\text{CO}} = 43.7\%$  on catalyst **22**, respectively 41.8 % on catalyst **23**), which can be rationalized by the similar metals loading. Furthermore, activity in terms of CO conversion can be

attributed to the copper contribution, since the monometallic cobalt catalyst shows highly diminished activity even at almost double metal loading ( $X_{\text{Co}} = 5.03\%$ ). This disagrees to the study of the group of Spivey,[86] who found that the CO conversions increased in the order  $\text{Cu}/\text{SiO}_2 < \text{CuCo}/\text{SiO}_2 < \text{Co}/\text{SiO}_2$ , which might be caused by different testing conditions (literature:  $\text{H}_2/\text{CO} = 2$ ;  $p = 10$  bar;  $\text{GHSV} = 24000$   $\text{scc}/\text{g}_{\text{cat}}/\text{h}$ ;  $T_{\text{max}} = 300^\circ\text{C}$ ).

Regarding the product spectrum, again, ethanol is only formed on the bimetallic catalysts, probably *via* CO dissociation on the cobalt sites, and molecular adsorption and CO insertion taking place at the copper sites.[125–127] Hence, the predictions made by Medford et al. are again correct as far as synergism between Co and Cu is generally necessary to form ethanol.[67] Nevertheless, the desired catalyst system seems to be unstable under reaction conditions and therefore not applicable for the StE reaction without further modifications. Thus, the ethanol selectivity on the bimetallic catalysts is very low, and a high amount of typical FT products is formed. That corresponds well to the results of DRIFTS investigation of the spent catalysts, showing that mainly Co-surface functionality is present after the catalytic reaction. Co is a known FT catalyst.

Deactivation of supported Co-Cu catalysts is discussed quite controversially in literature. In 2016, the group of Sun investigated changes in the catalytic performance and structural evolution during HAS conversion from syngas on  $\text{TiO}_2$ -supported Cu-Co catalysts with a Cu/Co atomic ratio of 1:2, and found decreased activity with TOS as well as reduction of the chain growth probabilities of both alcohols and hydrocarbons.[128] They explained their findings with a decrease in the amount of surface metallic cobalt ensembles due to severe sintering and formation of  $\text{Co}_x\text{C}$  on the catalyst surface. On the other hand, a study of Liu et al. from the same year regarding the behavior of La-stabilized,  $\text{ZrO}_2$ -supported Cu-Co model catalysts (molar ratio of Cu/Co of 0.7:0.3) under syngas conversion conditions identified phase separation and volatilization of cobalt as major reason for catalyst deactivation.[129] According to their findings, sintering of the alloy nanoparticles just as coke-deposition does not take place upon La-doping. Thus, morphological rearrangement of Cu-Co alloys under syngas conversions causing deactivation is a well-known problem and strongly dependent on the discrete catalyst system.

### 3.3 The Cu-Fe system

#### 3.3.1 Synthesis of the SSPs

The literature-known complexes  $[(C_2H_5)_4N]_3Cu_5Fe_4(CO)_{16}$  (**3**) and  $Na_2Cu_6Fe_4(CO)_{12} \cdot 3 THF$  (**4**) were chosen as Cu-Fe SSPs, due to several reasons: 1.) The compounds bear only carbonyl ligands as well as attached solvent molecules, which are quite small molecules with low molecular weight and consequently comparably volatile. 2.) Carbonyl ligands and attached solvent molecules consist only of C, H, and O, and thus contain no poisoning elements. 3.) The complexes are composed of a Cu-Fe core system with direct metal-to-metal bonds (**Figure 43**). 4.) The compounds are literature known, and accessible within few synthesis steps.[130] 6.) Due to the different cations as well as the different stoichiometry of metals in the two complexes, the influence of Na as well as the influence of the metal-to-metal ratio can be discussed on basis of those two examples.

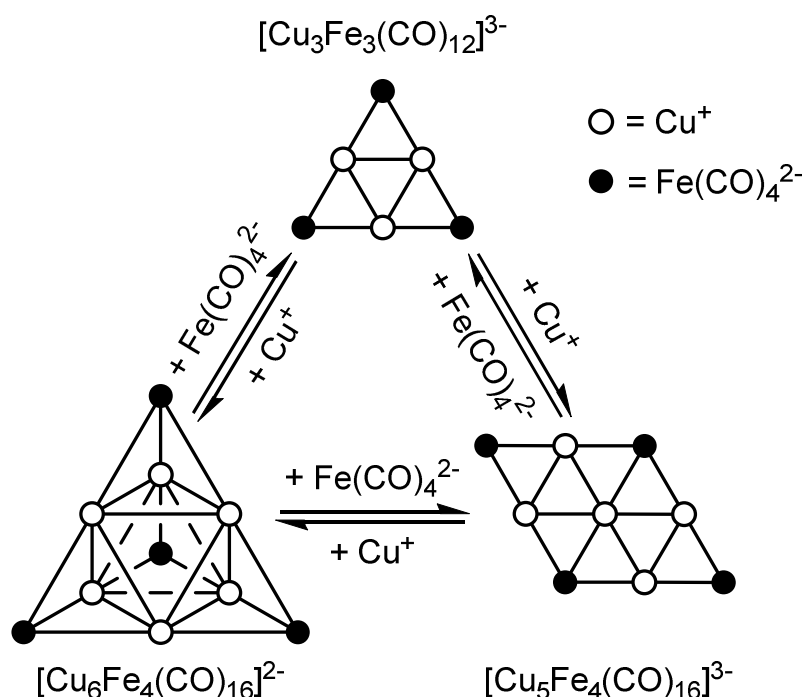
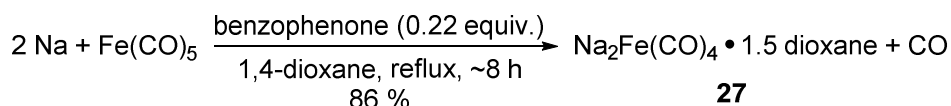


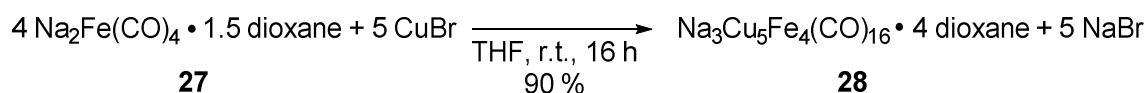
**Figure 43:** Reaction scheme showing the interconversion of the  $[Cu_3Fe_3(CO)_{12}]^{3-}$ ,  $[Cu_5Fe_4(CO)_{16}]^{3-}$ , and  $[Cu_6Fe_4(CO)_{16}]^{2-}$  cluster anions according to Doyle and co-workers.[130]

For synthesis of the clusters, so-called Collman's reagent, that is  $\text{Na}_2\text{Fe}(\text{CO})_4 \cdot 1.5$  dioxane (**27**), was synthesized first according to a procedure described by Finke and Sorrell (**Scheme 9**).[131]



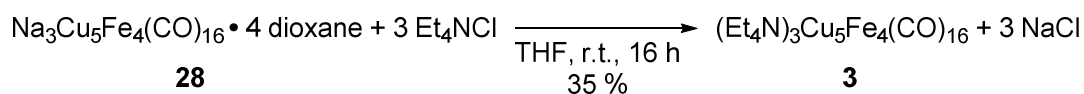
**Scheme 9:** Synthesis of Collman's reagent (**27**) according to the literature.[131]

Collman's reagent (**27**) was further used in combination with CuBr in respective stoichiometries for cluster formation reactions according to Doyle and co-workers (**Scheme 10**).[130]



**Scheme 10:** Synthesis of  $\text{Na}_3\text{Cu}_5\text{Fe}_4(\text{CO})_{16} \cdot 4$  dioxane (**28**) according to the literature.[130]

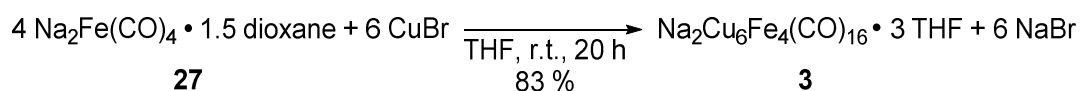
Existence of  $\text{Na}_3\text{Cu}_5\text{Fe}_4(\text{CO})_{16} \cdot 4$  dioxane (**28**) was verified using Nuclear Magnetic Resonance (NMR) and FT-IR spectroscopy, elemental analysis, and single-crystal XRD measurement (see chapter 5.5). The complex was then used to synthesize the sodium free Cu-Fe SSP (**3**) according to Doyle and co-workers.[130] Thus,  $\text{Na}_3\text{Cu}_5\text{Fe}_4(\text{CO})_{16} \cdot 4$  dioxane (**28**) was reacted with  $\text{Et}_4\text{NCl}$  in a salt metathesis reaction, in which NaCl as well as the sodium free Cu-Fe SSP  $(\text{Et}_4\text{N})_3\text{Cu}_5\text{Fe}_4(\text{CO})_{16}$  (**3**) was formed (**Scheme 11**).



**Scheme 11:** Synthesis of  $(\text{Et}_4\text{N})_3\text{Cu}_5\text{Fe}_4(\text{CO})_{16}$  (**3**) according to the literature.[130]

The product (**3**) was characterized using FT-IR spectroscopy, elemental analysis, and single-crystal XRD measurement (see chapter **5.5**).

Additionally, the biggest of the reported Cu-Fe clusters,  $\text{Na}_2\text{Cu}_6\text{Fe}_4(\text{CO})_{16} \cdot 3 \text{ THF}$  (**4**), was synthesized in order to investigate the influence of Cu-Fe stoichiometry, as well as the influence of sodium. Thus, Collman's reagent (**27**) was reacted with a stoichiometric amount of copper bromide (**Scheme 12**).



**Scheme 12:** Synthesis of  $\text{Na}_2\text{Cu}_6\text{Fe}_4(\text{CO})_{16} \cdot 3 \text{ THF}$  (**4**) according to the literature.[130]

Again, formation of the product (**4**) was confirmed *via* NMR and FT-IR spectroscopy, elemental analysis, and single-crystal XRD measurement (see chapter **5.5**).

### 3.3.2 Decomposition and characterization of the unsupported SSPs

As in the case of the Co-Pt and Co-Cu SSPs, the next step regarding the Cu-Fe SSPs was thermolysis of the Cu-Fe SSPs (**3** and **4**) in  $\text{H}_2$  atmosphere, monitored *via* MS, for identification of the ideal activation conditions for the final Cu-Fe catalyst (**Figure 44**).

In case of the Na-free Cu-Fe SSP (**3**), the TCD signal shows no  $\text{H}_2$  consumption. This indicates that any redox-reaction possibly taking place has to be intramolecular, involving  $\text{Cu}^+$ ,  $\text{Fe}^{2-}$ , as well as  $[\text{Et}_4\text{N}]^+$ . The MS signal shows ligand and parallel cation release starting at  $\sim 120$  °C. As in the case of the Co-Cu SSP (**2**), the  $\text{Et}_4\text{N}^+$  cation undergoes thermal degradation and is therefore mainly desorbed in form of fragments of triethylamine. Consequently, release of  $\text{CO}_2$  cannot be explicitly detected since the respective mass-to-charge ratio of  $m/z = 44$  also fits to a fragmentation product of triethylamine. Release of a little amount of  $\text{H}_2\text{O}$  ( $m/z = 18$ ) is attributed to Hoffmann elimination reaction taking place on the  $\text{Et}_4\text{N}^+$  cation.

The decomposed sample was passivated with 1 %  $\text{O}_2$  and investigated *via* XRD analysis (**Figure 45**).

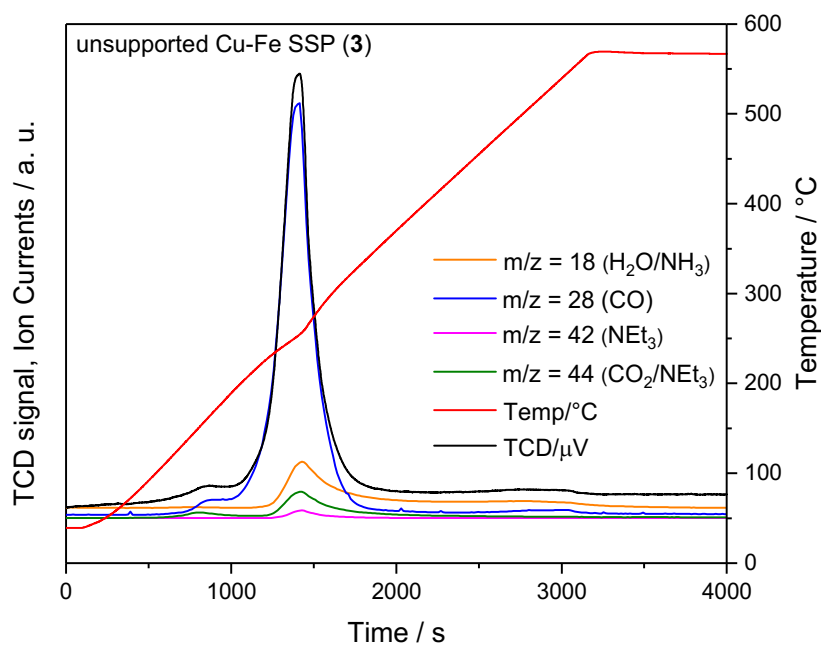


**Figure 44:** Thermolysis profile of the unsupported Cu-Fe SSP (3) in H<sub>2</sub> atmosphere, monitored via MS.

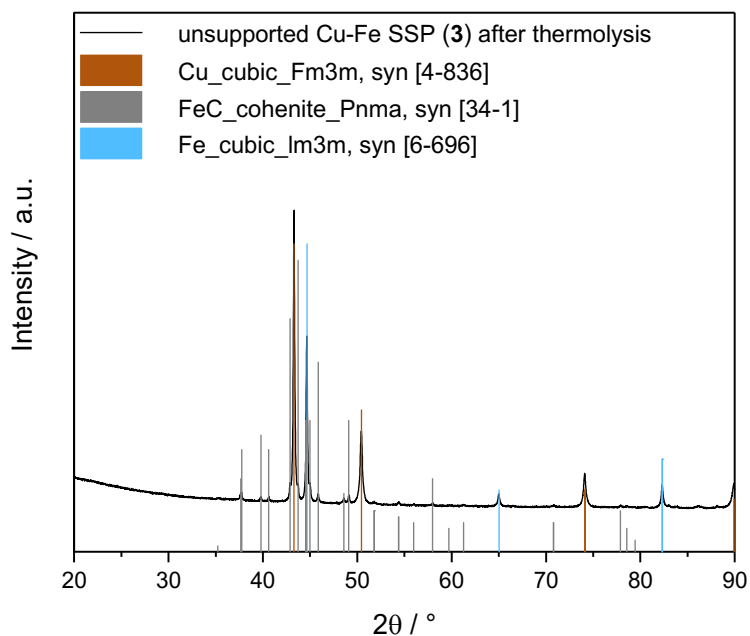


**Figure 45:** XRD analysis of the unsupported Cu-Fe SSP (3) after decomposition in H<sub>2</sub> atmosphere and passivation with 1 % O<sub>2</sub>, and comparison to database entries for metallic Cu and Fe as well as FeC.

Comparison of the diffractogram with database entries states the existence of Fe, Cu, and Fe<sub>3</sub>C. The estimation of the composition after fitting the data with the Rietveld method yielded an overall Cu-Fe ratio that fits well to the theoretical one (1.33 compared to 1.25). Fe<sub>3</sub>C formation can be explained by a side reaction of Fe with one of the fragmentation intermediates or products of the Et<sub>4</sub>N<sup>+</sup> cation. No peak shift compared to metallic Cu respectively Fe, and therefore no hint for alloy formation was detected, which fits well the Cu-Fe binary phase diagram.[28]

Next, the Na-Cu-Fe SSP (4) was thermolyzed in the same manner (**Figure 46**).

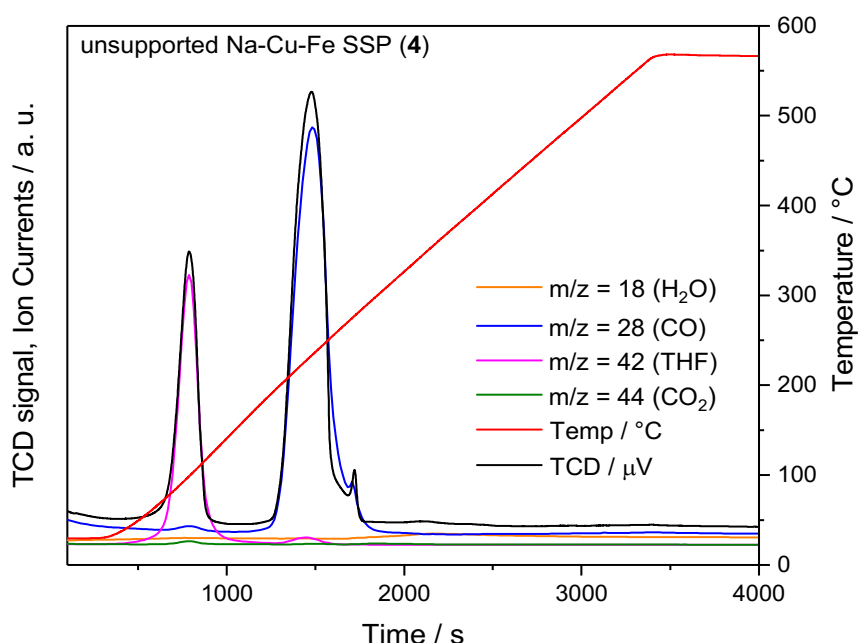


**Figure 46:** Thermolysis profile of the Na-Cu-Fe SSP (4) in H<sub>2</sub> atmosphere, monitored via MS.

At first, attached THF molecules are desorbed, starting at ~70 °C. The CO ligand is bound stronger to the complex molecule than the attached solvent molecules, and therefore released at higher temperatures, starting from ~190 °C. No H<sub>2</sub> consumption as well as no CO<sub>2</sub> release is monitored, indicating an intramolecular redox-reaction between Na<sup>+</sup>, Cu<sup>+</sup>, and Fe<sup>2+</sup> is taking place. Furthermore, no H<sub>2</sub>O release is detected,

supporting the theory that its release in case of  $\text{Et}_4\text{N}\{\text{Cu}[\text{Co}(\text{CO})_4]_2\}$  (**2**) and  $[\text{Et}_4\text{N}]_3\text{Cu}_5\text{Fe}_4(\text{CO})_{16}$  (**3**) is based on Hofmann elimination reaction of the  $\text{Et}_4\text{N}^+$  cation.

The spent sample was investigated *via* XRD measurement (**Figure 47**).

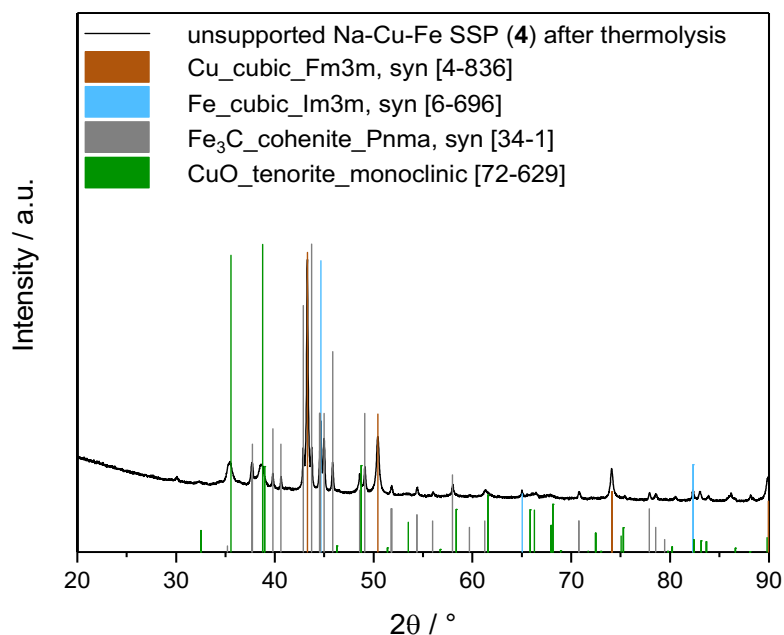


**Figure 47:** XRD analysis of the Na-Cu-Fe SSP (**4**) after decomposition in  $\text{H}_2$  atmosphere, and comparison to database entries for metallic Cu and Fe, as well as  $\text{Fe}_3\text{C}$ , and CuO.

The XRD of bulk decomposed Na-Cu-Fe SSP (**4**) shows few reflexes, proving the formation of defined metallic phases. Comparison of the reflexes with database entries states the formation of Fe, Cu,  $\text{Fe}_3\text{C}$  (Cohenite), and CuO. No peak shift compared to metallic Cu and Fe is detected, which would indicate Cu-Fe alloy formation. Due to the low intensity and overlap of signals, crystallite sizes could not be calculated *via* Scherrer equation. After fitting the data using the Rietveld method, an approximate estimation of the composition was possible, being 3.42 wt.% Fe, 31.95 wt.% Cu, 32.63 wt.%  $\text{Fe}_3\text{C}$ , and 32.00 wt.% CuO. This gives an overall ratio of  $n(\text{Cu})/n(\text{Fe}) = 1.49$ , which fits the theoretical value, being 1.50. Just in case as for the Cu-Fe SSP (**3**),  $\text{Fe}_3\text{C}$  formation can be explained by a side reaction of Fe with one of the fragmentation

intermediates or products of the  $\text{Et}_4\text{N}^+$  cation. In this case, CuO is detected additionally. This can be explained by oxidation of very small metallic Cu particles in air. Since sodium cannot be detected *via* XRD analysis at all, it must be present in amorphous form.

### 3.3.3 Supporting of the SSPs

Precursor  $[\text{Et}_4\text{N}]_3\text{Cu}_5\text{Fe}_4(\text{CO})_{16}$  (**3**) was immobilized on  $\text{SiO}_2$  using WI and SIWI with a loading of 5.0 wt.% regarding Cu (**Table 14**).

**Table 14:** Overview of SSP catalysts prepared by impregnation of the Cu-Fe SSP (**3**) on  $\text{SiO}_2$ .

Catalyst	Impregnation method	Theoretical loading [wt.%]	
		Cu	Fe
<b>29</b>	WI	5.00	3.52
<b>30</b>	SIWI	5.00	3.52

The precursor  $\text{Na}_2\text{Cu}_6\text{Fe}_4(\text{CO})_{16} \cdot 3 \text{ THF}$  (**4**) was immobilized on pre-dried  $\text{SiO}_2$  as well *via* WI, IWI, and SIWI with a Cu loading of 3.00 wt.% respectively 5.00 wt.% (**Table 15**).

**Table 15:** Overview of SSP catalysts prepared by impregnation of Na-Cu-Fe SSP (**4**) on  $\text{SiO}_2$ .

Catalyst	Impregnation method	Theoretical loading [wt.%]		
		Cu	Fe	Na
<b>31</b>	IWI	5.00	2.92	0.60
<b>32</b>	WI	3.00	1.76	0.36
<b>33</b>	WI	5.00	2.92	0.60
<b>34</b>	SIWI	3.00	1.76	0.36
<b>35</b>	SIWI	5.00	2.92	0.60

### 3.3.4 Decomposition of supported SSPs

To find the ideal conditions, thermolysis in  $\text{H}_2$  atmosphere was performed on catalysts **30** and **31** (**Figure 48** and **Figure 49**) and monitored *via* MS.

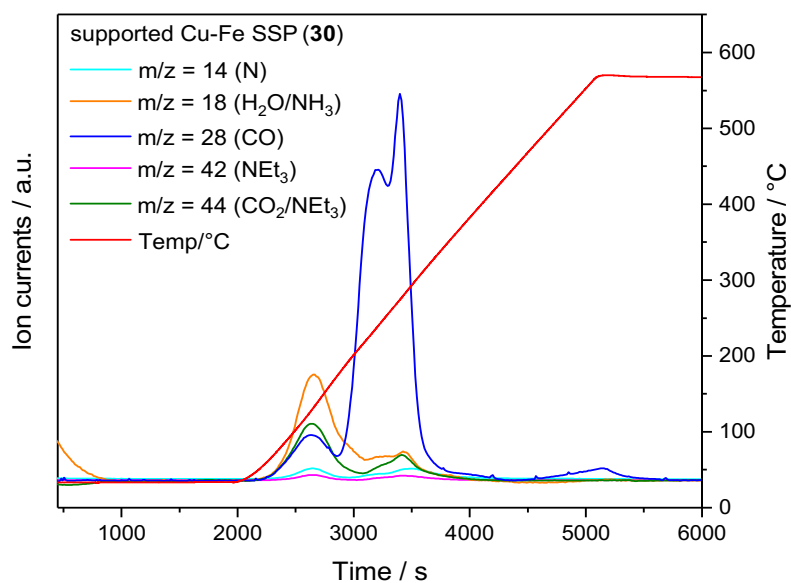


**Figure 48:** Thermolysis profile of SiO<sub>2</sub>-supported Cu-Fe SSP (30) in H<sub>2</sub> atmosphere, monitored via MS.

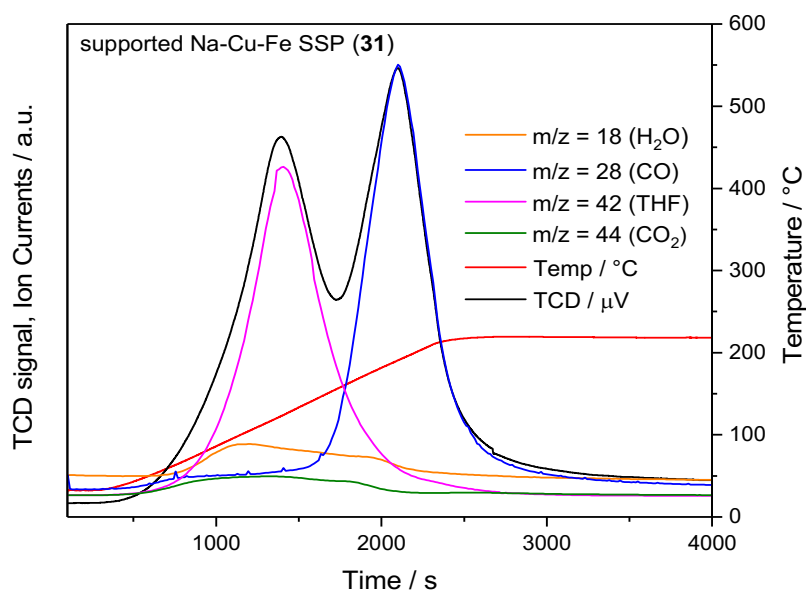


**Figure 49:** Thermolysis profile of SiO<sub>2</sub>-supported Na-Cu-Fe SSP (31) in H<sub>2</sub> atmosphere, monitored via MS.

The thermolysis profile of the supported Cu-Fe SSP (**30, Figure 48**) shows release of fragments of the  $\text{Et}_4\text{N}^+$  cation starting at  $\sim 70^\circ\text{C}$ . As described before, the  $\text{Et}_4\text{N}^+$  cation undergoes thermal degradation and is therefore mainly desorbed in form of fragments of triethylamine, which is in accordance to the literature.[105] Thus, release of  $\text{CO}_2$  cannot be explicitly detected, since the respective mass-to-charge ratio of  $m/z = 44$  also fits to a fragmentation intermediate of triethylamine. Furthermore, release of a little amount of  $\text{H}_2\text{O}$  can be detected ( $m/z = 18$ ), which is attributed to Hoffmann elimination reaction taking place on the  $\text{Et}_4\text{N}^+$  cation, as well as to  $\text{H}_2\text{O}$  left on the  $\text{SiO}_2$  support. Detachment of the CO ligand starts parallel to the fragments of  $\text{Et}_4\text{N}^+$  at  $\sim 70^\circ\text{C}$  and continues in two further steps at higher temperatures ( $\sim 230^\circ\text{C}$  and  $\sim 275^\circ\text{C}$ ). CO release takes places in three steps; thus, different species of the CO ligands are present on the supported complex, e.g. *via* non-flat, but edge- or corner-shared adsorption of the almost planar complex on the silica surface. Based on those results, Cu-Fe SSP catalysts for inert STEM and DRIFTS investigation and catalytic testing were activated by application of a maximum temperature of  $260^\circ\text{C}$ .

Regarding the thermolysis profile of the Na-Cu-Fe catalyst (**31, Figure 49**), just as in case of the unsupported complex release of attached THF molecules takes places first, followed by CO ligands. No  $\text{H}_2$  consumption is monitored, indicating an intramolecular redox-reaction between  $\text{Na}^+$ ,  $\text{Cu}^+$ , and  $\text{Fe}^{2-}$ . Release of a small amount of  $\text{H}_2\text{O}$  is detected, which is assigned to water left on the silica support.

### 3.3.5 Synthesis of reference catalysts

Reference catalysts containing the same theoretical loadings as the SSP catalysts were synthesized by immobilization of metal nitrates *via* IWI, and subsequent calcination at  $300^\circ\text{C}$ , on the basis of existing studies (**Table 16**).[132,133] In addition to the CoI catalysts, two more catalysts were prepared, containing only Cu respectively Fe in order to analyze the influence of the synergistic effect of the metals during syngas conversion.

**Table 16:** Overview of (Na-)Cu-Fe reference catalysts synthesized via IWI of metal salts.

Catalyst	Dual-source precursors	Theoretical loading [wt.%]		
		Cu	Fe	Na
<b>36</b>	$\text{Cu}(\text{NO}_3)_2 \cdot 3 \text{H}_2\text{O}, \text{Fe}(\text{NO}_3)_3 \cdot 9 \text{H}_2\text{O}$	5.00	3.52	/
<b>37</b>	$\text{Cu}(\text{NO}_3)_2 \cdot 3 \text{H}_2\text{O}, \text{Fe}(\text{NO}_3)_3 \cdot 9 \text{H}_2\text{O}, \text{NaNO}_3$	5.00	2.92	0.60
<b>24</b>	$\text{Cu}(\text{NO}_3)_2 \cdot 3 \text{H}_2\text{O}$	5.00	/	/
<b>38</b>	$\text{Fe}(\text{NO}_3)_3 \cdot 9 \text{H}_2\text{O}$	/	3.00	/

### 3.3.6 Characterization of catalysts

#### 3.3.6.1 Elemental analysis for determination of metal loading on the support

ICP-OES and XRF was used to determine the metal loadings and metal-to-metal ratios of (Na-)Cu-Fe SSP (**29-35**) and CoI catalysts (**24, 36-38, Table 17**).

Regarding the Cu-Fe SSP catalysts (**29** and **30**), the theoretical and measured loadings vary significantly, but can be considerably improved by applying SIWI instead of WI (mean deviation: 26 % instead of 63 %). A possible reason for that might be the use of a syringe filter, which was needed to separate unsolved complex from the precursor solution. Consequently, some of the complex might have clogged the filter pores. Although the theoretical and measured loadings differ drastically, the metal-to-metal ratio of Cu:Fe is perfectly preserved in both cases.

In case of the Na-Cu-Fe SSP catalysts (**31-35**), again the analytically determined loadings are greatly diminished compared to their theoretical loadings. The change of impregnation methods from WI (**32, 33**), to IWI (**31**), to SIWI (**34, 35**) led to an improved metals loading (mean deviation: 50 % (**32, 33**), 35 % (**31**), 22 % (**34, 35**)). A potential reason for the still noticeable difference between theoretical and measured metal loadings might again be the use of a syringe filter during impregnation. Furthermore, the metal-to-metal ratio strikingly deviates, too. This might be explained by decomposition of the cluster during impregnation. The (Na-)Cu-Fe SSPs are part of a sensitive equilibrium in which minor differences in stoichiometry of starting materials can lead to other clusters as side products (**Figure 43**), hence leading to a mismatch in theoretical loading and metal-to-metal ratio.

**Table 17:** Analysis of metal contents of (Na-)Cu-Fe SSP and reference catalysts. Analysis was performed via ICP-OES except of entry **36** (analyzed via XRF).

Entry	Type	Cu loading [wt.%]		Fe loading [wt.%]		Na loading [wt.%]		Cu : Fe : Na	
		Theoretical	Analysis	Theoretical	Analysis	Theoretical	Analysis	Theoretical	Analysis
<b>29</b>	SSP	5.00	1.87	3.52	1.34	/	/	1 : 1.4 : /	1 : 1.4 : /
<b>30</b>	SSP	5.00	3.74	3.52	2.60	/	/	1 : 1.4 : /	1 : 1.4 : /
<b>31</b>	SSP	5.00	3.12	2.92	1.71	0.60	0.44	1 : 1.7 : 8.3	1 : 1.8 : 7.1
<b>32</b>	SSP	3.00	1.52	1.76	0.89	0.36	0.09	1 : 1.7 : 8.3	1 : 1.7 : 16.9
<b>33</b>	SSP	5.00	3.16	2.92	1.84	0.60	0.30	1 : 1.7 : 8.3	1 : 1.7 : 10.5
<b>34</b>	SSP	3.00	2.49	1.76	1.50	0.36	0.41	1 : 1.7 : 8.3	1 : 1.7 : 6.1
<b>35</b>	SSP	5.00	3.20	2.92	2.13	0.60	0.48	1 : 1.7 : 8.3	1 : 1.5 : 6.7
<b>36</b>	Col	5.00	5.39	3.52	3.64	/	/	1 : 1.4 : /	1 : 1.5 : /
<b>37</b>	Col	5.00	4.53	2.92	2.54	0.60	0.49	1 : 1.7 : 8.3	1 : 1.8 : 9.2
<b>24</b>	reference	5.00	4.03	/	/	/	/	/	/
<b>38</b>	reference	/	/	3.00	2.68	/	/	/	/

Regarding the Col catalysts (**24, 36-38**), it can be found that the theoretical and measured loadings still vary but are in much better agreement than the SSP catalysts (mean deviation: 12 %). In comparison to the SSP catalysts, no syringe filter was needed during preparation of the reference catalysts due to the high solubility of the metal nitrates. This result promotes the thesis of the syringe filter being the reason for the low loading of the SSP catalysts. The RSD for the described ICP-OES and XRD measurements is less than 1% in all cases, and thus does not strikingly contribute to the aberrations.

### 3.3.6.2 Physisorption experiments for characterization of specific surface area, pore volume, and pore radii

The specific pore volume and radius as well as the respective surface area of the (Na-)Cu-Fe catalysts were calculated using BET and BJH theory after physisorption experiments using N<sub>2</sub>. The results for the Cu-Fe catalysts are summarized in **Table 18**, and compared to unloaded SiO<sub>2</sub> (**15**).

**Table 18:** Pore volume, pore radius, and surface area of SiO<sub>2</sub> (**15**) and (Na-)Cu-Fe catalysts **24, 29-38**.

Entry	Type	Loading [wt.%]		Pore volume [mL/g]	Pore radius [Å]	Surface area [m <sup>2</sup> /g]
		Cu	Fe			
<b>15</b>	SiO <sub>2</sub>	/	/	0.75	30.0	480
<b>29</b>	SSP	1.87	1.34	0.72	33.6	433
<b>30</b>	SSP	3.74	2.60	0.69	35.2	391
<b>31</b>	SSP	3.12	1.71	0.65	30.4	427
<b>32</b>	SSP	1.52	0.89	0.73	32.9	443
<b>33</b>	SSP	3.16	1.84	0.65	33.7	389
<b>34</b>	SSP	2.49	1.50	0.70	33.6	416
<b>35</b>	SSP	3.20	2.13	0.71	35.5	399
<b>36</b>	Col	5.39	3.64	0.72	35.9	402
<b>37</b>	Col	4.53	2.54	0.53	30.2	351
<b>24</b>	Col	4.03	/	0.75	34.6	432
<b>38</b>	Col	/	2.68	0.75	32.6	456

As expected, the specific surface area of unloaded SiO<sub>2</sub> (**15**) is higher than that of loaded SiO<sub>2</sub> in all cases. Furthermore, the surface area is approximately inversely correlated to the loading (catalysts **36** > **37** > **30** > **35** > **33** > **31** > **24** > **34** > **29** > **38** > **32** > **15**). Except of catalyst **37**, where a strong decrease of pore volume of ~29 % compared to unloaded SiO<sub>2</sub> is observed, pore volume and pore radius of all other catalysts stay in the same range as for unloaded SiO<sub>2</sub>, suggesting successful precursor deposition without major change of the morphology of the supporting material, e.g. due to clogging.

### 3.3.6.3 Investigation of the catalysts' bulk structure by means of powder XRD

Powder XRD measurement of the reductively activated SSP catalysts was performed in air. Hence, Cu-Fe SSP catalyst **29** shows reflexes that are corresponding to metallic Cu in cubic phase, as well as metallic Fe in cubic phase (**Figure 50**). Application of Scherrer equation (**Eq. 2**) yields Fe particles with an average size of approximately 53.8 nm, and Cu particles with an average size of 57.1 nm. The Cu-Fe SSP catalyst **30** prepared *via* SIWI shows reflexes for Cu particles of ~ 23.1 nm (**Figure 50**), and CuO particles with an average size of 23.7 nm can be detected. Additionally, Fe reflexes can be detected, but the signal-to-noise ratio is too low to properly determine the FWHM and therefore estimate the particle size *via* Scherrer equation. In both cases, the Fe particles seem to be big enough not to be oxidized upon contact to air.

In case of the Na-Cu-Fe SSP catalysts **31-33**, only a broad reflex at 20 ° belonging to the amorphous silica support can be detected, confirming integral homogeneity (**figure A14**). Regarding the Na-Cu-Fe SSP catalysts **34** and **35** prepared *via* SIWI, cubic Cu particles can be detected with an average particle size of 5.89 nm (**34**), respectively 20.3 nm (**35**, **Figure 51**). In case of catalyst **34**, additionally very small Fe crystallites are observed, whereas in case of catalyst **35**, CuO particles form. In both cases, Scherrer equation could not be applied, since the signal-to-noise ratio is too low.

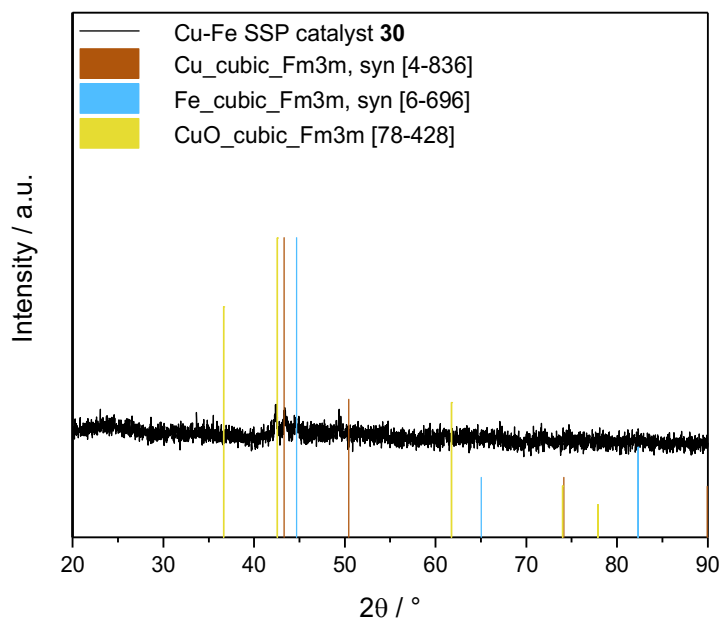
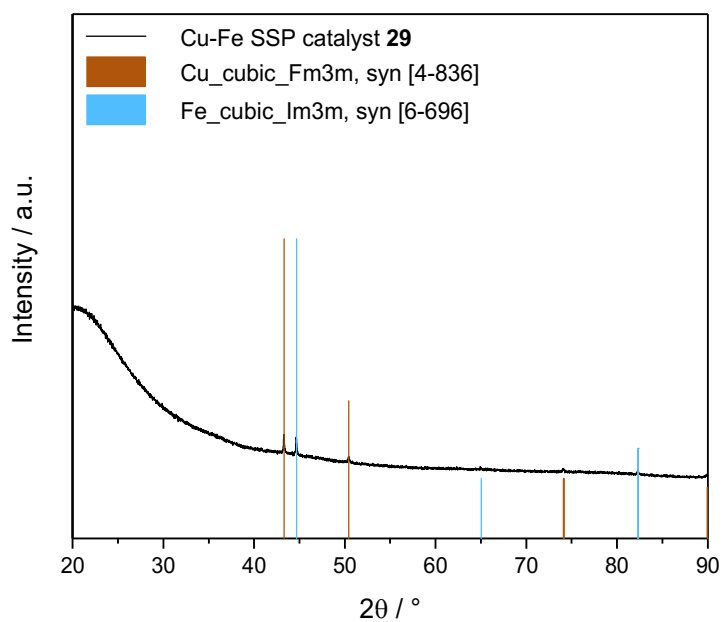


**Figure 50:** Powder XRDs of Cu-Fe SSP catalyst **29** (top), and Cu-Fe SSP catalyst **30** (bottom), stacked with the patterns of cubic Cu, Fe, and CuO.

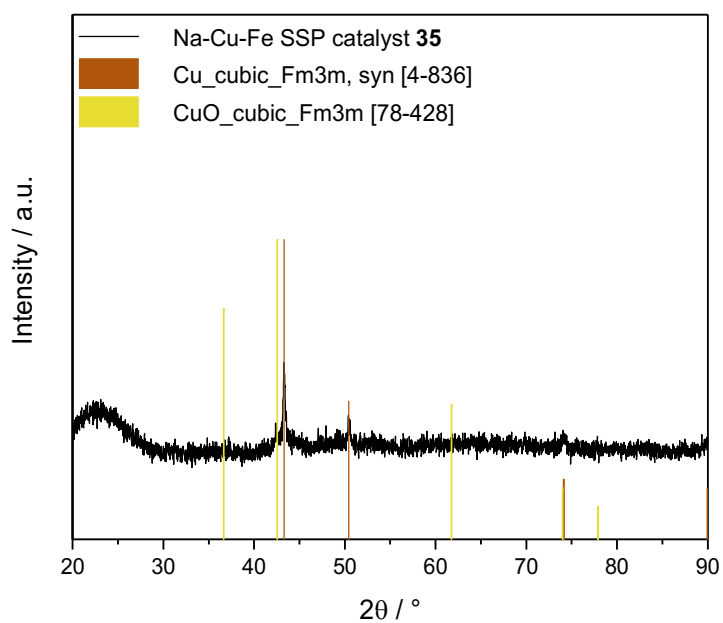
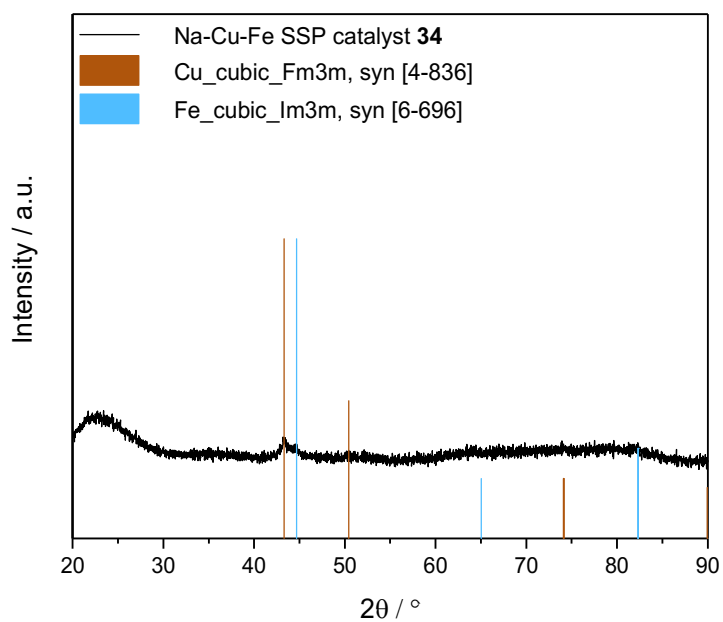


**Figure 51:** Powder XRD of Na-Cu-Fe SSP catalyst **34** (top), stacked with the patterns of cubic, metallic Cu, and cubic, metallic Fe, and Na-Cu-Fe SSP catalyst **35** (bottom), stacked with the patterns of cubic, metallic Cu, and CuO in cubic phase.

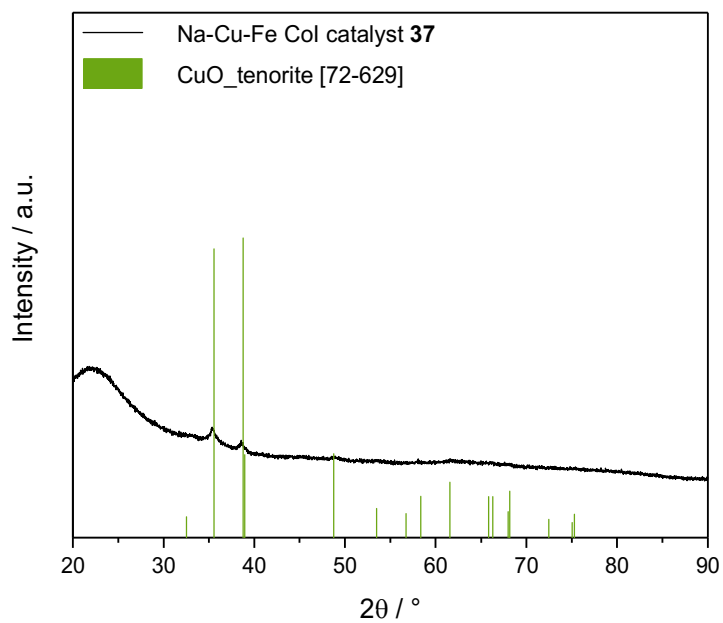
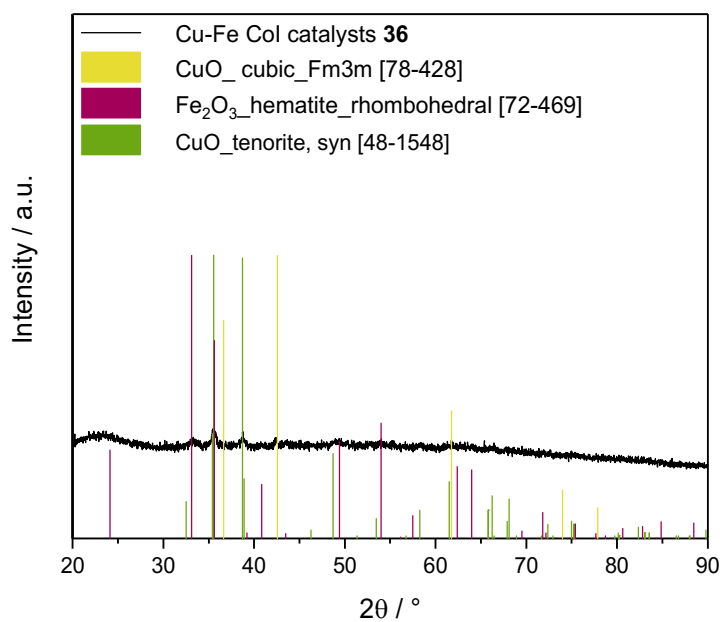


**Figure 52:** Powder XRD of Cu-Fe Col catalyst **36** (top) stacked with the patterns of cubic CuO, monoclinic CuO in tenorite phase, and rhombohedral Fe<sub>2</sub>O<sub>3</sub> in hematite phase, and Na-Cu-Fe Col catalyst **37** (bottom), stacked with the patterns of monoclinic CuO in tenorite phase.

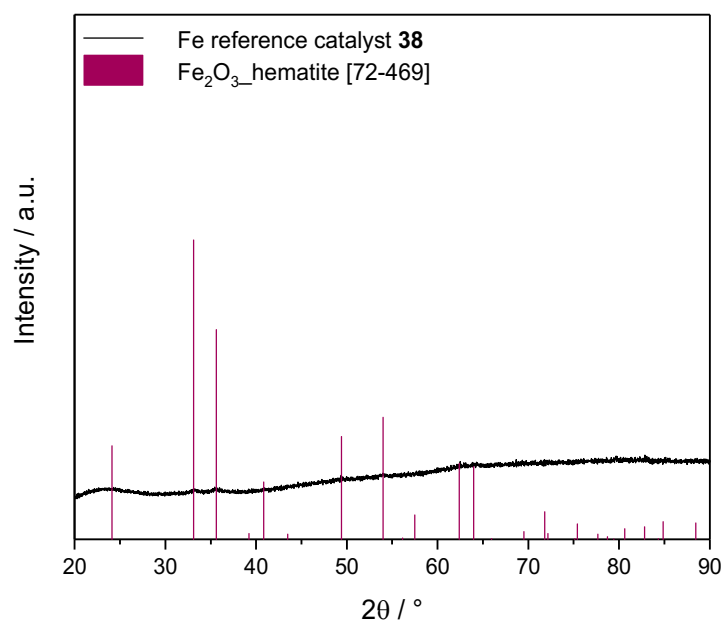
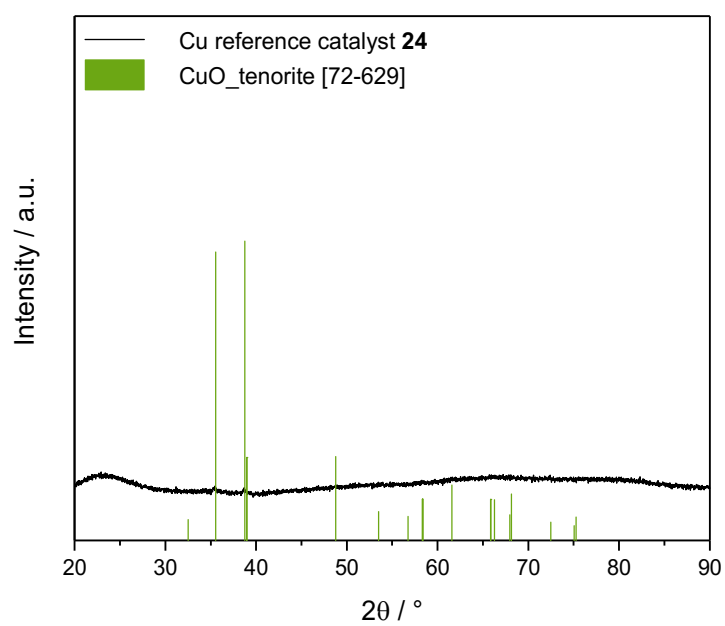


**Figure 53:** Powder XRD of Cu reference catalyst **24** (top), stacked with the pattern of monoclinic CuO in tenorite phase, and Fe reference catalyst **38** (bottom), stacked with the pattern of Fe<sub>2</sub>O<sub>3</sub> in hematite phase.

In comparison, XRD analysis of the calcined Cu-Fe Col catalyst (**36**) and Na-Cu-Fe Col catalyst (**37**) shows diffraction peaks matching with CuO in tenorite phase for both catalysts, and additional particles of monoclinic cubic CuO, and rhombohedral Fe<sub>2</sub>O<sub>3</sub> in hematite phase in case of catalyst **36** (**Figure 52**). Application of Scherrer equation (**Eq. 2**) yields CuO tenorite particles with an average size of approximately 21.6 nm for catalyst **36**, and 13.4 nm for catalyst **37**. The cubic CuO particles of catalyst **36** have an average size of 23.1 nm, and the Fe<sub>2</sub>O<sub>3</sub> particles are about 14.4 nm big.

Powder XRD of the monometallic reference catalysts shows characteristic reflexes for CuO in tenorite phase for catalysts **24**, and Fe<sub>2</sub>O<sub>3</sub> in hematite phase for catalyst **38** (**Figure 53**). Scherrer equation could not be performed in both cases, since the signal-to-noise ratio is too low.

#### **3.3.6.4 Investigation of surface morphology and composition of the activated catalysts using STEM, SAED, and EDX measurements**

To get more information about the morphology of the catalysts in the working state, a Cu-Fe SSP catalyst (**30**) was compared to the corresponding Col catalyst (**36**) *via* electron microscopy under inert atmosphere without previous air contact. Thus, SSP catalyst **30** was activated using a protocol based on the results obtained from thermolysis, that is heating to 100 °C for 4 h, then to 200°C for 4 h, to 225 °C for 1 h, and finally at 260 °C for 1 h, in an atmosphere of flowing 10 % H<sub>2</sub>/N<sub>2</sub>. To ensure comparability of both catalysts in their active state during syngas conversion, Col catalyst **36** was similarly activated in flowing 10 % H<sub>2</sub>/N<sub>2</sub> with two heating plateaus at 210 and 280 °C which were held for 5 h each. Then, both catalysts **30** and **36** were installed in the microscope and analyzed under inert atmosphere without any air contact.

STEM images of the activated catalysts show a much more homogeneous dispersion of smaller particles in case of the SSP catalyst (**30**) than for the Col catalyst (**36**, **Figure 54**).

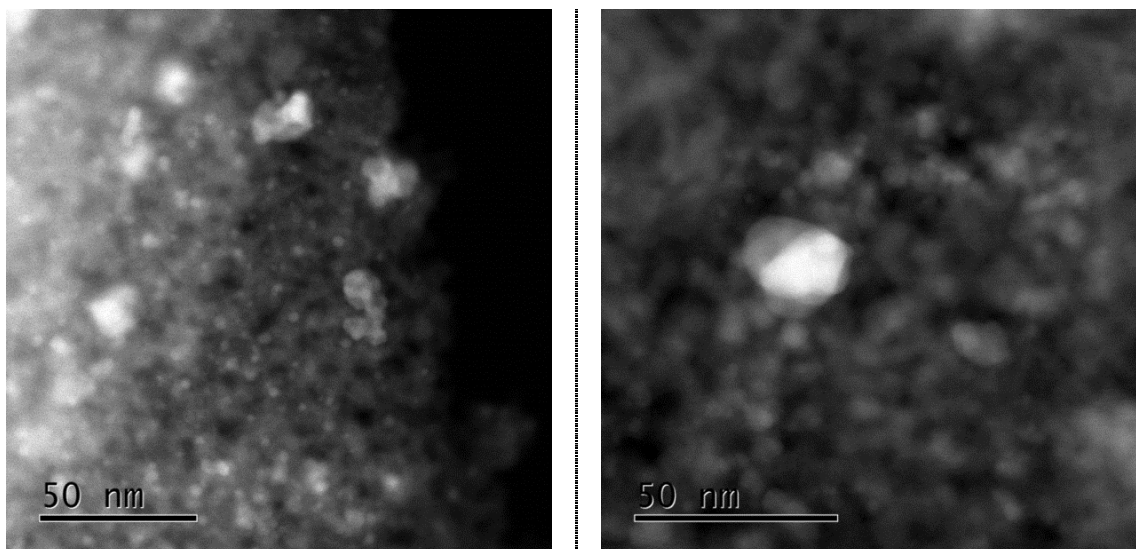


**Figure 54:** STEM analysis of Cu-Fe SSP catalyst **30** (left) and Col catalyst **36** (right).

Analysis of the particle size distribution shows a much narrower distribution range with much smaller particles in case of the SSP catalyst compared the supported Col catalyst (**Figure 55**). The maximum of SSP catalyst particles has a size of  $\sim 2.5$  nm, whereas the corresponding Col catalyst shows a maximum at  $\sim 8.6$  nm. In case of the Col catalyst (**36**), the particle size distribution curve goes up to 30 nm. In case of the SSP catalyst, only very few particles above 8 nm are detected.

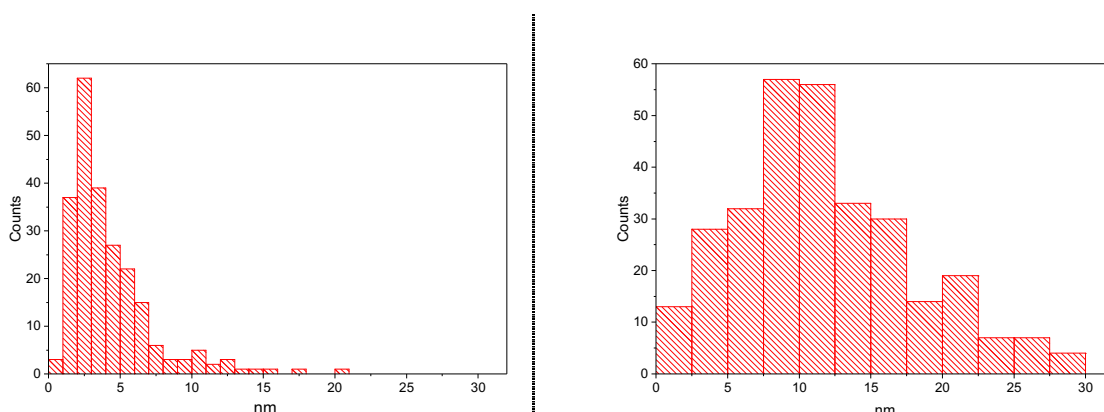


**Figure 55:** Particle size analysis of Cu-Fe SSP catalyst **30** (left) and Col catalyst **36** (right).

Composition analysis was performed using annular dark-field (ADF)-STEM combined with EDX mapping (**Figure 56**). In both cases, the investigated areas show small particles of Cu and Fe being in close contact to each other. Since Cu-Fe overlapping occurs only partially, the two metals do not seem to form a single-phase alloy. Nevertheless, the overlapped areas are bigger in case of the SSP particle, indicating a more intimate mixing than in case of the Col catalyst.

High resolution (HR)-TEM combined with SAED analysis shows diffraction rings that match with metallic Cu and metallic Fe, and therefore confirm the results obtained *via* EDX mapping (**Figure 57**). The Col catalyst (**36**) shows a higher number of diffraction rings than the SSP catalyst, since the investigated particle is larger than the SSP particle.

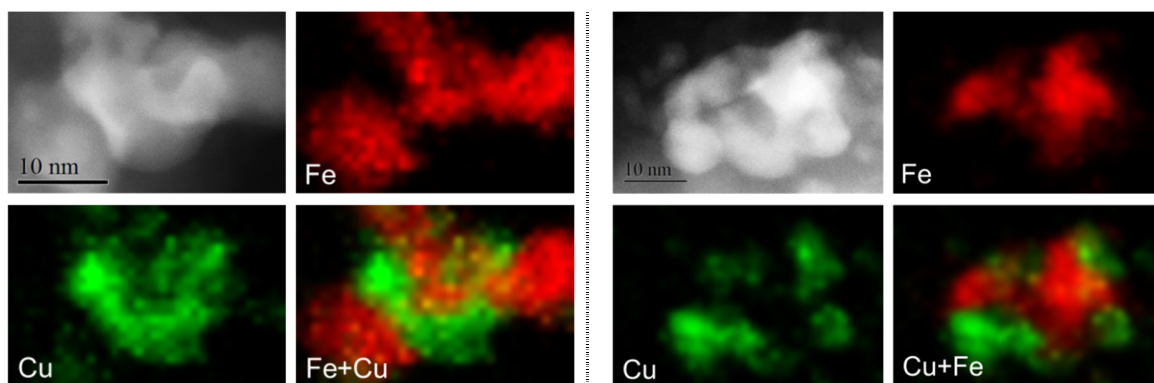


**Figure 56:** ADF-STEM and EDX analysis of Cu-Fe SSP catalyst **30** (left), and Col catalyst **36** (right).

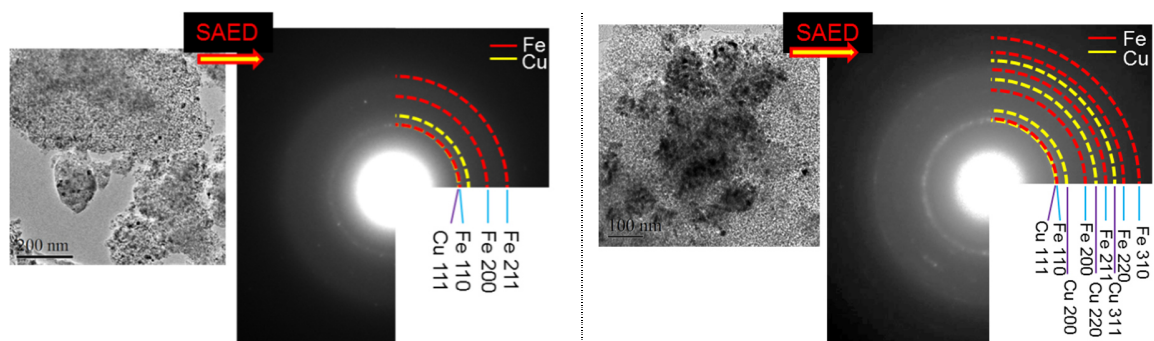


**Figure 57:** HR-TEM and SAED analysis of Cu-Fe SSP catalyst **30** (left), and Col catalyst **36** (right).

### 3.3.6.5 Investigation of the surface functionality of activated catalysts *via* DRIFTS analysis

For achieving better understanding of the catalyst in the working state, again DRIFTS measurement of the reductively activated catalysts was performed. Hence, the according single-metal reference catalysts (**24** and **38**) were activated using 13 %H<sub>2</sub>/Ar, a ramp of 10 K/min, and a temperature plateau of 360 °C for 1 h. After cooling down to r.t., the gaseous atmosphere was removed *in vacuo*, and CO dosing was performed on the catalysts, and monitored *via* DRIFTS (**Figure 58**).

The Cu reference catalyst shows one distinct band at 2121 cm<sup>-1</sup>. As in the case of the Co-Cu-SSP catalyst (**22**), the respective band is assigned to a copper adsorption site that is electropositive due to interaction with oxygen respectively hydroxyl groups of the supporting material.[86] The main band is furthermore not symmetrically shaped, but exhibits tailing towards lower wavenumbers. In case of the Fe reference catalyst (**38**), mainly free CO gas is detected. Further minor bands can be assigned to surface CO of Fe<sup>n+</sup> ions (2074 cm<sup>-1</sup>),[87] linear CO on metallic iron (2043 cm<sup>-1</sup>),[87] and CO chemisorbed on iron (1950 cm<sup>-1</sup>).[134] The band detected at 1891 cm<sup>-1</sup> is the repeatedly appearing measurement artefact.

Adjacently, the experiment was repeated on the corresponding bimetallic catalysts. The Cu-Fe Col catalyst (**36**) was activated like the monometallic reference catalysts (**24** and **38**), whereas the Cu-Fe SSP catalyst (**30**) was heated to 250 °C for 1 h in 13 %H<sub>2</sub>/Ar and with a ramp of 10 K/min. After cooling to r.t. and removal of the gaseous atmosphere *in vacuo*, CO dosing and monitoring *via* DRIFTS was performed (**Figure 59**). In case of the SSP catalyst (**30**), a distinct band at 2120 cm<sup>-1</sup> with a highly symmetrical shape is detected and denoted to an electropositive copper adsorption site strongly interacting with the silica support.[86] The band intensity is slightly decreased compared to the monometallic Cu reference catalyst, which can be explained by the influence of Fe. Regarding the Col catalyst (**36**), almost no adsorption takes place and mainly free CO gas is detected, indicating formation of a Fe-surface layer. The bands indicating free CO gas have an unusual pronunciation of the band at lower frequencies (~2120 cm<sup>-1</sup>), which is explained by the influence of copper.

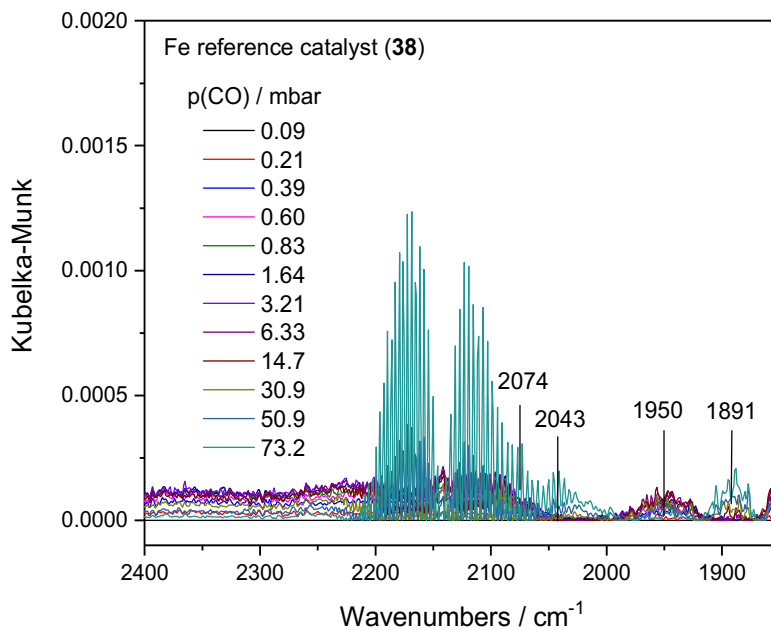
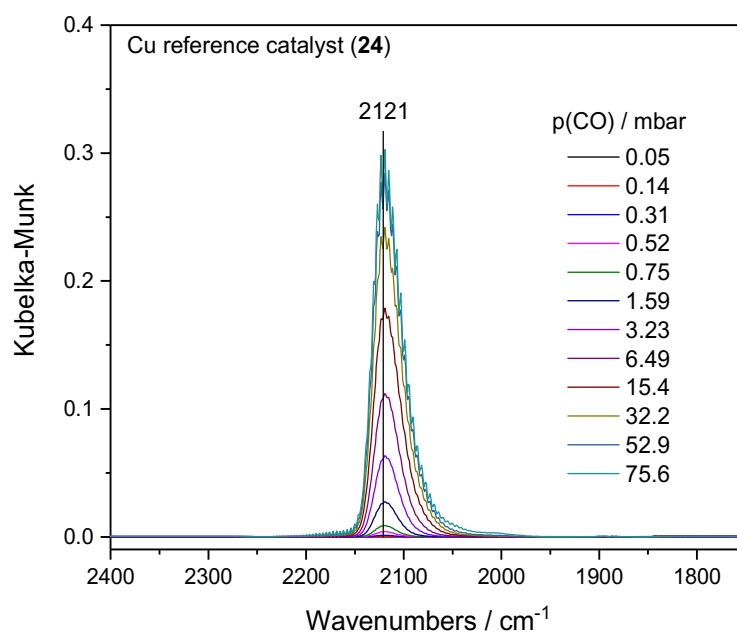


**Figure 58:** DRIFTS monitoring of CO adsorption of activated Cu reference catalyst (**24**, top), and activated Fe reference catalyst (**38**, bottom).

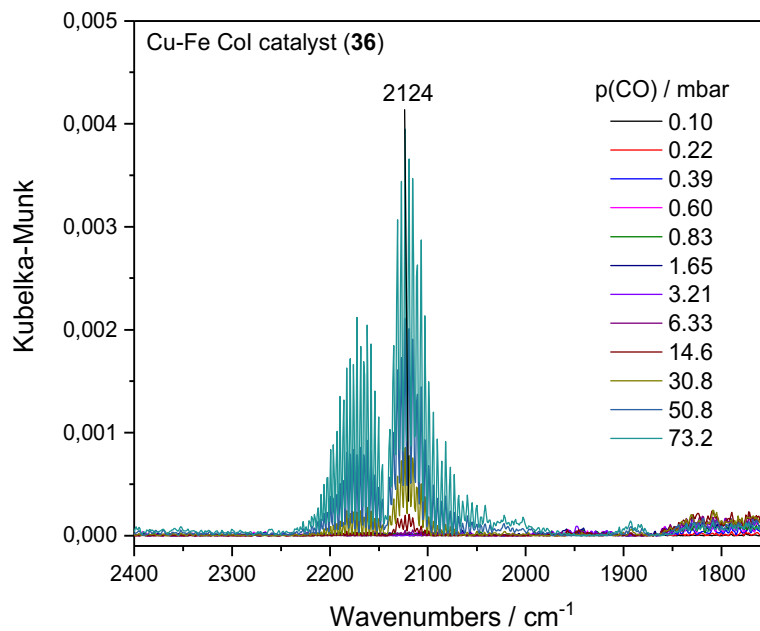
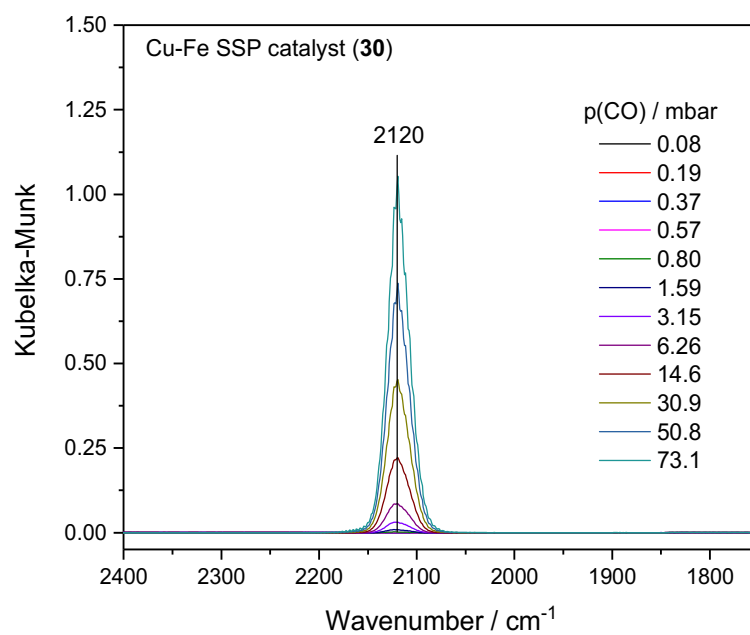


**Figure 59:** DRIFTS monitoring of CO adsorption of activated Cu-Fe SSP (30, top), and activated Cu-Fe Col (36, bottom).

Concludingly, the surface of the SSP catalyst (**30**) is dominated by Cu-Fe species, which is in accordance with results obtained from CO adsorption experiments on silica-supported Cu-Fe catalysts prepared *via* ultrasound-assisted WI, deposition-precipitation, solid-state impregnation, solid-state-chemical reaction, and citric acid combustion.[135] Contrary, the surface of the Col catalyst (**36**) consists of merely Fe, and Cu is completely suppressed. This morphological difference between the catalysts is highly surface specific, since it was not detectable *via* TEM measurements.

### 3.3.7 Application in syngas conversion

In case of the Cu-Fe system, six catalysts were investigated and compared regarding HAS from syngas: The Cu-Fe SSP catalyst **30**, the Cu-Fe Col catalyst **36**, the Na-Cu-Fe SSP catalyst **35**, the Na-Cu-Fe Col catalyst **37**, and two monometallic catalysts **24** (only Cu) and **38** (only Fe).

The samples were activated at 54 bar and 265 °C for 1 h in a flow of 58.3 ml/min of 5 %H<sub>2</sub>/N<sub>2</sub>. The reactors were then cooled to the reaction temperature at 360 °C. The measurement was performed with a pressure of 54 bar, a CO:H<sub>2</sub> ratio of 2:1, temperature steps of 260, 280, 300, 320, 300, 280, and 260 °C, and a GHSV of 3500 h<sup>-1</sup>. The total flow rate used was 58.3 ml/min. For the following discussion, activities are determined on basis of the highest CO conversions at 320 °C. Product selectivity of the respective catalysts are discussed at similar CO conversions, that is at 260 °C (catalysts **30**, **35**, and **36**), 280 °C (catalyst **37**), or (catalysts **24** and **38**). Furthermore, C<sub>2+</sub> alkanes are defined as *n*-alkanes with a carbon number of at least two, and olefins contain ethylene, propene, and 1-butene. All higher hydrocarbons (branched) are summarized as C<sub>4+</sub> hydrocarbons.

**Table 19** gives an overview of the tested (Na-)Cu-Fe catalysts, the metals loading, and the CO conversion at 320 °C. The CO conversion at 320 °C of the Na-Cu-Fe Col catalyst **37** is missing due to clogging of the fixed bed reactor that occurred during the measurement.

**Table 19:** Overview of CO conversion obtained over (Na-)Cu-Fe catalysts at 320 °C.

Catalyst	Catalyst type	Measured loading [wt.%]			X <sub>CO</sub> [%]
		Na	Cu	Fe	
24	Cu reference	/	4.03	/	5.0
38	Fe reference	/	/	2.68	3.0
30	Cu-Fe SSP	/	3.47	2.60	14
36	Cu-Fe Col	/	5.39	3.64	39
35	Na-Cu-Fe SSP	0.48	3.20	2.13	27
37	Na-Cu-Fe Col	0.48	4.53	2.54	/

Hence, the polymetallic catalysts show highly increased activity compared to the monometallic references due to synergism. The almost threefold CO-conversion over the Cu-Fe Col catalyst (**36**) compared to the corresponding SSP catalyst (**30**) can be explained by the increased metals loading.

The product spectra of the six catalysts were determined *via* GC (**Table 20**). For better comparability of the different catalysts, results measured at similar conversions are used.

**Table 20:** Catalytic performance of (Na-)Cu-Fe SSP and Col catalysts, and the corresponding monometallic reference catalysts. Selectivities and conversion are given in %.

Catalyst	24	38	30	36	35	37
Catalyst type	Cu reference	Fe reference	Cu-Fe SSP	Cu-Fe Col	Na-Cu-Fe SSP	Na-Cu-Fe Col
T [°C]	320	320	260	260	260	280
X(CO)	5.0	3.0	5.8	7.6	6.0	5.7
S(CH <sub>4</sub> )	13	45	22	22	12	22
S(C <sub>2+</sub> Alkanes)	4.8	20	30	33	28	19
S(Olefins)	0.3	16	14	9.8	21	24
S(MeOH)	64	0	7.8	13	4.2	5.4
S(EtOH)	0	0	6.2	6.9	6.4	9.0
S(PrOH)	0	0	3.2	1.1	2.0	1.0
S(CO <sub>2</sub> )	15	8.4	4.6	7.2	11	4.2
S(C <sub>2+</sub> Oxy)	0.9	1.4	1.2	0.5	0.5	0.0
S(C <sub>4+</sub> CHs)	1.5	9.4	11	6.8	16	15

As expected, the main product formed on the monometallic Cu reference catalyst (**24**) is MeOH (65 %). The second main product is CO<sub>2</sub> (15 %) which results from water-gas shift reaction of CO with *in situ* formed H<sub>2</sub>O. No formation of higher alcohols takes place.

Since Fe is a known FT catalyst, mainly hydrocarbons (45 % methane, 20 % C<sub>2+</sub> alkanes, 16 % olefines, 9.4 % C<sub>4+</sub> hydrocarbons), and CO<sub>2</sub> (8.4 %) as a product of water-gas shift reaction are formed over the Fe reference catalyst (**38**). Again, formation of alcohols is not observed.

Comparing the results of Cu-Fe SSP catalyst **30** and the corresponding Col catalyst **36**, it is again found that the product spectrum is highly similar, pointing towards assimilation of the surface morphology during catalytic reaction. In both cases, EtOH and PrOH are formed (6.2 % respectively 6.9 %), thus CO adsorption and insertion on Cu and carbon chain growth on Fe are interplaying due to synergism. Consequently, the amount of MeOH formed on the bimetallic catalysts is in-between those of the monometallic references, since the MeOH-catalyst Cu is diluted by Fe. A further synergistic effect is observed on the formation of C<sub>2+</sub> alkanes, since the amount formed on the bimetallic catalysts is strikingly higher than on both monometallic references. The increased Fe-surface functionality on the Col catalyst (**36**), which was detected by DRIFTS measurement, is not represented in the product spectrum, since the Col catalyst does not show a pronounced FT product distribution compared to the SSP catalyst (**30**).

Regarding the Na-Cu-Fe catalysts (**35** and **37**), again a synergistic effect is observed, leading to formation of EtOH and PrOH. Interestingly, the contained Na does not work as a poison reaction, since selectivity towards EtOH and PrOH is similar or even higher compared to the Cu-Fe catalysts (**30** and **36**). This effect might be caused by the difference Cu-Fe ratio compared to the Na-free catalysts. The highest amount of EtOH is formed over the Na-Cu-Fe Col catalyst (**37**), thus the morphological advantage obtained *via* the SSP synthesis route is not stable during catalytic testing. Furthermore, a higher

amount of olefins is formed compared to the Na-free catalysts, which might be caused either by the presence of Na, or by the different Cu-Fe ratio.

The results are summarized in **Figure 60** and **Figure 61**.

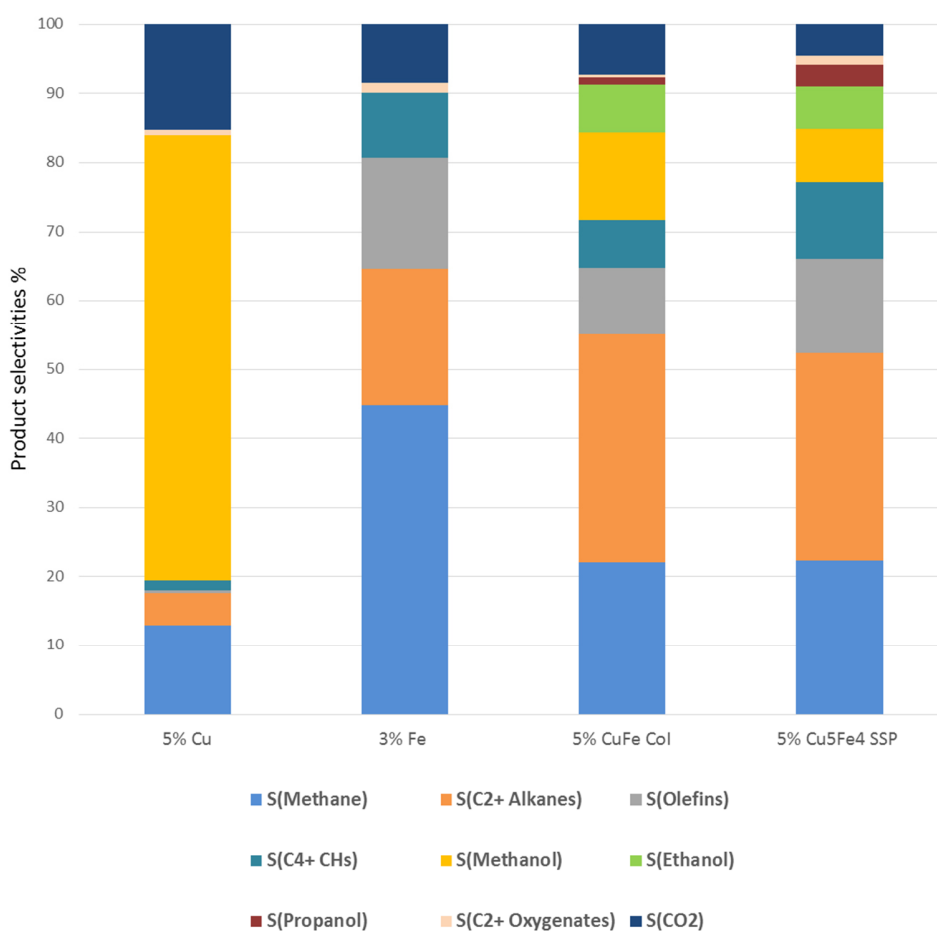


**Figure 60:** Product spectrum determined at 280 °C regarding the SSP catalyst, at 260 °C regarding the Col catalyst, and at 320 °C regarding the monometallic ones. From left to right: Monometallic Cu-catalyst (**24**,  $X_{CO} = 5.0\%$ ); monometallic Fe-catalyst (**38**,  $X_{CO} = 3.0\%$ ), Cu-Fe SSP catalyst (**30**,  $X_{CO} = 5.8\%$ ), and Cu-Fe Col catalyst (**36**,  $X_{CO} = 7.6\%$ ).

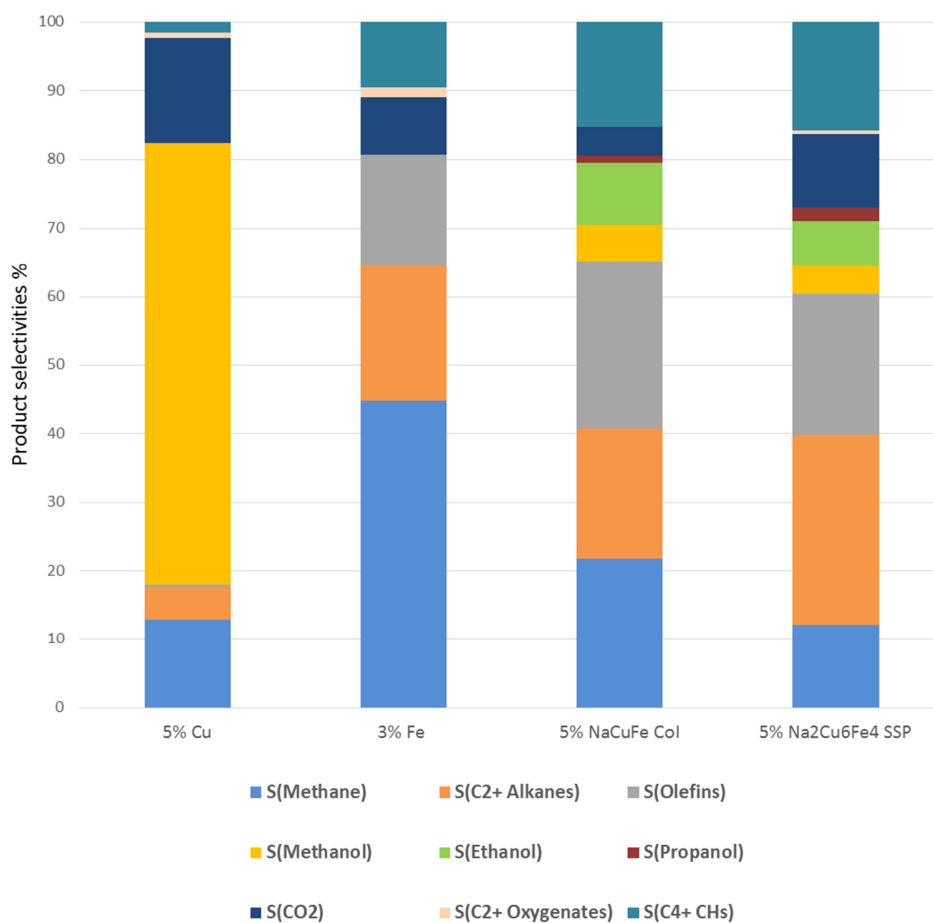


**Figure 61:** Product spectrum determined at 320 °C regarding the tri-metallic catalyst, and at 260 °C regarding the monometallic ones. From left to right: Monometallic Cu-catalyst (**24**,  $X_{CO} = 5.0\%$ ); monometallic Fe-catalyst (**38**,  $X_{CO} = 3.0\%$ ), Na-Cu-Fe SSP catalyst (**35**,  $X_{CO} = 6.0\%$ ), and Na-Cu-Fe Col catalyst (**37**,  $X_{CO} = 5.7\%$ ).

### 3.3.8 Investigation of spent catalysts

#### 3.3.8.1 Investigation of the bulk structure *via* XRD analysis

After catalytic testing, the spent Cu-Fe catalysts were analyzed *via* XRD analysis (**Figure 62**). Both spectra show cubic Cu particles and indication of additional Cu<sub>2</sub>O particles. Application of Scherrer equation (**Eq. 2**) yielded Cu particle sizes of 23.3 nm on the Col catalyst **40**. On the spent SSP catalyst **39**, particle sizes could not be determined due to the low signal-to-noise ratio.

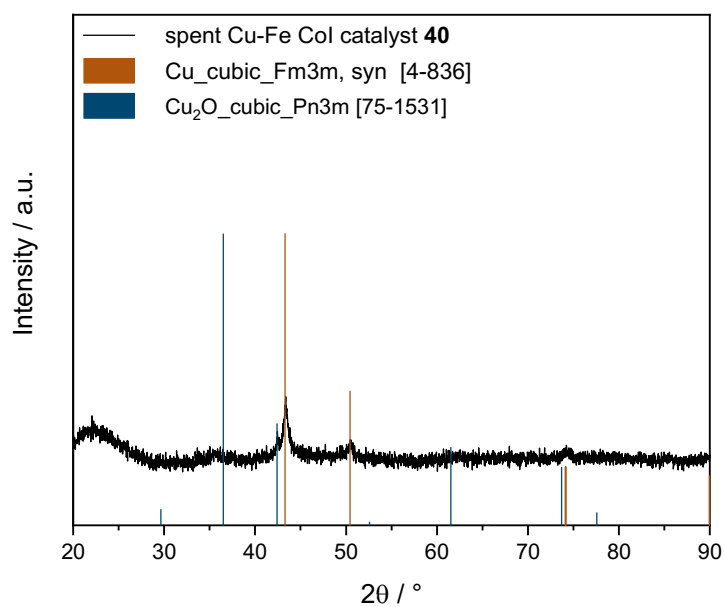
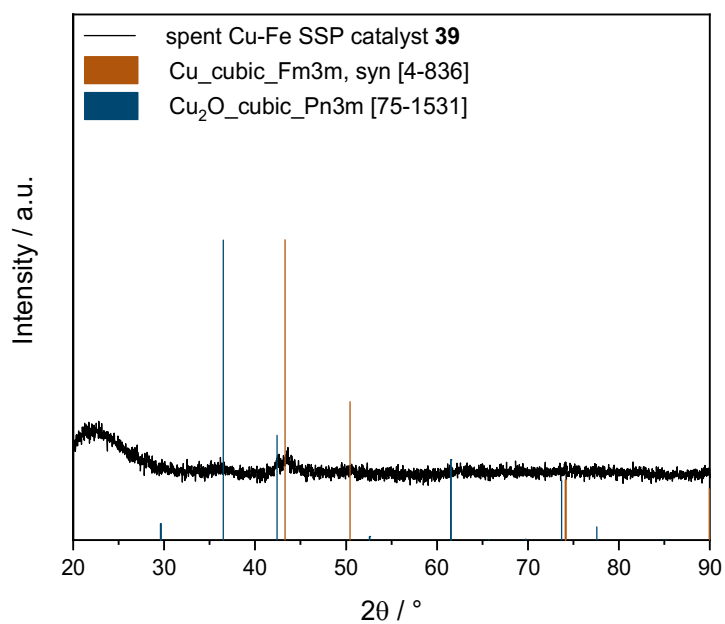


**Figure 62:** Powder XRD of spent Cu-Fe SSP catalyst **39** (top) and Col catalyst **40** (bottom), stacked with database XRD patterns of cubic Cu and Cu<sub>2</sub>O.

### 3.3.8.2 Investigation of the surface functionality *via* DRIFTS analysis

After catalytic testing, the spent Cu-Fe SSP catalyst (**39**) and Col catalyst (**40**) were investigated *via* DRIFTS-monitored CO adsorption experiments in order to determine morphological differences after catalytic testing (**Figure 63** and **Figure 64**). In both cases, the catalysts were prepared for the measurement by heating with a ramp of 10 K/min up to 250 °C in an atmosphere of 13 % H<sub>2</sub>/Ar, and a holding time of 1 h. In both cases, only very low adsorption takes place, indicating Fe surface functionality in both cases. In case of the SSP catalyst (**39**), three minor bands are detected: One at 2053 cm<sup>-1</sup>, being assigned to Fe<sup>δ+</sup>-CO complexes,[87] a band at 2021 cm<sup>-1</sup> denoted to CO on supported Fe,[136] as well as a band at 1889 cm<sup>-1</sup> being the measurement artefact. In case of the Col catalyst (**40**), only a minor band at 1945 cm<sup>-1</sup> is observed and denoted to CO chemisorbed on iron.[134] The spent Col catalyst (**40**) shows slightly less adsorption than the spent SSP catalyst (**39**), thus indicating formation of bigger particles.[88]

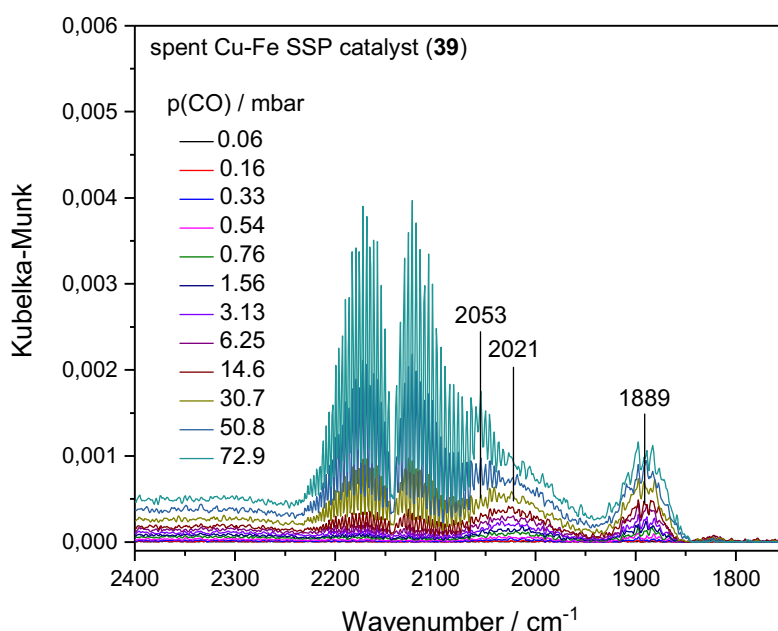


**Figure 63:** DRIFTS spectra measured during CO chemisorption on spent Cu-Fe SSP catalyst (**39**, top).

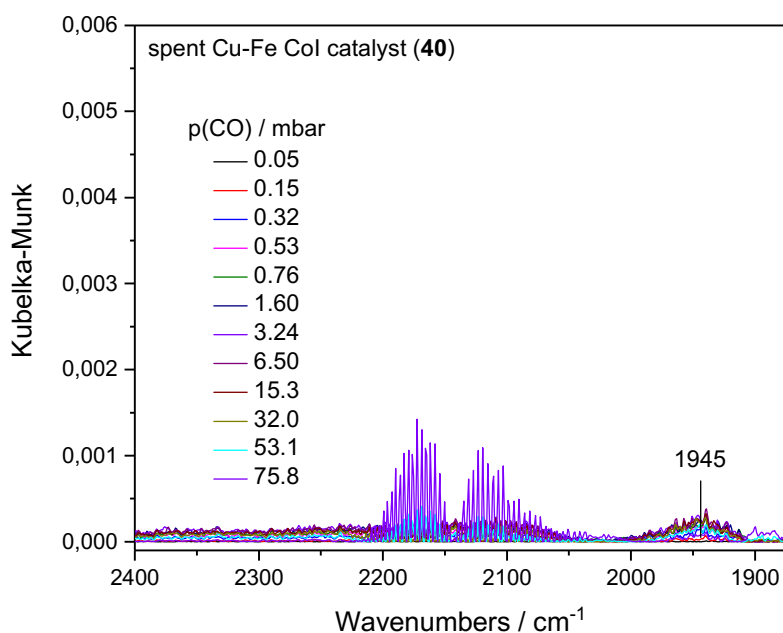


**Figure 64:** DRIFTS spectra measured during CO chemisorption on spent Cu-Fe Col catalyst (**40**).

### 3.3.9 Discussion: Cu-Fe catalysts

Due to its size and structural complexity, Cu-Fe is the intrinsically most difficult case of the herein investigated SSP systems. Thus, already the applicability of the deposition pathway differs in each case. Regarding the Cu-Fe SSP systems, either way of supporting (WI and SIWI, **29** and **30**) yielded perfect conservation of the metal-to-metal ratio on the support, whereas in both cases, the metal loading was strongly decreased. This contrasts with the corresponding Col catalyst (**36**), where the loading of the metals was increased, but the metal-to-metal ratio was deviating from the theoretical loading. Thus, SSP approach in this case shows its superiority in maintenance of the metal-to-metal ratio, especially with regard of the high number of nine metals provided in the SSP. Regarding the even more complex Na-Cu-Fe SSP system, initially starting from twelve atoms, situation is hampered. Thus, best results regarding preservation of the metals ratio were achieved for catalysts **33** and **34**, which were prepared *via* WI and SIWI. Catalysts **31**, **32**, and **35** prepared by the same methods showed as well very well maintenance of

the Cu-Fe ratio but suffered from deviance of the sodium content. Regarding achievement of the desired metals loading on the support, best results were obtained for catalyst **34** prepared *via* SIWI bearing the lower metals loading. This result fits the trend observed for the Co-Pt and Cu-Co catalysts and shows the possibility of improvement by changing the supporting method. In future, the drawbacks which were observable for the Na-Cu-Fe SSPs could be circumvented by choosing more stable SSPs which are not that easily interconverted, and where all metals are incorporated into the complex core by direct metal-to-metal bonds. By meeting this premise, the SSP approach is a valuable tool for the preparation of complex multimetallic supported catalysts.

BET measurements gave further information about the catalysts, showing strong reduction of surface area and pore size in case of the Na-Cu-Fe Col catalyst **37**, probably caused by the high temperatures applied during calcination. Thus, from a morphological point of view, the Col catalyst is inferior compared to the corresponding SSP catalysts **31**, **33**, and **35**, which all bear only slightly increased surface areas and pore sizes compared to unsupported silica.

Analytical results obtained from XRD measurements confirm integral homogeneity in case of SSP catalysts **31-33**. In all other cases, either Fe, Cu, CuO, Fe<sub>2</sub>O<sub>3</sub> or a mixture of those compounds could be identified. Where possible, Scherrer equation was applied to estimate particle sizes. Hence, the particles were in a range of ~5-23 nm. Only in case of the Cu-Fe SSP catalyst **29** prepared *via* WI, drastically increased Fe and Cu particles with a size of 53.8 nm respectively 57.1 nm were detected. The particles detected for the corresponding Cu-Fe SSP catalyst **30** prepared *via* SIWI are less than half as big as the ones detected for catalyst **29**, which again emphasizes the importance of the supporting method. Sodium could not be detected *via* XRD in any sample, meaning that it is present in amorphous form.

Investigation *via* electron microscopy of reductively activated Cu-Fe catalysts **30** and **36** under inert gas and without air contact after activation confirms the morphological superiority of the SSP catalysts. The SSP catalyst **30** shows better dispersed, smaller particles with a particle size maximum of 2.5 nm, whereas the Col catalyst **36** has a broader particle size distribution ranging from 0-30 nm with a maximum at 8.6 nm. SAED

measurement confirms the formation of bigger particles in case of the Col catalyst (**36**), and furthermore reveal coexistence of metallic Cu and Fe in both cases (catalyst **30** and **36**). This is verified from EDX analysis, indicating that the two metals are not alloying. Nevertheless, Cu and Fe are in close intimacy and in case of the SSP catalyst **30**, even partially overlapping. Concludingly, comparison of results from TEM and XRD analysis reveals that the formation of oxides detected in both cases *via* XRD must be caused by air contact after activation.

DRIFTS measurement of the reductively activated catalysts without air contact confirm the existence of major morphological differences. Furthermore, they suggest that the surface of the SSP catalyst (**30**) is Cu-Fe-functionalized, whereas the Col catalyst (**36**) has a pronounced Fe-surface functionality, suppressing Cu.

Results of catalytic testing for syngas formation show that generally, the bimetallic catalysts have a markedly increased activity compared to the monometallic references ( $X_{CO} = 3.00-5.03\%$  on the monometallic catalysts compared to  $14-39\%$  on the bimetallic ones at  $320\text{ }^{\circ}\text{C}$ ). Regarding the bimetallic catalysts, the Col Cu-Fe catalyst (**36**) shows an activity that is more than doubled compared to the activity of the SSP catalyst (**30**) ( $38.9\%$  vs.  $14.2\%$ ), which can be explained by the highly increased effective loading of both metals in the Col catalyst (**36**). Comparison of the Cu-Fe SSP catalyst (**30**) and the Na containing one (**35**) shows that Na is not deactivating the system, with Na-Cu-Fe SSP catalyst (**35**) showing a high CO conversion rate of  $27.2\%$ . Since the amount of Cu and Fe is slightly lower compared to the Cu-Fe SSP catalyst (**30**), additional sodium even seems to foster the activity. A study of Ding et al. from 2015 investigated the role of potassium incorporation in a Cu-Fe based catalyst.[137] They found an increase of activity and mixed alcohols selectivity with a gradually increasing potassium concentration and a maximum at  $0.5\text{ wt.}\%$  K-content, and explained it with a promotion of immigration of bulky iron species to surface layers, and a subsequent strengthening of Cu-Fe surface interaction. This explanation might also account for the increased activity of the Na-Cu-Fe SSP catalysts (**35**) compared to the sodium-free (**30**).

Regarding the product spectrum, again the necessity of synergism between the metals for higher ethanol formation is proven since none is formed on the monometallic reference

catalysts (**24** and **38**). Despite of the difference of metal loadings, the amount of ethanol and propanol formed on the Cu-Fe (**30** and **36**) and Na-Cu-Fe catalysts (**35** and **37**) is in a similar range at comparable CO conversion rates. The Cu-Fe catalysts and their sodium-doped analogues can be distinguished by the amount of MeOH formed, which is approximately halved on the latter ones (**35** and **37**). In contrast, the presence of sodium does not significantly change the amount of higher alcohols formed. Instead, an increased amount of heavy hydrocarbons is formed on the Na-Cu-Fe catalysts (**35** and **37**). The suppressive effect on methanol formation is in accordance with results of Bukur et al. obtained over Fe-based catalysts modified by potassium.[138] Ding et al. also found the suppressive effect of K on methane formation for Cu-Fe catalysts, which interestingly is only found on the Na-Cu-Fe SSP catalyst (**35**), forming only about half of the amount of methane than the Cu-Fe SSP (**30**) and CoI catalyst (**36**). The amount of methane formed on the Na-Cu-Fe SSP (**37**) catalysts stays in the same region as for the unpromoted catalysts.

Investigation of the spent catalysts *via* DRIFTS analysis shows that the two compounds have strongly adjusted during the catalytic measurements, showing only minor morphological differences. Thus, the spent catalysts show only little CO adsorption, which indicates a Fe-surface functionality. This is confirmed by the small bands that can be detected and assigned to different Fe-species in both cases. No bands belonging to CO adsorbed on copper are identified. This is in agreement with studies of Xiao et al., which investigated HAS from syngas on Cu-Fe catalysts prepared by co-reduction.[139] They found severe phase separation of Cu and Fe taking place during catalytic testing, whereas the FT performance of Fe remained dominant.

Just as in case of the Co-Pt and the Co-Cu catalysts, the selectivity towards ethanol does not match the predictions from the literature. One possible reason is that iron and copper are not forming an alloy. Even if the two metals are intimately mixed due to the target-oriented SSP approach, the closeness is probably not maintained during reaction conditions. Instead, the morphologies of single and dual source catalysts adjust, and segregation as well as sintering takes place.

## 4 Summary and outlook

In this thesis, the identification, synthesis, supporting, activation, and catalytic application of three different bimetallic systems is discussed. Therefore, a new bottom-up synthesis route for catalyst systems consisting of Co-Pt, Co-Cu, and Cu-Fe was identified, aiming on precise control over the mixing pattern and stoichiometry of the deployed metals on the support: The single-source precursor (SSP) method. Heteropolymetallic complexes, so-called SSPs, bear an intrinsic mixing pattern of the desired metals in a pre-defined ratio, thus favoring formation of supported single-phase alloy nanoparticles on the final catalyst. Further characterizations of an ideal SSP are containment of small, volatile ligands, that are in close proximity to each other and do not comprise any poisoning elements for further catalytic applications. For the considered bimetallic systems, four different SSPs were selected:

- a) *trans*-PtPy<sub>2</sub>[Co(CO)<sub>4</sub>]<sub>2</sub> for the Co-Pt system,
- b) Et<sub>4</sub>N{Cu[Co(CO)<sub>4</sub>]<sub>2</sub>} representing the Co-Cu system, and
- c) [Et<sub>4</sub>N]<sub>3</sub>Cu<sub>5</sub>Fe<sub>4</sub>(CO)<sub>16</sub> and Na<sub>2</sub>Cu<sub>6</sub>Fe<sub>4</sub>(CO)<sub>16</sub> • 3 THF for the Cu-Fe system.

The literature-known precursors were synthesized, immobilized, activated, and characterized using X-ray diffraction (XRD), inductively coupled plasma optical emission spectroscopy (ICP-OES), X-ray fluorescence (XRF), Brunauer-Emmet-Teller (BET) isotherm, scanning transmission electron microscopy (STEM), and diffuse reflectance infrared fourier transform spectroscopy (DRIFTS) measurement, respectively. In parallel, reference catalysts were prepared *via* conventional methods, that is co-impregnation (CoI) of metal salts, and investigated in the same manner. Furthermore, the catalysts were applied towards the conversion of syngas. The results of analytic investigations and the catalytic testing were finally used to compare the different synthesis routes.

In the first part, the Co-Pt system was investigated. Since Co-Pt alloys are known to be thermodynamically stable even in the bulk over a wide temperature and stoichiometry range, the Co-Pt system was used as a model case. Like this, it was proven that the SSP approach leads to homogeneously dispersed, small alloy nanoparticles. STEM and especially DRIFTS analysis stated immense differences between the activated SSP and

CoI catalysts. Thus, the SSP catalyst consisted of smaller nanoparticles with an increased Co-content on the particles surface, whereas the alloy nanoparticles of the CoI catalyst are bigger with a pronounced Pt-surface functionality. The morphological differences on the fresh catalysts are not sustained during the testing and lead to highly similar product spectra by application for syngas conversion.

The second system, that is Co-Cu, is more challenging since Co-Cu alloys are thermodynamically not stable as bulk in the desired temperature and stoichiometry range but were reported to exist as supported nanoparticles. In this case, the compounds achieved *via* the SSP approach show distinct morphological superiority compared to the reference catalyst, that is smaller and better dispersed particles. In both cases, single-phase alloys were formed. Again, the difference surface morphologies are assimilating during the catalytic reaction and led to almost identical product spectra.

The third system investigated is the most complex one for several reasons: First, the phase diagram of Cu-Fe resembles the one of Co-Cu, which means that for the desired ratio, formation of thermodynamically stable alloys is not possible. Furthermore, only few documentations of metastable single-phase Cu-Fe alloys exist, mainly under extreme conditions. On the other hand, the investigated SSPs consist of 9-10 metal atoms in the complex core, thus probability of particle migration is decreased compared to the smaller Co-Pt and Co-Cu systems due to the high weight of potentially formed alloy particles. In this case, again major differences between SSP and CoI catalysts were detected, like better dispersion on the support, reduced particle sizes, and increased intimacy of the metals in case of the SSP catalysts. Nevertheless, formation of single-phase alloy particles could not be demonstrated in both cases. Just as in the former cases, the morphological superiority of the SSP catalysts are not maintained under conditions applied for the conversion of syngas.

Thus, even if the cooperative effect of the integrated metals leads to the formation of the desired product, just as predicted by several calculations and modellings, it is currently not possible to make use of their full synergistic potential. The reason for this is particle migration under reaction conditions, caused by increased temperature, pressure, and adsorption-desorption processes.

Regarding the temperature influence, it is well-known that metal-metal diffusion and thus aggregation is favored by high temperatures.[140] For a first estimation, the Tammann rule can be applied here, stating that self-diffusion in crystallites starts at ~50 % of their absolute melting temperature, and surface diffusion starting already at ~30 %.[141,142] Regarding Co, Pt, Cu, and Fe, the melting temperatures are 1495, 1772, 1083, and 1535 °C.[143] Thus, regarding the Co-Pt system, surface diffusion is already expected starting from ~500 °C, and regarding the Co-Cu and the Cu-Fe system, it is already expected to start from ~300 °C. In our specific case, calcination of the Co-Pt Col catalysts was performed at 550 °C according to the literature, whereas the Co-Pt SSP catalysts were decomposed at 165 °C maximum. This temperature difference might have caused the slightly bigger alloy particles on the fresh Col catalyst compared to the SSP counterpart, as observed by STEM, CO chemisorption, and DRIFTS measurement. Since the temperature applied during catalytic testing was 320 °C maximum, surface diffusion on the Co-Pt systems as observed *via* DRIFTS measurement of the spent samples was rather caused by metal adsorbate bonds formed during the catalytic reaction. Regarding the Co-Cu system, the maximum activation temperature of the SSP catalyst was 260 °C, the calcination temperature of the Co-Cu Col catalyst was 300 °C, and the temperature applied during syngas conversion was 320 °C maximum. For the Cu-Fe system, activation of the SSP catalyst took place at 260 °C, calcination of the Col catalyst at 300 °C, and the temperature during syngas conversion reaction was again 320 °C maximum. Thus, the intrinsic advantage of the SSP approach being the lower activation temperature compared to their Col counterparts might be outrun at the stage of the catalytic reaction. The successfully established proximity of the different metals within the nanoparticles, as well as the high active mass due to high dispersion of the nanoparticles could not be maintained.

With regards to that, key towards successful design of bimetallic nanocatalysts is their stabilization during catalytic applications, e.g. by dosing of co-adsorbates that prevent from segregation caused by strong metal-adsorbate bonds. It is known that if one of the metals forms stronger metal-adsorbate bonds than the other component, the first one migrates to the surface.[140] This phenomenon was observed on the Co-Pt SSP catalyst (**10**), which – according to DRIFTS analysis – had a Co-surface functionality before the

catalytic testing, but showed pronounced Pt-surface functionality after testing. This is in accordance with the literature, where segregation in the presence of CO is reported, leading to preferential migration of Pt to the surface due to the formation of the stronger Pt-CO as compared to Co-CO.[92] Also on the spent Cu-Fe catalysts, a dominant Fe-surface functionality is indicated by results of DRIFTS analysis, whereas the fresh SSP catalyst (**30**) is covered by both metals. Again, this is in agreement with existing literature, where severe phase separation of Cu and Fe during catalytic syngas conversion was reported, with a Fe-dominated surface on the spent catalysts.[139] By application of co-adsorbates, adsorption-based pathways for particle migration could be inhibited, e.g. by sterical hindrance in an enzyme-like manner.

The question how far particle migration can be generally prevented is currently addressed by several studies using atomic layer deposition (ALD). Since ALD is a self-limiting process, restricted by the number of functional groups on the substrate's surface, it is theoretically possible to achieve supported nanoparticles composed of a distinct number of atoms by using this method. Thus, in a study by Li et al., platinum precursors were deposited *via* ALD on mesoporous silica gel in 3, 5, and 10 coating cycles.[144] Subsequent investigation by means of STEM and chemisorption experiments showed homogeneous deposition of 1.2, 1.9, and 2.3 nm particles, respectively. Further investigation of the thermal stability of the three-cycle sample by heating to 450 °C for 4 h, 8 h, and to 750 °C for 4 h showed that a particle size maximum of ~2 nm was reached after 4 h at 450 °C (**Figure 65**). Hence, the as-prepared three-cycle sample is not initially stable, but after 4 h of temperature treatment. It is suggested in the paper that the attractive force between the particles reaches a maximum at a certain distance, which cannot be increased more by further temperature exposure.

Marinokovic et al. correlated the particle size of Pt in FCC lattice with the total number of atoms included in cuboctahedral nanoparticles by means of extended X-ray adsorption fine structure (EXAFS) measurements (**Figure 66**).[145] According to this, the nanoparticles sizes of 1.2 nm for the initial three-cycle ALD sample, and 2.0 nm after treatment at 450 °C for 4 h as reported by Li et al. correspond to approximately 50 respectively 200 atoms within one nanoparticle according to the volume-corrected model.

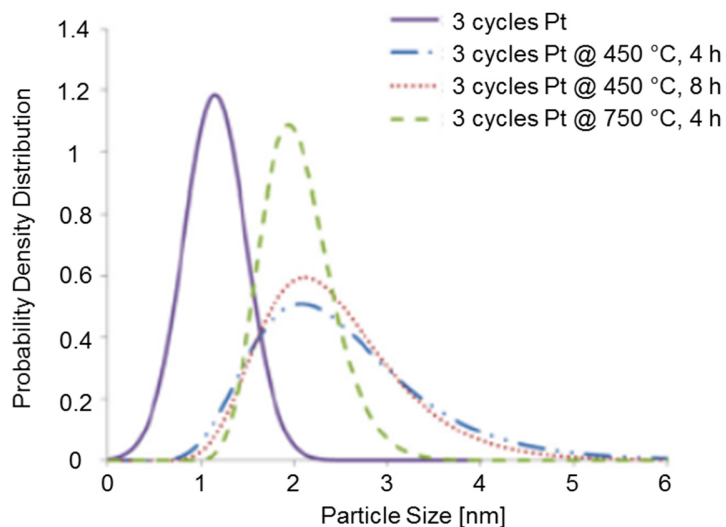


**Figure 65:** Particle size distribution of heat-treated Pt/SiO<sub>2</sub> particles, synthesized via ALD.[144]

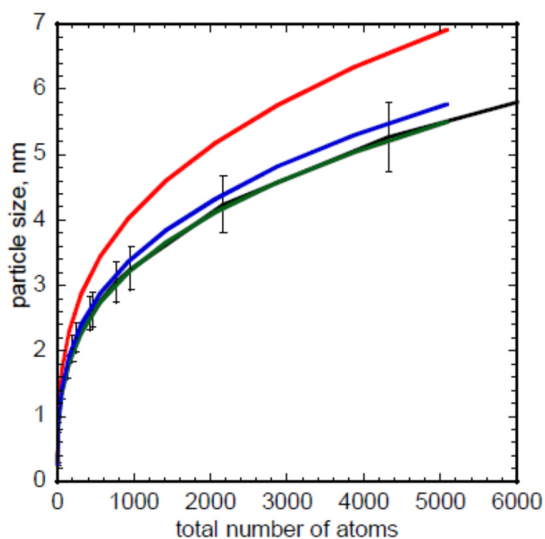


**Figure 66:** Dependence of particle size as a function of total number of atoms in cuboctahedrons, volume-corrected (blue), surface-corrected (red), and uncorrected (black).[145]

Thus, the energy entry during the temperature treatment was high enough to cause particle sintering. Since the Pt loading corresponded to 0.10 atom/nm<sup>2</sup> ( $3.1 \times 10^{-6}$  mg Pt/cm<sup>2</sup>) in case of the three-cycle sample, it can be deduced that the initially

deposited 50-atom-particles were singularly located within an area of  $30 \text{ nm}^2$ . According to this, each 50-atom-particle must have theoretically covered a distance of  $\sim 3.9 \text{ nm}$  during the sintering process at  $450 \text{ }^\circ\text{C}$  in order to form a thermally stable particle consisting of 200 Pt atoms according to the Pythagorean theorem (**Figure 67**, **Eq. 3-5**).

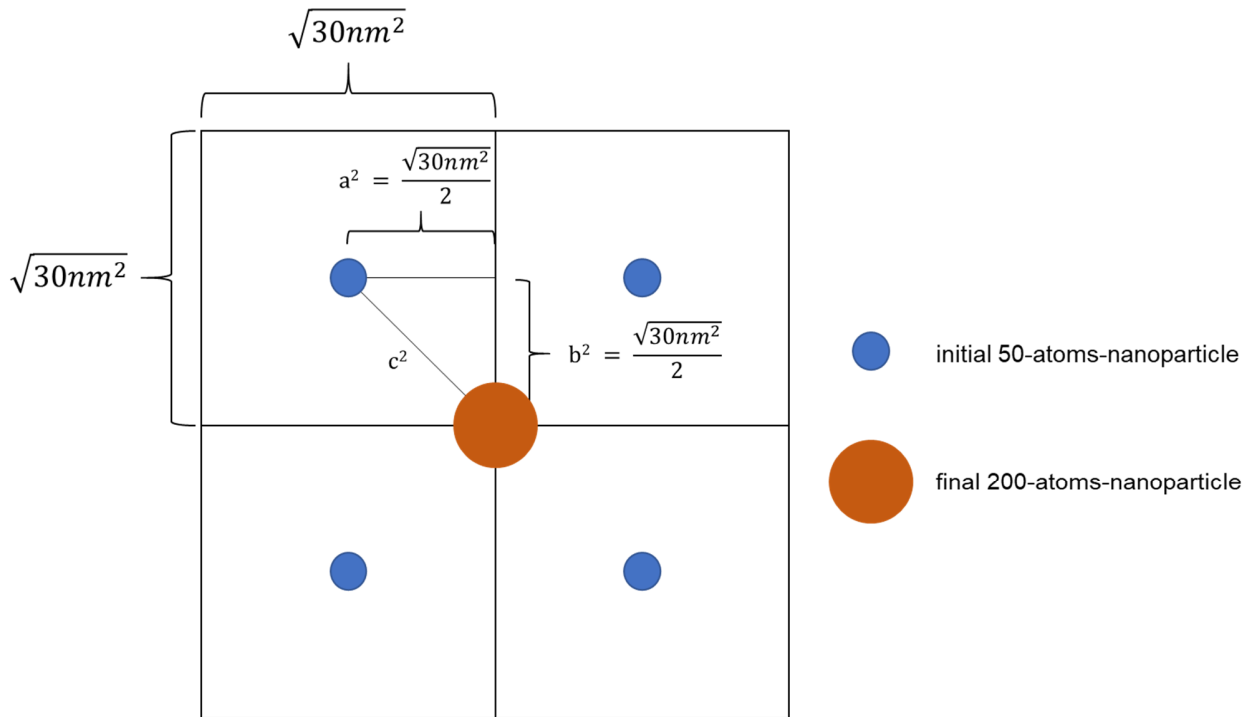


**Figure 67:** Theoretical model for the formation of nanoparticles consisting of 200 atoms starting from nanoparticles consisting of 50 atoms upon thermal treatment at  $450 \text{ }^\circ\text{C}$ .

Pythagorean theorem:

$$c^2 = a^2 + b^2 \quad (\text{Eq. 3})$$

$$\rightarrow c^2 = \left(\frac{\sqrt{30}}{2} \text{ nm}\right)^2 + \left(\frac{\sqrt{30}}{2} \text{ nm}\right)^2 = 2 \cdot \frac{30}{4} \text{ nm}^2 = 15 \text{ nm}^2 \quad (\text{Eq. 4})$$

$$\rightarrow c = 3.9 \text{ nm} \quad (\text{Eq.5})$$

In case of the Co-Pt SSP catalyst (**10**), Co<sub>2</sub>Pt particles with an average size of ~1.7 nm were achieved according to CO chemisorption measurement. Using the approximation of Marinkovic et al., this corresponds to nanoparticles consisting of ~150 atoms. Thus, 50 Co<sub>2</sub>Pt molecules formed one alloy particle upon reductive decomposition at 165 °C maximum. Since SSP catalyst (**10**) consists of 1 wt.% Pt being impregnated on SiO<sub>2</sub> with a surface area of 480 m<sup>2</sup>/g, the coverage is 2.1 x 10<sup>-6</sup> mg Pt/cm<sup>2</sup>, hence ~1 Co<sub>2</sub>Pt molecule per 14 nm<sup>2</sup> of SiO<sub>2</sub> was initially present upon supporting. Since the final Co<sub>2</sub>Pt alloy particles are made up of approximately 50 complex molecules after decomposition of the complex, this yields a maximum complex molecule migration of 19 nm during the thermal treatment (**Figure 68**, **Eq. 3** and **6-7**).

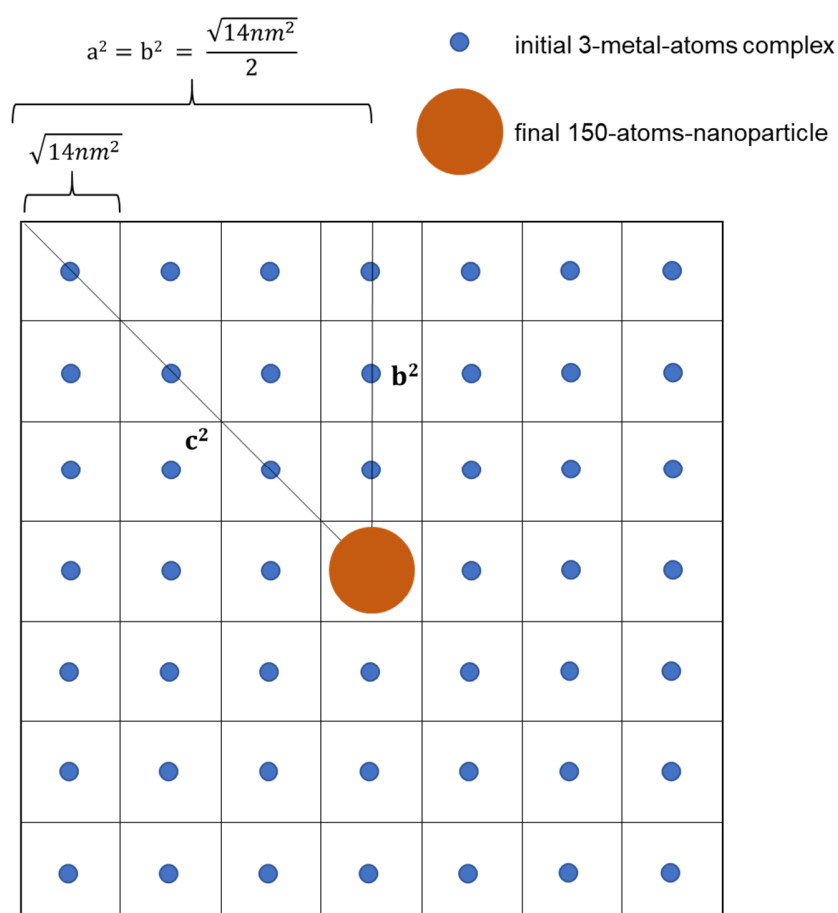


**Figure 68:** Theoretical model for the formation of nanoparticles consisting of 150 atoms starting from complexes consisting of 3 metal atoms upon thermal treatment at 165 °C.

$$\rightarrow c^2 = 2 \cdot \left( \frac{\sqrt{14 \text{ nm}^2}}{2} \cdot 7 \right)^2 = 2 \cdot \frac{14 \text{ nm}^2}{4} \cdot 49 = 343 \text{ nm}^2 \quad (\text{Eq. 6})$$

$$c = 19 \text{ nm} \quad (\text{Eq.7})$$

Since in both cases, the used supporting material is silica, it seems crucial to have a look at its specific anchoring sites, the surface silanol groups. The Kiselev-Zhuravlev constant states the number of OH groups per unit surface area  $\alpha_{\text{OH}}$  of a maximally hydroxylated silica surface to be 4.9 OH-groups per  $\text{nm}^2$ , that is  $\sim 2$  OH-groups per nm of silica.[146] Concludingly, in the two cases mentioned above, 8 respectively 38 OH groups were theoretically involved in passing the particles further for 3.9 respectively 19 nm. Thus, the supporting material used strongly fosters the mobility of particles on the surface. In order to disable this mobility, a strong diminution of anchoring sites would be necessary. In this specific case, only one OH group should be available in the migrated range of 15 respectively 343  $\text{nm}^2$ . According to Zhuravlev, thermal pretreatment up to more than 1100 °C would thus be necessary to decrease the surface silanol density to the desired amount of less than 0.15 OH groups per  $\text{nm}^2$  (**Figure 69**).[146]

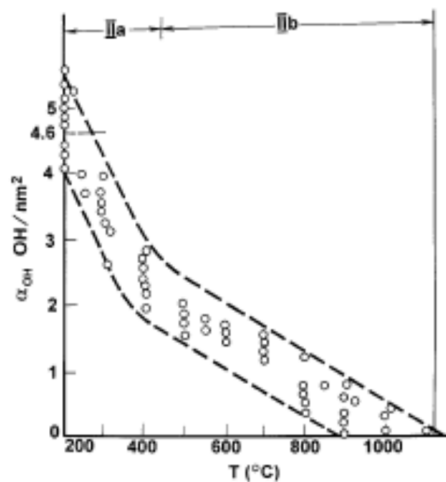


**Figure 69:** Silanol number  $\alpha_{\text{OH}}$  as a function of the temperature of pretreatment in vacuo for different samples of  $\text{SiO}_2$  according to Zhuravlev.[146]

Such a temperature treatment of silica would involve a crucial loss of its specific surface area, therefore it is not a suitable method regarding materials for catalytic applications.

Consequently, further potential lies in the variation of the supporting material. As mentioned before, generally, surface hydroxyl groups on oxide surfaces are the nucleation sites for metal island growth.[147] On the other hand, it is known from ALD that particle growth does not take place on high quality carbon-based materials, since the initiation requires nucleation sites, e.g. defects or functional surface groups.[148] The group of Sun took advantage of this knowledge by synthesizing single Pt atom catalysts on N-doped graphene, exhibiting highly increased activity and stability which is attributed to the preferential adsorption of Pt atoms on N-sites.[149] Like this, agglomeration under reaction conditions could be inhibited by stabilization of the active sites upon the carrier.

A further possibility to stabilize the mixing of the catalytic centers is incorporation of further elements. Hence, incorporation of manganese into a co-precipitated Cu-Fe catalyst was identified to lead to an enhanced dispersion of copper and iron. Like this, the number of active sites for CO hydrogenation was increased, leading to an improved catalytic activity for higher alcohols synthesis (HAS).[150]

Concludingly, this work showed that the SSP-approach represents a great possibility to synthesize polymetallic systems which are not achievable *via* conventional methods. By custom tailoring of the SSP complexes, mixing of several metals which are usually prone to segregate already during preparation is possible. Further identification of methods to stabilize the highly mixed and well-dispersed bimetallic nanoparticles under reaction conditions hence can lead to new forms of synergism, enabling completely new catalytic properties.

## 5 Experimental

### 5.1 General remarks

All experiments and manipulations involving air- and moisture sensitive organometallic compounds were carried out under an atmosphere of dry, oxygen-free argon by using standard Schlenk techniques on a high vacuum line, or in a glove box under a purified nitrogen (MBraun LABmaster Pro, SN 9919) atmosphere (O<sub>2</sub> and H<sub>2</sub>O levels were usually kept below 1 ppm). The solvents were taken from a solvent purification system (MBraun SPS-800) or purified using conventional procedures, freshly distilled under argon atmosphere, and degassed prior to use. The glassware used in all manipulations was dried at 130 °C, cooled down to ambient temperature under high vacuum, and flushed with argon.

Solvents or solutions were transferred *via* disposable syringes and needles or glass syringes with stainless steel cannulas, which were stored at 130 °C. Solid materials were added in solution or in an inert gas counter current.

In case of reactions at low temperatures, Dewar vessels were filled with acetone/dry-ice mixture to reach the desired temperature.

### 5.2 Analytical methods

#### NMR spectroscopy

NMR samples of air- and moisture-sensitive compounds were prepared in a J. Young NMR tube (sealed with a polytetrafluoroethylene valve) under nitrogen atmosphere inside a glove box. The deuterated solvents were dried over 4 Å molecular sieves and degassed prior to use. The <sup>13</sup>C-NMR spectra were recorded on a Bruker AvanceIII (125 MHz) spectrometer, and referenced to residual solvent signal as internal standards.[151]

### **FT-IR spectroscopy**

IR spectra (4000-400  $\text{cm}^{-1}$ ) of air- or moisture sensitive samples were recorded on a Nicolet iS5 spectrometer inside a glove box. Solid samples were measured with attenuated total reflectance (ATR) sampling technique and are directly placed on an ATR crystal (diamond). All other samples were placed as solid or as drop of a solution on an ATR crystal (diamond) of a Bruker ALPHA FT-IR spectrometer. The spectra were collected as data point tables by using OMNIC (Thermo Fisher Scientific Inc.) or OPUS (Bruker Corporation) software and were canalized with Origin (OriginLab Corporation).

### **Elemental analysis**

The determination of the mass fractions of carbon, hydrogen, and nitrogen were carried out on a Thermo Finnigan FlashEA 1112 Organic Elemental Analyzer *via* dynamic flash combustion analysis (CHN). Air- or moisture-sensitive samples were prepared in silver capsules in a glove box. Mass fractions of transition or alkali metals were achieved by use of a Varian ICP-OES 715 Emission Spectrometer, or by use of an ULTIMA Expert ICP-OES Spectrometer from HORIBA Scientific alternatively.

### **Single crystal XRD**

An analytically pure crystal was directly placed on a glass capillary with perfluorinated oil and measured in a cold nitrogen stream. The data of all measurements were collected on an Agilent Technologies SuperNova diffractometer at 150 K (Cu- $K_{\alpha}$ -radiation,  $\lambda = 1.5418 \text{ \AA}$ ). The structure was solved by direct methods using SHELXT,[152] space group determinations were performed with XPREP and crystal structure refinements were carried out with SHELXL. All programs were handled with Olex<sup>2</sup> Crystallography Software.

### **Powder XRD measurements**

Powder XRDs were obtained on a Bruker AXS D8 ADVANCE diffractometer (Cu-K $\alpha$ -radiation,  $\lambda = 1.5418 \text{ \AA}$ ). The angle variation was performed from 6 to 140°, with a step size of 0.02°. The diffractograms were analyzed with the program STOE WinXPOW. The resulting diffractograms were analyzed by comparison with database entries of the International Centre for Diffraction Data (ICDD).

### **Electron microscopy**

The samples were investigated by an aberration-corrected JEOL JEM-ARM200CF Transmission electron microscope. The microscope is equipped with a high-angle silicon drift EDX detector with the solid angle of up to 0.98 steradians from a detection area of 100 mm<sup>2</sup> that allows for EDX measurement.

### **Thermolysis-MS experiments**

Thermolysis-MS experiments in H<sub>2</sub> atmosphere were performed with a MicrotracBEL BelCat II setup, which was coupled to a mobile Pfeiffer Vacuum QMG 220 mass spectrometer. In a typical experiment, a certain amount of the sample (100-200 mg) was placed in the sample cell inside a glove box and placed in the BelCat II setup. Helium was used as carrier gas with a flow rate of 6 mL/min. The temperature was linearly and continuously increased from r.t. with a temperature ramp of 5-10 K/min. The reaction products were analyzed by the computer-controlled quadrupole mass spectrometer.

### **BET isotherms**

N<sub>2</sub> physisorption measurements were performed at liquid N<sub>2</sub> temperature on a Quantachrome Autosorb-6B analyzer. Prior to the measurement, the samples were degassed in dynamic vacuum at 120 °C for 20 h. Full adsorption and desorption

isotherms were measured. The specific surface area  $S_{\text{BET}}$  and the pore volume and radius were calculated according to the multipoint BET method.

### **DRIFTS measurements**

*In-situ* DRIFTS measurements were conducted using an Agilent Cary 680 FT-IR spectrometer equipped with a mercury cadmium telluride (MCT) detector with a spectral resolution of  $2\text{ cm}^{-1}$  and accumulation of 512 scans. A Praying Mantis *in-situ* cell from Harrick Scientific Corporation with a high-temperature reaction chamber HVC-000-4 with ZnSe windows was employed for the spectroscopic investigations. A spectrum of potassium bromide was collected at r.t. and was used as background. The holder within the chamber was filled with ~70 mg of the powder sample. Regarding the air-sensitive samples, preparation of the cell was performed in an argon glove box. In addition, two valves were adjusted to the inlet and outlet flow lines of the *in-situ* cell to prevent contact of the sample with air. Prior to CO adsorption, the samples were reduced. The reduction process includes treatment with 13%  $\text{H}_2$  in Ar at the desired temperatures (115-360 °C), with a heating rate varying from 2-10 °C/min for 1-2 h, depending on the nature of the sample. As a next step, the samples cooled to r.t. with subsequent evacuation (residual pressure:  $\sim 3.7 \times 10^{-5}$  mbar). DRIFT spectra of sequential dosing of CO (equilibrium pressure: 0.1–75 mbar) were collected at r.t.

### **5.3 Purchased starting materials**

All following chemicals were used as received without further purification. Air- or moisture-sensitive compounds were stored in a glove box under inert gas atmosphere.

**Table 21:** Used chemicals with supplier and purities.

<b>Chemical</b>	<b>Supplier</b>	<b>Purity</b>
Acetone, anhydrous	Acros Organics	99.8 %
Ammonium hydroxide solution, 25 % in H <sub>2</sub> O	Acros Organics	Pro analysi (p.a.)
Benzophenone	Sigma-Aldrich Chemie GmbH	99 %
Cobalt(II) nitrate hexahydrate	Acros Organics	99 %
Copper(I) bromide	Sigma-Aldrich Chemie GmbH	99 %
Copper(I) chloride	Sigma-Aldrich Chemie GmbH	≥ 99 %
Copper(II) nitrate trihydrate	Acros Organics	99 %
Dicobalt octacarbonyl, stabilized	Sigma-Aldrich Chemie GmbH	95 %
Diethyl ether, anhydrous	Acros Organics	99.5 %
N,N-Dimethylformamide, anhydrous	Sigma-Aldrich Chemie GmbH	99.8 %
1,4-Dioxane, anhydrous	Acros Organics	99.5 %
Ethanol, anhydrous	Acros Organics	99.5 %
Hydrochloric acid, 37 % in H <sub>2</sub> O	VWR International	p.a.
Iron(III) nitrate nonahydrate	Acros Organics	≥ 99 %
Iron pentacarbonyl	Acros Organics	99.5 %
Isopropyl alcohol, anhydrous	Acros Organics	99.5 %
Methanol, anhydrous	Sigma-Aldrich Chemie GmbH	99.8 %
<i>n</i> -Pentane, anhydrous	Alfa Aesar	99.8 %
Potassium tetrachloroplatinate(II)	abcr GmbH	99.9 %
Potassium tri- <i>sec</i> -butylborohydride 1.0 M in THF	Sigma-Aldrich Chemie GmbH	/
Pyridine	Alfa Aesar	99.5+ %
Silica gel, Davisil grade 635, 60-100 mesh, 100-200 μ	Sigma-Aldrich Chemie GmbH	-
Sodium	Alfa Aesar	99.95 %
Sodium mercury amalgam, Na 20 %	Sigma-Aldrich Chemie GmbH	≥ 99.9 %
Sodium nitrate	Carl Roth GmbH + Co.KG	99 %
Sodium sulfate, anhydrous	Fluka Analytical	≥ 99.0 %
Tetraammineplatinum(II) nitrate	Sigma-Aldrich Chemie GmbH	99.9 %
Tetraethylammonium chloride	Sigma-Aldrich Chemie GmbH	98 %
Tetraethylammonium chloride monohydrate	abcr GmbH	98 %
Tetramethylethylenediamine	Sigma-Aldrich Chemie GmbH	99 %
Toluene	Alfa Aesar	99.5 %
Water	VWR International	HPLC grade

#### 5.4 Preparation and characterization of starting materials

**Na<sub>2</sub>Fe(CO)<sub>4</sub> • 1.5 dioxane (27):** Collman's reagent (**27**) was prepared according to the literature.[131] Sodium (2.65 g, 115.3 mmol, 1 equiv.) was placed in a dry, three-necked, round-bottomed flask equipped with a reflux condenser flushed with nitrogen. 150 mL of dry, deoxygenated 1,4-dioxane, and benzophenone (2.27 g, 12.48 mmol, 0.22 equiv.) were added, and the solution was stirred vigorously and heated under reflux, until the deep blue color of the benzophenone ketyl appeared. With a gas-tight syringe, 7.79 mL (11.32 g, 57.81 mmol, 1 equiv.) of Fe(CO)<sub>5</sub> was added dropwise through one neck of the flask tightened with a septum to the solution. The blue solution was then titrated to a slightly yellow end point over several hours. The suspension was heated at reflux for another 60 minutes to make sure that the end point of the titration is reached, and then allowed to cool to r.t. Precipitation of disodium tetracarbonylferrate sesquidioxanate (**27**) was completed by adding 150 mL of dry, deoxygenated *n*-hexane. The solvent was then removed *via* filtration, and the product was washed with two 100 mL portions of *n*-hexane. Like this, Na<sub>2</sub>Fe(CO)<sub>4</sub> • 1.5 dioxane (**27**) was yielded as a slightly yellow powder (17.24 g, 49.82 mmol, 86 %).

<sup>13</sup>C-NMR (175 MHz; CDCl<sub>3</sub>): δ [ppm] = 230.5.

Anal. calcd. for C<sub>10</sub>H<sub>12</sub>FeNa<sub>2</sub>O<sub>7</sub>: C, 34.71; H, 3.50. Found: C, 33.50, H, 3.50.

**Na<sub>3</sub>Cu<sub>5</sub>Fe<sub>4</sub>(CO)<sub>16</sub> • 4 dioxane (28):** The cluster (**28**) was synthesized according to the literature.[130] To a suspension of CuBr (1.43 g, 10.0 mmol, 1.25 equiv.) in 100 mL of THF, Na<sub>2</sub>Fe(CO)<sub>4</sub> • 1.5 dioxane (**27**, 2.77 g, 8.0 mmol, 1.00 equiv.) was added, and the mixture was stirred for 16 h at r.t. The suspension was then filtered, and the filtrate was evaporated to dryness, giving the desired product (**28**, 2.38 g, 1.80 mmol, 90 %) in form of a yellow solid. The structure was confirmed by determination of the crystal parameters using single-crystal XRD measurement.

$^{13}\text{C}$ -NMR (175 MHz;  $\text{CDCl}_3$ ):  $\delta$  [ppm] = 217.7.

IR ( $\text{cm}^{-1}$ ):  $\tilde{\nu}$  (CO) = 1940, 1803.

Anal. calcd. for  $\text{C}_{32}\text{H}_{32}\text{Cu}_5\text{Fe}_4\text{Na}_3\text{O}_{24}$ : C, 27.25; H, 2.28. Found: C, 27.65, H, 2.26.

**Na[Co(CO)<sub>4</sub>] (6)**: The compound (6) was synthesized according to the literature.[77] 10 g of 20 % sodium mercury amalgam (containing 2 g Na, 86.99 mmol, 3 equiv.) was suspended in 140 mL THF. Then,  $\text{Co}_2(\text{CO})_8$  (9.91 g, 28.99 mmol, 1 equiv.) was added, and the reaction mixture was stirred at r.t. for 2 h, whereas a color change from red to brown took place. The suspension was filtered, and the residue was washed with additional 50 mL of THF. The combined THF fractions were evaporated to dryness *in vacuo*, yielding the product (6, 10.23 g, 52.73 mmol, 91 %) in form of a brown solid.

IR ( $\text{cm}^{-1}$ ):  $\tilde{\nu}$  (CO) = 1908, 1842.

Anal. calcd. for  $\text{C}_4\text{CoNaO}_4$ : C, 24.77. Found: C, 24.77.

***cis*-[Pt(C<sub>5</sub>H<sub>5</sub>N)<sub>2</sub>Cl<sub>2</sub>] (7)**: The complex (7) was prepared following the literature procedure.[153] To a solution of  $\text{K}_2[\text{PtCl}_4]$  (5 g, 12.05 mol, 1 equiv.) in 50 mL of  $\text{H}_2\text{O}$ , a solution of pyridine (1.96 g, 24.75 mmol, 2.05 equiv., 2.0 mL) in 12.5 mL of  $\text{H}_2\text{O}$  was added under continuous stirring. After a few minutes, a sulfur-yellow precipitate formed. The mixture was stirred at r.t. for 4.5 h, and then placed into a fridge for 24 h for completion of precipitation. The precipitate was filtered off, washed with several portions of ice water, air-dried, and finally dried at 100 °C for 1 h. Like this, 4.57 g of the product was yielded as yellow powder (7, 7.85 mol, 65 %).

Anal. calcd. for  $\text{C}_{10}\text{H}_{10}\text{Cl}_2\text{N}_2\text{Pt}$ : C, 28.32; H, 2.38; N, 6.60. Found: C, 29.19; H, 2.47; N, 6.73.

***trans*-[Pt(C<sub>5</sub>H<sub>5</sub>N)<sub>2</sub>Cl<sub>2</sub>] (5):** The complex (5) was synthesized according to the literature.[153] To 4.57 g (7.84 mmol, 1 equiv.) of *cis*-[Pt(C<sub>5</sub>H<sub>5</sub>N)<sub>2</sub>Cl<sub>2</sub>] (7) a solution of 18.26 mL (excess) of pure pyridine in 45.65 mL H<sub>2</sub>O was added. The reaction mixture was stirred and heated until a clean, colorless solution of [Pt(C<sub>5</sub>H<sub>5</sub>N)<sub>4</sub>]Cl<sub>2</sub> formed. After filtration, the reaction mixture was evaporated to dryness. 45 mL of concentrated (conc.) HCl solution in H<sub>2</sub>O was added to the white residue, and the mixture was again evaporated to dryness, yielding some pale-yellow residue. Since there was some white [Pt(C<sub>5</sub>H<sub>5</sub>N)<sub>4</sub>]Cl<sub>2</sub> left, the procedure was repeated by adding another 23 mL of conc. HCl and evaporating the solution to dryness. This yielded small yellow crystals, which were washed on a fritte with several portions of ice water, then ~50 mL of EtOH, and ~50 mL of Et<sub>2</sub>O. The crystals were dried in air and recrystallized from boiling CH<sub>2</sub>Cl<sub>2</sub> (~350 mL). Repeated recrystallization from the mother liquor yielded the desired product (5, 3.30 g, 5.67 mmol, 72 %) in form of slightly yellow crystals.

Anal. calcd. for C<sub>10</sub>H<sub>10</sub>Cl<sub>2</sub>N<sub>2</sub>Pt: C, 28.32; H, 2.38; N, 6.60. Found: C, 28.54; H, 2.42; N, 6.56.

**NEt<sub>4</sub>[Co(CO)<sub>4</sub>] (18):** The complex 18 was synthesized according to the literature procedure.[102] Na[Co(CO)<sub>4</sub>] (6, 1.70 g, 8.8 mmol, 1 equiv.) was dissolved in 12.5 mL H<sub>2</sub>O, and the solution was added dropwise to a stirring solution of NEt<sub>4</sub>Cl • H<sub>2</sub>O (1.61 g, 8.8 mmol, 1 equiv.) in 36.4 mL H<sub>2</sub>O. After stirring at r.t. for 75 min, the precipitated solid was filtered off, washed with 2 x 15 mL Et<sub>2</sub>O, then with 2 x 30 mL *n*-pentane, and dried *in vacuo*. Like this, the product was yielded in form of a colorless powder (18, 1.73 g, 5.76 mmol, 65 %).

IR (cm<sup>-1</sup>):  $\tilde{\nu}$  (CO) = 1860.

Anal. calcd. for C<sub>12</sub>H<sub>20</sub>CoNO<sub>4</sub>: C, 47.85; H, 6.69; N, 4.65. Found: C, 47.43; H, 6.59; N, 4.23.

**[(NH<sub>3</sub>)<sub>2</sub>CuCo(CO)<sub>4</sub>] (19)**: The complex (19) was synthesized following the literature procedure.[103] CuCl (1.98 g, 20 mmol, 1 equiv.) was dissolved in 50 mL of degassed conc. aq. NH<sub>3</sub>, and the solution was added dropwise to Na[Co(CO)<sub>4</sub>] (6, 3.87 g, 20 mmol, 1 equiv.) under stirring. The suspension was cooled to 5 °C and further stirred for 1.5 h at this temperature. Meanwhile, a brownish precipitate formed that was filtrated off and washed with 10 mL of degassed conc. aq. NH<sub>3</sub>, and redissolved in 80 mL of CH<sub>2</sub>Cl<sub>2</sub> afterwards. The solution was dried using Na<sub>2</sub>SO<sub>4</sub>. After the drying agent was filtered off, the orange solution was saturated with NH<sub>3</sub> gas for 2 h. Afterwards, ~20 mL of *n*-pentane was added, and the mixture was cooled to -20 °C, whereat a mass of yellow crystals formed. Filtration yielded the desired product (19, 2.62 g, 10.41 mmol, 52 %). The crystal structure was confirmed by single crystal XRD measurement.

IR (cm<sup>-1</sup>):  $\tilde{\nu}$  (CO) = 2053, 2022, 1953, 1922, 1876.

**[(tmeda)CuCo(CO)<sub>4</sub>] (20)**: The reaction was proceeded according to the literature with small modifications.[104] CuCl (0.52 g, 5.3 mmol, 1 equiv.) was dissolved in 125 mL of dry CH<sub>2</sub>Cl<sub>2</sub>. Tmeda (0.62 g, 5.3 mmol, 1 equiv.) was added dropwise, and the reaction mixture was stirred for 30 min. Then, NaCo(CO)<sub>4</sub> (6, 1.02 g, 5.3 mmol, 1 equiv.) was added, and the reaction mixture was stirred for further 2 h. The mixture was then filtered, and the filtrate was evaporated to dryness *in vacuo*, yielding the desired product in form of a slightly yellow powder (20, 1.43 g, 4.08 mmol, 77 %).

IR (cm<sup>-1</sup>):  $\tilde{\nu}$  (CO) = 2014, 1918, 1814.

Anal. calcd. for C<sub>10</sub>H<sub>16</sub>CoCuN<sub>2</sub>O<sub>4</sub>: C, 34.25; H, 4.60; N, 7.99. Found: C, 34.20; H, 5.01; N, 7.92.

## 5.5 Preparation and characterization of SSPs

### CoPt

***trans*-Pt(C<sub>5</sub>H<sub>5</sub>N)<sub>2</sub>[Co(CO)<sub>4</sub>]<sub>2</sub> (1)**: The complex (1) was synthesized according to the literature procedure.[74] Under inert conditions, *trans*-[Pt(C<sub>5</sub>H<sub>5</sub>N)<sub>2</sub>Cl<sub>2</sub>] (5) (2.12 g, 5 mmol, 1 equiv.) was added to a stirring solution of Na[Co(CO)<sub>4</sub>] (6) (2.33 g, 12 mmol, 2.4 equiv.) in 200 mL of dry THF. The reaction mixture was refluxed for 3.5 h. After cooling down to r.t., the reaction mixture was filtrated, and the filtrate was evaporated to dryness *in vacuo*, yielding a red-brownish crystalline powder. The bulk product was purified *via* column chromatography from *n*-hexane/CH<sub>2</sub>Cl<sub>2</sub> (v:v = 1:1). Like this, the desired complex was yielded in form of red-brownish crystals (1, 2.48 g, 3.56 mmol, 71 %). The crystal structure was confirmed by single crystal XRD measurement.

IR (cm<sup>-1</sup>):  $\tilde{\nu}$  (CO) = 2012, 1955, 1874.

Anal. calcd. for C<sub>18</sub>H<sub>10</sub>Co<sub>2</sub>N<sub>2</sub>O<sub>8</sub>Pt: C, 31.10; H, 1.45; N, 4.03. Found: C, 30.93; H, 1.40; N, 3.81.

### CoCu

**NEt<sub>4</sub>{Cu[Co(CO)<sub>4</sub>]<sub>2</sub>}** (2): The complex (2) was synthesized following the literature procedure.[101] CuI (0.65 g, 3.44 mmol, 1.0 equiv.) was added to a solution of Na[Co(CO)<sub>4</sub>] (6, 1.37 g, 6.89 mmol, 2.0 equiv.) in anhydrous *i*-PrOH (12.5 mL). After 15 min, the unreacted solid was removed by filtration, and the filtrate was evaporated to dryness *in vacuo*. A solution of Et<sub>4</sub>NI (2.00 g, 7.70 mmol, 2.26 equiv.) in degassed water (30.0 mL) was then added to the solid. The dark green suspension was stirred for 15 min. The precipitate was separated by filtration, washed with water (2 x 10 mL), and dried *in*

*vacuo*. Redissolution in ~30 mL of CH<sub>3</sub>OH and filtration yielded a dark green solution, which was overlaid with ~20 mL of degassed H<sub>2</sub>O. Like this, the product precipitated overnight. The solid was filtered off the solution and washed with 2 x 5 mL of degassed H<sub>2</sub>O. Evaporation to dryness *in vacuo* yielded the product in form of a light-yellow powder (**2**, 0.66 g, 1.24 mmol, 36 %).

IR (cm<sup>-1</sup>):  $\tilde{\nu}$  (CO) = 2022, 1922, 1880.

Anal. calcd. for C<sub>16</sub>H<sub>20</sub>Co<sub>2</sub>CuNO<sub>8</sub>: C, 35.87; H, 3.76; N, 2.61. Found: C, 36.03; H, 3.84; N, 2.51.

Alternative approach:

**NEt<sub>4</sub>{Cu[Co(CO)<sub>4</sub>]<sub>2</sub>}** (**2**): The compound (**2**) was synthesized according to the literature.[102] Therefore, [(NH<sub>3</sub>)<sub>2</sub>CuCo(CO)<sub>4</sub>] (**19**, 0.188 g, 0.75 mmol, 1 equiv.) was dissolved in 20 mL of CH<sub>2</sub>Cl<sub>2</sub> and cooled to -20 °C. A solution of NEt<sub>4</sub>[Co(CO)<sub>4</sub>] (**18**, 0.225 g, 0.75 mmol, 1 equiv.) in 10 mL of CH<sub>2</sub>Cl<sub>2</sub> was added dropwise, and the suspension was stirred for 80 min at -20 °C. The solution was evaporated to dryness *in vacuo*, redissolved in 30 mL of CH<sub>2</sub>Cl<sub>2</sub>/Et<sub>2</sub>O (v:v = 2:1), cooled to 0 °C, and overlaid with 50 mL Et<sub>2</sub>O. Cooling to -20 °C and subsequent filtration yielded the product in form of a crystalline, light yellow powder (**2**, 0.22 g, 0.41 mmol, 55 %).

IR (cm<sup>-1</sup>):  $\tilde{\nu}$  (CO) = 2022, 1922, 1880.

Anal. calcd. for C<sub>16</sub>H<sub>20</sub>Co<sub>2</sub>CuNO<sub>8</sub>: C, 35.87; H, 3.76; N, 2.61. Found: C, 35.95; H, 3.75; N, 2.58.

## CuFe

**[(C<sub>2</sub>H<sub>5</sub>)<sub>4</sub>N]<sub>3</sub>Cu<sub>5</sub>Fe<sub>4</sub>(CO)<sub>16</sub> (3)**: The compound (3) was synthesized according to the literature procedure.[130] To a solution of Na<sub>3</sub>Cu<sub>5</sub>Fe<sub>4</sub>(CO)<sub>16</sub> • 4 dioxane (28) (1.32 g, 1.00 mmol, 1.00 equiv.) in 140 mL THF, (C<sub>2</sub>H<sub>5</sub>)<sub>4</sub>NCl (0.51 g, 3.10 mmol, 3.10 equiv.) was added. The reaction mixture was stirred for 16 h at r.t. and filtered. The residue was washed with 100 mL of acetone in four portions, and the combined acetone fractions were evaporated to ~ 50 mL *in vacuo*. The solution was overlaid with 50 mL of toluene. After 24 h, the product was yielded in form of yellow crystals, which were collected *via* filtration and dried *in vacuo* (3, 0.48 g, 0.35 mmol, 35 %). The structure was confirmed by determination of the crystal parameters using single-crystal XRD measurement.

IR (cm<sup>-1</sup>):  $\tilde{\nu}$  (CO) = 1940, 1897, 1849, 1825.

Anal. calcd. for C<sub>40</sub>H<sub>60</sub>N<sub>3</sub>Cu<sub>5</sub>Fe<sub>4</sub>O<sub>16</sub>: C, 34.81; H, 4.38; N, 3.04. Found: C, 34.85, H, 4.76; N, 3.08.

**Na<sub>2</sub>Cu<sub>6</sub>Fe<sub>4</sub>(CO)<sub>12</sub> • 3 THF (4)**: The complex (4) was prepared following the literature procedure.[130] To a suspension of CuBr (1.43 g, 10.0 mmol, 1.5 equiv.) in 150 mL of THF, Na<sub>2</sub>Fe(CO)<sub>4</sub> • 1.5 dioxane (27, 2.31 g, 6.7 mmol, 1.0 equiv.) was added, and the mixture was stirred at r.t. for 20 h. The suspension was then filtered, and the volume of the filtrate was reduced *in vacuo* to approximately 25 mL. The solution was overlaid with 100 mL of *n*-hexane and rested overnight, whereat a mass of crystals formed. Subsequent removal of the solvent *via* filtration yielded the desired product (4, 1.82 g, 1.38 mmol, 83 %) in form of golden crystals. The structure was confirmed by determination of the crystal parameters using single-crystal XRD measurement.

<sup>13</sup>C-NMR (175 MHz; CDCl<sub>3</sub>):  $\delta$  [ppm] = 214.9.

IR (cm<sup>-1</sup>):  $\tilde{\nu}$  (CO) = 1986, 1850.

Anal. calcd. for  $C_{28}H_{24}Cu_6Fe_4Na_2O_{19}$ : C, 25.57; H, 1.84. Found: C, 25.02; H, 1.88.

## 5.6 Supporting of the SSPs

The catalysts have been prepared by sequential impregnation of the heterobimetallic carbonyl clusters on  $SiO_2$  (Davisil grade 635, bearing a pore size of 60 Å, particle size distribution of 60-100 mesh, particle size of 100-200 μm, surface area of 480 m<sup>2</sup>/g, and a pore volume of 0.75 mL/g). The support was activated *in vacuo* at 100 °C for 16 h and stored under  $N_2$  prior to use. In a typical experiment, a saturated solution of the precursor in degassed DMF was added dropwise to  $SiO_2$ . After resting the solids overnight, the solvent was removed in vacuum at r.t. This procedure was repeated until the desired loadings were reached.

## 5.7 Thermolysis of the SSPs

For activation, the samples were thermally treated in flowing 10%  $H_2/N_2$ . **Table 22-Table 25** show the temperature procedures generally applied for thermolysis of the SSPs. The temperature steps for thermolysis were adapted after screening of the decomposition process of the unsupported complexes (**Figure 12, Figure 28, Figure 44, Figure 46**).

**Table 22:** Temperature steps used for the decomposition of Co-Pt SSP catalysts.

Step	Temperature [°C]	Holding time [min]
1	128	360
2	165	300
3	260	60

**Table 23:** Temperature steps used for the decomposition of Co-Cu SSP catalysts.

Step	Temperature [°C]	Holding time [min]
1	150	240
2	260	240

**Table 24:** Temperature steps used for the decomposition of Cu-Fe SSP catalysts.

Step	Temperature [°C]	Holding time [min]
1	100	240
2	200	240
3	225	60
4	260	60

**Table 25:** Temperature steps used for the decomposition of Na-Cu-Fe SSP catalysts.

Step	Temperature [°C]	Holding time [min]
1	200	300
2	300	60

## 5.8 Synthesis of reference catalysts

Reference catalysts were synthesized by immobilization of metal nitrates *via* IWI (**Table 26-Table 28**). In a typical impregnation procedure, the corresponding metal nitrates were dissolved in high pressure liquid chromatography (HPLC)-grade water. The solution was added dropwise to silica and homogenized with a spatula for 15 min. The solid was rested overnight and calcined in stagnant air afterwards.

### Co-Pt system

**Table 26:** Procedure for synthesis of Co-Pt reference catalysts **11-14**.

Catalyst No.	Pt(NH <sub>3</sub> ) <sub>4</sub> (NO <sub>3</sub> ) <sub>2</sub> [mg]	Co(NO <sub>3</sub> ) <sub>2</sub> • 6 H <sub>2</sub> O [mg]	SiO <sub>2</sub> [mg]	H <sub>2</sub> O [μL]
11	215	322	2000	1500
12	40	59	1968	1476
13	209	/	2000	1500
14	/	313	2000	1500

The samples were subsequently calcined in two steps: First 120 °C for 2 h with a heating rate of 2 K/min, then at 550 °C for 1 h with a heating rate of 2 K/min.

## Co-Cu system

**Table 27:** Procedure for synthesis of Co-Cu reference catalysts **23** and **24**.

Catalyst No.	Co(NO <sub>3</sub> ) <sub>2</sub> • 6 H <sub>2</sub> O [mg]	Cu(NO <sub>3</sub> ) <sub>2</sub> • 3 H <sub>2</sub> O [mg]	SiO <sub>2</sub> [mg]	H <sub>2</sub> O [μL]
<b>23</b>	495	205	1846	1385
<b>24</b>	/	205	1946	1460

The samples were subsequently calcined at 300 °C for 3 h with a heating rate of 10 K/min.

## (Na)-Cu-Fe system

**Table 28:** Procedure for synthesis of (Na-)Cu-Fe reference catalysts **36-38**.

Catalyst No.	Cu(NO <sub>3</sub> ) <sub>2</sub> • 3 H <sub>2</sub> O [mg]	Fe(NO <sub>3</sub> ) <sub>3</sub> • 9 H <sub>2</sub> O [mg]	NaNO <sub>3</sub> [mg]	SiO <sub>2</sub> [mg]	H <sub>2</sub> O [μL]
<b>36</b>	760	1013	/	3660	2745
<b>37</b>	285	318	33	1372	1030
<b>38</b>	/	434	/	1940	1455

The samples were calcined at 300 °C for 3 h with a heating rate of 10 K/min.

## 5.9 Catalytic testing

After supporting, decomposition, and characterization, the catalysts were tested for the conversion of synthesis gas to ethanol (StE). In all measurements, 1 mL of catalyst was placed in a fixed bed reactor and reductively activated before measurement at 54 bar and 265 °C for 1 h in a flow of 58.3 ml/min of 5 %H<sub>2</sub>/N<sub>2</sub>. The measurement was performed with a pressure of 54 bar, a CO:H<sub>2</sub> ratio of 2:1, temperature steps of 260 °C, 280 °C, 300 °C, 320 °C, 300 °C, 280 °C, 260 °C, and a GHSV of 3500 h<sup>-1</sup>. All products were detected by GC. The catalyst's activity was determined by comparing the highest CO conversion at 320 °C. In the following, C<sub>2+</sub> alkanes are defined as *n*-alkanes with a carbon number of at least two, whereas the term "olefins" includes ethylene, propene, and 1-butene. All higher hydrocarbons (branched) are summarized as C<sub>4+</sub> hydrocarbons.

## 6 Appendix

### 6.1 STEM analysis

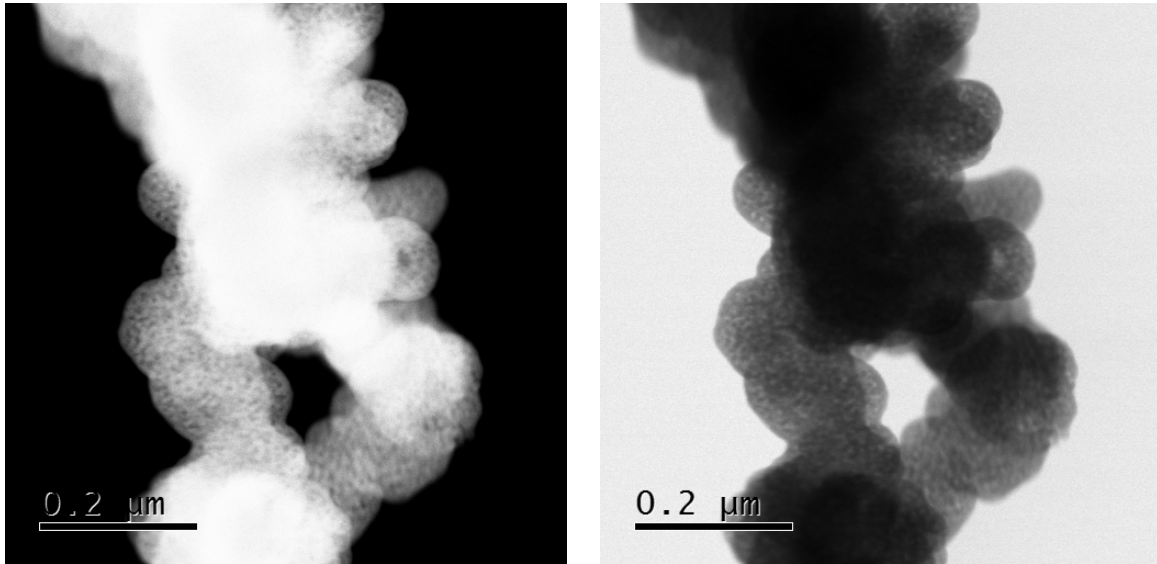


**Figure A1:** High-angle ADF- (left) and bright field-STEM image (right) of Co-Pt SSP catalyst **8**.

## 6.2 Physisorption isotherms

### 6.2.1 Co-Pt

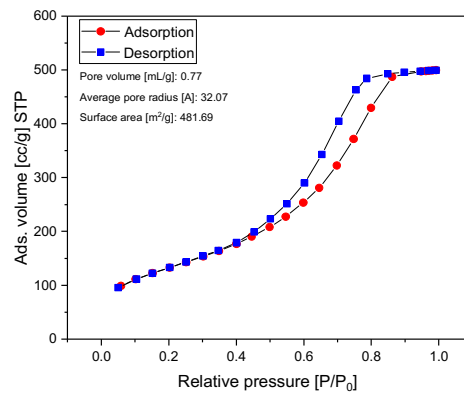
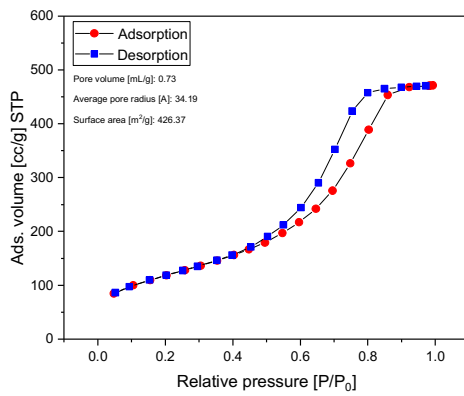


Figure A2:  $N_2$  physisorption isotherms of Co-Pt SSP catalysts **9** (left) and **10** (right).

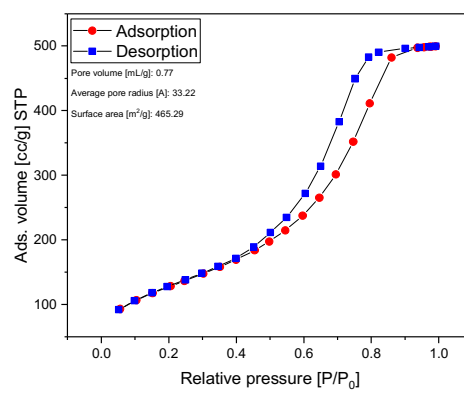
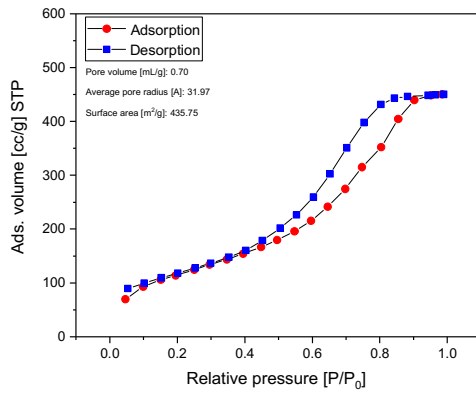
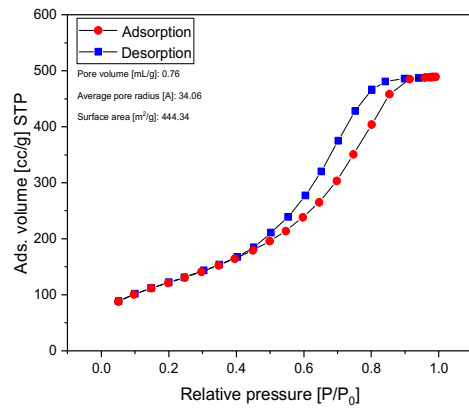
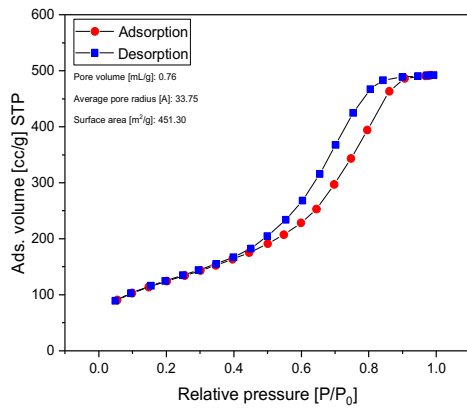
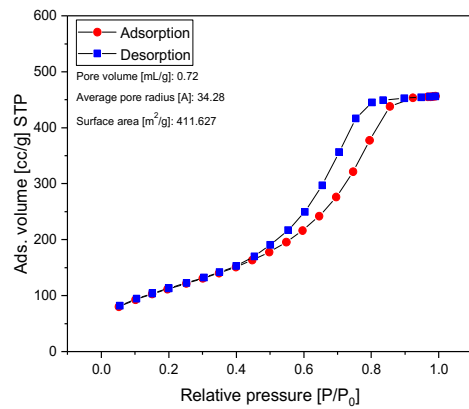
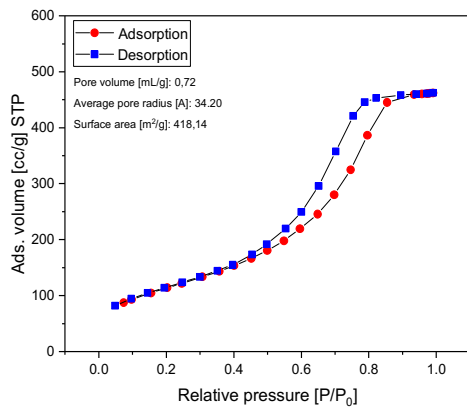


Figure A3:  $N_2$  physisorption isotherms of Co-Pt Col catalysts **11** (left) and **12** (right).



**Figure A4:**  $N_2$  physisorption isotherms of Pt Col catalysts **13** (left) and **14** (right).

## 6.2.2 Co-Cu



**Figure A5:**  $N_2$  physisorption isotherms of Co-Cu SSP catalysts **21** (left) and **22** (right).

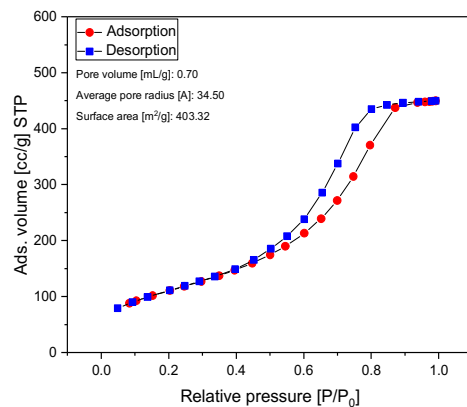


**Figure A6:** *N*<sub>2</sub> physisorption isotherm of Co-Cu Col catalyst **23**.

### 6.2.3 Cu-Fe

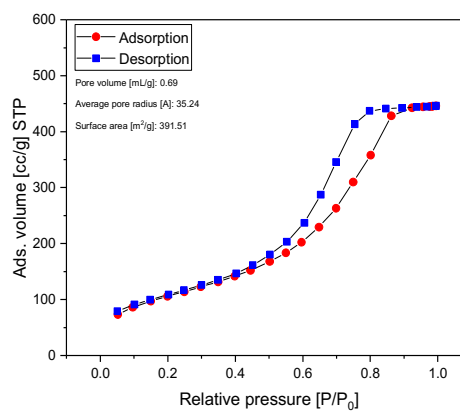
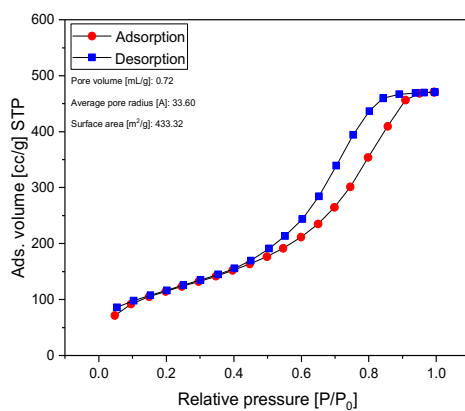


**Figure A7:** *N*<sub>2</sub> physisorption isotherms of Cu-Fe SSP catalysts **29** (left) and **30** (right).

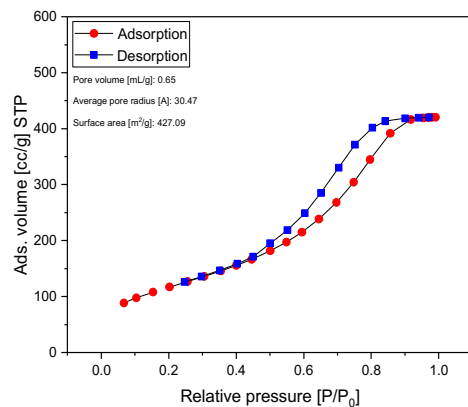


**Figure A8:**  $N_2$  physisorption isotherm of Na-Cu-Fe SSP catalyst **31**.

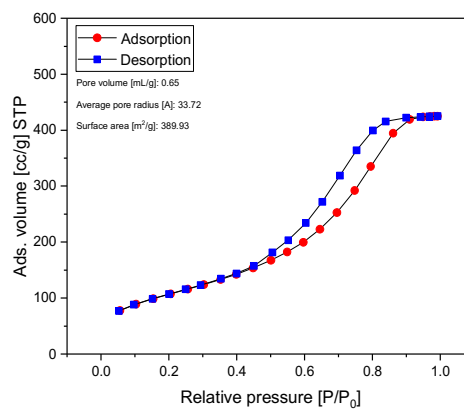
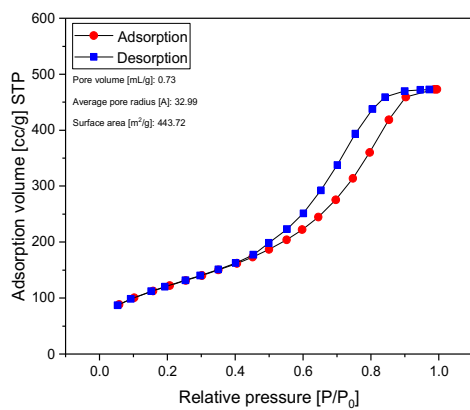


**Figure A9:**  $N_2$  physisorption isotherms of Na-Cu-Fe SSP catalyst **32** (left) and **33** (right).

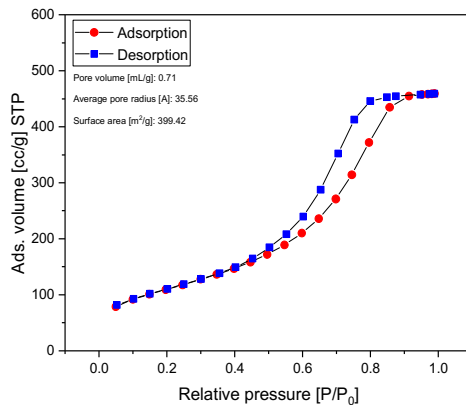
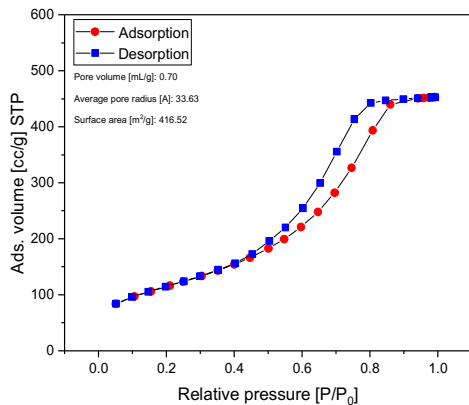


**Figure A10:**  $N_2$  physisorption isotherms of Na-Cu-Fe SSP catalyst **34** (left) and **35** (right).

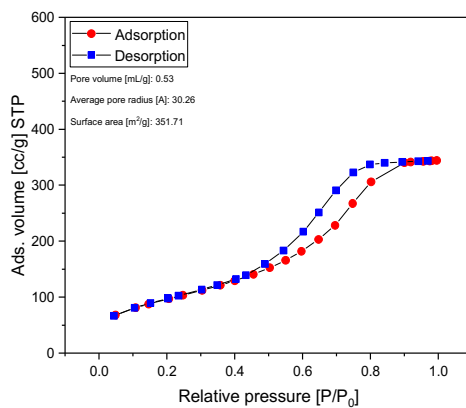
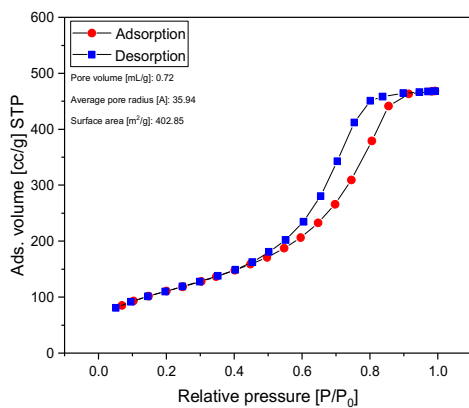


**Figure A11:**  $N_2$  physisorption isotherms of Cu-Fe Col catalyst **36** (left) and **37** (right).

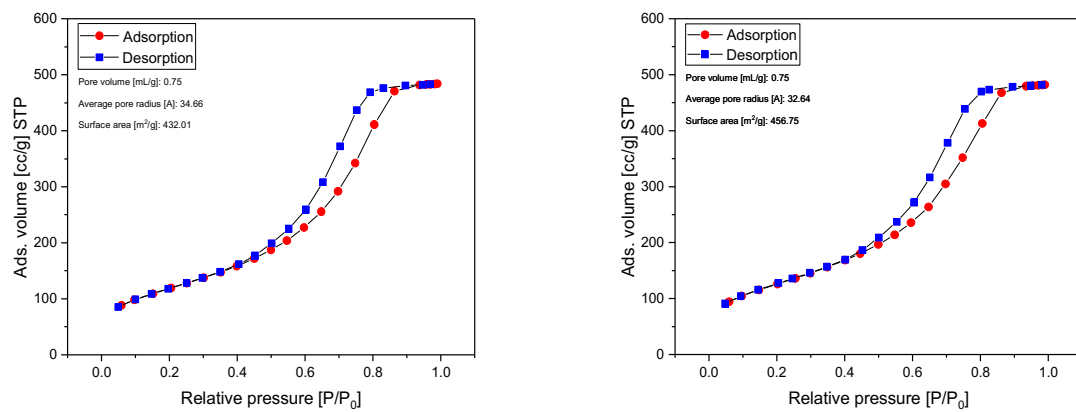


**Figure A12:**  $N_2$  physisorption isotherms of Cu Col catalysts **24** (left) and **38** (right).

## 6.3 XRD analysis

### 6.3.1 Values used for calculation of particle sizes

**Table A1:** Values used for calculation of particle sizes via Scherrer equation

Catalyst No.	System	Compound	$\beta$ [rad] $\times 10^{-3}$	$\theta$ [°]	D [nm]
1	Unsupported decomposed Co-Pt SSP	Co <sub>2</sub> Pt	17.2	21.3	8.66
11	Co-Pt Col	Co <sub>3</sub> O <sub>4</sub>	19.1	18.2	7.62
		Pt	3.83	19.8	38.4
13	Co-Pt Col	Pt	18.1	19.9	8.13
14	Co-Pt Col	Co <sub>3</sub> O <sub>4</sub>	21.4	18.3	6.81
16	Spent Co-Pt SSP	CoO	5.23	42.4	35.9
17	Spent Co-Pt Col	CoO	6.62	42.4	30.2
21	Co-Cu SSP	Co <sub>0.52</sub> Cu <sub>0.48</sub>	7.85	26.8	19.8
		CoO	4.36	21.1	34.1
22	Co-Cu SSP	Co <sub>0.52</sub> Cu <sub>0.48</sub>	9.07	21.8	16.4
		CoO	5.58	21.2	26.6
23	Co-Cu Col	Cu <sub>0.92</sub> Co <sub>2.08</sub> O <sub>4</sub>	12.0	18.3	12.1
25	Spent Co-Cu SSP	CoO	4.63	42.4	40.5
26	Spent Co-Cu Col	CoO	5.66	42.4	33.2
29	Cu-Fe SSP	Cu	2.61	21.6	57.1
		Fe	1.91	22.3	53.8
30	Cu-Fe SSP	CuO	6.28	21.2	23.7
		Cu	6.45	21.6	23.1
34	Na-Cu-Fe SSP	Cu	25.3	21.6	5.89
35	Na-Cu-Fe SSP	Cu	7.33	21.6	20.3
36	Cu-Fe Col	CuO cubic	4.53	21.1	23.1
		CuO tenorite	6.80	19.3	21.6
		Fe <sub>2</sub> O <sub>3</sub>	10.1	17.7	14.4
37	Na-Cu-Fe Col	CuO	10.8	17.6	13.4
40	Spent Cu-Fe Col	Cu	8.16	43.3	23.3
41	Spent Na-Cu-Fe SSP	Cu	5.12	43.3	37.2

### 6.3.2 Co-Pt

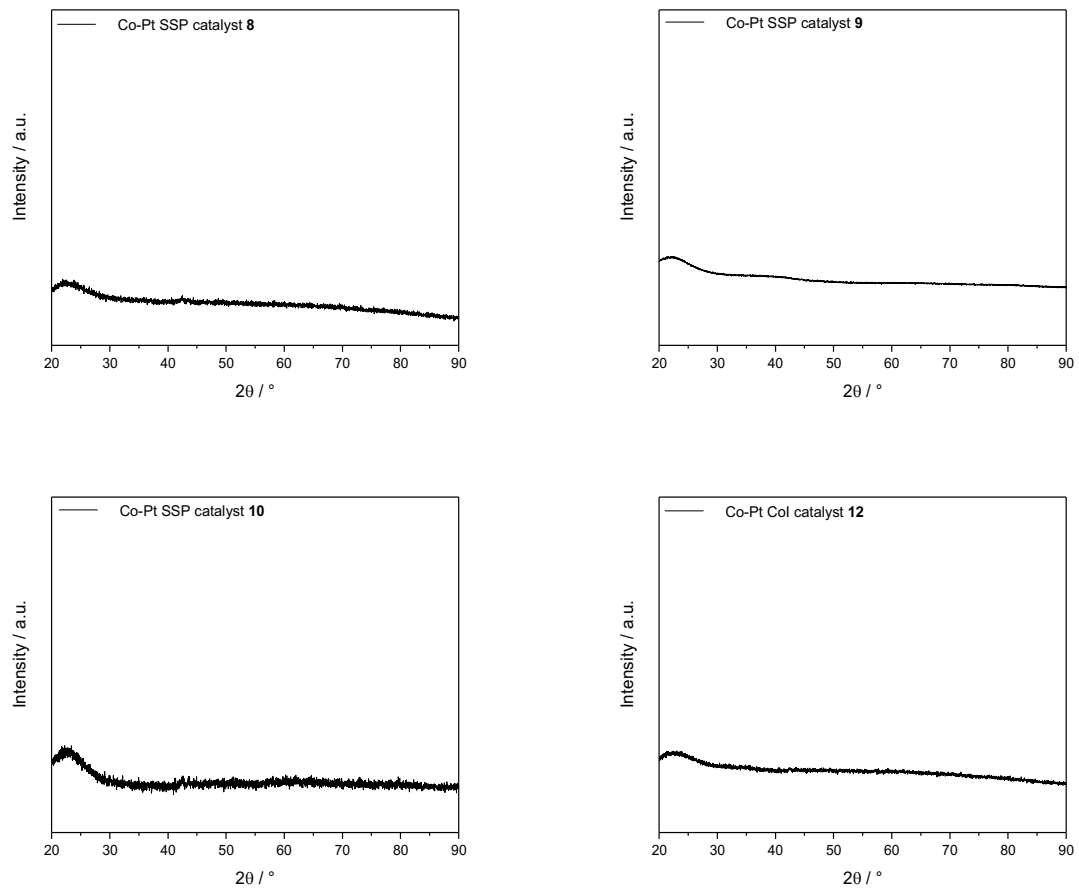


**Figure A13:** Powder XRDs of Co-Pt SSP catalysts 8, 9, 10, and 12.

### 6.3.3 Cu-Fe

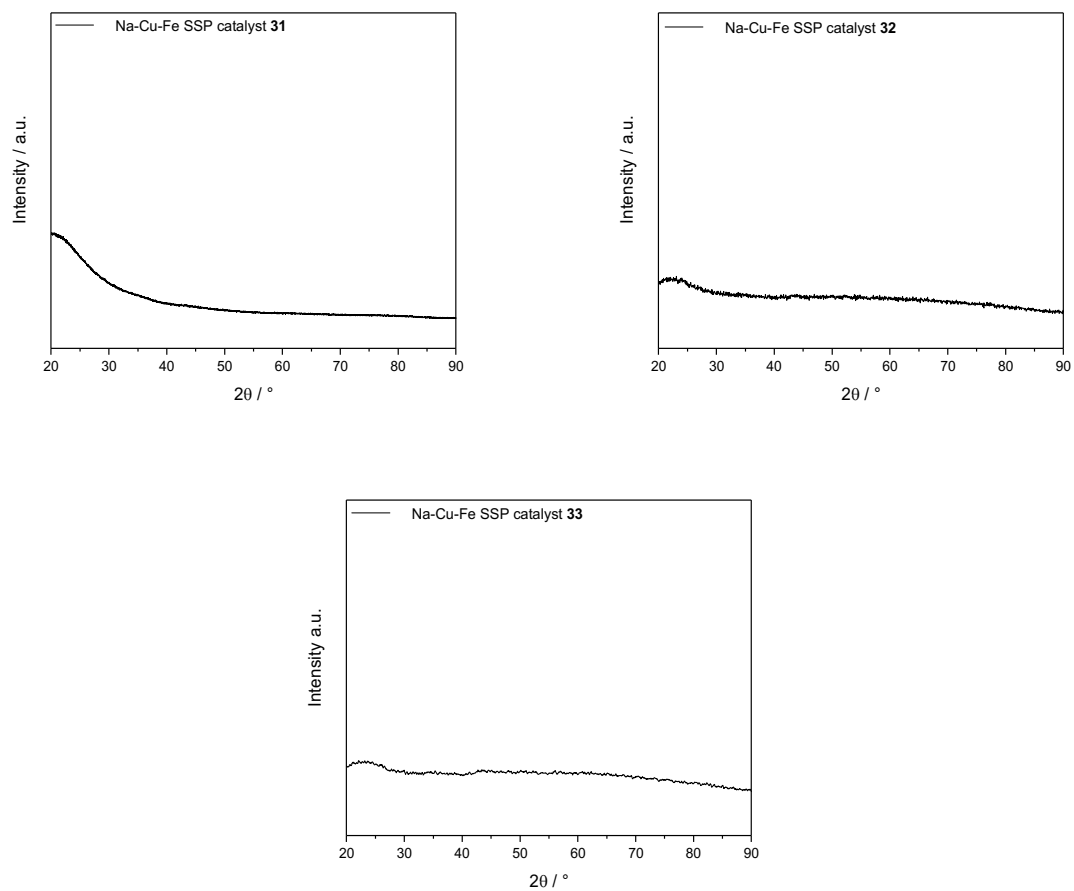


**Figure A14:** Powder XRD of Na-Cu-Fe SSP catalysts **31** (upper row, left), **32** (upper row, right), and **33** (below).

## 6.4 DRIFTS

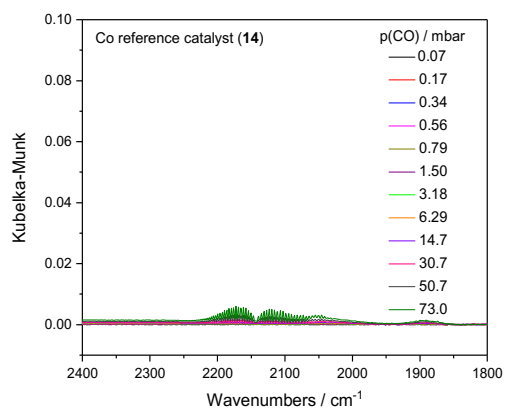


**Figure A15:** DRIFTS monitoring of CO adsorption on activated Co reference catalyst (14).

## 6.5 Catalytic data

In all measurements 1 mL of catalyst was placed in a fixed bed reactor and the measurement was performed with a pressure of 54 bar, a CO:H<sub>2</sub> ratio of 2, temperature steps are 260 °C, 280 °C, 300 °C, 320 °C, 300 °C, 280 °C, 260 °C and a GHSV of  $3500 \frac{\text{mL (Gas)}}{\text{h} \cdot \text{mL (Cat)}}$ . All products were detected by GC.

### 6.5.1 Co-Pt

**Table A2:** CO conversions and product selectivity of catalysts at 320 °C, except of catalyst **14** (at 260 °C), in %.

Entry	X(CO)	S(CH <sub>4</sub> )	S(C <sub>2+</sub> Alkanes)	S(Olefins)	S(MeOH)	S(EtOH)	S(PrOH)	S(CO <sub>2</sub> )	S(C <sub>2+</sub> Oxy)	S(C <sub>4+</sub> CHs)
<b>10</b>	3.11	16.1	9.57	0.65	51.9	1.74	4.23	11.6	0.91	3.35
<b>12</b>	2.89	18.4	7.55	0.45	54.3	2.11	3.88	9.06	0.95	3.23
<b>13</b>	2.67	12.7	35.7	0.12	0.00	0.22	0.38	0.00	3.39	47.5
<b>14</b>	5.52	29.3	20.2	9.35	8.14	0.00	0.15	0.00	1.45	31.5

### 6.5.2 Co-Cu

**Table A3:** CO conversions and product selectivity at 260 °C, except of catalyst **24** (at 320 °C) in %.

Entry	X(CO)	S(CH <sub>4</sub> )	S(C <sub>2+</sub> Alkanes)	S(Olefins)	S(MeOH)	S(EtOH)	S(PrOH)	S(CO <sub>2</sub> )	S(C <sub>2+</sub> Oxy)	S(C <sub>4+</sub> CHs)
<b>24</b>	5.03	12.9	4.75	0.27	64.5	0.00	0.00	15.2	0.86	1.49
<b>14</b>	5.52	29.3	20.2	9.35	8.14	0.00	0.15	0.00	1.45	31.5
<b>22</b>	8.97	35.4	32.6	14.7	2.59	3.50	1.41	1.16	0.57	8.13
<b>23</b>	9.30	32.8	29.9	17.3	1.35	3.42	0.92	1.09	0.91	12.4

### 6.5.3 Cu-Fe

**Table A4:** CO conversions and product selectivity of catalysts **24** and **38** (at 320 °C), **30** and **36** (at 260 °C), **35** (at 260 °C), and **37** (at 280 °C) in %.

Entry	X(CO)	S(CH <sub>4</sub> )	S(C <sub>2+</sub> Alkanes)	S(Olefins)	S(MeOH)	S(EtOH)	S(PrOH)	S(CO <sub>2</sub> )	S(C <sub>2+</sub> Oxy)	S(C <sub>4+</sub> CHs)
<b>24</b>	5.03	12.9	4.75	0.27	64.4	0.00	0.00	15.2	0.86	1.49
<b>38</b>	3.00	44.7	19.8	16.1	0.00	0.00	0.00	8.42	1.44	9.44
<b>30</b>	5.77	22.3	29.9	13.7	7.76	6.15	3.18	4.57	1.21	11.0
<b>36</b>	7.62	22.1	32.9	9.79	12.7	6.86	1.05	7.21	0.49	6.81
<b>35</b>	6.01	12.1	27.6	20.6	4.20	6.35	2.02	10.6	0.46	15.7
<b>37</b>	5.67	21.8	18.9	24.4	5.41	8.95	1.04	4.24	0.00	15.1

## 6.6 Citations

- [1] S. Furukawa, T. Komatsu, Intermetallic Compounds: Promising Inorganic Materials for Well-Structured and Electronically Modified Reaction Environments for Efficient Catalysis, *ACS Catal.* 7 (2017) 735–765. doi:10.1021/acscatal.6b02603.
- [2] A.E. Russell, A. Rose, X-ray absorption spectroscopy of low temperature fuel cell catalysts, *Chem. Rev.* 104 (2004) 4613–4635. doi:10.1021/cr020708r.
- [3] Y. Cao, R. Jin, C.A. Mirkin, DNA-modified core-shell Ag/Au nanoparticles, *J. Am. Chem. Soc.* 123 (2001) 7961–7962. doi:10.1021/ja011342n.
- [4] R. Ferrando, J. Jellinek, R.L. Johnston, Nanoalloys: From theory to applications of alloy clusters and nanoparticles, *Chem. Rev.* 108 (2008) 845–910. doi:10.1021/cr040090g.
- [5] S. Zafeirotos, S. Piccinin, D. Teschner, Alloys in Catalysis: Phase Separation and Surface Segregation Phenomena in Response to the Reactive Environment, *Catal. Sci. Technol.* 2 (2012) 1787. doi:10.1039/c2cy00487a.
- [6] F. Besenbacher, I. Chorkendorff, B.S. Clausen, B. Hammer, A.M. Molenbroek, J.K. Nørskov, I. Stensgaard, Design of a Surface Alloy Catalyst for Steam Reforming, 279 (1998) 1913–1916.
- [7] M.P. Andrews, S.C. O'Brien, Gas-phase molecular alloys of bulk immiscible elements:  $\text{fexAg}_y$ , *J. Phys. Chem.* 96 (1992) 8233–8241. doi:10.1021/j100200a007.
- [8] J.H. Sinfelt, Catalysis by Alloys and Bimetallic Clusters, *Acc. Chem. Res.* 10 (1977) 15–20. doi:10.1021/ar50109a003.
- [9] V. Ponec, Alloy catalysts: The concepts, *Appl. Catal. A Gen.* 222 (2001) 31–45. doi:10.1016/S0926-860X(01)00828-6.
- [10] E.K. Vestergaard, R.T. Vang, J. Knudsen, T.M. Pedersen, T. An, E. Lægsgaard, I. Stensgaard, B. Hammer, F. Besenbacher, Adsorbate-induced alloy phase

- separation: A direct view by high-pressure scanning tunneling microscopy, *Phys. Rev. Lett.* 95 (2005) 1–4. doi:10.1103/PhysRevLett.95.126101.
- [11] G. Ertl, H. Knözinger, J. Weitkamp, *Ion exchange and impregnation*, 1st ed., WILEY-VCH Verlag, Weinheim, 2008. doi:10.1002/9783527610044.hetcat0022.
- [12] P. Munnik, P. de Jongh, K. de Jong, *Recent Developments in the Synthesis of Supported Catalysts*, *Chem. Rev.* (2015) 150619062952001. doi:10.1021/cr500486u.
- [13] J.R. Regalbuto, *Catalyst Preparation Science and Engineering*, CRC Press Taylor & Francis Group, Boca Raton, 2007.
- [14] X. Zhang, L. Zhong, Q. Guo, H. Fan, H. Zheng, K. Xie, Influence of the calcination on the activity and stability of the Cu/ZnO/Al<sub>2</sub>O<sub>3</sub> catalyst in liquid phase methanol synthesis, *Fuel*. 89 (2010) 1348–1352. doi:10.1016/j.fuel.2009.06.011.
- [15] A.S. Darling, *Cobalt -Platinum Alloys*, *Platin. Met. Rev.* 7 (1963) 96–104.
- [16] S. Doi, F. Wang, K. Hosoiri, T. Watanabe, Preparation and Characterization of Electrodeposited Co-Pt Binary Alloy Film, *Mater. Trans.* 44 (2003) 649–652. doi:10.2320/matertrans.44.649.
- [17] J.I. Park, J. Cheon, Synthesis of “solid solution” and “core-shell” type cobalt-platinum magnetic nanoparticles via transmetalation reactions, *J. Am. Chem. Soc.* 123 (2001) 5743–5746. doi:10.1021/ja0156340.
- [18] V. Tzitzios, D. Niarchos, M. Gjoka, N. Boukos, D. Petridis, Synthesis and characterization of 3D CoPt nanostructures, *J. Am. Chem. Soc.* 127 (2005) 13756–13757. doi:10.1021/ja053044m.
- [19] T. Nishizawa, K. Ishida, The Co-Cu (Cobalt-Copper) system, *Bull. Alloy Phase Diagrams*. 5 (1984) 161–165. doi:10.1007/BF02868953.
- [20] C. Bale, *Cobalt copper phase diagram*, (n.d.). [http://www.crct.polymtl.ca/fact/phase\\_diagram.php?file=Cu-Co.jpg&dir=FS Copp](http://www.crct.polymtl.ca/fact/phase_diagram.php?file=Cu-Co.jpg&dir=FS Copp)

(accessed January 23, 2019).

- [21] S. Xue, C. Cao, F. Ji, Y. Xu, D. Wang, H. Zhu, Highly uniform Cu<sub>90</sub>Co<sub>10</sub> alloy nanorod arrays: Fabrication and characterization, *Mater. Lett.* 59 (2005) 3173–3176. doi:10.1016/j.matlet.2005.04.052.
- [22] J. Ahmed, A. Ganguly, S. Saha, G. Gupta, P. Trinh, A.M. Mugweru, S.E. Lofland, K. V. Ramanujachary, A.K. Ganguli, Enhanced electrocatalytic activity of copper-cobalt nanostructures, *J. Phys. Chem. C.* 115 (2011) 14526–14533. doi:10.1021/jp202396r.
- [23] P. Allia, M. Coisson, P. Tiberto, F. Vinai, Magnetic and magnetotransport properties in Joule-heated granular Cu<sub>95</sub>Co<sub>5</sub> ribbons, *J. Alloys Compd.* 434–435 (2007) 601–603. doi:10.1016/j.jallcom.2006.08.089.
- [24] W. Wang, F. Zhu, W. Lai, J. Wang, Microstructure, magnetic properties and giant magnetoresistance of granular Cu – Co alloy, 32 (1999) 1990–1996.
- [25] O. Drbohlav, W.J. Botta, A.R. Yavari, Nanostructure of Melt-Spun Cu<sub>80</sub>Fe<sub>20</sub>, *Mater. Sci. Forum.* 225–227 (1996) 359–366. doi:10.4028/www.scientific.net/MSF.225-227.359.
- [26] C. Bale, Copper iron phase diagram, (n.d.). [http://www.crct.polymtl.ca/fact/phase\\_diagram.php?file=Cu-Fe.jpg&dir=FS Copp](http://www.crct.polymtl.ca/fact/phase_diagram.php?file=Cu-Fe.jpg&dir=FS Copp) (accessed January 23, 2019).
- [27] O. Kubaschewski, J.F. Smith, D.M. Bailey, A Thermodynamic Analysis of Phase Relationships in the Iron-Copper System, *Zeitschrift Für Met.* 68 (1977) 495–499.
- [28] O. Kubaschewski, *Iron - Binary Phase Diagrams*, Springer-Verlag Berlin Heidelberg, 1982. doi:10.1007/978-3-662-08024-5.
- [29] B.C. Gates, Supported Metal Clusters: Synthesis, Structure, and Catalysis, *Chem. Rev.* 95 (1995) 511–522. doi:10.1021/cr00035a003.
- [30] J. Guzman, B.C. Gates, Supported molecular catalysts: metal complexes and

- clusters on oxides and zeolites, *Dalt. Trans.* 17 (2003) 3303–3318.  
doi:10.1039/b303285j.
- [31] Y. Xia, X. Yang, Toward Cost-Effective and Sustainable Use of Precious Metals in Heterogeneous Catalysts, *Acc. Chem. Res.* 50 (2017) 450–454.  
doi:10.1021/acs.accounts.6b00469.
- [32] J.M. Thomas, B.F.G. Johnson, R. Raja, G. Sankar, P.A. Midgley, High-performance nanocatalysts for single-step hydrogenations, *Acc. Chem. Res.* 36 (2003) 20–30. doi:10.1021/ar990017q.
- [33] O.S. Alexeev, G.W. Graham, M. Shelef, R.D. Adams, B.C. Gates, Gamma-Al<sub>2</sub>O<sub>3</sub>-supported PtRu clusters prepared from [Pt<sub>2</sub>Ru<sub>4</sub>(CO)<sub>18</sub>]: Characterization by infrared and extended X-ray absorption fine structure spectroscopies, *J. Phys. Chem. B.* 106 (2002) 4697–4704. doi:10.1021/jp014342i.
- [34] S. Albonetti, R. Bonelli, J. Epoupa Mengou, C. Femoni, C. Tiozzo, S. Zacchini, F. Trifirò, Gold/iron carbonyl clusters as precursors for TiO<sub>2</sub> supported catalysts, *Catal. Today.* 137 (2008) 483–488. doi:10.1016/j.cattod.2007.11.003.
- [35] A.S. Fung, M.J. Kelley, D.C. Koningsberger, B.C. Gates,  $\gamma$ -Al<sub>2</sub>O<sub>3</sub>-supported Re-Pt cluster catalyst prepared from [Re<sub>2</sub>Pt(CO)<sub>12</sub>]: Characterization by extended X-ray absorption fine structure spectroscopy and catalysis of methylcyclohexane dehydrogenation, *J. Am. Chem. Soc.* 119 (1997) 5877–5887.  
doi:10.1021/ja962816z.
- [36] M.S. Nashner, A.I. Frenkel, D.L. Adler, J.R. Shapley, R.G. Nuzzo, Structural characterization of carbon-supported platinum-ruthenium nanoparticles from the molecular cluster precursor PtRu<sub>5</sub>C(CO)<sub>16</sub>, *J. Am. Chem. Soc.* 119 (1997) 7760–7771. doi:10.1021/ja971039f.
- [37] R. Raja, T. Khimyak, J.M. Thomas, S. Hermans, B.F.G. Johnson, Single Step, Highly Active, and Highly Selective Nanoparticle Catalysts for the Hydrogenation of Key Organic Compounds, *Angew. Chemie Int. Ed.* 113 (2001) 4774–4778.  
doi:10.1002/1521-3757(20011217)113:24<4774::AID-ANGE4774>3.0.CO;2-H.

- [38] I. Robinson, S. Zacchini, L.D. Tung, S. Maenosono, N.T.K. Thanh, Synthesis and characterization of magnetic nanoalloys from bimetallic carbonyl clusters, *Chem. Mater.* 21 (2009) 3021–3026. doi:10.1021/cm9008442.
- [39] W.M.H. Ponc, V.; Sachtler, The reactions between cyclopentane and deuterium on nickel and nickel-copper alloys, *J. Catal.* 24 (1972) 250–261.
- [40] D.J.C. Sinfelt, J.H.; Carter, J.L.; Yates, Catalytic hydrogenolysis and dehydrogenation over copper-nickel alloys, *J. Catal.* 24 (1972) 283–296.
- [41] F. Buatier de Mongeot, M. Scherer, B. Gleich, E. Kopatzki, R.. Behm, CO adsorption and oxidation on bimetallic Pt/Ru(0001) surfaces – a combined STM and TPD/TPR study, *Surf. Sci.* 411 (1998) 249–262. doi:10.1016/S0039-6028(98)00286-6.
- [42] P. Hermann, J. Guigner, B. Tardy, Y. Jugnet, The Pd/Ni (110) bimetallic system: surface characterisation by LEED, AES, XPS, and LEIS techniques; new insight on catalytic properties, ... *Catal.* 175 (1996) 169–175. doi:10.1006/jcat.1996.0316.
- [43] K. XIAO, Z. BAO, X. QI, X. WANG, L. ZHONG, K. FANG, M. LIN, Y. SUN, Advances in bifunctional catalysis for higher alcohol synthesis from syngas, *Chinese J. Catal.* 34 (2013) 116–129. doi:10.1016/S1872-2067(11)60496-8.
- [44] J.J.F. Xiaoding, Xu; Doesburg, E.B.M.; Scholten, Synthesis of higher alcohols from syngas - recently patented catalysts and tentative ideas on the mechanism, *Catal. Today.* 2 (1987) 125–170.
- [45] N.D. Subramanian, G. Balaji, C.S.S.R. Kumar, J.J. Spivey, Development of cobalt-copper nanoparticles as catalysts for higher alcohol synthesis from syngas, *Catal. Today.* 147 (2009) 100–106. doi:10.1016/j.cattod.2009.02.027.
- [46] C. Miret, P. Chazara, L. Montastruc, S. Negny, S. Domenech, Design of bioethanol green supply chain: Comparison between first and second generation biomass concerning economic, environmental and social criteria, *Comput. Chem.*

- Eng. 85 (2016) 16–35. doi:10.1016/j.compchemeng.2015.10.008.
- [47] A. Morschbacker, Bio-Ethanol Based Ethylene, *Polym. Rev.* 49 (2009) 79–84. doi:10.1080/15583720902834791.
- [48] J. Goldemberg, Ethanol for a Sustainable Energy Future, *Science* (80-. ). 315 (2007) 808–810. doi:10.1126/science.1137013.
- [49] M.D. Jones, Catalytic transformation of ethanol into 1,3-butadiene, *Chem. Cent. J.* 8 (2014) 53. doi:10.1186/s13065-014-0053-4.
- [50] W. Zhou, Z. Zhou, S. Song, W. Li, G. Sun, P. Tsiakaras, Q. Xin, Pt based anode catalysts for direct ethanol fuel cells, *Appl. Catal. B Environ.* 46 (2003) 273–285. doi:10.1016/S0926-3373(03)00218-2.
- [51] L. Siwale, L. Kristóf, T. Adam, A. Bereczky, A. Penninger, M. Mbarawa, K. Andrei, Performance Characteristics of n-Butanol-Diesel Fuel Blend Fired in a Turbo-Charged Compression Ignition Engine, *J. Power Energy Eng.* 1 (2013) 77–83. doi:10.4236/jpee.2013.15013.
- [52] J.R. Rostrup-Nielsen, CHEMISTRY: Making Fuels from Biomass, *Science* (80-. ). 308 (2005) 1421–1422. doi:10.1126/science.1113354.
- [53] K.A. Gray, L. Zhao, M. Emptage, Bioethanol, *Curr. Opin. Chem. Biol.* 10 (2006) 141–146. doi:10.1016/j.cbpa.2006.02.035.
- [54] F.W. Bai, W.A. Anderson, M. Moo-Young, Ethanol fermentation technologies from sugar and starch feedstocks, *Biotechnol. Adv.* 26 (2008) 89–105. doi:10.1016/j.biotechadv.2007.09.002.
- [55] J. Hu, Y. Wang, C. Cao, D.C. Elliott, D.J. Stevens, J.F. White, Conversion of biomass-derived syngas to alcohols and C2 oxygenates using supported Rh catalysts in a microchannel reactor, *Catal. Today.* 120 (2007) 90–95. doi:10.1016/j.cattod.2006.07.006.
- [56] J. Yu, D. Mao, L. Han, Q. Guo, G. Lu, The effect of Fe on the catalytic

- performance of Rh-Mn-Li/SiO<sub>2</sub> catalyst: A DRIFTS study, *Catal. Commun.* 27 (2012) 1–4. doi:10.1016/j.catcom.2012.06.010.
- [57] J. Yu, D. Mao, L. Han, Q. Guo, G. Lu, CO hydrogenation over Fe-promoted Rh-Mn-Li/SiO<sub>2</sub> catalyst: The effect of sequences for introducing the Fe promoter, *Fuel Process. Technol.* 112 (2013) 100–105. doi:10.1016/j.fuproc.2013.03.004.
- [58] C.H. Ma, H.Y. Li, G.D. Lin, H. Bin Zhang, Ni-decorated carbon nanotube-promoted Ni-Mo-K catalyst for highly efficient synthesis of higher alcohols from syngas, *Appl. Catal. B Environ.* 100 (2010) 245–253. doi:10.1016/j.apcatb.2010.07.040.
- [59] J.J. Wang, J.R. Xie, Y.H. Huang, B.H. Chen, G.D. Lin, H. Bin Zhang, An efficient Ni-Mo-K sulfide catalyst doped with CNTs for conversion of syngas to ethanol and higher alcohols, *Appl. Catal. A Gen.* 468 (2013) 44–51. doi:10.1016/j.apcata.2013.08.026.
- [60] T. Toyoda, T. Minami, E.W. Qian, Mixed alcohol synthesis over sulfided molybdenum-based catalysts, *Energy and Fuels.* 27 (2013) 3769–3777. doi:10.1021/ef400262a.
- [61] Y. Liu, K. Murata, M. Inaba, I. Takahara, K. Okabe, Synthesis of Mixed Alcohols from Syngas over Cs-modified Cu/Ce(1-x)Zr(x)O(2) Catalysts, *J. Japan Pet. Inst.* 53 (2010) 153–159. doi:10.1627/jpi.53.153.
- [62] R. Xu, C. Yang, W. Wei, W.H. Li, Y.H. Sun, T.D. Hu, Fe-modified CuMnZrO<sub>2</sub> catalysts for higher alcohols synthesis from syngas, *J. Mol. Catal. A Chem.* 221 (2004) 51–58. doi:10.1016/j.molcata.2004.07.003.
- [63] A. Cao, G. Liu, L. Wang, J. Liu, Y. Yue, L. Zhang, Y. Liu, Growing layered double hydroxides on CNTs and their catalytic performance for higher alcohol synthesis from syngas, *J. Mater. Sci.* 51 (2016) 5216–5231. doi:10.1007/s10853-016-9823-9.
- [64] X.M. Wu, Y.Y. Guo, J.M. Zhou, G.D. Lin, X. Dong, H. Bin Zhang, Co-decorated

- carbon nanotubes as a promoter of Co-Mo-K oxide catalyst for synthesis of higher alcohols from syngas, *Appl. Catal. A Gen.* 340 (2008) 87–97.  
doi:10.1016/j.apcata.2007.09.051.
- [65] A. Cao, G. Liu, Y. Yue, L. Zhang, Y. Liu, Nanoparticles of Cu–Co alloy derived from layered double hydroxides and their catalytic performance for higher alcohol synthesis from syngas, *RSC Adv.* 5 (2015) 58804–58812.  
doi:10.1039/C5RA05190H.
- [66] H.T. Luk, C. Mondelli, D.C. Ferré, J.A. Stewart, J. Pérez-Ramírez, Status and prospects in higher alcohols synthesis from syngas, *Chem. Soc. Rev.* 46 (2017) 1358–1426. doi:10.1039/C6CS00324A.
- [67] A.J. Medford, A.C. Lausche, F. Abild-Pedersen, B. Temel, N.C. Schjødt, J.K. Nørskov, F. Studt, Activity and selectivity trends in synthesis gas conversion to higher alcohols, *Top. Catal.* 57 (2014) 135–142. doi:10.1007/s11244-013-0169-0.
- [68] W. Arabczyk, D. Moszyński, U. Narkiewicz, R. Pelka, M. Podsiadły, Poisoning of iron catalyst by sulfur, *Catal. Today.* 124 (2007) 43–48.  
doi:10.1016/j.cattod.2007.02.003.
- [69] D.E. Sparks, G. Jacobs, M.K. Gnanamani, V.R.R. Pendyala, W. Ma, J. Kang, W.D. Shafer, R.A. Keogh, U.M. Graham, P. Gao, B.H. Davis, Poisoning of cobalt catalyst used for Fischer-Tropsch synthesis, *Catal. Today.* 215 (2013) 67–72.  
doi:10.1016/j.cattod.2013.01.011.
- [70] J.K. Dunleavy, Final Analysis, *Platin. Met. Rev.* 50 (2006) 110–110.  
doi:10.1595/147106706X111456.
- [71] C.H. Hutchings, G. J.; King, F.; Okoye, I. P.; Rochester, Influence of sulphur poisoning of copper/alumina catalyst on the selective hydrogenation of crotonaldehyde, *Appl. Catal. A, Gen.* 83 (1992) L7–L13.
- [72] J.A. Heldal, P.C. Mørk, Chlorine-Containing compounds as copper catalyst poisons, *J. Am. Oil Chem. Soc.* 59 (1982) 396–398. doi:10.1007/BF02636051.

- [73] J.M. Christensen, A.J. Medford, F. Studt, A.D. Jensen, High pressure CO hydrogenation over bimetallic Pt-Co catalysts, *Catal. Letters*. 144 (2014) 777–782. doi:10.1007/s10562-014-1220-x.
- [74] R.G. Pearson, J. Dehand, trans-bis(tetracarbonylcobaltato)bis(pyridine)platinum(II) and trans-bis(pentacarbonylmanganato)bis(pyridine)-platinum(II), *J. Organomet. Chem.* 16 (1969) 485–490.
- [75] S. Di, *C. R. Acad. Sc. Paris*, 296 (1983) 127–129.
- [76] G. Kauffman, R.J. Thompson, cis- and trans-dichloro(dipyridine)-platinum(II), *Inorg. Syn.*, 1963. <https://doi.org/10.1002/9780470132388.ch65>.
- [77] S. Banerjee, M.K. Karunananda, S. Bagherzadeh, U. Jayarathne, S.R. Parmelee, G.W. Waldhart, N.P. Mankad, Synthesis and characterization of heterobimetallic complexes with direct Cu-M bonds (M = Cr, Mn, Co, Mo, Ru, W) supported by N-heterocyclic carbene ligands: A toolkit for catalytic reaction discovery, *Inorg. Chem.* 53 (2014) 11307–11315. doi:10.1021/ic5019778.
- [78] A.L. Patterson, The scherrer formula for X-ray particle size determination, *Phys. Rev.* 56 (1939) 978–982. doi:10.1103/PhysRev.56.978.
- [79] D. Lorito, C. Ruocco, V. Palma, A. Giroir-Fendler, F.C. Meunier, Reconstruction of ceria-supported Pt-Co particles under H<sub>2</sub> and CO at 220 °C, *Appl. Catal. B Environ.* 197 (2016) 56–61. doi:10.1016/j.apcatb.2016.01.037.
- [80] S. Brunauer, P.H. Emmett, E. Teller, Gases in Multimolecular Layers, *J. Am. Chem. Soc.* 60 (1938) 309–319. doi:citeulike-article-id:4074706.
- [81] E.P. Barrett, L.G. Joyner, P.P. Halenda, The Determination of Pore Volume and Area Distributions in Porous Substances. I. Computations from Nitrogen Isotherms, *J. Am. Chem. Soc.* 73 (1951) 373–380. doi:10.1021/ja01145a126.
- [82] K.S.W. Sing, D.H. Everett, R. a. W. Haul, L. Moscou, R. a. Pierotti, J. Rouquérol, T. Siemieniewska, Reporting Physisorption Data for Gas/Solid Systems with

- Special Reference to the Determination of Surface Area and Porosity, *Pure Appl. Chem.* 57 (1985) 603–619. doi:10.1351/pac198557040603.
- [83] K.S.W. Singh, J. Rouquerol, G. Bergeret, P. Gallezot, M. Vaarkamp, D.C. Koningsberger, A.K. Datye, J.W. Niemantsverdriet, T. Butz, G. Engelhardt, G. Mestl, H. Knözinger, H. Jobic, Characterization of Solid Catalysts, *Handb. Heterog. Catal.* (2008) 427–582.
- [84] G. Kortüm, *Reflexionsspektroskopie. Grundlagen, Methodik, Anwendungen.*, Springer-Verlag, Berlin, Heidelberg, New York, 1969.
- [85] M. Primet, Electronic transfer and ligand effects in the infrared spectra of adsorbed carbon monoxide, *J. Catal.* 88 (1984) 273–282. doi:10.1016/0021-9517(84)90003-4.
- [86] M.L. Smith, N. Kumar, J.J. Spivey, CO adsorption behavior of Cu/SiO<sub>2</sub>, Co/SiO<sub>2</sub>, and CuCo/SiO<sub>2</sub> catalysts studied by in situ DRIFTS, *J. Phys. Chem. C.* 116 (2012) 7931–7939. doi:10.1021/jp301197s.
- [87] K.I. Hadjiivanov, G.N. Vayssilov, Characterization of oxide surfaces and zeolites by carbon monoxide as an IR probe molecule, *Adv. Catal.* 47 (2002) 307–511. doi:10.1016/S0360-0564(02)47008-3.
- [88] H.G. Hecht, The Interpretation of Diffuse Reflectance Spectra, *J. Res. NBS A Phys. Ch.* 80 (1976) 567–583.
- [89] A. Bartok, M.; Sarkany, J.; Sitkei, Investigation of interactions between metals and adsorbed organic compounds by infrared spectroscopic study of adsorbed CO: I. Infrared study of CO adsorption and desorption on Pt/Cab-O-Sil catalyst, *J. Catal.* 72 (1981) 236–245.
- [90] V. Dees, M.J.; Ponec, The influence of sulfur and carbonaceous deposits on the selectivity and activity of PtCo catalysts in hydrocarbon reactions, *J. Catal.* 119 (1989) 376–387.
- [91] C.A. Menning, J.G. Chen, Regenerating Pt-3d-Pt model electrocatalysts through

- oxidation-reduction cycles monitored at atmospheric pressure, *J. Power Sources*. 195 (2010) 3140–3144. doi:10.1016/j.jpowsour.2009.11.109.
- [92] K.J.J. Mayrhofer, V. Juhart, K. Hartl, M. Hanzlik, M. Arenz, Adsorbate-Induced surface Segregation for core-shell nanocatalysts, *Angew. Chemie - Int. Ed.* 48 (2009) 3529–3531. doi:10.1002/anie.200806209.
- [93] M.K. Gnanamani, M.C. Ribeiro, W. Ma, W.D. Shafer, G. Jacobs, U.M. Graham, B.H. Davis, Fischer-Tropsch synthesis: Metal-support interfacial contact governs oxygenates selectivity over CeO<sub>2</sub> supported Pt-Co catalysts, *Appl. Catal. A Gen.* 393 (2011) 17–23. doi:10.1016/j.apcata.2010.11.019.
- [94] B. Jacobs, G.; Chaney, J. A.; Patterson, P. M.; Das, Maillot, J. C.; Davis, Fischer-Tropsch synthesis: study of the promotion of Pt on the reduction property of Co/Al<sub>2</sub>O<sub>3</sub> catalysts by in situ EXAFS of Co K and Pt LIII edges and XPS, *J. Synchrotron Radiat.* 11 (2004) 414–422.
- [95] N. Tsubaki, S. Sun, K. Fujimoto, Different Functions of the Noble Metals Added to Cobalt Catalysts for Fischer–Tropsch Synthesis, *J. Catal.* 199 (2001) 236–246. doi:10.1006/jcat.2001.3163.
- [96] D. Lorito, A. Paredes-Nunez, C. Mirodatos, Y. Schuurman, F.C. Meunier, Determination of formate decomposition rates and relation to product formation during CO hydrogenation over supported cobalt, *Catal. Today*. 259 (2016) 192–196. doi:10.1016/j.cattod.2015.06.027.
- [97] N.A.G. P. Wynblatt, A model study of catalyst particle coarsening, *Scr. Metall.* 7 (1973) 969–975.
- [98] G.Z. Bian, N. Fujishita, T. Mochizuki, W.S. Ning, M. Yamada, Investigations on the structural changes of two Co/SiO<sub>2</sub> catalysts by performing Fischer-Tropsch synthesis, *Appl. Catal. A Gen.* 252 (2003) 251–260. doi:10.1016/S0926-860X(03)00470-8.
- [99] J.A. Moulijn, A.E. Van Diepen, F. Kapteijn, Catalyst deactivation: Is it predictable?

- What to do?, *Appl. Catal. A Gen.* 212 (2001) 3–16. doi:10.1016/S0926-860X(00)00842-5.
- [100] D.J. Darensbourg, C.-S. Chao, J.H. Reibenspies, C.J. Bischoff, Crystal Structure and Reactivity of  $[\text{Cu}(\text{dmpe})_2][\text{Cu}(\text{Co}(\text{CO})_4)_2]$  (dmpe = 1,2-Bis(dimethylphosphino)ethane): Staggered and Eclipsed Conformations of  $[(\text{CO})_4\text{CoCuCo}(\text{CO})_4]^-$  Anions, *Inorg. Chem.* 29 (1990) 2153–2157.
- [101] P. Chini, S. Martinengo, G. Longoni, Synthesis of the trinuclear anions  $\{\text{Cu}[\text{Co}(\text{CO})_4]_2\}^-$  and  $\{\text{Ag}[\text{Co}(\text{CO})_4]_3\}^-$ , *Gazz. Chim. Ital.* 105 (1975) 203–204.
- [102] R. Fuchs, P. Klüfers, Heteronukleare Komplexverbindungen mit Metall-Metall-Bindungen, V [1] Umsetzungen mit  $[(\text{NH}_3)_2\text{CuCo}(\text{CO})_4]$ : Synthese und Struktur von  $[(\text{PPh}_3)_2\text{CuCo}(\text{CO})_4]$ ,  $[\text{Cu}\{\text{P}(\text{OMe})_3\}_4][\text{Cu}\{\text{Co}(\text{CO})_4\}_2]$  und  $(\text{Ph}_3\text{P})_2\text{N}[\text{Cu}\{\text{Co}(\text{CO})_4\}_2]$ , *Z. Naturforsch.* 46 b (1991) 507–518.
- [103] T. Kawase, S.A. Batcheller, S. Masamune, C. Lett, M. Kuroda, Y. Kabe, M. Hashimoto, S. Masamune, A. Chem, B.R. Adams, R. West, J.A.C. Soc, V.M. Achternbosch, H. Braun, R. Fuchs, P. Klufers, A. Selle, Heteronucleare Komplexe mit  $\text{CuCo}(\text{CO})_4$ -Baueinheiten und Stickstoffliganden \*\*, 101 (1989) 1989–1990.
- [104] D. Van Engent, Preparation of Binuclear Copper-Cobalt Compounds. Crystal Structure of  $(\text{t med})\text{CuCo}(\text{CO})_4$ , 15 (1985) 877–881.
- [105] M. Ohashi, R.P. Barron, W.R. Benson, Electron-Impact-Induced Fragmentation of Quarternary Ammonium Cations, *J. Am. Chem. Soc.* 103 (1981) 3943–3945.
- [106] J. Wang, P.A. Chernavskii, A.Y. Khodakov, Y. Wang, Structure and catalytic performance of alumina-supported copper-cobalt catalysts for carbon monoxide hydrogenation, *J. Catal.* 286 (2012) 51–61. doi:10.1016/j.jcat.2011.10.012.
- [107] Z.-J. Zuo, F. Peng, W. Huang, Efficient Synthesis of Ethanol from  $\text{CH}_4$  and Syngas on a Cu-Co/ $\text{TiO}_2$  Catalyst Using a Stepwise Reactor, *Sci. Rep.* 6 (2016) 34670. doi:10.1038/srep34670.
- [108] N. Topsøe, H. Topsøe, FTIR studies of dynamic surface structural changes in Cu-

- based methanol synthesis catalysts, *J. Mol. Catal. A Chem.* 141 (1999) 95–105. doi:10.1016/s1381-1169(98)00253-2.
- [109] J. Llorca, N. Homs, J. Arana, J. Sales, P. Ramirez De La Piscina, FTIR study of the interaction of CO and CO with 2 silica-supported PtSn alloy, *Appl. Surf. Sci.* 134 (1998) 217–224. doi:10.1016/S0169-4332(98)00225-6.
- [110] A. Dandekar, M.A. Vannice, Determination of the dispersion and surface oxidation states of supported Cu catalysts, *J. Catal.* 178 (1998) 621–639. doi:10.1006/jcat.1998.2190.
- [111] K. Hadjiivanov, T. Tsoncheva, M. Dimitrov, C. Minchev, H. Knözinger, Characterization of Cu / MCM-41 and Cu / MCM-48 mesoporous catalysts by FTIR spectroscopy of adsorbed CO, *J. Catal.* 241 (2003) 331–340.
- [112] T. Tsoncheva, T. Venkov, M. Dimitrov, C. Minchev, K. Hadjiivanov, Copper-modified mesoporous MCM-41 silica: FTIR and catalytic study, *J. Mol. Catal. A Chem.* 209 (2004) 125–134. doi:10.1016/j.molcata.2003.08.008.
- [113] J. Greeley, A.A. Gokhale, J. Kreuser, J.A. Dumesic, H. Topsøe, N.-Y. Topsøe, M. Mavrikakis, CO vibrational frequencies on methanol synthesis catalysts: a DFT study, *J. Catal.* 213 (2003) 63–72. doi:10.1016/S0021-9517(02)00040-4.
- [114] G. a. Beitel, A. Laskov, H. Oosterbeek, E.W. Kuipers, Polarization Modulation Infrared Reflection Absorption Spectroscopy of CO Adsorption on Co(0001) under a High-Pressure Regime, *J. Phys. Chem.* 100 (1996) 12494–12502. doi:10.1021/jp960045f.
- [115] G. Prieto, A. Martínez, P. Concepción, R. Moreno-Tost, Cobalt particle size effects in Fischer-Tropsch synthesis: structural and in situ spectroscopic characterisation on reverse micelle-synthesised Co/ITQ-2 model catalysts, *J. Catal.* 266 (2009) 129–144. doi:10.1016/j.jcat.2009.06.001.
- [116] M. Jiang, N. Koizumi, T. Ozaki, M. Yamada, Adsorption properties of cobalt and cobalt-manganese catalysts studied by in situ diffuse reflectance FTIR using CO

- and CO+H<sub>2</sub> as probes, *Appl. Catal. A Gen.* 209 (2001) 59–70.  
doi:10.1016/S0926-860X(00)00755-9.
- [117] J. Zhang, J. Chen, J. Ren, Y. Sun, Chemical treatment of  $\gamma$ -Al<sub>2</sub>O<sub>3</sub> and its influence on the properties of Co-based catalysts for Fischer–Tropsch synthesis, *Appl. Catal. A Gen.* 243 (2003) 121–133. doi:10.1016/S0926-860X(02)00541-0.
- [118] F.M.T. Mendes, C.A.C. Perez, F.B. Noronha, C.D.D. Souza, D. V. Cesar, H.J. Freund, M. Schmal, Fischer–Tropsch Synthesis on Anchored Co/Nb<sub>2</sub>O<sub>5</sub>/Al<sub>2</sub>O<sub>3</sub> Catalysts: The Nature of the Surface and the Effect on Chain Growth, *J. Phys. Chem. B.* 110 (2006) 9155–9163. doi:10.1021/jp060175g.
- [119] H. Xiong, Y. Zhang, K. Liew, J. Li, Fischer-Tropsch synthesis: The role of pore size for Co/SBA-15 catalysts, *J. Mol. Catal. A Chem.* 295 (2008) 68–76.  
doi:10.1016/j.molcata.2008.08.017.
- [120] S. Sun, N. Tsubaki, K. Fujimoto, The reaction performances and characterization of Fischer–Tropsch synthesis Co/SiO<sub>2</sub> catalysts prepared from mixed cobalt salts, *Appl. Catal. A Gen.* 202 (2000) 121–131. doi:10.1016/S0926-860X(00)00455-5.
- [121] R.G. Heal, M. J.; Leisegang, E. C.; Torrington, Infrared studies of carbon monoxide and hydrogen adsorbed on silica-supported iron and cobalt catalysts, *J. Catal.* 51 (1978) 314–325. [https://doi.org/10.1016/0021-9517\(78\)90269-5](https://doi.org/10.1016/0021-9517(78)90269-5).
- [122] G. Kadinov, C. Bonev, S. Todorova, A. Palazov, IR spectroscopy study of CO adsorption and of the interaction between CO and hydrogen on alumina-supported cobalt, *J. Chem. Soc. Faraday Trans.* 94 (1998) 3027–3031.  
doi:10.1039/a804315i.
- [123] E.L. Rodrigues, J.M.C. Bueno, Co/SiO<sub>2</sub> catalysts for selective hydrogenation of crotonaldehyde II: influence of the Co surface structure on selectivity, *Appl. Catal. A Gen.* 232 (2002) 147–158. doi:10.1016/S0926-860X(02)00090-X.
- [124] L.E.S. Rygh, O.H. Ellestad, P. Klæboe, C.J. Nielsen, Infrared study of CO adsorbed on Co/ $\gamma$ -Al<sub>2</sub>O<sub>3</sub> based Fischer-Tropsch catalysts; semi-empirical

- calculations as a tool for vibrational assignments, *Phys. Chem. Chem. Phys.* 2 (2000) 1835–1846. doi:10.1039/b000188k.
- [125] M. Gupta, V. Schwartz, S.H. Overbury, K. More, H.M. Meyer, J.J. Spivey, Novel Pulse Electrodeposited Co-Cu-ZnO Nanowire/tube Catalysts for C1-C4 Alcohols and C2-C6 (Except C5) Hydrocarbons from CO and H<sub>2</sub>, *J. Phys. Chem. C.* 116 (2012) 10924–10933. doi:10.1021/jp301965s.
- [126] P. Chaumette, P. Courty, A. Kiennemann, R. Kieffer, S. Boujana, G.A. Martin, J.A. Dalmon, P. Meriaudeau, C. Mirodatos, B. Hölhein, D. Mausbeck, A.J. Hubert, A. Germain, A. Noels, Evolution of Alcohol Synthesis Catalysts under Syngas, *Ind. Eng. Chem. Res.* 33 (1994) 1460–1467. doi:10.1021/ie00030a005.
- [127] R.M. Bailliard-Letournel, A.J. Gomez Cobo, C. Mirodatos, M. Primet, J.A. Dalmon, About the nature of the Co-Cu interaction in Co-based catalysts for higher alcohols synthesis, *Catal. Letters.* 2 (1989) 149–156. doi:10.1007/BF00775064.
- [128] Y. Yang, X. Qi, X. Wang, D. Lv, F. Yu, L. Zhong, H. Wang, Y. Sun, Deactivation study of CuCo catalyst for higher alcohol synthesis via syngas, *Catal. Today.* 270 (2016). doi:10.1016/j.cattod.2015.06.014.
- [129] G.L. Liu, T. Niu, A. Cao, Y.X. Geng, Y. Zhang, Y. Liu, The deactivation of Cu-Co alloy nanoparticles supported on ZrO<sub>2</sub> for higher alcohols synthesis from syngas, *Fuel.* 176 (2016) 1–10. doi:10.1016/j.fuel.2016.02.057.
- [130] G. Doyle, K.A. Eriksen, D. Van Engent, Mixed Copper/Iron Clusters. The Preparation and Structure of the Large Planar Cluster Anions, Cu<sub>3</sub>Fe<sub>3</sub>(CO)<sub>12</sub><sup>3-</sup> and Cu<sub>5</sub>Fe<sub>4</sub>(CO)<sub>15</sub><sup>3-</sup>, *J. Am. Chem. Soc.* 108 (1986) 445–451.
- [131] R.G. Finke, T.N. Sorrell, Nucleophilic acylation with disodium tetracarbonylferrate: Methyl 7-oxoheptanoate and methyl 7-oxooctanoate, *Org. Synth.* 59 (1979) 807. doi:10.15227/orgsyn.059.0102.
- [132] R. Lu, D. Mao, J. Yu, Q. Guo, Enhanced activity of Cu – Fe / SiO<sub>2</sub> catalyst for CO hydrogenation to higher alcohols by pretreating the support with ammonia, *J. Ind.*

- Eng. Chem. 25 (2014) 1–6. doi:10.1016/j.jiec.2014.11.013.
- [133] C. Sun, D. Mao, L. Han, J. Yu, Effect of preparation method on performance of Cu–Fe/SiO<sub>2</sub> catalysts for higher alcohols synthesis from syngas, RSC Adv. 6 (2016) 55233–55239. doi:10.1039/C6RA07366B.
- [134] G. Blyholder, Infrared Spectrum of CO Chemisorbed on Iron\*, J. Chem. Phys. 36 (1961) 2036–2039. doi:10.1063/1.1732824.
- [135] C. Sun, D. Mao, L. Han, J. Yu, Effect of impregnation sequence on performance of SiO<sub>2</sub> supported Cu-Fe catalysts for higher alcohols synthesis from syngas, Catal. Commun. 84 (2016) 175–178. doi:10.1016/j.catcom.2016.07.003.
- [136] L.R. Benziger, Jay B.; Larson, An infrared spectroscopy study of the adsorption of CO on Fe/MgO, J. Catal. 77 (1982) 550–553.
- [137] M. Ding, J. Tu, M. Qiu, T. Wang, L. Ma, Y. Li, Impact of potassium promoter on Cu-Fe based mixed alcohols synthesis catalyst, Appl. Energy. 138 (2015) 584–589. doi:10.1016/j.apenergy.2014.01.010.
- [138] D.B. Bukur, D. Mukesh, S.A. Patel, Promoter Effects on Precipitated Iron Catalysts for Fischer-Tropsch Synthesis, Ind. Eng. Chem. Res. 29 (1990) 194–204. doi:10.1021/ie00098a008.
- [139] K. Xiao, X. Qi, Z. Bao, X. Wang, L. Zhong, K. Fang, M. Lin, Y. Sun, CuFe, CuCo and CuNi nanoparticles as catalysts for higher alcohol synthesis from syngas: A comparative study, Catal. Sci. Technol. 3 (2013) 1591–1602. doi:10.1039/c3cy00063j.
- [140] R.J. Meyer, Q. Zhang, A. Kryczka, C. Gomez, R. Todorovic, Perturbation of Reactivity with Geometry: How Far Can We Go?, ACS Catal. 8 (2018) 566–570. doi:10.1021/acscatal.7b03228.
- [141] Georg Thieme Verlag KG, Tammann-Regel, (n.d.).  
<https://roempp.thieme.de/roempp4.0/do/data/RD-20-00170> (accessed November 3, 2018).

- [142] R. Merkle, J. Maier, On the Tammann-Rule, *Z. Anorg. Allg. Chem.* 631 (2005) 1163–1166. doi:10.1002/zaac.200400540.
- [143] A.F. Hollemann, N. Wiberg, *Lehrbuch der Anorganischen Chemie*, 34., De Gruyter, 1995.
- [144] J. Li, X. Liang, D.M. King, Y.B. Jiang, A.W. Weimer, Highly dispersed Pt nanoparticle catalyst prepared by atomic layer deposition, *Appl. Catal. B Environ.* 97 (2010) 220–226. doi:10.1016/j.apcatb.2010.04.003.
- [145] N. Marinkovic, K. Sasaki, R. Adzic, Nanoparticle size evaluation of catalysts by EXAFS: Advantages and limitations, *Zast. Mater.* 57 (2016) 101–109. doi:10.5937/ZasMat1601101M.
- [146] L.T. Zhuravlev, The surface chemistry of amorphous silica . Zhuravlev model, 173 (2000) 1–38.
- [147] T.D. Gould, A.M. Lubers, A.R. Corpuz, A.W. Weimer, J.L. Falconer, J.W. Medlin, Controlling nanoscale properties of supported platinum catalysts through atomic layer deposition, *ACS Catal.* 5 (2015) 1344–1352. doi:10.1021/cs501265b.
- [148] J. Lu, J.W. Elam, P.C. Stair, Atomic layer deposition - Sequential self-limiting surface reactions for advanced catalyst “bottom-up” synthesis, *Surf. Sci. Rep.* 71 (2016) 410–472. doi:10.1016/j.surfrep.2016.03.003.
- [149] N. Cheng, S. Stambula, D. Wang, M.N. Banis, J. Liu, A. Riese, B. Xiao, R. Li, T.-K. Sham, L.-M. Liu, G.A. Botton, X. Sun, Platinum single-atom and cluster catalysis of the hydrogen evolution reaction, *Nat. Commun.* 7 (2016) 13638. doi:10.1038/ncomms13638.
- [150] M. Ding, M. Qiu, J. Liu, Y. Li, T. Wang, L. Ma, C. Wu, Influence of manganese promoter on co-precipitated Fe-Cu based catalysts for higher alcohols synthesis, *Fuel.* 109 (2013) 21–27. doi:10.1016/j.fuel.2012.06.034.
- [151] G.R. Fulmer, A.J.M. Miller, N.H. Sherden, H.E. Gottlieb, A. Nudelman, B.M. Stoltz, J.E. Bercaw, K.I. Goldberg, NMR chemical shifts of trace impurities:

Common laboratory solvents, organics, and gases in deuterated solvents relevant to the organometallic chemist, *Organometallics*. 29 (2010) 2176–2179.

[152] G.M. Sheldrick, Crystal structure refinement with SHELXL, *Acta Crystallogr. Sect. C Struct. Chem.* 71 (2015) 3–8. doi:10.1107/S2053229614024218.

[153] P. Colamarino, P.L. Oriolo, Crystal and Molecular Structures of cis- and trans-Dichlorobispyridine-platinum(II), *J. Chem. Soc., Dalt. Trans.* 0 (1975) 1656–1659. doi:10.1039/DT9750001656.

## 6.7 Abbreviations

ADF	Annular dark-field
aq.	Aqueous
ATR	Attenuated total reflectance
BCC	Body-centered cubic
BET	Brunauer-Emmett-Teller
BJH	Barrett, Joyner, Halenda
Col	Co-impregnation
conc.	Concentrated
DFT	Density functional theory
DMF	Dimethylformamide
DRIFTS	Diffuse reflectance infrared fourier transform spectroscopy
EDX	Energy-dispersive X-ray spectroscopy
Et	Ethyl
EtOH	Ethanol
Eq.	Equation
equiv.	Equivalent
EXAFS	Extended X-ray adsorption fine structure
FCC	Face-centered cubic
FCT	Face-centered tetragonal
FWHM	Full width at half maximum

FT	Fischer-Tropsch or fourier transform
GC	Gas chromatography
GHSV	Gas hourly space velocity
HCP	Hexagonal close packed
HPLC	High pressure liquid chromatography
HR	High resolution
ICDD	International centre for diffraction data
ICP-OES	Inductively coupled plasma atomic emission spectroscopy
( <i>i</i> -)PrOH	(iso-)Propyl alcohol
IR	Infrared
IUPAC	International Union of Pure and Applied Chemistry
max	Maximum
MS	Mass spectroscopy
NMR	Nuclear magnetic resonance
p.a.	<i>Pro analysi</i>
Py	Pyridine
RSD	Relative standard deviation
r.t.	Room temperature
SAED	Selected area electron diffraction
(S)IWI	(Sequential) Incipient wetness impregnation
SSP	Single-source precursor

StE	Syngas to ethanol
(S)TEM	(Scanning) Transmission electron microscopy
Syngas	Synthesis gas
TCD	Thermal conductivity detector
THF	Tetrahydrofuran
tmeda	Tetramethylethylenediamine
WI	Wet impregnation
XRD	X-ray diffraction
XRF	X-ray fluorescence